Durham E-Theses

Photostop

ROWLAND, ADRIAN,MURRAY

How to cite:

ROWLAND, ADRIAN,MURRAY (2013) *Photostop*, Durham theses, Durham University. Available at Durham E-Theses Online: http://etheses.dur.ac.uk/7304/

Use policy

Photostop

Adrian Murray Rowland

Department of Chemistry

University of Durham

A thesis submitted in partial fulfilment of the requirements for the degree of Doctor of Philosophy

2013

Abstract

The use of photodissociation to produce cold, slow molecules from a molecular beam of cold, fast molecules is dubbed "photostop". The essence of the scheme is thus: a pulsed molecular beam of a precursor molecule AB seeded in a noble carrier gas is crossed by a laser beam. The laser light dissociates AB, producing fragments A and B. These recoil from the dissociation site. The speed of the molecular beam and the wavelength of the laser beam are tuned so that the recoil velocity of those A molecules recoiling opposite to the molecular beam direction cancels out their initial velocity. This leaves a certain amount of A close to stationary in the laboratory frame.

The photostop technique was first demonstrated with the production of cold, slow NO by the photodissociation of NO_2, both at Durham and in South Korea. The work described in this thesis began as a development of the NO photostop experiment, with an attempt made to magnetically trap NO. Latterly, the photostop project became part of the Millikelvin Molecules in a Quantum Array (MMQA) collaboration, the aim of which is the trapping of 10^7 cold, polar molecules. To this end, the photostop of SH by the photodissociation of H_2S was demonstrated.

CONTENTS

Declaration

The material contained within this thesis has not previously been submitted for a degree at the University of Durham or at any other university. The research reported within this thesis has been conducted by the author unless indicated otherwise.

Copyright

Acknowledgements

Within academia, my thanks first of all to Dr Eckart Wrede, whose dedication, expertise, patience, and (I suspect on occasion) forbearance I have come greatly to admire. I am extremely grateful for the effort he has put into helping me, despite the fact that I am not officially "his" student. I began this PhD as an inorganic chemist with no practical experience of physical chemistry beyond the second year teaching lab: whatever competence I may have attained since is due almost entirely to his guidance.

Also, my thanks to Drs Jan Verlet and Hendrik Nahler for their occasional advice, loan of textbooks and so forth, and to Dr David Carty for the same, and additionally for recruiting me in 2008, his suggestion of the literature review contained in chapter seven, and his comments on sections of this thesis. Finally, I wish to express my sincere gratitude to Dr Margaret Masson for her sympathetic and extremely efficient manner.

Outside academia, my time in Durham has been made special by my very dear friends, and this seems to be a good place to state how happy I am to know them. In relation to the conduct of this PhD, I am most grateful for the friendship of Drs Rachael Houchin and Alexander Pym. Alex, I thank for our culinary excursions, which helped to keep a little colour in an otherwise extremely grey period of life; for his handy little Excel data-importing macro; and above all for being such a very good friend to me. Rachael, I thank for likewise being a very good friend, and particularly for empathy, hugs, and science fiction of a Sunday evening.

Most of all, I am deeply indebted to Mrs Jean and Dr Colin Woodward, who have been my friends as well as my landlords, and provided over the years a great deal of excellent company and food, along with lifts, occasional nursing, the loan of many items of cookware, and the odd nip of late night gin when it was all getting a bit too much. Having a home in Durham rather than merely a lodging has been such a pleasure and, particularly during the latter stages of this work, a very great comfort to me.

Finally, it seems appropriate to finish by returning to the beginning and expressing my gratitude to my parents and family, for encouraging the love of learning that has led me to this point.

This work, such as it is, is dedicated to the memory of my very dear maternal grandmother, Phyllis Durand, who hung about just long enough to see its completion.

"... only those with their feet on rock can build castles in the air."

"The wages of sin is death but so is the salary of virtue, and at least the evil get to go home early on Fridays."

1   Cold and ultracold molecules are interesting because…

1.1   What are cold and ultracold molecules?

There is not a clear-cut Kelvin-scale definition of 'cold' or 'ultracold'. 'Cold' is most frequently taken to mean a temperature of less than 1 K,[1,2] but Carr *et al.*[3] define the cold regime as being variously between 1K and 1mK, and between 2K and 1mK, within the same review article (page 2 and page 17); and in a similar vein, Bell and Softley[4] assert that cold usually means a temperature from 10K down to 1mK, and a temperature below 1 K, on the same page of the same review article. The definition of 'cold' as '[above] 1 mK' by Dulieu[5] is presumed to be unintended!

'Ultracold', meanwhile, is much more consistently defined as being a temperature below 1 mK,[4,3,2,5] although there is still some variation: Krems[1] puts a minimum bound on the definition (ultracold is between 1 mK and 1 nK), and Quemener[6] and Nesbitt[7] both state that the ultracold regime begins below 1 µK.

This elasticity is explained by the fact that behind these definitions in terms of absolute temperature lie lines drawn on the basis of molecular properties, most especially in relation to the thermal de Broglie wavelength of the gas under consideration,

$$\lambda_{db} = \frac{h}{\sqrt{2\pi mkT}}$$

where m is the molecular mass, and T is the temperature. The gas is cold if the thermal de Broglie wavelength of the particles exceeds their classical size, and 'ultracold' if the thermal de Broglie wavelength is of similar magnitude to the average interparticle separation.

A wider temperature range is pinned upon 'cold' because the term is also used to indicated the temperatures below which interesting physical phenomena which cannot otherwise be observed begin to emerge (see for example section 1.3.1 on cold chemistry) and below which the atom or molecule in question can easily be manipulated or confined by external fields.[8]

Note that 'cold' and 'ultracold' are usually applied to the translational temperature of a sample, although cooling techniques generally also cool the vibrational and rotational degrees of freedom.[5]

1.2   What is temperature?

It is worth taking a step backward at this point and addressing the question of what is meant by "temperature".

In thermodynamics, which deals with bulk matter, temperature is a property of a closed system in thermal equilibrium with its surroundings,[9] and indicates the direction of the flow of energy through a thermally conducting, rigid wall: "A is hotter than B" means "energy will flow from A to B".[*]   Statistical thermodynamics relates temperature to the properties of individual molecules within the bulk: temperature is a parameter which determines the distribution of the molecules in a system over the available energy levels.[10]

As stated above, temperatures quoted for cold and ultracold molecules are generally translational temperatures.   Statistical thermodynamics quantifies the translational temperature for a gas as a parameter in the description of the velocity distribution of the sample – the Maxwell-Boltzmann distribution,[10]

$$f(v) = 4\pi \left(\frac{m}{2\pi kT}\right)^{3/2} v^2 e^{-mv^2/2kT}$$

where $f(v)$ is the distribution of speeds, m is the molar mass, and v is the speed.

A proper discussion of temperature in isolated gases is beyond the scope of this review; it is noted simply that the Maxwell-Boltzmann distribution is often still used to assign a temperature to a cold or ultracold gas, despite the fact that it is not in thermal equilibrium with its surroundings.[11] Frequently, the one dimensional form is used:

$$f(v) = Ae^{-mv^2/2kT}$$

For gases whose centre-of-mass velocity in the laboratory frame is not zero (*e.g.* molecular beams – see section 1.5.1) the velocity spread is characterised using a "floating" Maxwell-Boltzmann distribution in one dimension:

$$f(v) = Ae^{-m(v-v_1)^2/2kT}$$

---

[*] Temperature is more formally defined by the zeroth law of thermodynamics.

1.2.1   Assignment of temperature *via* average kinetic energy

It is known from kinetic gas theory that the temperature and average kinetic energy of a gas are directly related, *via*

$$\langle E_k \rangle = \frac{1}{2} k_B T$$

for the kinetic energy per degree of freedom. The use of this relationship to assign a temperature to gases of "cold" atoms whose distribution of velocities is distinctly non-Gaussian, but whose average kinetic energy can be estimated, is well-established.[9]

1.2.2   Alternative descriptions of temperature

The above methods of defining temperature are by no means used in all work on cold molecular gases. In fact, a statement made by the group of Chandler in their first paper on the kinematic cooling of NO suggests that the above methodology would be the exception rather than the rule: "by convention and for comparison to the results of other researchers, we report the temperature as the ratio of [E_{trans}(NO)/k_B]."[12]

No more authoritative statement than this on standard practice in the field could be found in the course of preparing this literature review, but it is hard to judge its truth when counter-examples exist (*e.g.* the work of Trottier *et al*.[13] or Rangwala *et al*.,[14] both of which papers give "true" Maxwell-Boltzmann temperatures); when many papers do not explicitly state the manner in which they have calculated the temperatures they give; and when no proper review of the matter appears to have been made – despite the many reviews published in the cold molecules field, none read by the author explicitly addressed the issue of assigning temperatures to cold molecular gases.

In any case, it can at least be said that some temperatures given in cold molecules papers are "true" Maxwell-Boltzmann temperatures, and some are simply labels used as a direct description of kinetic energy – kinetic energy is converted to a quantity with units of Kelvin by division by k_B. For clarity and brevity, "temperatures" of this latter kind will be referred to in this thesis as "kinetic temperatures"; it should be stressed that this is not a convention of the field.

There are three things worth noting about the use of kinetic temperatures. Firstly, whilst the difficulty of assigning a temperature to a gas with a non-Gaussian velocity distribution was presumably the original motivation for the use of kinetic temperature, its use does not necessarily imply that the velocity distribution *is* non-Gaussian – for an

example, see the brief discussion in section 3.3.1 on the temperatures claimed by Elioff *et al.*[12] and Trottier *et al.*[13] for their work on NO.

Secondly, the way in which the average kinetic energy ($<E_k>$) is defined is not consistent. As an example, consider again the kinematic cooling work conducted by the group of Chandler (see section 1.5.3). In the first kinematic cooling paper,[12] $<E_k>$ is taken to be the root-mean-squared speed (*i.e.* the standard deviation) of the stopped molecules, but in a later paper published concerning the technique,[15] $<E_k>$ is taken to be the HWHM speed.

Finally, kinetic temperatures can be specified for individual particles, for example as a description of trap depth (*e.g.* Trottier *et al.*[13]).[11]

In summary, when comparing the "temperatures" claimed by different researchers, one must take care that one is comparing comparable values. There is scope for confusion between Maxwell-Boltzmann temperature and kinetic temperature, and for the basis on which kinetic temperature is calculated. It is also worth noticing that the lab frame velocities of *e.g.* molecular beams are often reported in terms of their kinetic temperature rather than, or as well as, their velocity (for example by Kay)[15] and so that care must be taken to be sure whether a kinetic temperature refers to a velocity spread or a centre-of-mass velocity. More usefully, sometimes temperatures are avoided altogether and only velocities and velocity spreads are reported, for example by Hutzler *et al.*[16] in their review of buffer gas cooling.

1.3   Applications of cold and ultracold molecules

At room temperature, the de Broglie wavelength of molecules in a gas is very small, and the particles may be regarded as discrete entities. As described, at cold and ultracold temperatures the thermal velocities of molecules in a gas are vastly reduced, and the de Broglie wavelength increases. It is hoped that a great deal of fundamental physics will be learned through the study of phenomena generated by the concomitant transition from classical to quantum mechanical behaviour, such as Bose-Einstein condensates and Fermi liquids.[3] Aside from the study of quantum degenerate states such as these, and the possibility of quantum simulation (see section 5.1), the main areas of interest are high resolution spectroscopy, and cold collisions and cold chemistry.

1.3.1   Cold and ultracold chemistry

There is a great deal of interest in the prospect of low temperature reaction studies. The motivations for low temperature chemistry may broadly be divided three ways.

Firstly, the sorts of reactions that can occur will also be different: in the absence of external manipulation as described below, molecules will not possess the thermal energy to surmount even the smallest activation energy[4] and so only barrierless or tunnelling reactions may proceed.   More profoundly, the nature of molecular interaction at very low temperatures is fundamentally quantum mechanical.[1] Due to the long de Broglie wavelength of the reacting species, the traditional chemical model of colliding spheres must be disregarded; the wave-like properties of molecular motion – *i.e.*, quantum mechanics – will dominate scattering for small molecules,[4] and be significant even for large.[1] Specifically, scattering at low temperatures is dealt with *via* partial wave analysis, in which the wavefunction describing the motion of the colliding particles is built from a basis set of Legendre polynomials. Collisions are labelled by the angular momentum of the dominant contribution to the scattering amplitude: *S*-wave scattering, *P*-wave scattering *etc*. in just the same way as atomic orbitals are labelled according to their orbital angular momentum.[17] There is a centrifugal barrier to collisions (higher for greater angular momentum) so reactions at very cold temperatures tend to be dominated by *S*-wave scattering.

The second motivation for cold chemistry is that collisions and reactions occurring at low temperatures will involve fewer internal states, collision angular moment states, and scattering channels than reactions occurring at room temperature.[16] This should allow the examination of the effects of specific quantum states of reactants on reactions, and of reactions on the quantum states of their products, details which at room temperature tend to be averaged out by the large number of internal energy states and collisional angular momentum states available to the reactants.[4]

Lastly, long-range intermolecular forces, which are usually overpowered by thermal motion, become important at low temperatures, and can control the orientation of molecules during collisions, and hence the outcome of reactions;[4] overpowering these forces with external fields should allow control to be imposed.[18] Similarly, because the influence of external fields is comparable to the thermal energy at low temperatures, manipulation of the PES with external electric, magnetic or optical fields should lead to control over reactions.[19]

Reactions have been studied at temperatures well below room temperature for quite some time,[20] but only in the last few years has experiment begun to catch up with theory and provided cold and ultracold molecules with sufficient densities to allow the conduct of reaction studies at cold and ultracold temperatures. In 2010, Ospelkaus *et al.*[21] published their work on the reactions of $^{40}K^{87}Rb$ at ultracold temperatures, which demonstrated clearly the quantum mechanical nature of cold collisions discussed above. Two colliding $^{40}K^{87}Rb$ molecules can react to form $K_2 + Rb_2$. The centrifugal barrier height for *P*-wave collisions exceeds the available thermal energy, so *P*-wave collisions lead to reaction *via* tunnelling through the centrifugal barrier. There is no centrifugal barrier to *S*-wave collisions, so the rate of reaction is faster when *S*-wave collisions can occur. Because $^{40}K^{87}Rb$ molecules are fermions, *P*-wave collisions are the lowest energy collisions permitted by symmetry considerations. If the $^{40}K^{87}Rb$ molecules are prepared in a mixture of hyperfine states, *S*-wave collisions become permitted and the rate of reaction increases dramatically.

Other examples of recent work studied resonances. Resonances are very important in cold collisions. For most chemists, the most familiar examples of resonances are found in spectroscopy, where spectra have peaks corresponding to the energetic separation of atomic or molecular energy levels. As for scattering resonances, Fernadez-Alonso and Zare state that "the operational definition of a resonance is a scattering feature that changes sharply as a function of the total energy of the reaction system and which may be associated with metastability of the compound system." Such metastability may for instance be caused by the trapping of a rotational state behind a centrifugal barrier.[22]

In 2012, Chefdeville *et al.*[23] made the first experimental observation of orbiting resonances in inelastic collisions (CO($J = 0$) + H_2($J = 0$) $\rightarrow$ CO($J = 1$) + H_2($J = 0$)), using crossed molecular beams with a 12.5^0 intersection angle. Later in the year, Henson *et al.*[24] published their observations of orbiting resonances in the sub-Kelvin Penning ionisation of both H_2 and Ar with metastable He, using merged molecular beams (section 1.5.4).

An alternative approach to solving the density problem in the study of cold and ultracold chemistry involves the use of Coulomb crystals to study molecule-ion reactions. Due to their extremely localised nature, the component ions of a Coulomb crystal can be individually monitored, allowing the study of their reactions even when the reactant densities are extremely low. This technique has been applied to the study of several ion-molecule reactions.[25]

1.3.2 High resolution spectroscopy

Cooling also finds application in spectroscopy. Spectroscopic resolution is greatly enhanced when the species under investigation is internally cold. Internally cold samples can – and long have been – generated using molecular beams (see section 1.5.1).[26] However, whilst molecular beams are internally cold, they have a large velocity in the lab frame, and so for conventional spectroscopy on molecular beams, the interaction time between applied radiation and the sample is only a few hundred microseconds. Due to the lifetime broadening relation ($\delta E = \dfrac{h}{2\tau}$, where δE is the uncertainty in energy, and τ is the lifetime of the excited state being probed)[17] this limits the resolution of such spectroscopy. If the beam can be slowed, the interaction time is increased, reducing δE and allowing ultra-high-resolution spectroscopy.[27] Narrowing the velocity distribution also reduces the Doppler contribution to broadening.[4]

To give an early example of the utility of spectroscopy conducted on decelerated molecular beams, a Stark-decelerated beam of ND_3 has been slowed sufficiently to allow an interaction time in the region of a millisecond for microwave spectroscopy.[27] ND_3 had previously been studied by microwave spectroscopy on a molecular beam with a velocity as low as conventionally possible (generated from a cooled pulsed source and using the heaviest rare carrier gas, Xe). Whilst the conventional beam had a mean velocity of 280ms^{-1} and produced a linewidth of 10kHz, the decelerated beam had a mean velocity of 52 ms^{-1}, which gave a linewidth of 1kHz and so allowed complete resolution of the hyperfine structure.[28]

It is thought that the improved resolution allowed by the use of slow or trapped cold molecules will allow the study of some fundamental physics: experiments are currently in progress with the aims of measuring the electron electric dipole moment, weak nuclear currents, and anapole moments, and in the search for time variation in various of the fundamental constants, experiments that may produce some of the most important results in physics.[16, 29] For example, the accurate measurement of the electron dipole moment will allow a number of extensions to the standard model to be disqualified, if the dipole moment is found to be smaller than the values predicted by these models. The electron dipole moment has been measured to varying degrees of accuracy by a number of groups, with the most accurate measurements to date being an upper bound of 10.5 x 10^{-28} *e* cm (compared to 10^{-38} *e* cm predicted by the standard

model) by the group of Hinds at Imperial College from measurements on a molecular beam of ytterbium fluoride in argon.[29] The sensitivity of this measurement is expected to be further refined by a series of improvements, including the use of a buffer gas beam source (section 1.5.7) which will provide a more intense and slower beam, and the incorporation of laser cooling (section 1.4.2) to slow the beam further.[30]

1.4   Producing and trapping cold and ultracold molecules

So, how to make cold and ultracold molecules? To achieve very low temperatures in a gas, it is first necessary to confine it in a magnetic, electric, or optical trap – in a material container, it would stick to the walls at low temperatures.[31] For a gas to be held in a trap, its thermal energy must be less than the potential energy barrier of the trap walls, and, for a neutral species, this condition requires significant pre-cooling of the gas:[32] the effective depth of such traps for neutral species is of the order of a single Kelvin.[33]

The generation of ultracold atoms is a well-established science: laser light is used to precool an atomic gas, which is confined in a magnetic trap and evaporatively cooled to ultracold temperatures.[31] The 1997 Nobel prize in physics was awarded "for development of methods to cool and trap atoms with laser light",[34] and the 2001 Nobel prize in physics "for the achievement of Bose-Einstein condensation in dilute gases of alkali atoms…",[35] which was achieved *via* schemes of the type described.

1.4.1   Cooling atoms with laser light

Manipulation of micron-sized particles with laser light was first reported in 1970;[36] proposals for the laser cooling of atoms followed in 1975. The theories describing the force exerted upon atoms by light, and of laser cooling, are complex[37] and will not be discussed here; instead, a simplified view will be given, based mostly on the Nobel lectures[38-40] given for the 1997 Nobel prize in physics, to provide a flavour of the field.

The force first intentionally used to slow and cool atoms was the scattering force, which results from the absorption and emission of an incident photon by an atom.[40] To exploit the scattering force for atomic cooling, an atomic beam and a laser beam of suitable wavelength are directed towards each other. A photon carries not only an energy equal to $h\nu$, but also a momentum equal to $\hbar k$, where k is the wavevector of the photon. When an atom absorbs a photon, it not only gains energy (stored within the

atom by the transition to the excited state), but also momentum: it recoils from the impact with the photon, being slowed by a recoil velocity $v_{rec} = \hbar k/m$. This process must be repeated many times in order appreciably to slow an atom, which means that the atom must relax following absorption.[40] Relaxation requires the emission of a photon, but since emission occurs in a random direction with a symmetric average distribution, emission has no net effect on the momentum of the atom.[38]

Simply directing an appropriately tuned laser at an atomic beam does not bring atoms to rest, however: the Doppler shift – whereby as atoms slow, the relative frequency of the incident light decreases, so that the atoms move out of resonance with the cooling transition – means that the effect is to narrow the velocity distribution of the sample and so to produce a fast moving gas of cold atoms. The problem is usually avoided by the use of chirped laser light (where the frequency of the light is changed to maintain the resonance as the atoms slow), or Zeeman slowing (where a magnetic field is applied to the atomic beam, which shifts the atomic energy levels; the field is stronger at the beam source, and so changes the energy of the transition along the path of the atomic beam to keep it in resonance with the light). By these techniques, atoms can be brought to rest and trapped.[40]

There are more complex laser cooling effects for atoms, which allow cooling to temperatures lower than the minimum temperature attainable by Doppler cooling (the so-called Doppler limit, T_D, is reached when Doppler cooling is balanced by heating of the atoms due to emission,[25] and is typically of the order of several hundred μK[9]) but this brief look at the scattering force provides sufficient background for the following discussion.

1.4.2   The laser cooling of molecules

As stated, cooling with laser light has been very successfully applied to atomic gases. However, it cannot easily be applied to the vast majority of molecules (or indeed to the majority of atoms[41]) due to a problem that has been glossed over thusfar: optical pumping into dark states. The cooling processes described require repeated absorption and emission (usually in the order of 10,000 cycles):[16] hence, if the excited state of the cooling transition has a reasonable probability of relaxing to a state other than that from which it was excited, effective cooling is not possible. In atoms with simple energy level structures, this problem is overcome by pumping the sample with further "re-pumping" lasers, which stimulate transitions that return the atom to the

correct ground state.[40] Most molecules, with their much more complex energy level structure, would require an unfeasibly large number of repumping lasers in order for a straightforward adaptation of this scheme to succeed.[4]

A number of molecular candidates for laser cooling have been proposed. Di Rosa[42] identified the properties required of a molecule for laser cooling to be applied: a strong one photon absorption band (to allow rapid laser cooling); leading to an electronic excited state unlikely to decay to any state but the ground state (to allow a closed cooling transition); with a strongly diagonal Franck-Condon array for the relaxation, so that the relaxation returns the molecule to the correct vibrational level in the ground state (again to allow a closed cooling transition). This last requirement is the one on which most molecules fail: relaxation frequently results in dispersion across a number of vibrational levels, which when combined with the limited spread of rotational relaxation ($\Delta J = 0, \pm 1$, leading to up three rotational levels being populated for each vibrational transition), implies the necessity for the experimentally taxing number of repump lasers mentioned above. This situation is illustrated nicely by the relaxation of excited CO in Figure 1.1.
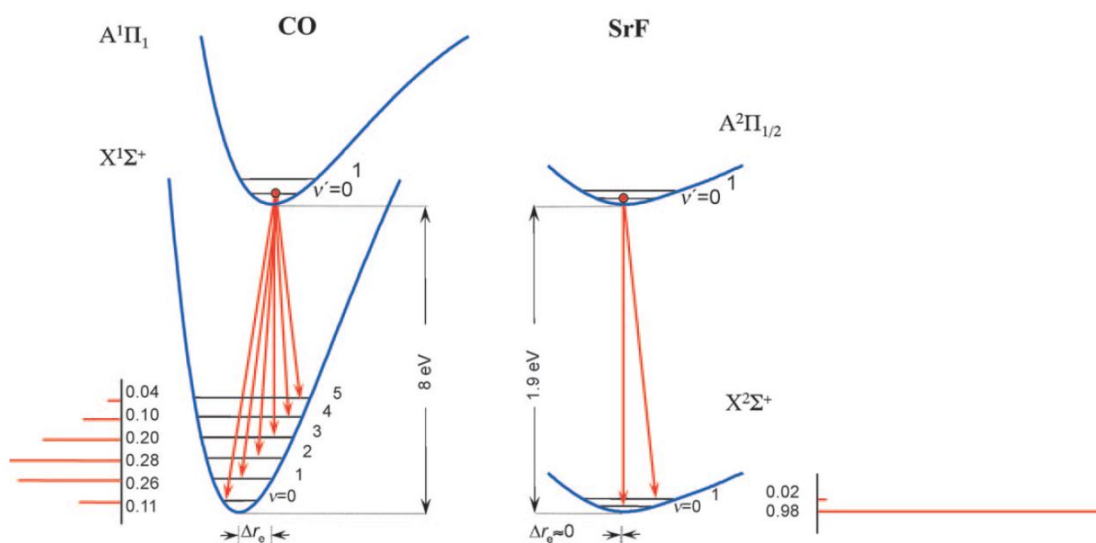
Figure 1.1: a comparison of relaxation from the first excited state in CO and SrF. The relaxation of CO produces a substantial ground state population in six vibrational levels, rendering it unsuitable for laser cooling. The relaxation of SrF, by contrast, leads to a substantial population in only two ground state vibrational levels, and laser cooling of SrF was demonstrated in 2010. Figure reproduced from Marian and Friedrich.[43]

Di Rosa suggested a number of diatomic molecules with highly diagonal Franck-Condon arrays, to which laser cooling could likely be applied: BeH, MgH, CaH, SrH, BaH,

NH, BH, AlH, AlF, and AlCl. Stuhl *et al.*[29] identified a group of molecules for which laser cooling might be even easier: those fulfilling the requirements of Di Rosa, and also having an absence of nuclear spin, to preclude hyperfine splitting, and having a ground state with a higher angular momentum than the excited state so that the relaxation step can occur to only a single rotational level (e.g. if the lowest rotational level in the ground state was $J = 1.5$, and the excitation was made to a $J = 0.5$ state, decay could only occur back to the $J = 1.5$ level). Molecules identified as bearing these properties included TiO, TiS, FeC, ZrO, HfO, ThO, and SeO.

The first successful laser cooling of a molecule was demonstrated in 2010,[44] when a cryogenic buffer gas beam of SrF was cooled in one (transverse) dimension to a temperature of 300 μK. SrF satisfies the strong absorption and Franck-Condon requirements, and also takes advantage of the rotational restriction noted by Stuhl *et al*. Molecules that decayed into undesired spin-orbit or hyperfine states were re-excited by sidebands on the cooling lasers. Decay also resulted in the population of dark Zeeman sublevels of the ground state; these were forced to Larmor precess into bright states by application of a magnetic field (at any angle not parallel or perpendicular to the linear laser polarisation).

Following this success, it was demonstrated that laser slowing of an SrF buffer gas beam was also possible; it was thought that combination of laser slowing and transverse cooling should allow loading of a trap with SrF.[45] It has also been shown that the Franck-Condon factors of YbF and TlF (both used in measurements of the electron dipole moment) should make them amenable to a similar laser cooling scheme to SrF.

More complex schemes have also been proposed, to make laser cooling applicable to a wider variety of molecules by showing that Doppler cooling is possible between electronic states with an intermediate electronic level (which apparently makes BO, AlO, GaO, InO, and TlO available);[46] or to apply the more powerful bichromatic force, which involves many cycles of excitation and emission occurring for each laser pulse, to make decelerating molecules easier.[47]

1.5   Techniques aside from laser cooling

Despite the recent demonstration of laser cooling of molecules, and the possibility of further accomplishments, laser cooling of molecules seems likely to be applicable to

only a tiny minority of molecules for the moment. Further, laser cooling has only been applied to buffer gas beams – which are slow and substantially precooled: *i.e.* laser cooling has only been demonstrated to work in combination with another cooling technique. So, whilst laser cooling of molecules is a valuable addition to the field (particularly in its potential use in bridging the gap between the temperatures attainable by most molecular cooling techniques, and the ultracold regime, a theme explored in section 1.5.11) its advent does not diminish the importance of the molecular cooling techniques developed in its absence. These techniques are surveyed below.

1.5.1   Molecular beams

Many cooling techniques work to slow molecules that have been cooled in a molecular beam. A molecular beam is generated (in the simplest scheme) as follows. Gas is expanded through a nozzle from a (relatively) high-pressure reservoir into a chamber at lower pressure, forming a gas jet. If the size of the hole through which the jet escapes is much smaller than the mean free path of the molecules in the source, molecules find their way out without colliding, and so form a jet with the same distribution of velocities and internal energies as the source – an effusive beam. If, however, the mean free path of the molecules in the source is smaller than the orifice – because the orifice is larger, or the source pressure is higher, than for the effusive case – many collisions occur in the expansion region, and a supersonic beam is produced.[27]

What does this mean? The many elastic collisions occurring in the expansion region (a situation known as hydrodynamic flow) transfer momentum into the direction of the jet,[10] and narrow the velocity spread of the gas jet in this direction, so that the gas becomes translationally cold.[26] Away from the expansion region, the combination of translational cooling and the decrease in density resulting from expansion leads to the jet entering a condition of molecular flow, where very few collisions take place between the molecules.[10] After this point, the jet passes through a skimmer. The resulting collimation removes the warmer, divergent outer portions of the jet, and after this point it is referred to as a molecular beam.[26]

Inelastic collisions also occur during the expansion, and cause rotational and vibrational cooling, with the energy being transferred to translational motion – Levy[26] describes the cooled translational degrees of freedom as being a cold bath for the internal degrees of freedom. Rotational and vibrational modes equilibrate more slowly

than translational modes (the latter the slower) so rotational and vibrational temperatures on the order of 10 K and 100K respectively are achieved[10] (although it should be noted that rotational temperatures following expansion are frequently non-Boltzmann in nature, and are sometimes quantified by a quantity related to the average rotational energy of a molecule in the beam).[48]

Gases can either be expanded pure or mixed with ("seeded in") a carrier gas, which is generally one of the noble gases. Being monoatomic, the noble gases do not have vibrational or rotational degrees of freedom and cannot undergo inelastic collisions, which serves to increase the efficiency of both translational and internal cooling.

1.5.2 Slowing molecular beams, and the difference between slowing and cooling

So, expansion of a gas into a molecular beam is a simple mechanical means to produce a translationally cold gas, whilst simultaneously cooling its internal degrees of freedom. However, there is a fly in the ointment, as might be guessed from the term "*supersonic* molecular beam": the cooling in the hydrodynamic flow region means that the molecules in the beam are moving slowly relative to each other, but it also dramatically raises the average velocity of the gas, so that in the frame of the laboratory the beam is moving very fast indeed. In the work described in chapter four of this thesis, for example, a molecular beam of NO_2 seeded in xenon has a translational temperature of 2.6 K along its axis of travel, but a speed approaching 400 ms^{-1} in the laboratory frame. In order to make use of expansion-cooled molecules for many of the sorts of applications described in section 1.3, they must be slowed or brought to a halt in the lab frame, as depicted schematically in Figure 1.2. A number of techniques have been developed to do this. Some – kinematic cooling, mechanical cooling, and the photostop technique that is the subject of this thesis – achieve this in a single event; some – Stark and Zeeman deceleration – over many repeated applications of the slowing force.

It is appropriate at this point to make explicit a distinction this account has thusfar ignored: that not all processes that slow molecules decrease their temperature. To quote Elioff *et al.*,[12] "The term "cooling" is reserved for processes that compress the velocity distribution by slowing the particles with higher velocities more efficiently than they slow particles with lower velocities." This distinction is apparent from consideration of Figure 1.2. The first step (upper panel) which transforms the room temperature backing gas into the cold molecular beam, involves a sharp tightening of

the velocity distribution, which can only be achieved by a force that acts more upon faster molecules than slower ones, and must plainly change the parameter T in the function that describes the velocity distribution. The second step (lower panel) acts to change the velocity centre of the molecular beam within the laboratory frame, but does nothing to change the velocity spread, and hence the parameter T in the description of the velocity spread remains unchanged.
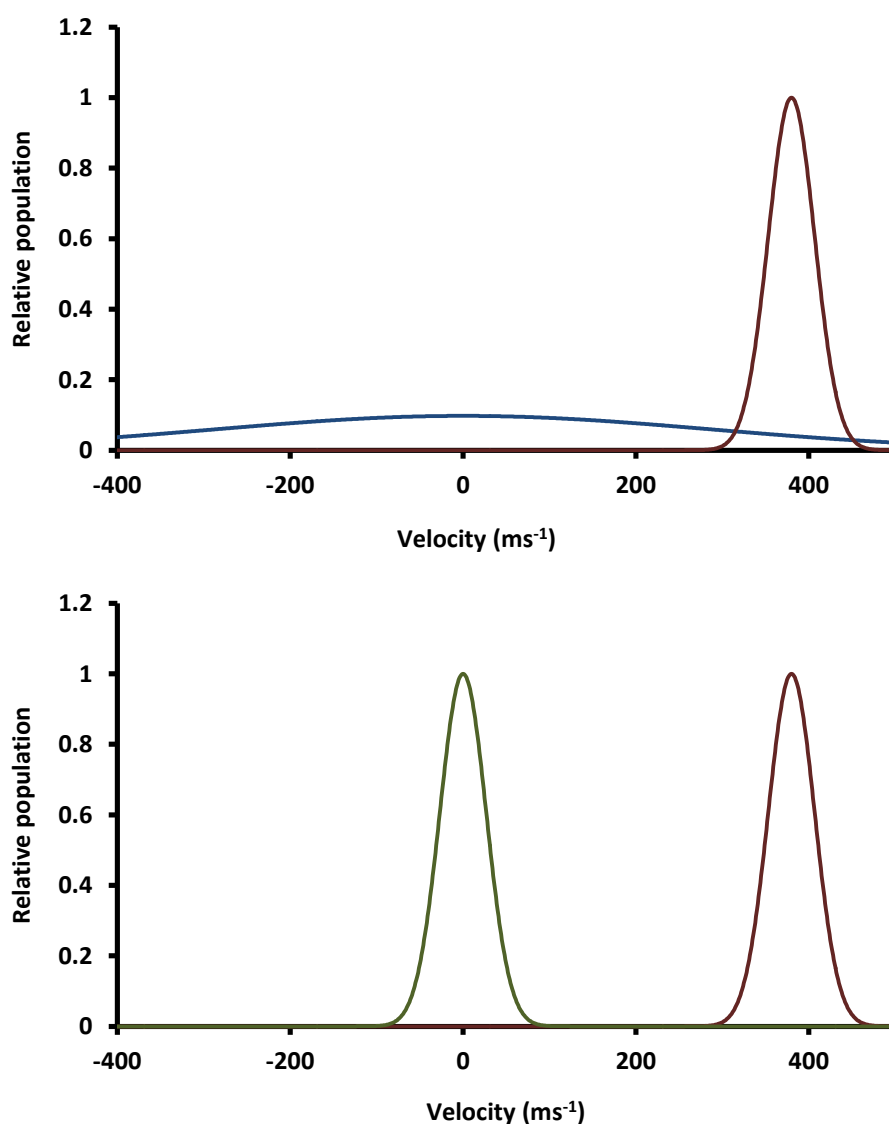
Figure 1.2: upper panel: the generation of a molecular beam converts a high T distribution centred at zero velocity (blue) into a low T distribution centred at high velocity (red). Lower panel: slowing processes must be used to re-centre the low T distribution at zero velocity (green). These graphs are generated using the typical parameters for the NO_2/Xe molecular beams used in chapters 4 and 5, and display the velocity distribution of NO_2. Blue: T = 298 K, v_1 = 0 m s^{-1}; red: T = 2.6 K, v_1 = 380 m s^{-1}; green: T = 2.6 K, v_1 = 0 m s^{-1}.

The above quotation from Elioff continues "[Cooling] increases the phase space density of the molecules." Phase space density (ρ) is given by

$$\rho = n\lambda_{deB}^{\;3}$$

where n is the number density of the gas, and $\lambda_{deB}^{\;3}$ is here the thermal de Broglie wavelength.

Phase space density quantifies intermolecular separation in terms of the de Broglie wavelength, and so accounts for both temperature and density;[4] as described in chapter one, both are critical to many of the novel features of cold matter, and as such phase space density is often used as a measure of "coldness".[49]

There follows a survey of the techniques used to slow molecular beams: kinematic cooling, mechanical cooling, Zeeman deceleration, and Stark deceleration. The photostop technique that is the subject of this thesis is addressed in chapter three.

1.5.3   Kinematic cooling

In kinematic cooling, molecules in a molecular beam are brought to a halt by collisions with a second, crossed, molecular beam (the use of trapped atoms as the collision partner has also been proposed).[50] Most of the molecules recoiling from the collision are lost, but the fraction whose recoil velocity is approximately equal and opposite to the centre of mass velocity is left almost stationary in the lab frame. It is potentially a very general technique, because it relies only upon the relative momenta of the colliding molecules rather than any specific molecular properties.[12] Despite this, it has been demonstrated only for NO seeded in argon,[12, 51,52] and for ND_3 seeded in neon.[15]

The NO work was able to produce samples of $NO(^2\Pi_{1/2}, v = 0, J = 7.5)$ with densities of 10^8 to 10^9 cm^{-3}, centred at zero velocity and with a kinetic temperature of 400mK.[12] A later experiment, using a lower concentration of argon, produced molecules at temperatures estimated at only 35mK with a lifetime in excess of 150 µs (contrasted with less than 10 µs in the previous experiments) but with a lower density estimated at 10^6 cm^{-3} at the end of the measured decay.[52] The ND_3 work produced samples of ND_3 moving at a few tens of metres per second, with centre-of-mass temperatures of similar magnitude (although calculated and asserted to be lower) and unknown density.[15]

Use of reactive scattering to achieve the same effect has also been demonstrated. A beam of slow KBr was generated, with a peak velocity of 20 ms^{-1} and a density of about 10^7 cm^{-3}.[53]

1.5.4 Mechanical cooling methods

A couple of mechanical cooling methods have been demonstrated. In one, a beam of the species to be decelerated was reflected from a fast-receding atomic mirror (a silicon wafer mounted on a fast spinning rotor). Whilst its proponents asserted it should be applicable at least to light molecules, this technique has been demonstrated only in a proof of principle experiment in which the speed of a beam of helium atoms was approximately halved whilst its translational distribution was maintained.[54]

The other mechanical method has been pioneered by Herschbach, and is based on the simple observation that the forward velocity of a molecular beam may be largely cancelled out if the beam source has a large velocity in the opposite direction. This has been achieved experimentally by using a nozzle counter-rotating with sufficient velocity to negate the speed of the gas jet issuing from it. The rotating nozzle is contained behind a barrier pierced by a small aperture: obviously, the nozzle issues gas in all directions, and those molecules in a small angular range are selected by the aperture to form a slow molecular beam[55] (later refinements substituted this constant gas emission for a pulsed source).[56] In theory, the velocity spread of the beam should also be reduced by increased pressure created in the nozzle tip by the centrifugal force generated by the rotation, but whilst this effect has been observed in some cases, the opposite has been true in others.[55]

This method of cooling has been demonstrated for several noble gases, pure beams of SF_6, and pure and seeded beams of O_2 and CH_3F,[57] and ND_3.[58] Beam speeds as low as a few tens of metres per second, with a velocity spread of comparable magnitude were achieved in some cases, the slowest being CH_3F in xenon with a speed of 91 ms^{-1} and a FWHM velocity spread of 94 ms^{-1} (corresponding to kinetic temperatures of 17 K and 18 K respectively).

The technique suffers from the problem that the transverse spread of a molecular beam increases markedly for slower beams, causing for instance a factor of 100 decrease in density for a xenon beam at 100 ms^{-1} produced by a rotation source compared to a xenon beam produced with a speed of about 300 ms^{-1} by a stationary

source. Strebel *et al.*[58] used an electrostatic quadrupole guide to counteract this tendency, but this is only useful for molecules with a Stark shift. Sheffield *et al.*,[56] meanwhile, have proposed that the use of merged molecular beams, one originating from a conventional beam source, the other from a rotating nozzle and tuned to match very closely the speed of the first, could be extremely useful in the study of collisions in the mK range whilst bypassing the need to make – in the lab frame – slow molecules.

1.5.5   Zeeman deceleration

When moving through a magnetic field that is inhomogeneous along the axis of their motion, paramagnetic molecules can gain Zeeman energy (potential energy) and, concomitantly, lose kinetic energy, as discussed in section 5.2.1. A Zeeman decelerator is a series of solenoids, which are switched so that the pulsed magnetic fields thus generated can decelerate such molecules in a manner superficially reminiscent of Sisyphus cooling of atoms (except that Zeeman deceleration is a slowing rather than a cooling technique),[59] or which are used to generate a moving magnetic trap.[19] The only molecular species to which its successful application has been reported is oxygen, which was slowed from 389 ms^{-1} to 83 ms^{-1},[60] but it should be applicable to any species with a permanent magnetic moment – which is to say, any paramagnetic species, which includes most molecular radicals.[60] Indeed, it has been used to decelerate a number of atomic species: hydrogen,[59, 61, 62] deuterium,[61] metastable argon,[63] and metastable neon;[64,65] metastable neon has been brought to a halt,[66] and atomic hydrogen has been magnetically trapped following Zeeman deceleration.[67]

1.5.6   Stark deceleration

Stark deceleration is the electric analogue of Zeeman deceleration: a Stark decelerator is a series of electrode pairs, which are switched rapidly so that the pulsed electric fields thus generated can decelerate polar molecules in appropriate quantum states, which experience a change in Stark energy (potential energy) on moving through an inhomogeneous electric field.[68, 69]

Stark deceleration has been applied to molecular beams of CO, H_2CO, LiH, NH, ND_3, NH_3, OH, OD, SO_2, YbF, CaF, and benzonitrile. The technique can bring beams to zero velocity with densities typically between 10^6 and 10^9 cm^{-3}.[70] Just like Zeeman deceleration, Stark deceleration can also be achieved using travelling potential wells.

Such decelerators require a lower field strength, which allows the slowing of heavy diatomic molecules to which conventional Stark deceleration could not be applied.[70]

The groups of Softley and Merkt have developed the application of Stark deceleration to Rydberg molecules, which, potentially, allows its use for all molecules: Rydberg states usually have a very large first order Stark shift, which has the same effect as a molecular dipole, and makes the molecule amenable to Stark deceleration. It is also noteworthy that the large size of the Stark shift means that much weaker electric fields can be used for Stark deceleration.[71] There are limitations to the use of Rydberg states – they must be generated in sufficient density, and are short-lived, and made more so by the very electric fields used in deceleration – but nonetheless, H_2 has been slowed[71] and trapped by this method, with an estimated trapped density of $10^6 – 10^7$ cm^{-3}.[72,73] Atomic H[74] and Ar[75] have also been slowed.

Slowing can also be achieved *via* the second order Stark shift. High intensity lasers are used to induce a dipole in the molecule to be slowed, which interacts with the electric field gradient of the light. In the first (and simplest) application of the technique, a 15 ns laser pulse was fired through a molecular beam along a perpendicular axis. This single pulse was sufficient to slow the molecular beam by 15 ms^{-1}.[76] Optical deceleration should be a very general cooling technique, as any molecule in a cold molecular beam should in theory be a candidate;[77] the optical lattice method of deceleration has so far been applied to NO,[77] benzene,[78] and molecular hydrogen,[79] removing a significant percentage of the molecular beam velocity (up to 75% for benzene) at a cost of broadening the starting velocity distribution.[79]

1.5.7   Buffer gas cooling

Not all techniques for produced cold molecules begin from a supersonic molecular beam. The technique of buffer gas cooling was proposed[80] and developed for neutral atoms and molecules by the group of Doyle, and more recently has been adopted by several other groups. Buffer gas cooling occurs by elastic collisions between the gas being cooled and a very low temperature buffer gas; the buffer gas is usually cryogenically cooled helium, as it is the only stable substance with an appreciable vapour pressure at $\sim$1K,[41] but neon has also been used. The atoms or molecules are cooled by collisions with the buffer gas. The great advantage of buffer gas cooling is its generality: as it relies only upon elastic collisions with the buffer gas, rather than the

internal structure of the particle being cooled, it can be applied to almost any atom or small molecule, and some larger molecules.[16]

The initial buffer gas cooling experiments mostly followed the same general method.[41] The cooling process was conducted in a cryogenically cooled helium cell, itself contained within a magnetic trap. The atoms or molecules to be cooled were in most cases introduced to the area of the trap by laser ablation of a solid sample fixed within the cell. Before the start of the experiment, the helium buffer gas was condensed on the walls of the cell; the correct density of helium vapour was generated either by heating the walls of the cell, or by desorption from the walls with the same laser pulse used for ablation of the sample. Once the atoms or molecules had cooled, the helium was removed from the trap by cooling the cell, which caused the helium to condense on its walls; the helium was not itself trapped as it has a very small magnetic moment.[81] Paramagnetic molecules in low field seeking states cooled to lower kinetic energies than the trap depth were trapped. A number of neutral species, both atomic (europium,[82] chromium,[83] molybdenum,[84] and number of rare earth metals[85]) and molecular (CaH,[86] NH,[87] and CrH and MnH[88]) were cooled and trapped, and several more cooled but not trapped (VO,[89] PbO,[90] and CaF[91]).

This combined cooling/magnetic trapping scheme restricts buffer gas cooling to paramagnetic molecules (and more specifically to paramagnetic molecules for which the rate of spin relaxation induced by collision with He is low).[41] Buffer gas cooling is more generally applied by the production of buffer gas beams from a cryogenic cell with a small hole in the wall. The cell is continually loaded (by ablation with a pulsed laser) with the atoms or molecules being cooled, and also with helium buffer gas. The majority of the species/buffer gas mixture adheres to the walls, but a fraction exits the cell through the hole, forming a beam. Such beams are typically more intense and slower than supersonic beams, and their characteristics are reviewed in detail by Hutzler *et al*.[16] Buffer gas beams of BaF, CaH, CH_3F, H_2CO, ND_3, O_2, PbO, SrF, SrO, ThO, YbF, and YO have been generated; beams of the atomic species K, Na, Rb, and Yb have also been made. Kinetic temperatures of the beams have been as low as 190 mK, with velocity spreads on the order of a few Kelvin; fluxes have been in the region of 10^8-10^{12} s^{-1}, or 10^8-10^{11} sr^{-1} $pulse^{-1}$.[16]

1.5.8   Velocity selection

Velocity selection is a very different approach to all others outlined: it does nothing to cool or to slow molecules, but instead selects the coldest molecules from a beam by picking out the tail of its Maxwell-Boltzmann distribution with a bent electrostatic or magnetic guide. It is included in this section because it has been applied to buffer gas beams.

The gas moves through the guide, and at the bend only those molecules with kinetic energies lower than their Stark or Zeeman shift (in the case of low field seeking molecules) are deflected and guided around the curve; most molecules overshoot and are lost, and in this manner the guide picks out a continuous, cold sample. H_2CO, ND_3,[14] D_2O,[92] CH_3F, CH_3CN, CH_3CHO, CH_3NO_2,[93] C_6H_5CN, CH_3I, and C_6H_5Cl[94] have all been velocity selected, with kinetic temperatures as low as a few Kelvin, similar longitudinal translational spreads, and fluxes of up to 10^9 s^{-1}. It should be noted that the coldest temperatures and the highest fluxes were not in the same experiment: the work of Bell *et al.*[93] is representative of the lowest temperatures achieved and reports fluxes in the region of 10^6 s^{-1}.

1.5.9   Photoassociation and Feshbach resonance tuning

As discussed in section 1.4.1, atomic cooling is a mature field, and very cold, dense atomic gases are routinely made. Photoassociation and Feshbach tuning bypass the need to cool molecules by producing molecules from ultracold atoms – a totally different approach to those surveyed above.

If two colliding atoms simultaneously absorb a photon of the right frequency, the collision can result in the formation of a molecule in an electronically excited state. This is photoassociation, and can happen if the sum of the collision energy and the photon energy is equal to the energy of the bound state.[95]   Experimentally, photoassociation is achieved by continuously irradiating the sample with laser light detuned slightly below the excitation transition. When two free atoms move close enough together, their energy levels are perturbed by their interaction, and the excitation can occur.[4] The excited complex can then relax to a more tightly bound state by emission of a photon, although decay back to separate molecules is also likely.

For some years, photoassociation has been a tool for making short-lived molecules for high resolution spectroscopy, but more recently has been used to produce longer lived

ultracold molecules.[95] This has required some modification of the technique: in most cases, the overlap between the excited and ground states is poor, and relaxation to the ground state is greatly outweighed by decay back to separate atoms. Formation of a significant number of molecules requires either an unusual energy level structure (as for Cs_2, for example)[95] or the use of various stimulated emission processes to enhance relaxation to the ground state,[4, 96, 97] or at least to a metastable state;[95] perhaps the best known of these processes is stimulated Raman adiabatic passage, or STIRAP.[98]

Feshbach tuning is likewise performed on cold atoms, and involves the tuning of their hyperfine energy levels with an applied magnetic field, in order to enhance the probability of collisions between atoms resulting in the formation of molecules.[99] As with photoassociation, molecules are produced by Feshbach tuning in highly vibrationally excited states, and must be transferred to more tightly bound states by similar means to those described above.[4, 100] The greatest phase space density gas of cold molecules thusfar produced by any method was made by Fesbach resonance tuning followed by STIRAP, by which means were made approximately 3×10^4 $^{40}K^{87}Rb$ molecules with a peak density of 10^{12} cm^{-3} and a translational temperature of 350 nK.[96]

1.5.10 Trapping techniques

Much work of the sort described above is carried out in the eventual aim of confining the molecules so slowed in a trap, to allow further cooling to ultracold temperatures. Trapping does not require stationary molecules – molecules decelerated to a few tens of metres per second in the lab frame have been trapped (see section 5.2.1, for example), so there is scope for trapping to be combined with many of the techniques discussed above.

Trapping forces can be provided by electric, magnetic, and optical fields, by the same principles by which these fields are applied to slow molecules. The Stark effect can be used to trap polar molecules; likewise, molecules with a permanent magnetic moment can be held within a magnetic trap. Combined electrostatic and magnetic traps have also been employed.[70] Both tightly focussed single laser beams and optical lattices have been used to trap molecules.[4]   Magnetic trapping, which was employed in the course of this PhD, is discussed further in chapter 5.

1.5.11 Achieving high phase space densities with molecules

The sorts of temperatures and densities achieved by the cooling and slowing techniques described largely fall short of those required for many of the applications discussed earlier in this chapter. Until very recently, only Feshbach tuning has been able to produce very cold, dense samples of molecules, with the first molecular Bose-Einstein condensates having been made *via* Feshbach tuning.[35]

Unfortunately, Feshbach tuning (like its closest competitor, photoassociation) can only be used to make simple alkali dimers. The creation of cold, dense samples of a more diverse range of species will require the use of the other cooling techniques described above to produce high density trapped samples of cold molecules, and then the application of further cooling techniques developed for atoms: laser cooling, sympathetic cooling, and evaporative cooling.

The laser cooling of molecules was discussed in section 1.4.2. Whilst the 2010 work of Di Rosa demonstrated that laser cooling might be an extremely effective cooling technique for a very limited range of molecules, other more general techniques had not been demonstrated, until at the end of 2012 Zeppenfeld *et al*.[101] published work on the Sisyphus cooling of a polyatomic molecule (CH_3F), a technique that would still require combination with sympathetic or evaporative cooling.[102] There are other laser based techniques under investigation,[70] such as cavity assisted laser cooling, which has again been successful for atoms,[103] and might be applicable to molecules because the cooling force is largely independent of the internal energy structure of the target[104] – but this scheme too has not yet been realised.[70]

Sympathetic cooling is similar to buffer gas cooling, except that where buffer gas cooling immerses the sample in helium to reduce its temperature to ~ 1K, sympathetic cooling should be able to bring the temperature of the sample down to the μK regime by mixing the sample with ultracold alkali metal atoms – which can, as discussed, be produced as a matter of routine. Sympathetic cooling has been successfully applied to atoms, but success with molecules is yet to be forthcoming.[70]

Evaporative cooling has likewise been very successfully applied to atoms. It is conceptually simple: from a trapped population of molecules, those with the highest kinetic energy are allowed to evaporate; the remaining molecules rethermalize through collisions, with a lower average temperature than before, and the process is repeated.[105] The application of evaporative cooling to molecules is often difficult, because the rate of elastic collisions (required to thermalize the trapped population) is

usually lower than the rate of inelastic collisions that lead to trap loss.[106]   However, Stuhl *et al.* recently demonstrated that evaporative cooling can be used to cool at least some molecular species, by evaporatively cooling OH.[107]

2 Experimental techniques

This chapter provides an introduction to the most important experimental techniques used in this PhD: laser induced fluorescence spectroscopy, resonance enhanced multiphoton ionisation, and velocity mapped ion imaging. The relevant aspects of molecular beam theory have already been reviewed in chapter one, and magnetic trapping will be dealt with in chapter five.

2.1 Laser induced fluorescence spectroscopy

When exposed to light of a wavelength corresponding to the energetic separation of two of its electronic energy levels, an atom or molecule may be able to absorb this light and be excited to the higher energy state. The excited complex can relax to a lower lying state in a number of ways; one is to re-emit its excess energy as a photon of the appropriate wavelength, a process termed fluorescence.

Laser induced fluorescence, commonly abbreviated to LIF, is a spectroscopic technique in which laser light is used to excite an atom or molecule to a higher energy state, and the intensity of the consequent fluorescence is measured using a photomultiplier tube (PMT).[10]

Because laser light has a very narrow bandwidth, LIF is highly state specific: excitation occurs from a single specific ro-vibrational lower state to a single specific ro-vibrational upper state, as depicted in Figure 2.1. The measured fluorescence intensity can therefore be ascribed to the population of this specific lower state, and fluorescence excitation spectra are produced by measuring fluorescence signal as a function of excitation laser wavelength. LIF can also be used to monitor the variation over time in the population of a specific lower state, by fixing the excitation laser on a single transition. Some of the considerations that must be made when planning a LIF experiment are discussed below.

The transitions that can be excited are limited by the absorption cross section of the molecule in question, which is in turn determined by the relevant selection rules, and by the Franck-Condon principle. The wavelength of the fluorescence produced is determined by the Franck-Condon principle, and the time over which it can be

collected is dictated by the fluorescence lifetime. The amount of fluorescence produced must also be considered, and this is quantified by the fluorescence quantum yield.

2.1.1 Excitation considerations

The starting point when selecting a LIF transition is to choose an electronic transition that is allowed by the specific selection rules. For diatomic molecules (the only sort to which LIF is applied in this work), the selection rules governing electronic transitions are:[108]

$$\Delta\Lambda = 0, \pm 1$$

$\Delta S = 0$ (considerably relaxed for molecules containing heavy atoms and so having strong spin-orbit coupling)

$\Delta\Sigma = 0$ (for Hund's case a)

$$\Delta\Omega = 0, \pm 1$$

$\Sigma^+ \leftrightarrow \Sigma^+$ and $\Sigma^- \leftrightarrow \Sigma^-$ can occur, but $\Sigma^+ \leftrightarrow \Sigma^-$ cannot

$$g \leftrightarrow u$$

Selection of an allowed transition should produce a reasonable absorption strength; in many cases, this can be cross-checked by reference to a measured absorption cross-section for the molecule (for which the MPI-Mainz-UV-VIS Spectral Atlas of Gaseous Molecules[109] is a very useful source).

The strengths of the vibrational transitions available within the selected electronic band are given by the relevant Franck-Condon factors. The rotational structure depends upon the electronic ground and excited states, and is best discussed on a case-by-case basis.

2.1.2 Emission considerations

<u>For how long can/must signal be collected? The fluorescence lifetime</u>

The fluorescence lifetime, τ_i, is the time taken for the population of the excited state i, from which fluorescence occurs, to fall to 1/e of its initial value. It is given by

28

$$\tau_i = \frac{1}{A_i}$$

where A_i is the Einstein coefficient of spontaneous emission.[10]

How much signal can be collected? The fluorescence quantum yield

An excited complex might not decay to the ground state by fluorescence. For gaseous diatomic molecules in a largely collision free environment – the only type of molecule to which LIF was applied in this PhD – there are two other routes available for relaxation. They might be able to phosphoresce – that is, undergo a spin forbidden transition to the ground state – after having first undergone intersystem crossing to an excited state of different spin to the initial excited state. They might also undergo internal conversion to a highly vibrationally excited level of the ground electronic state, although relaxation to a lower vibrational level must still involve emission of a photon. Both of these alternative relaxational routes are illustrated in Figure 2.1.
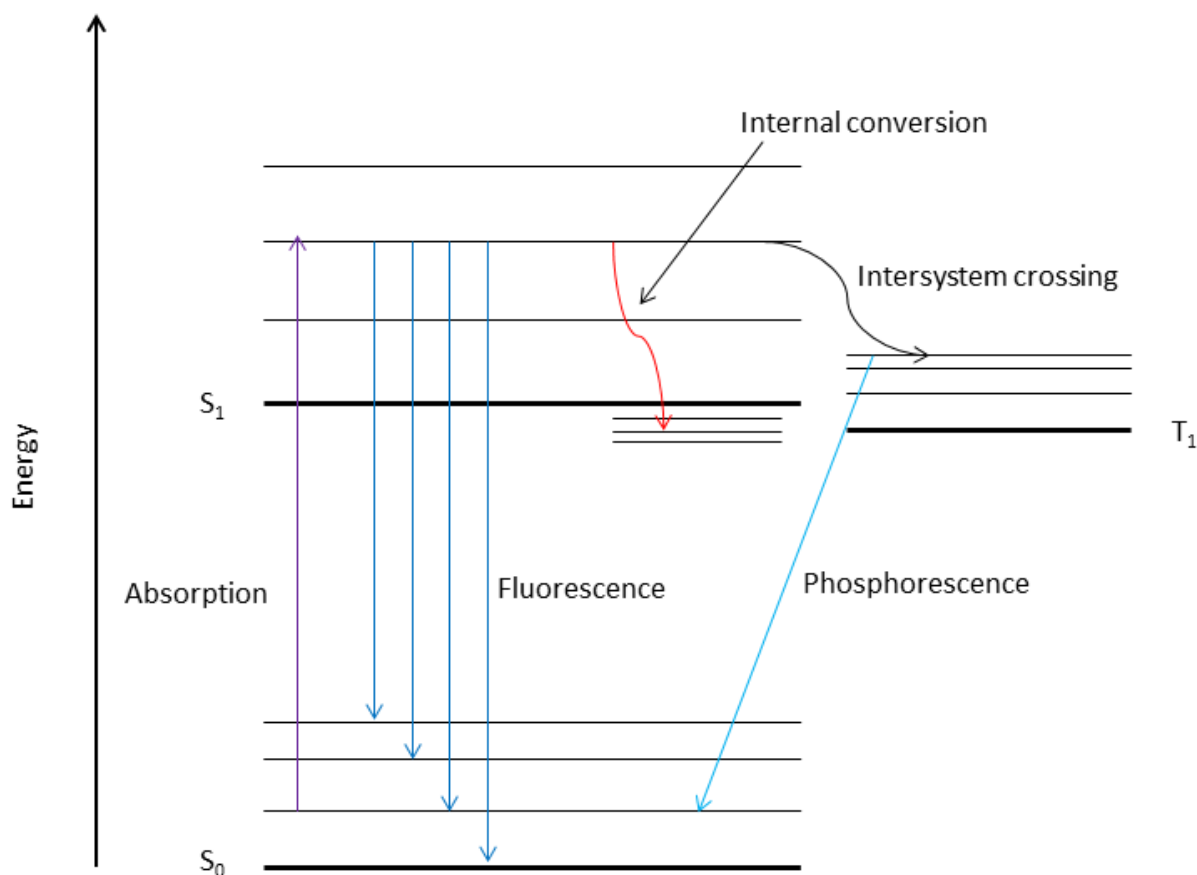
Figure 2.1: a schematic diagram of LIF, showing the excitation and fluorescence steps, and alternative relaxation routes.

The overall efficiency of the fluorescence process is measured by the fluorescence quantum yield of the molecule, which is simply the number of fluorescence photons emitted per excitation photon absorbed:[110]

$$\Phi_F = \frac{number\ of\ fluorescence\ photons\ emitted}{number\ of\ excitation\ photons\ absorbed}$$

<u>At which wavelengths will signal be produced? The Franck-Condon principle</u>

The Franck-Condon principle is a consideration applied to the change in vibrational quantum number during an electronic transition. It states that electronic motion is so much faster than nuclear motion as to be effectively instantaneous by comparison, and hence that nuclei do not move appreciably during electronic transitions. So, those

transitions that leave the nuclei in a similar position in the final state as in the starting state are favoured over those that result in substantial nuclear motion.

The Franck-Condon principle has two consequences for LIF. For the excitation step, in which the transition is selected by the narrowband laser light, it will merely affect the intensity of the selected transition; *in extremis*, it may disqualify certain transitions if there is no overlap at all between the initial and excited state vibrational wavefunctions. For the fluorescence step, it dictates which transitions occur in the return to the ground state, and in what proportion – which is to say, it dictates the wavelength of the fluorescence. This is an important factor to consider when planning a LIF experiment, because it will inform the choice of filters (used for noise reduction) and perhaps of PMT.

2.1.3   Absorption cross-sections and all that

Reference was made in section 2.1 to the absorption cross-section. This is a parameter in the Beer-Lambert law, which describes the change of intensity of light passing through a gas:

$$I = I_0 e^{-\sigma \rho l}$$

where I is the intensity of light re-emerging from the sample, I_0 is the intensity of light entering the sample, ρ is the particle density (cm^{-3}), l is the pathlength (cm), and σ is the absorption cross-section of the atom or molecule in question (cm^2).

The absorption cross-section of a molecule at a given wavelength, then, is a measure of the absorption efficiency of the molecule at that wavelength. Absorption efficiency can also be expressed in terms of the Einstein coefficient for stimulated absorption (B), the oscillator strength (f), and the line strength (S). All these qualities are intimately related, and their interconversion is discussed in depth by Bernath[108] and by Hilborn.[111]

2.2   Resonance enhanced multiphoton ionisation

Multiphoton ionisation (MPI) involves the ionisation of a molecule or atom by absorption of multiple photons with a total photon energy higher than the ionisation energy of the molecule. Requiring as this does the simultaneous absorption of several photons, MPI is unlikely to occur.

The probability of absorption is greatly increased if the ionisation occurs in two steps: excitation to an electronically excited state, and then further absorption from this state to cause ionisation.[112] This situation is termed resonance enhanced multiphoton ionisation, more usually referred to by the acronym REMPI. REMPI does still not have, objectively, a very high transition probability, and pulsed lasers are needed to provide enough power density (in the order of 10^8 W cm^{-2}).[113]

Because REMPI is much more favourable than MPI, by tuning the ionisation laser to a suitable resonance transition, molecules in a given ro-vibrational state can be selectively ionised.[10] This state selectivity is one of the great advantages of REMPI. Other advantages of the technique include high sensitivity and mass selectivity but these rely on its combination with other techniques and are discussed below in Figure 2.2.
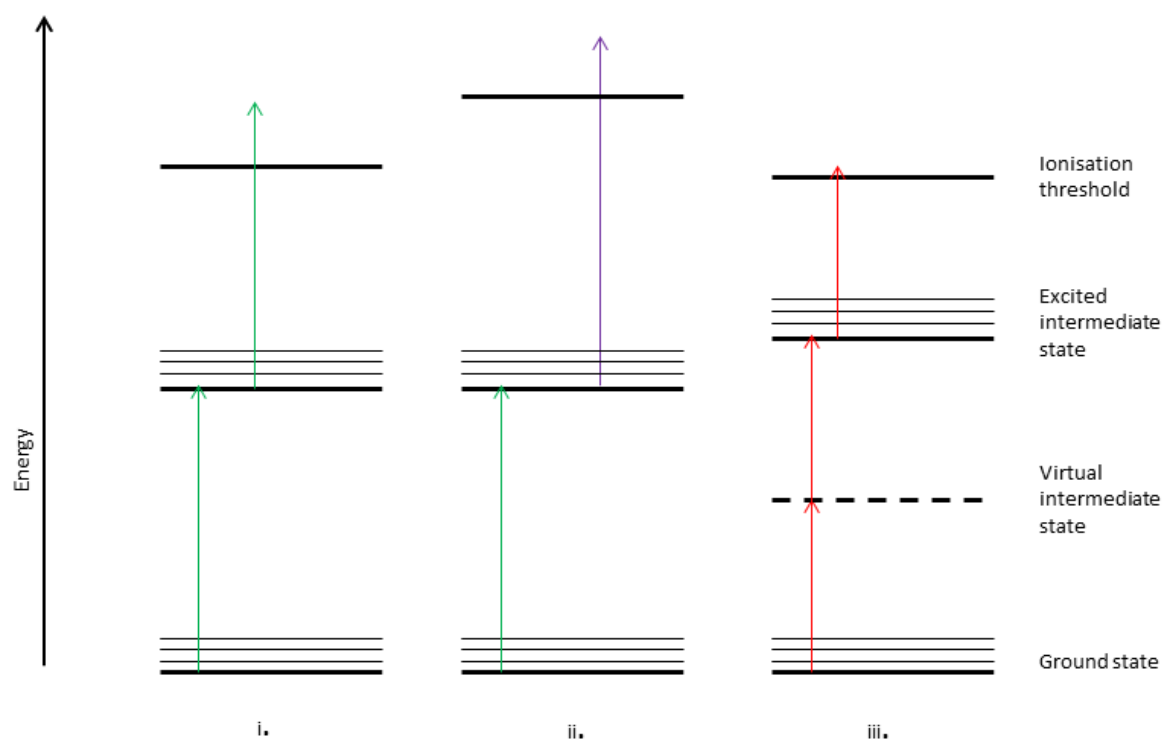
Figure 2.2: schematic illustrations of various REMPI schemes: i.) 1 + 1, with a single photon absorbed to reach the intermediate state, and another single photon to cause ionisation; ii.) 1 + 1', with a single photon absorbed to reach the intermediate state, and another single photon of different energy to the first to cause ionisation; and iii.) 2 + 1 REMPI, with two photons required to reach the intermediate state and a further one to cause ionisation.

2.3 Ion imaging

Imagine a billion dissociation events occurring in a small region of space. From each event, two fragments recoil in opposite directions. With the dissociating molecules randomly oriented, the multiple dissociations create an expanding sphere of fragments in velocity space, known as a Newton sphere. The fragments are often unevenly distributed over the surface of their Newton sphere, in which case the dissociation is said to be anisotropic (discussed in chapter three).

If the Newton sphere is captured at a certain point in time – by impact upon a detector – it may be converted to a spherical distribution of particle velocity vectors by the application of a suitable speed/distance scaling constant. Ion imaging is the process of ionising a Newton sphere, accelerating it onto a detector (a microchannel plate (MCP), used in combination with a phosphor screen and a charge coupled device (CCD) camera) to produce a 2D compression of the sphere, and then applying a reconstruction algorithm to recover an image of the original Newton sphere.

In other words, ion imaging is a means of capturing a reaction as a picture in product velocity. From this picture in velocity, fragment recoil speeds and directions can be deduced; further, by consideration of the conservation of energy, the velocity measured for the detected fragment can be used to deduce the internal state(s) of co-fragment(s).

The following discussion is largely informed by Parker and Eppink,[114] and by Houston.[115]

2.3.1 The creation of the Newton sphere: photodissociation

Newton spheres can be formed by chemical reactions, inelastic scattering, and photoionisation as well as photodissociation, but only photodissociation is relevant to this thesis, and so this discussion will refer only to photodissociation.

A photodissociation actually produces many Newton spheres. As discussed in chapter 3, a certain minimum photon energy, the dissociation energy, D_0, must be provided in order for dissociation to occur. Any excess energy is partitioned according to the particular dissociation dynamics of the molecule in question between the kinetic energy of the fragments, E_k, and their internal (electronic, vibrational, and rotational) excitation, E_i. That is to say:

$$E_{photon} - D_0 = E_k + E_i$$

Briefly, translational energy is split between the fragments according to their mass so that fragments with different masses recoil with different speeds; this of course means that different isotopes of chemically identical fragments recoil at different speeds. Because increasing the amount of energy partitioned into internal energy decreases the amount available for translation, every electronic and ro-vibrational state of a fragment will also have its own set of Newton spheres, according to the amount of energy assigned to the internal energy levels of both it and its co-fragment(s).

2.3.2   The ionisation of the Newton sphere: REMPI

Ion imaging captures the Newton sphere by ionising the expanding photofragments and accelerating the ions onto a detector. The ionisation process used is REMPI. As described previously, REMPI is highly state specific, allowing the imaging of only the Newton spheres of the fragment quantum state of interest. Other ionisation techniques are available (electron impact, or XUV light from synchrotron sources) but these are not state specific, do not allow for such a precisely defined ionisation time as a nanosecond REMPI laser (useful for the analysis of time of flight (TOF) spectra), and, in the case of electron impact, are likely to cause the fragmentation of ions.

There are a number of practical factors to consider when using of REMPI for ion imaging, including Doppler shifts, ion recoil, Coulomb explosion, and in some cases the problem of finding a suitable REMPI scheme. These will be considered as required in the relevant experimental chapters.

2.3.3   Mass discrimination

The ions created by REMPI are accelerated by a stack of annular electrodes towards the detector. One requirement of this ion collection stage is that it should allow the detector to discriminate between ions of different masses, to permit the selective imaging of the desired fragment. To a large extent, fragment selectivity is provided by the very specific REMPI ionisation process as described above, but it is still often the case that other species are also ionised – pump oil or other impurities, or background gas, or perhaps ions formed by non-resonant ionisation by a high energy photodissociation laser. Examples of this will be seen in chapter six.

Mass discrimination is achieved by TOF mass spectrometry, which requires electrodes arranged and charged to produce a field geometry such that flight time has a known

relationship to the mass/charge ratio of the ion, and further that all ions with the same mass/charge ratio arrive at the detector at approximately the same time regardless of where within the finite source volume they are produced. Such an arrangement was first demonstrated by Wiley and McLaren, in whose apparatus ionisation occurred between a charged repeller plate and an extractor plate, as shown in Figure 2.3. This arrangement satisfies the requirement of mass discrimination: ions starting further from the electrodes experience the accelerating field for longer, which compensates for their offset position.

The detector is spaced from the ion optics by a flight tube, the passage of the ions along which gives ions of different masses time to spread sufficiently for mass discrimination to occur by the gating of the detector. The length of the flight tube also determines the amount by which each ion sphere spreads out in space, and so places a limit on the velocity resolution of the detector.
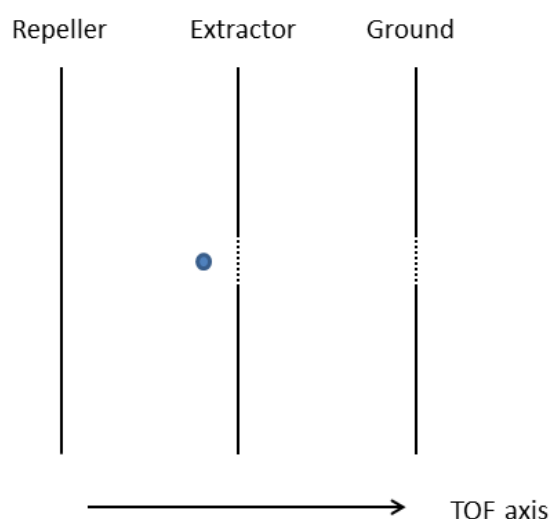
Figure 2.3 the ion optics of a Wiley-McLaren TOF mass spectrometer. The dashed lines represent grids, and the blue circle represents the laser beam passing into the plane of the page.

2.3.4   Velocity mapped ion imaging

The other major requirement of the ion collection stage is that it should allow high resolution imaging of the Newton sphere. Of course, as stated above, ionisation occurs over a finite volume of space as defined by the overlap of the molecular beam and the dissociation laser, not at a single infinitesimal point. In the absence of any preventative measures, this would result in significant blurring of the Newton sphere – as was indeed the case for the first ten years of ion imaging experiments.

The TOF mass spectrometers used in these early ion imaging experiments had grids present over the holes in the electrodes, to give an entirely homogenous field along the TOF axis. The presence of the grids brought the twin disadvantages of blurring of the ion image, and of signal decrease from the collision of ions with the grids. Removing the grids not only removes both the blurring and the ion loss caused by the grids, but also makes velocity mapped ion imaging possible by giving a field that is inhomogeneous in the centre, and can act as a velocity mapping lens: an electrostatic lens that focuses the ions such that all ions with the same velocity strike the same point upon the detector.

2.3.5 Sensitivity

Ion imaging is an extremely sensitive technique. For molecules with typical absorption cross-sections (in the order of 10^{-17} cm^{-2}) being ionised by pulsed lasers, ionisation can be close to 100% efficient.[116] The extraction of ions by the ion optics is similarly efficient, as is their detection by the MCP/phosphor/CCD array, leading to a theoretical detection efficiency of near to 100%. In practice, the detection efficiency is limited by noise.[13, 117]

3 Photostop – an overview

Chapter one outlined the state of the cold molecules field. The slowing technique known as photostop, which has been developed at this institution, was mentioned briefly. In this chapter, the technique will be explained, and a review made of its achievements prior to the work described in this thesis. The chapter begins with a short examination of the process at the heart of photostop: photodissociation by a single photon.

3.1 Single photon photodissociation

Except where otherwise referenced, this section is informed mostly by Schinke,[118] and also by Telle *et al.*[117] and Sato.[119] Simply, single photon photodissociation is the process

$$AB + h\nu \rightarrow (AB)^* \rightarrow A + B \qquad \text{(Eq. 3.1)}$$
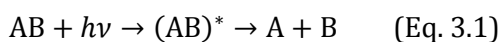
Here, a precursor molecule AB has absorbed a photon of frequency ν, and, *via* a brief existence as the excited molecule (AB)*, broken apart to yield two fragments A and B, which may be atoms or molecules.

3.1.1 Direct photodissociation

Photodissociation may broadly be classified as direct or indirect. Direct photodissociation is the case for which dissociation occurs from the initially excited state of the molecule: *i.e.*, if (AB)* in equation 3.1 occupies a repulsive electronic excited state of the molecule (Figure 3.1(a)), or occupies a continuum level of a bound state above the dissociation limit of that state (Figure 3.1(b)).[†]

[†] For completeness, note that dissociation can occur in this second manner in the electronic ground state.
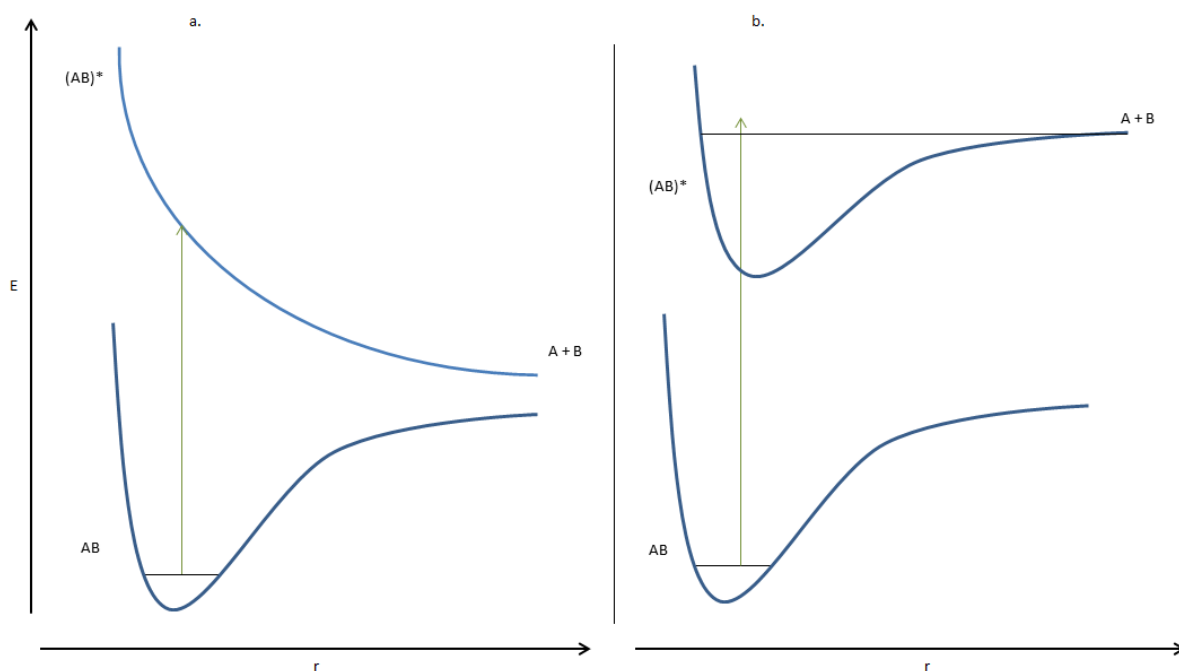
Figure 3.1: a.) direct photodissociation *via* a repulsive state; b.) direct photodissociation *via* continuum levels of a bound state. The line on the upper state of b.) represents the dissociation threshold, above which absorption occurs in a continuum – the absence of boundary conditions above the dissociation limit means that the vibrational energy is no longer quantised. Absorption in figure a.) is likewise occurring to a dissociative continuum.

Fragmentation of (AB)* occurs very quickly, taking less than the duration of a vibrational period of the complex (typically tens of femtoseconds). This allows no time for internal energy redistribution, and the state distribution of the products depends strongly upon that of the dissociating molecules – *i.e.*, most excess energy (*vide infra*) is partitioned into product translation. Likewise, it takes less time than a single rotational period, which means that the vector relationships between the transition dipole moment of AB and the velocity and rotational angular momentum vectors of A and B are maintained (see section 3.2.3 below).

3.1.2   Predissociation

Indirect photodissociation is also known as predissociation. If (AB)* occupies a binding electronic state below its dissociation limit, dissociation can still occur if (AB*) lies above the dissociation threshold of a dissociative continuum to which it can couple. The transition to the dissociative state can take time – many times the vibrational or

rotational period of the molecule – and so the state dependence of the products on the parents, and the vector correlations, tend to be averaged out.

Vibrational predissociation

If the bound state has a dissociative region at a different geometry, from which the bound portion is separated by a potential barrier, the molecule may be able to tunnel through the barrier to reach the dissociative region. The same end can be achievement by internal vibrational energy redistribution (IVR) if the molecule is at least triatomic. This is vibrational predissociation, and is illustrated for the two dimensional case in Figure 3.2.

Alternatively, the molecule may be able to undergo a radiationless transition to an unbound electronic state. To allow the discussion of such transitions, it is necessary to introduce the concept of the potential energy surface.
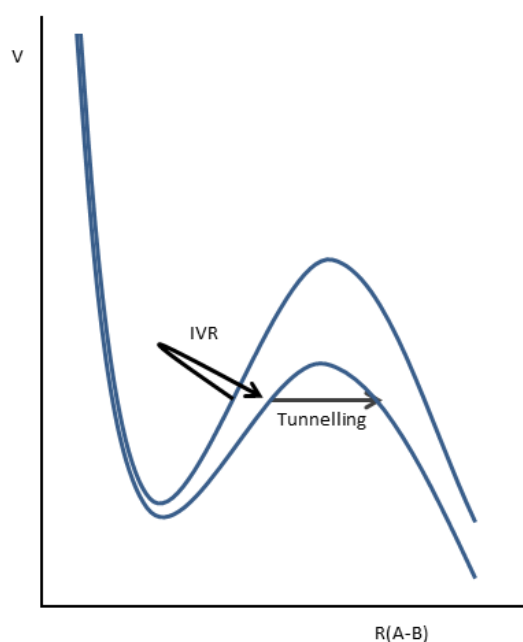
Figure 3.2: vibrational predissociation, showing IVR and tunnelling working in concert.

Potential energy surfaces and electronic predissociation

The potential energy surface (PES) of a molecule is a representation of its potential energy as a function of its geometry. For a diatomic molecule, the only geometric

variable is bond length, so the PES is a curve of potential energy against bond length; it is plotted as a two dimensional graph such as has been seen in the figures above. For a triatomic molecule, there are three variables; polyatomic molecules have many-dimensional PESs (number of dimensions = number of internal degrees of freedom = $3N - 6$, where N is the number of atoms in the molecule). Often, it is useful to fix certain variables so that a two-dimensional PES can be visualised on a three dimensional graph – for instance, by fixing the bond angle of a triatomic molecule, variation of potential energy as a function of both bond lengths can be examined – or to fix all but one variable, so that two-dimensional potential curves of the sort seen above can be produced.[120]

A molecule possesses many different PESs, one for each of its electronic states. A region in which a pair of PESs are degenerate is termed a conical intersection, being so named for the appearance of such regions on a three dimensional slice of the PES.

The concept of the PES relies upon the Born-Oppenheimer approximation, and so PESs are said to be adiabatic. At a conical intersection, the molecule is able to cross from one PES to the other in a radiationless transition. Movement between states in this fashion requires redistribution of potential energy to or from molecular vibration, so that the total energy of the molecule is conserved. Thus, it is said that the adiabatic representation of the PES breaks down in the region of the conical intersection. This is the means by which electronic predissociation occurs, if the state to which the molecule crosses is dissociative.

3.2   Photostop: the basics

The photostop technique involves the generation of cold atoms or molecules by the photodissociation of a precursor molecule. For clarity, the following discussion will proceed by consideration of the photostop of the generic fragment A by photodissociation of the precursor AB.

To give a simple explanation: a pulsed molecular beam of AB seeded in a noble carrier gas is crossed by a laser beam. The laser light dissociates AB, producing fragments A and B. These recoil from the dissociation site. The speed of the molecular beam and the wavelength of the laser beam are tuned so that the recoil velocity of those A molecules recoiling opposite to the molecular beam direction cancels out their initial

velocity. This leaves a certain amount of A stationary (or close to it) in the laboratory frame. This situation is depicted in Figure 3.3.
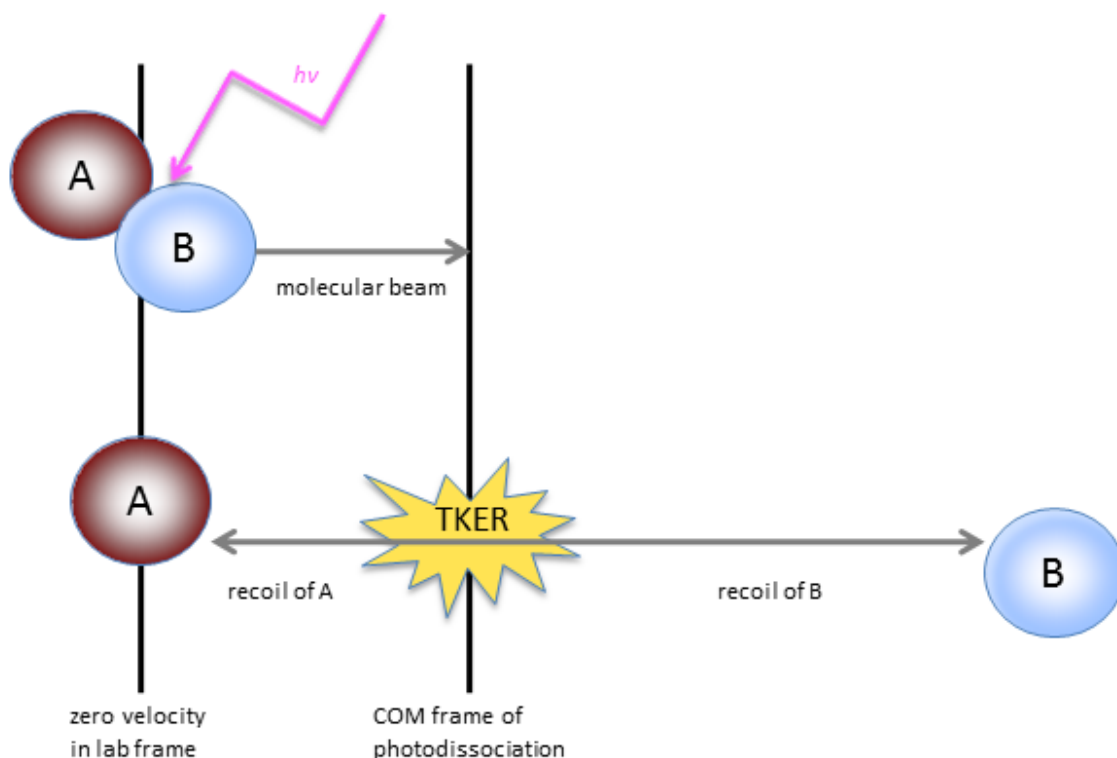
Figure 3.3: schematic illustration of the photostop process, showing the production of stationary A by photodissociation of the moving precursor AB.

3.2.1 Vector treatment of photostop

The photostop experiment can be considered more formally in terms of vectors. The experiment begins with AB in the molecular beam, travelling with the molecular beam velocity, v_{beam}, in the lab frame. The photodissociation occurs, producing A.

The recoil velocity of A is best considered in the centre-of-mass (COM) frame of the photodissociation. The recoil velocity of A in the COM frame is u_A. u_A depends upon the wavelength of the dissociation laser and the particular photodissociation dynamics of AB.

The object of photostop is to produce A with a lab frame velocity (v_A) of zero. v_A, u_A, and v_{beam} are related *via*

$$v_A = v_{beam} + u_A$$

41

since v_{beam} is identical to v_{CM}, the lab frame velocity of the centre-of-mass frame. This relationship is shown in Figure 3.4.

It is apparent that photostop is achieved (*i.e.* $v_A = 0$) when $v_{beam} = -u_A$: that is, photostop is achieved when the recoil velocity of A in the COM frame is equal in magnitude and opposite in direcion to the velocity of the molecular beam in the lab frame. To achieve photostop, control over the magnitude of u_A must be achieved, and control over the direction of u_A is desirable. This is discussed below.
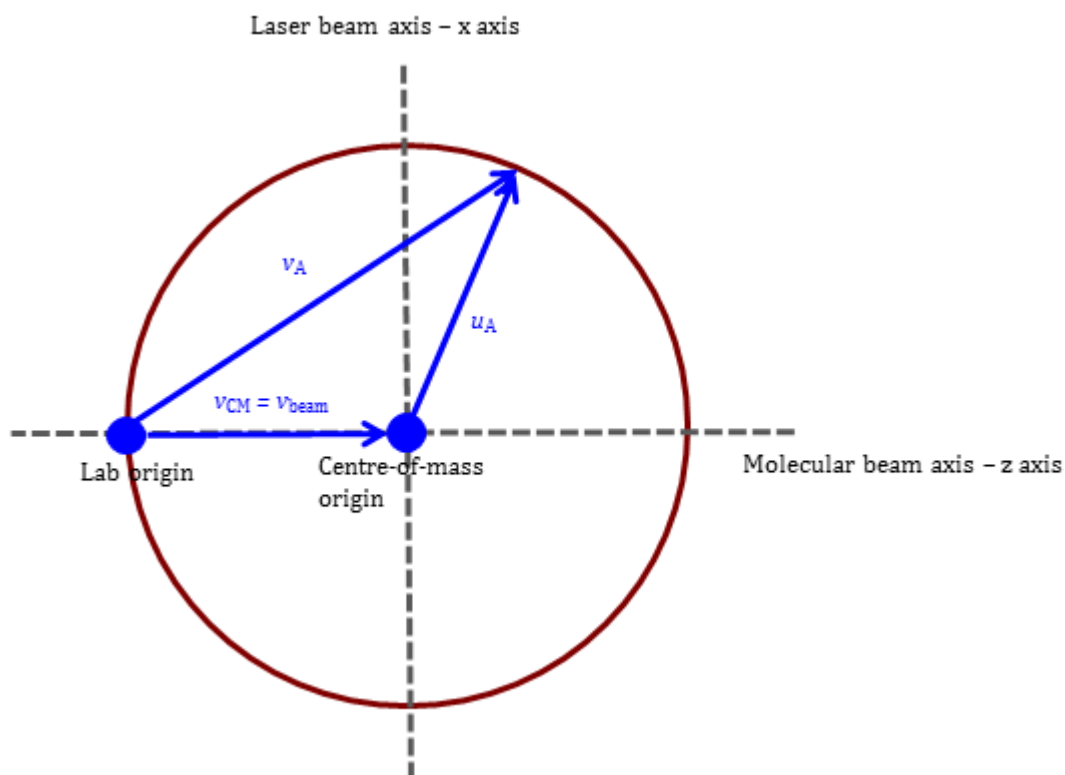
Figure 3.4: Newton diagram of the photostop process.

3.2.2 Photostop wavelength – control of the magnitude of u_A

Absorption of a photon can cause the dissociation of a molecule by a variety of pathways as described above. A certain minimum photon energy, the dissociation energy D_0, must be provided in order for dissociation to occur. Any excess energy is partitioned, according to the particular dissociation dynamics of the molecule in question, between the (relative) kinetic energy of the fragments, E_k, and their internal (electronic, vibrational, and rotational) excitation, E_i. That is to say:

$$E_{photon} = D_0 + E_k + E_i \qquad \text{(Eq. 3.2)}$$

42

Since u_A depends upon E_k, control over the magnitude of u_A is achieved by variation of E_{photon}: *i.e.*, by changing the dissociation wavelength.

The dissociation wavelength required to photostop the fragment A can be calculated. The relevant equation is derived as follows.

In the COM frame of the photofragments, their kinetic energy E_k is given by

$$E_k = \frac{1}{2}\mu u_{rel}^2$$

where μ is the reduced mass of A and B, and u_{rel} is their relative velocity in the COM frame.

Since $u_{rel} = u_A - u_B$,

$$E_k = \frac{1}{2}\mu(u_A - u_B)^2$$

where u_A and u_B are the COM frame velocities of A and B respectively. In the centre-of-mass frame, the total momentum of A and B is zero, which allows the substitution

$$E_k = \frac{1}{2}\mu\left(u_A + u_A\frac{m_A}{m_B}\right)^2$$

where m_A and m_B are the masses of A and B. This simplifies to give

$$E_k = \frac{1}{2}\frac{m_A m_{AB}}{m_B}u_A^2$$

As discussed above, the production of stationary A requires that $v_A = 0$, and this in turn requires that $\mu_A = -v_{beam}$. So, the required total kinetic energy for the photostop of A is

$$E_k = \frac{1}{2}\frac{m_A m_{AB}}{m_B}v_{beam}^2 \qquad \text{(Eq. 3.3)}$$

Substitution of equation 3.3 into equation 3.2 yields

$$E_{photon} = D_0 + E_i + \frac{1}{2}\frac{m_A m_{AB}}{m_B}v_{beam}^2$$

It follows that λ_A, the photodissociation wavelength required to photostop A, is given by

$$\lambda_A = hc \left(D_0 + E_i + \frac{1}{2} \frac{m_A m_{AB}}{m_B} v_{beam}^2 \right)^{-1} \qquad \text{(Eq. 3.4)}$$

COM frame velocities of A and B

As an aside, formulae for the COM frame velocities of the fragments A and B can be given:

$$u_A = \sqrt{2E_k \frac{m_B}{m_A m_{AB}}}$$

and

$$u_B = \sqrt{2E_k \frac{m_A}{m_B m_{AB}}}$$

Note that the velocity of (and hence the partition of kinetic energy between) the fragments is inversely proportional to their mass.

3.2.3 Angular distribution of A – the direction of u_A

Angular distribution and the β parameter

The probability, P, for an electronic transition to occur in an irradiated molecule is given by

$$P = |\mu E|^2$$

where μ is the transition dipole moment and E is the electric field vector of the light.[119] This is a scalar vector product, so P is greatest when the two vectors are parallel, and zero when they are perpendicular.

From this can be derived a distribution for the angular distribution of photofragments:[121]

$$I(\theta) = \frac{1}{4\pi}[1 + \beta P_2(\cos\theta)] \qquad \text{(Eq. 3.4)}$$

where θ is the angle between E and the fragment velocity vector v, $P_2(\cos\theta)$ is the second-order Legendre polynomial $\left(P_2(a) = \frac{3}{2}a^2 - \frac{1}{2}\right)$, and β is a parameter describing the degree of anisotropy, often termed the anisotropy factor. The factor of 4π normalises the function over the whole solid angle.[114, 119]

If the photodissociation is fast, so that the direction of v does not change during the photodissociation process (*i.e.* direct photodissociation as discussed above), β is given as $\beta = 2P_2(\cos\alpha)$, where α is the angle between μ and v. For a diatomic molecule, μ can either lie along (parallel to) the bond, or perpendicular to it.

In the parallel case, α is zero and β is 2, so that the angular distribution function has its maxima when θ is 0 or π, producing a polar distribution as shown in Figure 3.5.
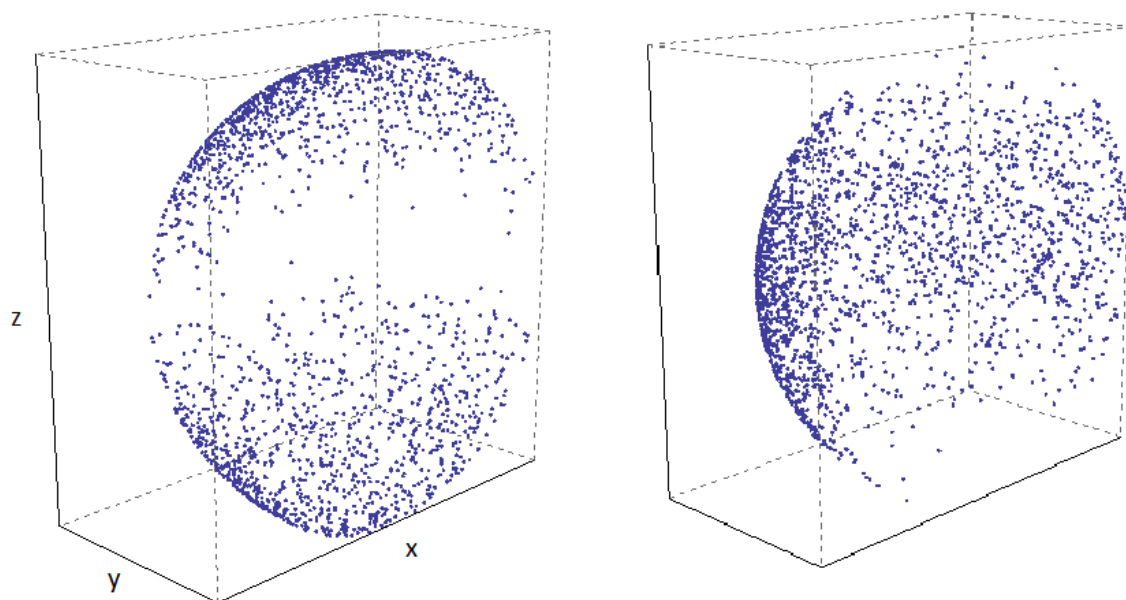
Figure 3.5: cut away views of simulated photofragment distributions produced by a photodissociation laser with linear polarisation along the z direction. The distribution on the left is produced by the parallel case discussed in the text, and the distribution on the right by the equatorial distribution.

In the perpendicular case, α is $\frac{\pi}{2}$ and β is -1, so that the angular distribution function has its maxima when θ is $\frac{\pi}{2}$ or $\frac{3\pi}{2}$, producing an equatorial distribution as shown in Figure 3.5.

For polyatomic molecules, μ is not restricted to be parallel or perpendicular to the breaking bond, leading to intermediate values of β.

If dissociation is not rapid, then the molecule is able to rotate in the time between excitation and dissociation, and the expression for β becomes time dependent and more complicated. Also, if dissociation occurs *via* a number of pathways with different individual β values, the "overall" β of the photodissociation becomes a linear combination of these. A detailed exposition of such cases is not germane; the important point to note is that such cases are still described by equation 3.3 as for the simple rapidly dissociating case.

The β parameter in photostop

It was stated above, in reference to the photostop of a hypothetical fragment *A* by dissociation of the hypothetical parent *AB*: "the recoil velocity of those *A* molecules recoiling opposite to the molecular beam direction cancels out their initial velocity. This leaves *A* stationary (or close to it) in the lab frame." Obviously, the proportion of A that actually does recoil opposite to the molecular beam direction is dictated by β, and by the orientation of the laser polarisation.

Figure 3.6 demonstrates the effect of β on the number of photostopped fragments. It can be seen that a photodissociation with a positive β value produces greater photostop density when a horizontally polarised dissociation laser is used, so that one lobe of the polar fragment distribution is aligned counter to the molecular beam direction; and a photodissociation with a negative β value produces greater photostop density when a vertically polarised dissociation laser is used, so that the ring of fragments is aligned with the molecular beam axis.

The most favourable situation for photostop is to have a β value of 2 combined with a horizontally polarised dissociation laser, directing the maximum possible number of fragments back along the molecular beam axis. It is also worth noticing that even quite low positive values of β, down to about 0.5, are more favourable than even the largest magnitude negative values.
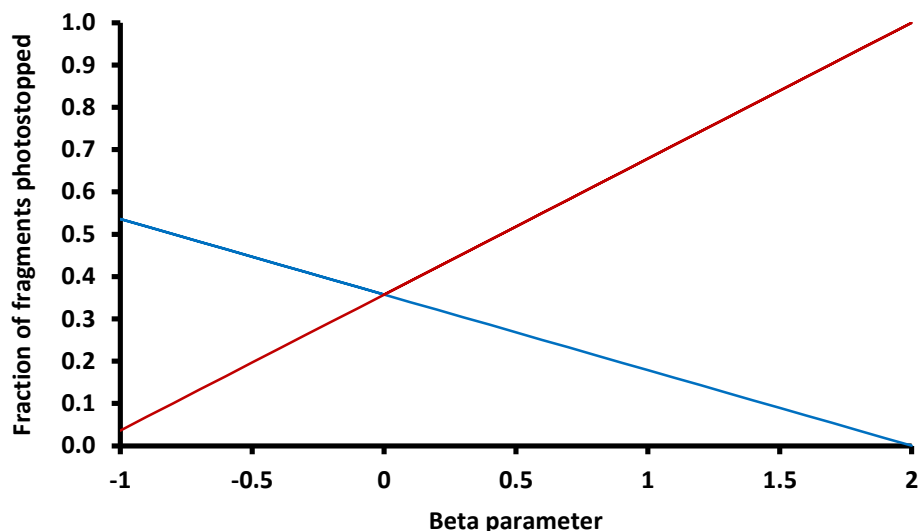
Figure 3.6: graph showing the number of fragments photostopped as a fraction of the theoretical maximum when a horizontally polarised photodissociation laser (red) and a vertically polarised photodissociation laser (blue) are used. ("As a fraction of the theoretical maximum" implies as a fraction of the number of fragments photostopped for the β = 2 case with horizontal polarisation, not as a fraction of the total number of fragments produced by photodissociation).

It should be noted at this point that the angular distribution of the photodissociation is addressed here simply because it seems apposite to explain the significance of the direction of u_A at the same time as explaining the significance of its magnitude. There are other, more critical parameters that affect photostop density – energy partition, absorption cross sections, achievable gas pressures, *etc*. – and these are all addressed in the review of potential photostop precursors in chapter seven.

3.3   Achievements of the photostop technique prior to this thesis

Whilst the photostop technique is in theory easily accessible to any researcher in possession of a molecular beam machine and tuneable lasers, little use has been made of it to this point.

The technique was first suggested in the literature by Matthews *et al*. in 2007,[122] as a possible method of producing cold atomic oxygen; the first experimental paper published on the technique was by Zhao *et al*. in 2009,[123] who used a non-tuneable 355 nm YAG laser to dissociate NO_2 and so produce slow NO. Failing to match recoil velocity to molecular beam speed, this was a crude proof-of-principle work rather than a serious attempt to make cold molecules.

Work performed concurrently and independently at Durham used a tuneable dye laser to dissociate NO_2. The use of a tuneable dissociation laser allowed the selection of the correct recoil energy of NO to cancel out the molecular beam velocity.[13] The following two chapters build upon this work.

Photostop has also been used at Durham (in collaboration with the Softley group from Oxford) for atomic cooling, with cold bromine atoms being generated by the photodissociation of Br_2[124] All these results are collected in

Table 3.1, giving a flavour of the achievements of the technique prior to the work described in this thesis.

Table 3.1: a summary of work using the photostop technique prior to this thesis.

Parent molecule	NO_2	NO_2	Br_2
Probed fragment	NO ($^2\Pi_{1/2}$, v = 1, J ~ 8.5)	NO ($^2\Pi_{3/2}$, v = 0, J ~ 1.5)	Br($^2P_{3/2}$)
Longest time delay between photodissocation and probe (μs)	0.3	10	100
Average fragment velocity at longest delay (m s^{-1})	130	0	0
Velocity spread (FWHM) along molecular beam axis at longest delay (m s^{-1})	28	50	17
Fragment density following longest delay (cm^{-3})	Not stated	10^7	10^8
Authors	Zhao *et al.*[123]	Trottier *et al.*[13]	Doherty *et al.*[124]

3.3.1 Comparison of photostop to other techniques for slowing molecular beams

Perhaps the most obvious comparison to draw between photostop and the rest of the cold molecules field is with the kinematic cooling experiment of Elioff *et al.* in which NO was brought to rest by collisions with argon.[12] On the face of it, Elioff's work was more successful, not only producing zero velocity NO with a higher density (10^8 – 10^9 cm^{-3} for kinematic cooling vs. 10^7 cm^{-3} for photostop) but also at a lower temperature (0.406 K vs 1.3 K). However, this is an example of the necessity to understand the meaning of the "temperature" quoted by individual research papers. The temperature given by

Trottier *et al.* is a "true" temperature, the parameter T from a one dimensional Maxwell-Boltzmann fit to the longitudinal velocity spread of NO, whereas the temperature given by Elioff *et al.* is a "kinetic" temperature (as coined in section 1.2.2) derived from the standard deviation of the longitudinal velocity distribution.

A true comparison of the photostop and kinematic cooling experiments can be made by converting Trottier's temperature into a kinetic temperature, or Elioff's kinetic temperature into a Maxwell-Boltzmann temperature. The comparison is direct, because both velocity distributions are Gaussian – Elioff's unnecessary use of the kinetic temperature is an example of how the kinetic temperature has become the standard measurement for the field (see section 1.2.2).

For a Gaussian distribution,

$$g(x) = Ae^{-\frac{(x-x_1)^2}{2\sigma^2}}$$

the standard deviation is σ. The relationship between σ from a Gaussian distribution and T from a Maxwell-Boltzmann distribution is

$$\sigma = \sqrt{\frac{kT}{m}}$$

and the kinetic temperature in this case is given by

$$T_k = \frac{1}{2}m\sigma^2$$

Hence, the kinetic temperature for Trottier's photostop experiment was 0.325 K – *lower* than the temperature claimed by Elioff (although of course the photostop experiment still produced a lower density of stopped fragments).

More broadly, the photostop technique as demonstrated for NO is comparable with the other techniques for slowing molecular beams in terms of temperatures and densities reported – Stark deceleration, for instance, the most extensively employed technique, brings molecules to rest with densities of 10^6-10^9 cm^{-3} (section 1.5.6). It remains important to develop new techniques for cold molecule production – to give a single example, the first experimental observation of cold collisions between two different species of state-selected neutral polar molecules was made by combining the techniques of Stark deceleration and buffer gas beams.[125]

The photostop technique having been demonstrated, there were three obvious avenues for its development: to trap the slow, cold molecules produced by photostop; to achieve higher densities/lower temperatures by selection of a more suitable candidate molecule; and to achieve higher densities/lower temperatures by refinement of the photostop technique. Chapter five details an attempt at the first of these aims, and chapter six the second; the third aim is discussed in chapter seven. Firstly, though, chapter four introduces the apparatus with which the work in this thesis was conducted, and records some further studies made to complement Trottier's work.

4 The photostop of NO by dissociation of NO_2 *via* the (1) $^2B_2$ state

4.1 Introduction

As described at the end of the last chapter, the photostop technique has previously been used at Durham to produce cold $NO(^2\Pi_{3/2}, v = 0, J = 1.5)$ molecules by the dissociation of NO_2.[13] In that previous work, the evaporation of NO from the photodissociation volume was monitored; with the passage of time, faster moving molecules were lost, and the velocity distribution narrowed. The density of molecules could not be measured directly, but was instead inferred by simulation, using simulation code written by Eckart Wrede (hereinafter, "phstop"). The phstop program is briefly described in appendix A.

Whilst the simulated $NO(^2\Pi_{3/2}, v = 0, J = 1.5)$ decay curve could be put in reasonable agreement with the experimental NO population decay curve, the comparison was of limited validity because the diameters of the photodissociation and probe lasers used in the experimental work were not properly characterised. Work was therefore undertaken to produce a decay curve using properly measured laser beam diameters, to allow the experimental density to be given with confidence.

This work would also allow more rigorous testing of the phstop program. Beyond its use in experimental planning and trouble shooting, having an accurate simulation program would also be useful in relation to the long term aim of the work on NO/NO_2: the magnetic trapping of cold NO (see chapter 5). One way to provide evidence of trapping would be to compare the decay curve produced by a trapped population with a simulated decay curve for an untrapped population with the same experimental parameters: for this to be a convincing proof of trapping would require a demonstrably accurate simulation program.

An image of photostopped $NO(^2\Pi_{3/2}, v = 0, J = 1.5)$, acquired with a delay of 10 μs between the photodissociation and probe lasers, is also recorded in this chapter, along with a brief discussion of an alternative photodissociation scheme.

4.2 Experimental overview

A mixture of nitrogen dioxide and xenon was expanded into the first of two differentially pumped vacuum chambers. The jet thus produced was skimmed by its passage into a second chamber, where it was intersected at 90° by a photodissociation laser. The action of the photodissociation laser yielded NO molecules, which were interrogated by a REMPI laser counterpropagating along the dissociation laser axis.

The above processes occurred in the centre of an ion lens system, and NO^+ ions formed by the REMPI laser were accelerated upwards by the ion lens onto a Photek VID240 vacuum compatible detector (hereafter, "the detector"), consisting of a pair of MCPs, a phosphorescent screen and a CCD camera.

The molecular beam defines the *z*-axis used in discussion and analysis, the lasers define the *x*-axis, and the ion optics stack, the *y*-axis. A schematic view of the experimental apparatus with axes marked is shown in Figure 4.1.
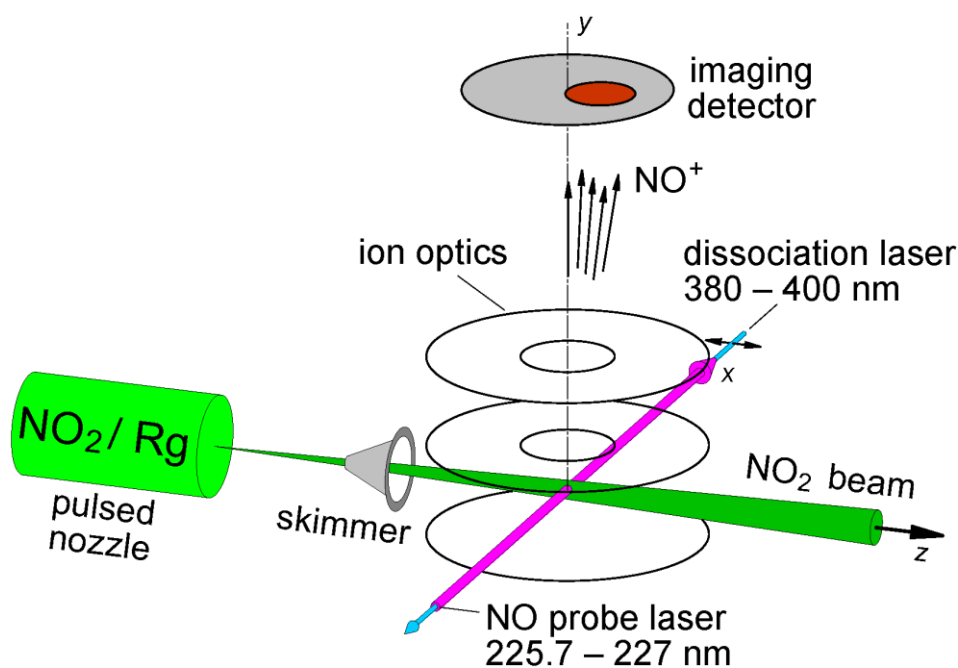
Figure 4.1: schematic diagram of the photostop experiment.

4.2.1 Photodissociation scheme

The photodissociation scheme used was that described by Trottier *et al*.[13] Briefly, NO_2 is excited by absorption of a single photon from its ground X $^2A_1$ state to its $^2B_2$ state. From here it predissociates, returning *via* a conical intersection to the continuum of

vibrational levels above the dissociation limit of the X state. The dissociation produces NO in its $^2\Pi$ electronic ground state, and is illustrated in Figure 4.2.
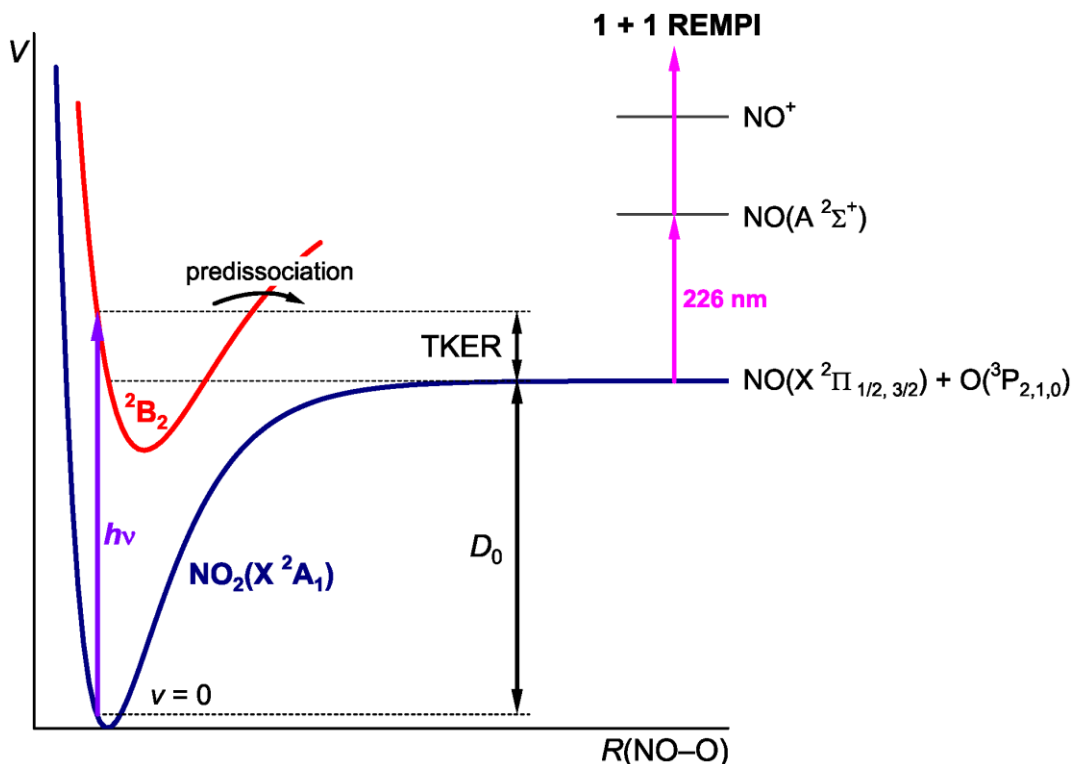
Figure 4.2: schematic diagram of the NO₂ potential energy surfaces involved in the photodissociation process. D_0, the dissociation energy, is the minimum energy input required to excite NO₂ into those levels of the $^2B_2$ state that lie above the bound levels of the X $^2A_1$ state. The 1 + 1 REMPI scheme used to detect NO is also shown.

4.2.2 Detection scheme

Both the $^2\Pi_{1/2}$ and $^2\Pi_{3/2}$ spin-orbit states of NO($^2\Pi$) are produced by the photodissociation of NO₂ at ≈ 387 nm. Despite its being produced in the minority, the $^2\Pi_{3/2}$ state was chosen as the target for photostop, for two reasons. Firstly, the $^2\Pi_{1/2}$ state has no magnetic moment and so is impossible to magnetically trap, which as described in section 4.1 was the ultimate end of the NO₂ photostop experiment. Secondly, the detection of photostopped NO is complicated by the fact that NO₂ gas contains small amounts of NO. Whilst this is only a trace impurity, it is more than sufficient to produce a background strong enough to compete with the signal produced by photostopped molecules. The ratio of NO($^2\Pi_{3/2}$) to NO($^2\Pi_{1/2}$) is less than 1:40 in the cold molecular beam,[13] and about 1:3 for thermal NO, so photostopped NO($^2\Pi_{3/2}$) can be detected with less competition from background gas.

NO was detected through the combination of REMPI and velocity mapped ion imaging. Ion imaging is an excellent detection technique for photostop: it is extremely sensitive; it allows direct and simple measurement of molecular beam speed and spread, and of the recoil velocity and the velocity spread of photostopped molecules; and it allows the evaporation of hotter molecules from the photostop volume to be displayed over time as images, which provides a convincing demonstration of the photostop technique. Just as importantly, a detection technique that provides an image of the dissociation event is extremely useful when trouble shooting.

The use of UV radiation of approximately 226 nm allows 1 + 1 REMPI *via* the A $^2\Sigma^+$ state, as indicated in Figure 4.2. There are four branches associated with this transition for each spin-orbit state, the origins of which can be seen in the diagram in appendix B. Tabulated peak positions for the X $^2\Pi$ -> A $^2\Sigma^+$ spectrum are given in appendices C and D.

4.3   Experimental apparatus

4.3.1   The vacuum system

All work described in this thesis was conducted in a molecular beam machine originally designed for studying the reactive scattering of hydrogen Rydberg atoms, and described in detail by Flynn.[126] Briefly, it was based around a cuboid chamber custom built from 20 mm stainless steel, with outer dimensions 780 x 336 x 336 mm, and internally divided into two chambers: the source chamber (in which the molecular beam expansion occurred) and the photostop chamber (in which photostop occurred).

Vacuum in the source chamber was maintained by a diffusion pump (Edwards Diffstak CR 250/2000M, pumping speed: N_2 1700 l s^{-1}, H_2 3000 L s^{-1})‡ backed by a rotary pump (Leybold Trivac D40B, pumping speed: 40 m^3 h^{-1}) with an aluminium oxide adsorption trap. Vacuum in the photostop chamber was maintained by a turbomolecular pump (Leybold Turbovac 600C, pumping speed: N_2 560 L s^{-1}) backed by a rotary pump (Leybold Trivac D25B, pumping speed: 25.7 m^3 h^{-1}) with an aluminium oxide adsorption trap.

---

‡ Note that these pumping speeds are specified for operation with a cryogenically cooled baffle. The baffle was not used in this experiment, so the pumping speed was slower than might be imagined.

In contrast to the arrangement used by Flynn, the ion optics and detector were mounted perpendicular to the molecular beam axis (rather than along it), extending above the photostop chamber. Separating the detector and the ion optics were a TOF drift tube and a four way cross; on one side of the latter was mounted a second turbomolecular pump (Leybold Turbovac 151C, pumping speed: N_2 145 l s^{-1}) backed by a rotary pump (Leybold Trivac 16 B, pumping speed: 16.5 m^3 h^{-1}) with an aluminium oxide adsorption trap.

Mounted at the end of the photostop chamber, at the end of the molecular beam axis (z axis) were a fast ionisation gauge (Beam Dynamics FIG-1, hereafter "FIG") for characterisation of the molecular beam pulse shape, and a residual gas analyser (Stanford Research Systems RGA 200, hereafter "RGA") used for molecular beam content analysis, and for helium leak testing.

A schematic view of the apparatus is given in Figure 4.3, and a photograph is shown in Figure 4.4. Table 4.1 gives the standard pressures with and without load for each chamber.

Table 4.1: typical pressures with and without load, by region.

Region	Pressure without load (mbar)	Pressure with load (mbar)
Source chamber	1×10^{-6}	1×10^{-4}
Photostop chamber	9×10^{-8}	2×10^{-7}
TOF/detection chamber	2×10^{-8}	2×10^{-7}
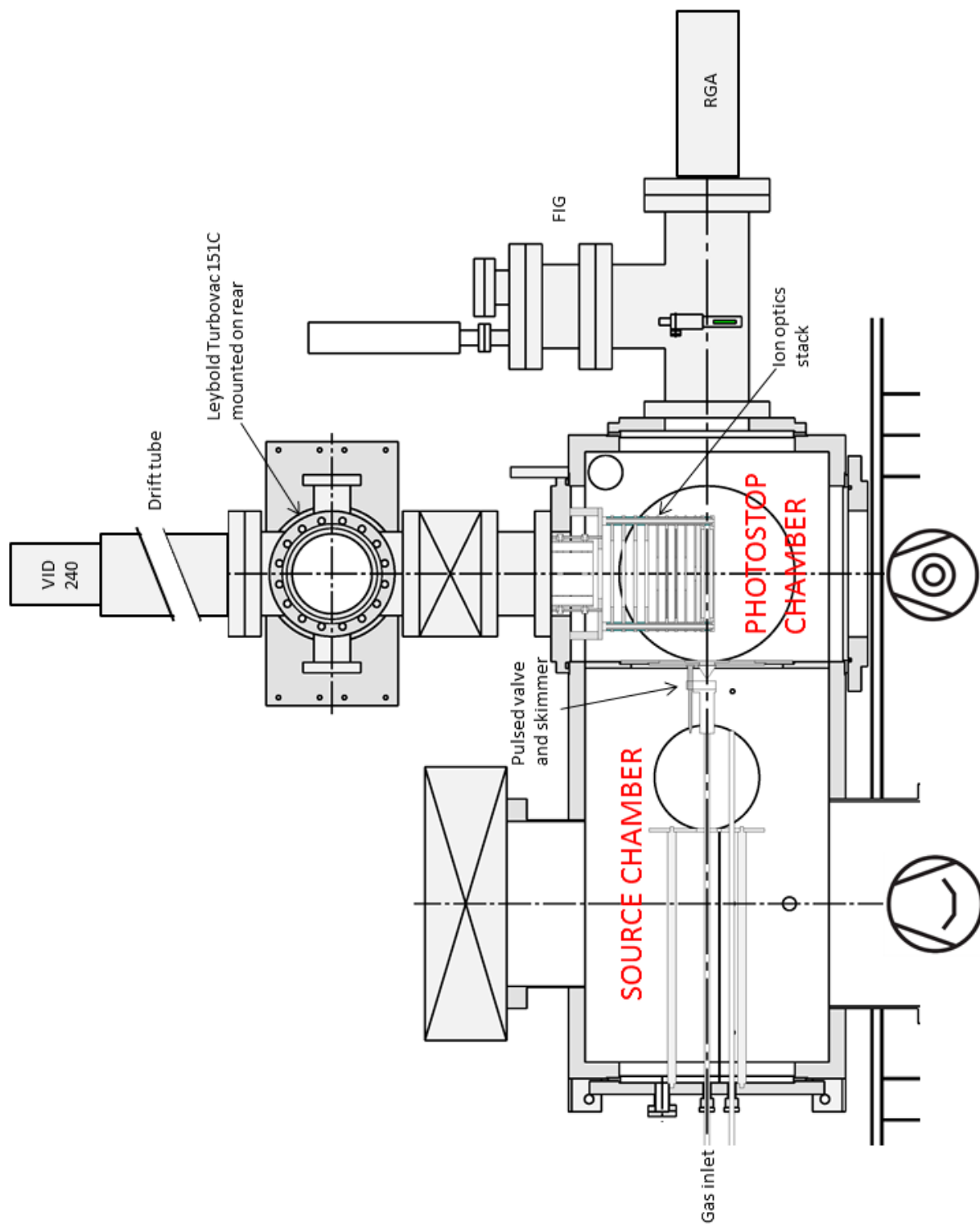
Figure 4.3: vertical cut through the vacuum chambers and mounted vacuum pumps, detectors *etc.*
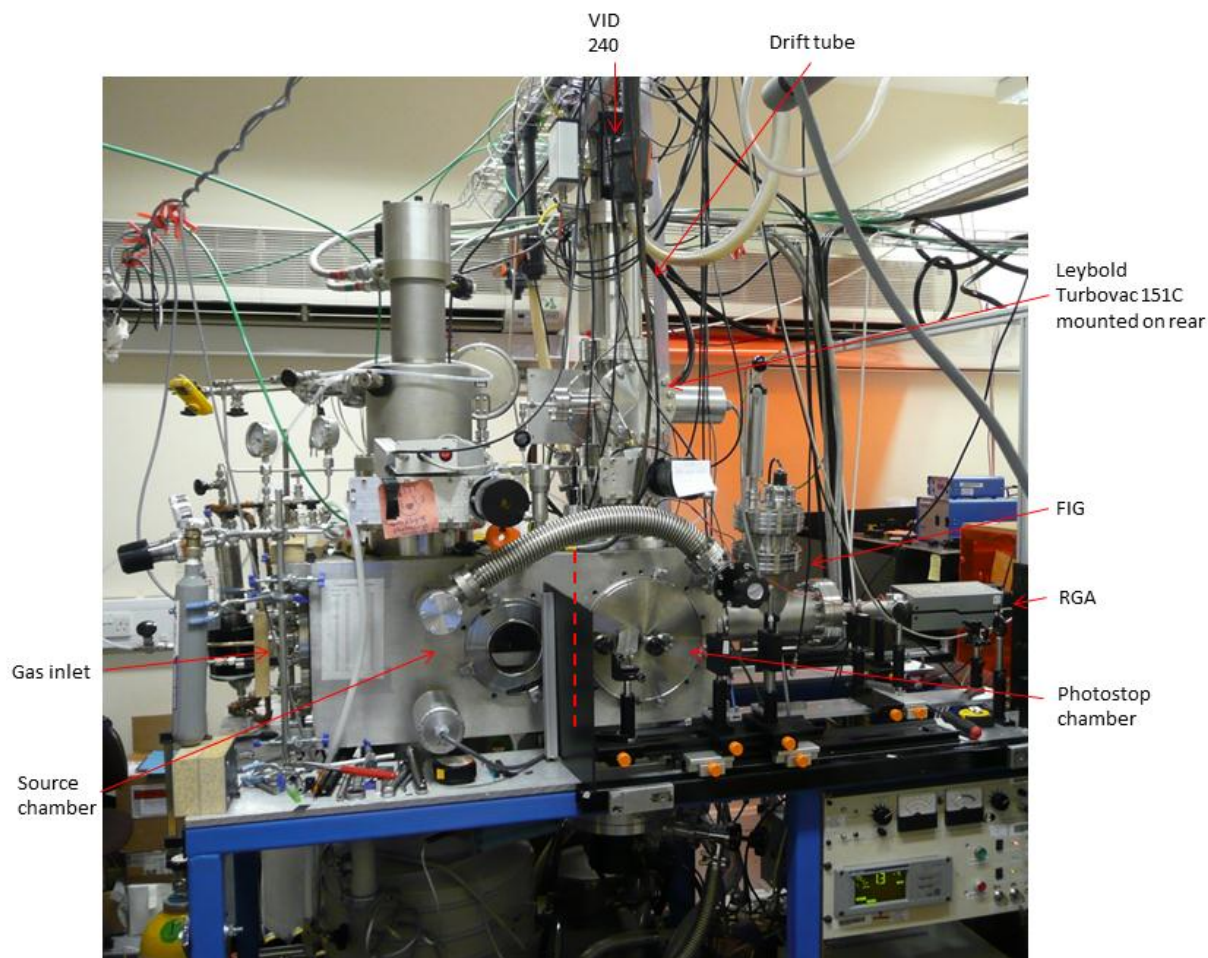
Figure 4.4: photograph of the experimental array.

4.3.2 The laser system

The dissociation laser was a Lambda-Physik FL2002 dye laser (Exalite 389, 0.2 g/L in p-dioxane), pumped by the third harmonic output of a Continuum Powerlite Nd:YAG laser (typical Powerlite output: 94-104 mJ pulse^{-1}). The probe (REMPI) laser was a Sirah Cobra dye laser (Coumarin 2, 0.2 g/L in methanol) fitted with a second harmonic generation BBO crystal and Pellin-Broca wavelength separator, and pumped by the third harmonic output of a Continuum Surelite Nd:YAG laser (typical Surelite output: 80-85 mJ pulse^{-1}). See appendix G for relevant dye laser output energies.

The laser arrangement is shown schematically in Figure 4.5. All lasers ran at a frequency of 10 Hz. The photodissociation laser light was passed through a Fresnel rhomb to convert its polarisation to horizontal. Both lasers were focused with f = 500 mm lenses to control the beam diameter in the photostop region.
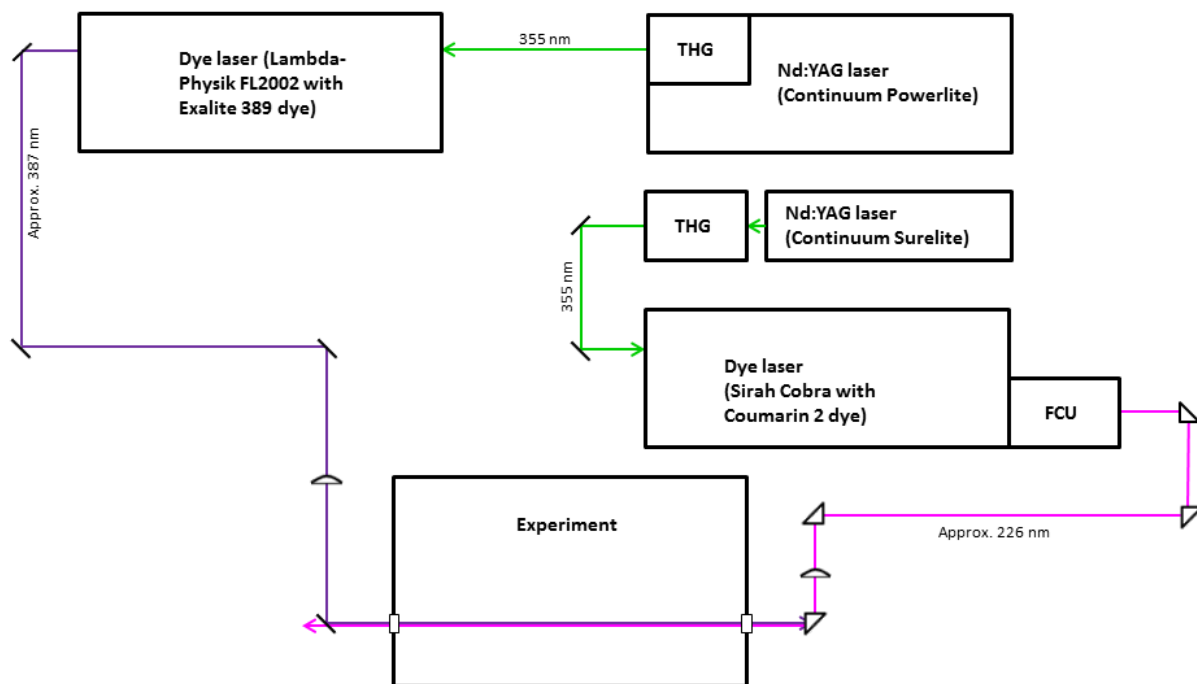
Figure 4.5: schematic diagram of the laser systems.

4.3.3 Ion optics

The ion optics arrangement was a refinement on the basic scheme presented in chapter two, and has been described in detail by Flynn. Briefly, the ions optics stack contained eight additional electrodes after the extractor, to give more control and flexibility in focusing according to the work of Townsend *et al.*;[127] and an additional stabiliser electrode between the repeller and extractor, to homogenise the field in the ionisation region, a feature which has been found by Wrede *et al.* to yield optimal focusing.[128]

4.3.4 Data collection, timing and control

FIG traces, pyroelectric energy sensor readings, and time of flight signal from the MCPs were displayed on a digital oscilloscope (LeCroy Waverunner LT 584). The CCD camera output was processed, displayed and recorded by image acquisition and processing software (Photek IFS32) running on a Windows PC. Spectra were taken using a labVIEW program written by Trottier, which controlled both dye lasers and integrated TOF signal from the oscilloscope.

The flash lamps and Q-switches of both the photodissociation and probe lasers, the molecular beam nozzle, the CCD camera trigger, and the oscilloscope were all controlled by a pulse/delay generator (BNC model 575).

4.3.5   The molecular beam

Gas mixtures for the molecular beam were made in a convection mixing bottle to ensure thorough combination. The mixture composition was 4% NO_2 (Sigma Aldrich, 99.8% purity) in xenon (BOC, 99.999% purity) with a total pressure of 6 bars. The pulsed nozzle through which the mixtures were expanded (Parker Hannifin Series 9 Pulse Valve, controlled by a Parker Instrumentation Iota One Pulse Driver) was run at 10 Hz. The molecular beam pulse shape could easily be monitored using the FIG and modified by adjustment of the nozzle opening time and translation of the nozzle position relative to the skimmer. For more information on the molecular beam apparatus, see the thesis of Flynn, and the thesis of Willis.[129] A typical FIG profile is shown in Figure 4.6. Whilst the expansion has a significant tail, the quality of the leading and central portions is good, with efficient cooling occurring in the expansion: Figure 4.7 displays a REMPI spectrum of trace NO molecules from the earlier part of the beam, showing that only the first and second rotational levels of the trace $NO(^2\Pi_{1/2},$ $v = 0)$ in the molecular beam are occupied.
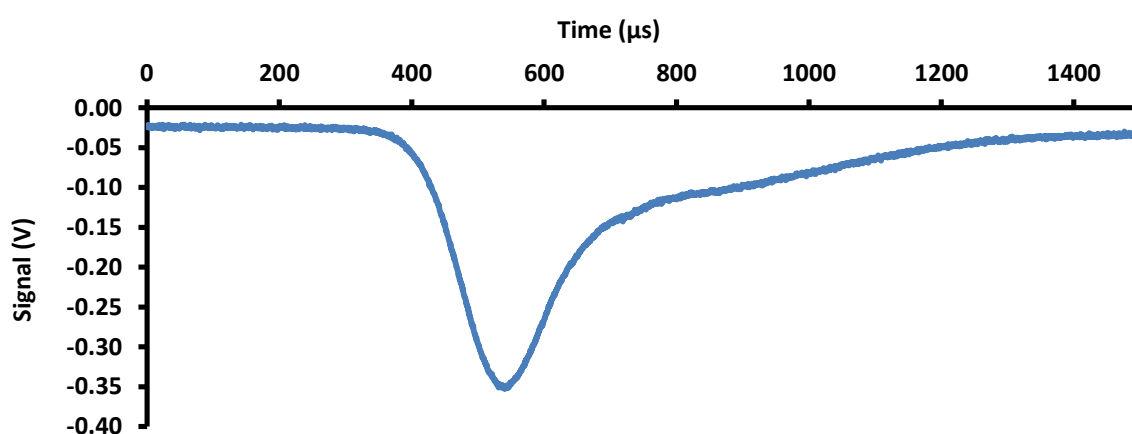
Figure 4.6: the molecular beam pulse as revealed by a typical FIG measurement.
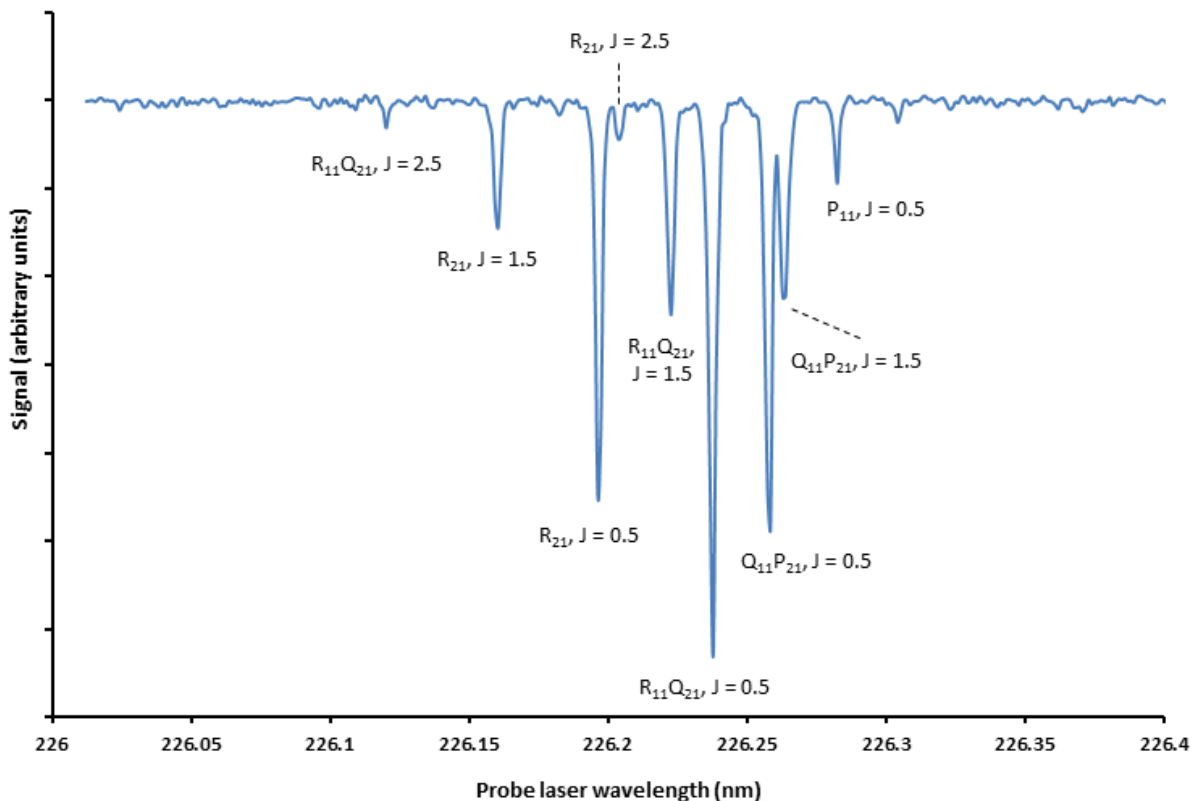
Figure 4.7: rotational spectrum of trace NO($^2\Pi_{1/2}$, $v = 0$) in the molecular beam.

4.4 Acquisition of NO ($^2\Pi_{3/2}$, $v = 0$, $J = 3/2$) population decay curve

4.4.1 Matching of photodissociation wavelength and molecular beam speed

A pixel calibration of the ion imaging apparatus was made by recording photodissociation images across a range of photodissociation wavelengths for the $^2\Pi_{3/2}$, $v = 0$, $J = 1.5$ quantum state, which when analysed gave a pixel calibration value of 6.93 ± 0.01 m s^{-1} pixel^{-1}.

Molecular beam images and velocity origin images were then taken (observing trace NO in/from the molecular beam). A Gaussian fit to the molecular beam profile along the z axis gave a molecular beam speed of 380 ms^{-1}, with a FWHM velocity spread of 51 ms^{-1}. Maxwell-Boltzmann fits to the x and z profiles of the beam yielded a longitudinal temperature of 0.93 ± 0.09 K and a transverse temperature of 0.6 ± 0.06 K, giving an inferred longitudinal temperature of NO$_2$ of 2.63 ± 0.06 K, and an inferred transverse temperature of 1.71 ± 0.04 K. The molecular beam ion image and its longitudinal profile are shown in Figure 4.8. A program written by Eckart Wrede (referred to hereinafter as "image") was used for ion image analysis.[128]
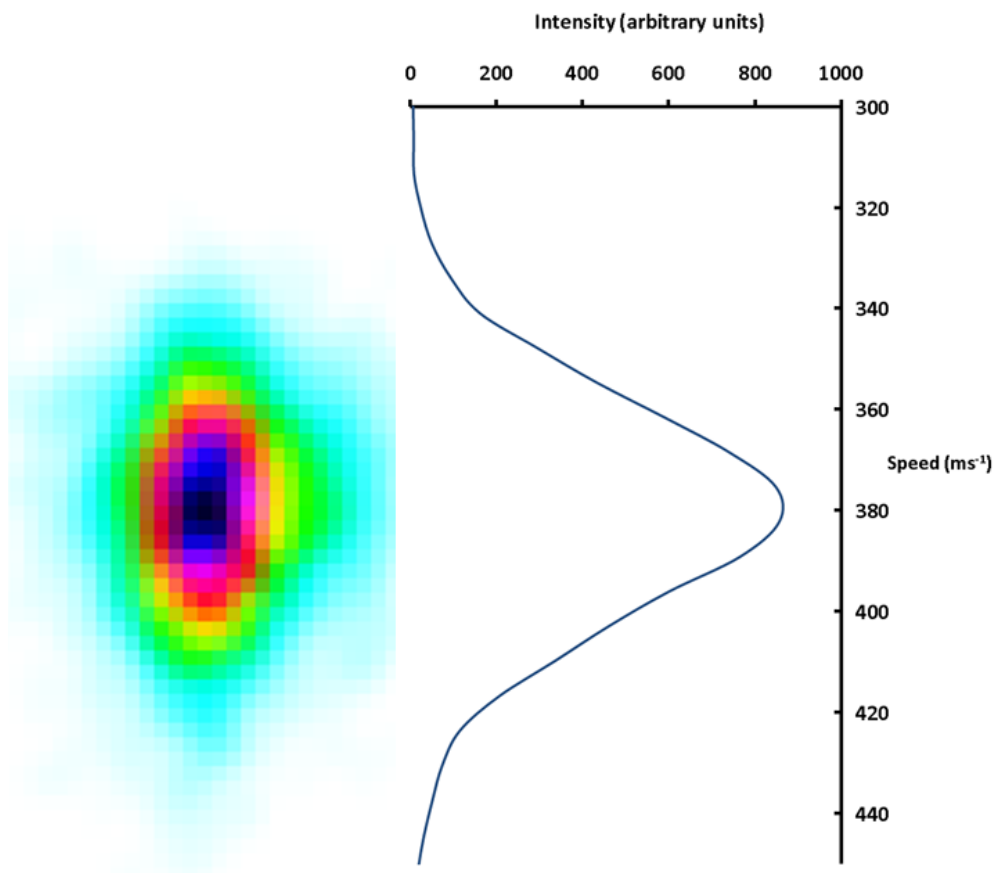
Figure 4.8: ion image of trace NO $^2\Pi_{1/2}$ in the molecular beam (detected *via* the R11Q21, *J* = 0.5 transition) and the velocity profile of the molecular beam along the experimental *z* axis. Note that this is a snap-shot of the centre of the molecular beam pulse, not a profile of the whole beam.

Given the established molecular beam velocity and velocity spread, and using equation 3.3, and a dissociation threshold of 25128.57 cm^{-1},[130] a photodissociation wavelength of 386.7 to 389.5 nm was calculated to be necessary to photostop an appreciable quantity of NO($^2\Pi_{3/2}$, *v* = 0, *J* = 1.5). A photodissociation wavelength of 387.518 nm was chosen, because this was near to the centre of this wavelength range and at an absorption maximum in the photofragment action spectrum taken previously by Trottier (Figure 4.9).
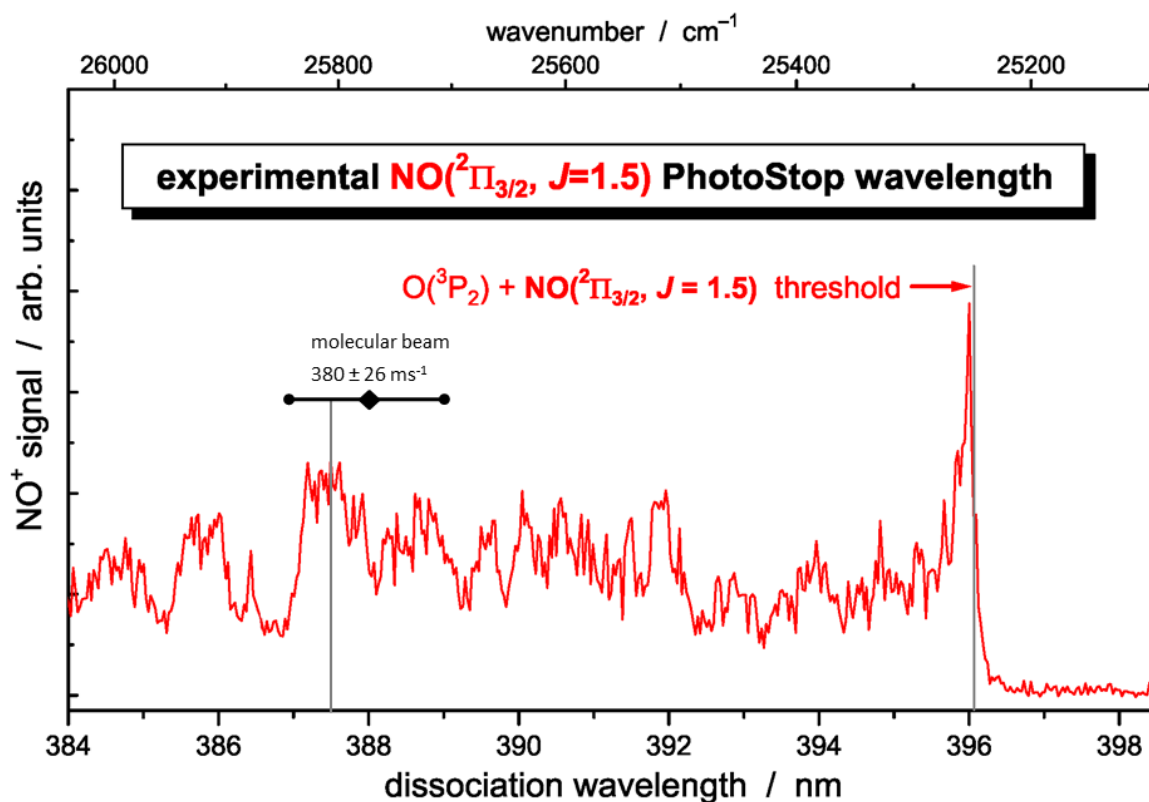
Figure 4.9: photofragment action spectrum. The black line indicates the full width half maximum velocity spread of the molecular beam. The grey lines mark the chosen dissociation wavelength and the dissociation threshold.

4.4.2   Measurement of laser beam diameters

Both the dissociation and probe lasers were focussed through nominal f = 500 mm plano-convex lenses, to reduce and match their diameters and so provide a defined region for photostop (and also a sufficient probe laser intensity for successful REMPI). Trottier had estimated the laser beam diameter in the photostop region by estimating the beam diameter before the lens, and then applying simple geometric optics. This approach is of limited utility, firstly because the unfocussed beam diameter can be guessed only very roughly by eye, and secondly because even if the unfocussed beam diameter is known, geometric optics does not hold near to the focus of a Gaussian beam.

For this work, the photodissociation and probe laser diameters were measured directly, using a razor blade and energy meter as described in appendix E. The beam diameters used for the acquisition of the decay curve, and the distances between focal lens and photostop region used to achieve these diameters, are given in Table 4.2.

Table 4.2: beam diameters of the photodissociation and probe lasers in the photostop region.

Laser	Distance between focal lens and photostop region (mm)	Horizontal $1/e^2$ diameter (mm)	Vertical $1/e^2$ diameter (mm)
Photodissociation	411	0.41	0.68
Probe	583	0.41	1.04

4.4.3 Decay curve data acquisition and the normalisation process

Trottier's decay curve was taken using the photon counting mode of the IFS32 software. This approach is advantageous in that it allows an ion image for each probe laser delay to be captured simultaneously with the decay curve data point. It is limited, however, in that the IFS32 software cannot distinguish multiple simultaneous impacts on the same camera pixel; to avoid under-reporting, then, the probe laser power must be reduced sufficiently that multiple impacts are rare.

This study used the alternative approach of integrating the TOF signal from the MCPs. The response here remains linear with respect to signal over a larger range of signal intensity, allowing the use of a higher probe laser energy and shorter acquisition times.

The REMPI signal of NO($^2\Pi_{3/2}$, $v = 0$, $J = 3/2$) was monitored in the P12 band. The P12 transition was chosen because it is isolated: in large part, the four spectral branches of the X $^2\Pi_{3/2}$ -> A $^2\Sigma^+$ transition overlap (see appendix C).

16 different photodissociation-probe delays were sampled. To account for shot-to-shot fluctuations in laser power and molecular beam composition, each delay data point was averaged over 6000 repetitions. It was noticed that there were significant long term fluctuations in the signal level – hypothesised to be due in part to the air conditioning cycle, and in part to the general trend for signal level to decline as the experiment was run, perhaps as the nozzle heated up, or the tuning of the frequency doubling crystal in the probe laser wandered.

To counteract this fluctuation, all delay data points were normalised against data for a 20 ns delay, normalisation being achieved as follows. Data were collected in 600 shot batches, each 600 shot batch being recorded in a separate data file using Trottier's

labVIEW program. Data files containing data from the delay being sampled (referred to hereafter as delay data files) were interspersed with data files containing data from a delay of 20 ns (referred to hereafter as normalisation data files). The data were then adjusted by dividing each delay data file by its temporally adjacent normalisation data file.

Background measurements were taken in a similar fashion. As a final precaution against signal fluctuations distorting the curve, the data points were taken in a random order, the randomness being generated by atmospheric noise.

The efficacy of the normalisation procedure can be seen in Figure 4.10, which compares the normalised and un-normalised data sets. The difference in data quality is particularly apparent for the 2 μs delay, for which two data points were acquired on different days. In the un-normalised graph, they differ widely, with the larger value being more than 100% larger than the smaller. In the normalised graph, the two points are so close in value as to be indistinguishable on the scale to which the graph is drawn.

The primary source of background signal was thought to be native $NO(^2\Pi_{3/2}, v = 0, J = 3/2)$ in the molecular beam. Preliminary measurements taken with the photodissociation laser severely mistimed detected no difference in $NO(^2\Pi_{3/2}, v = 0, J = 3/2)$ signal level with the photodissociation blocked or unblocked, suggesting that once NO produced by photodissociation departed the photostop volume it did not contribute in any meaningful way to the background $NO(^2\Pi_{3/2}, v = 0, J = 3/2)$ signal within the chamber. Hence, background data were collected with the probe laser and molecular beam in operation but the photodissociation laser blocked.
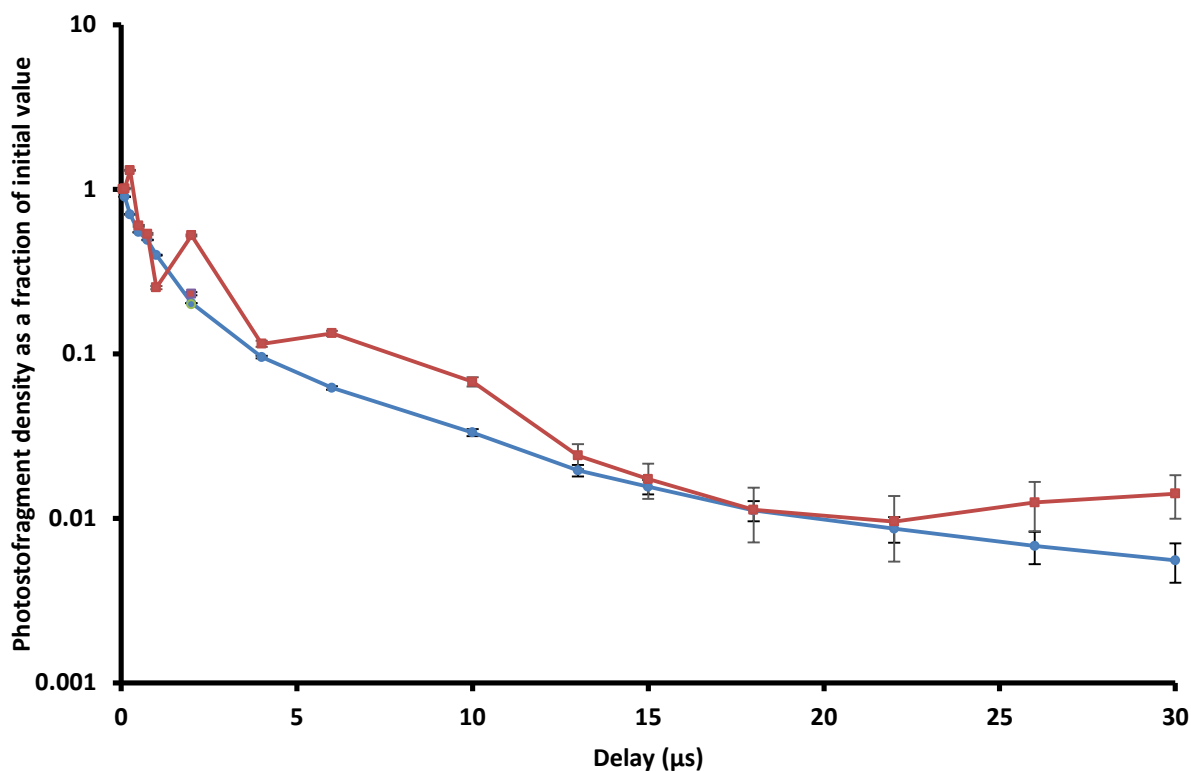
Figure 4.10: normalised (blue) and un-normalised (red) decay curves for the photostop of NO($^2\Pi_{3/2}$, v = 0, J = 3/2) at 387.518 nm. The error bars represent the standard error to the one-sigma confidence level.

4.4.4 Comparison of experiment and simulation

The parameters used by the phstop program to provide the simulated curve below are given in appendix G. The experimental and simulated decay curves are plotted in Figure 4.11. There is good agreement between the simulated and experimental decay curves at shorter photodissociation-probe delays. At longer delays, the phstop program underestimates the experimental signal.

The explanation for this tendency towards underestimation is not immediately obvious. It is tempting to suggest that the background subtraction method used in the acquisition of the experimental curve was not as effective as might be hoped, artificially inflating the experimental signal level. However, if this were the case, one would expect the rate of divergence of the entirely background-free simulation from the experimental curve – when plotted on a logarithmic scale as in Figure 4.11 – to be initially imperceptible and then become increasingly severe with increasing time delay. This effect is illustrated in Figure 4.12, in which the experimental decay curve is plotted on a logarithmic scale alongside a curve created by subtracting a small constant from all of the experimental points. Comparison of the 4-30 μs regions of figures Figure 4.11

and Figure 4.12 strongly suggests that inadequate background subtraction is not the cause of the simulation/experiment variation.

In any case, whilst the phstop program does not perfectly reproduce the latter portion of the experimental decay curve, the disparity between the experimental and simulated decay curves at 30 μs (the longest delay sampled here) was barely more than a factor of two. It may be concluded that the phstop program provides a good description of the photostop process at short time delays, and a reasonable description at longer time delays.
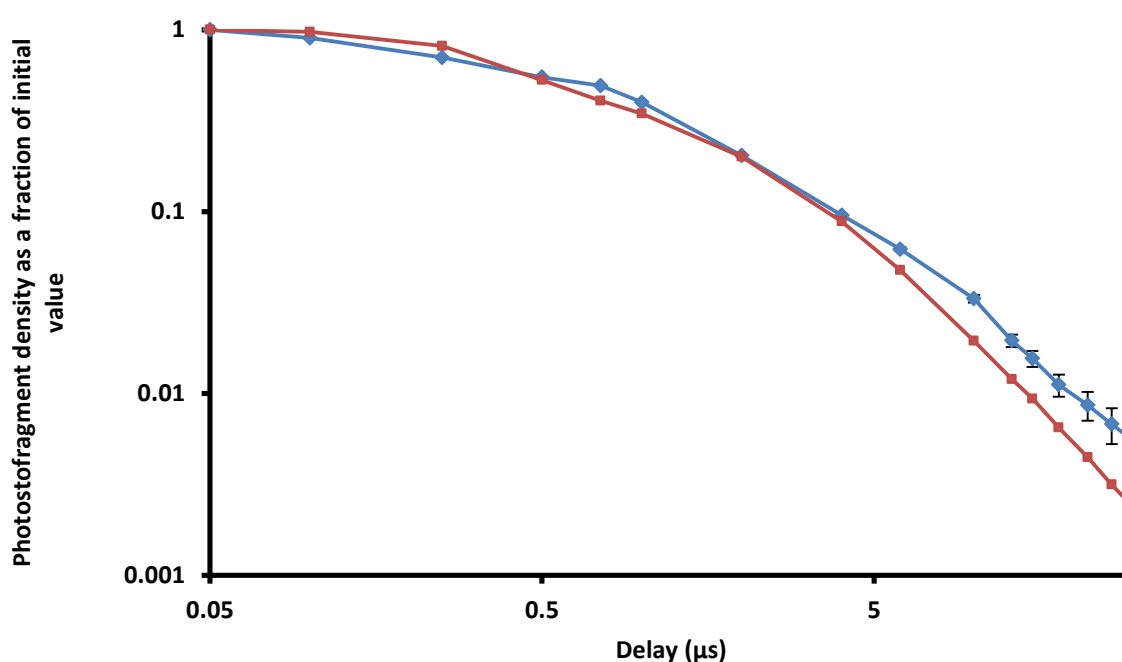
Figure 4.11: experimental (blue) and simulated (red) population decay curves following the photodissociation of NO_2 at 387.518 nm.
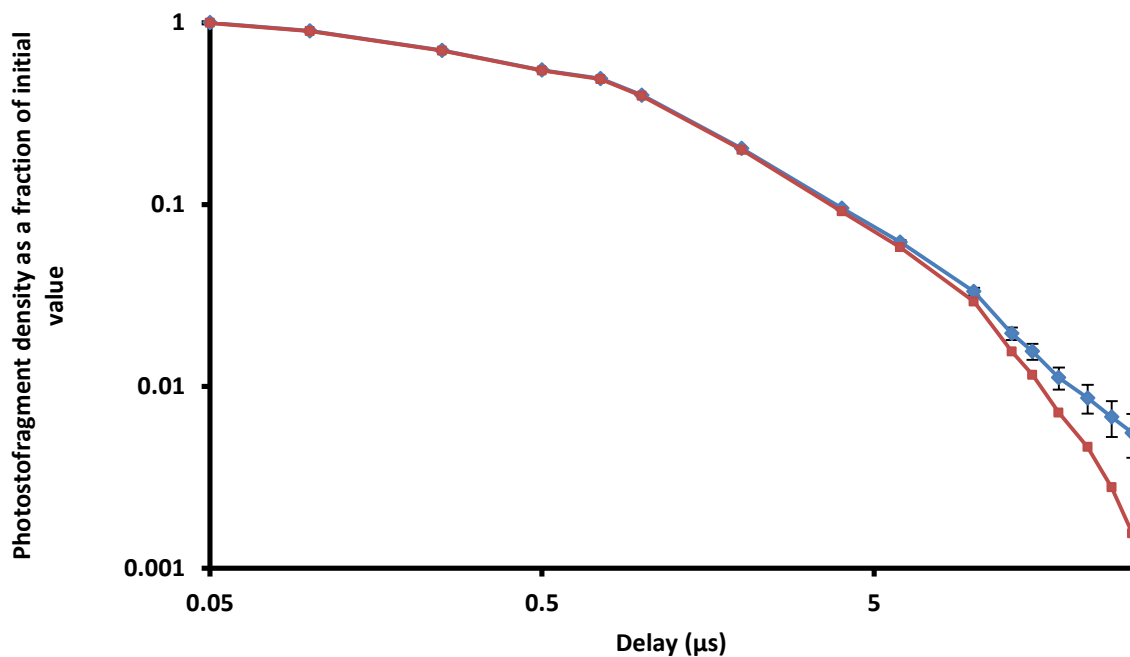
Figure 4.12: experimental (blue) and modified experimental (red) decay curves. The modified curve illustrates the effect of subtracting a small constant from each experimental data point, to imitate the effect of inadequate background subtraction.

4.5   Acquisition of a new 10 μs dissociation-probe delay image

With the experiment fully optimised, a 10 μs delay image was acquired. It is shown in Figure 4.13, analysis of which gave a temperature of stopped $NO(^2\Pi_{3/2}, v = 0, J = 1.5)$ of 1.6 K.
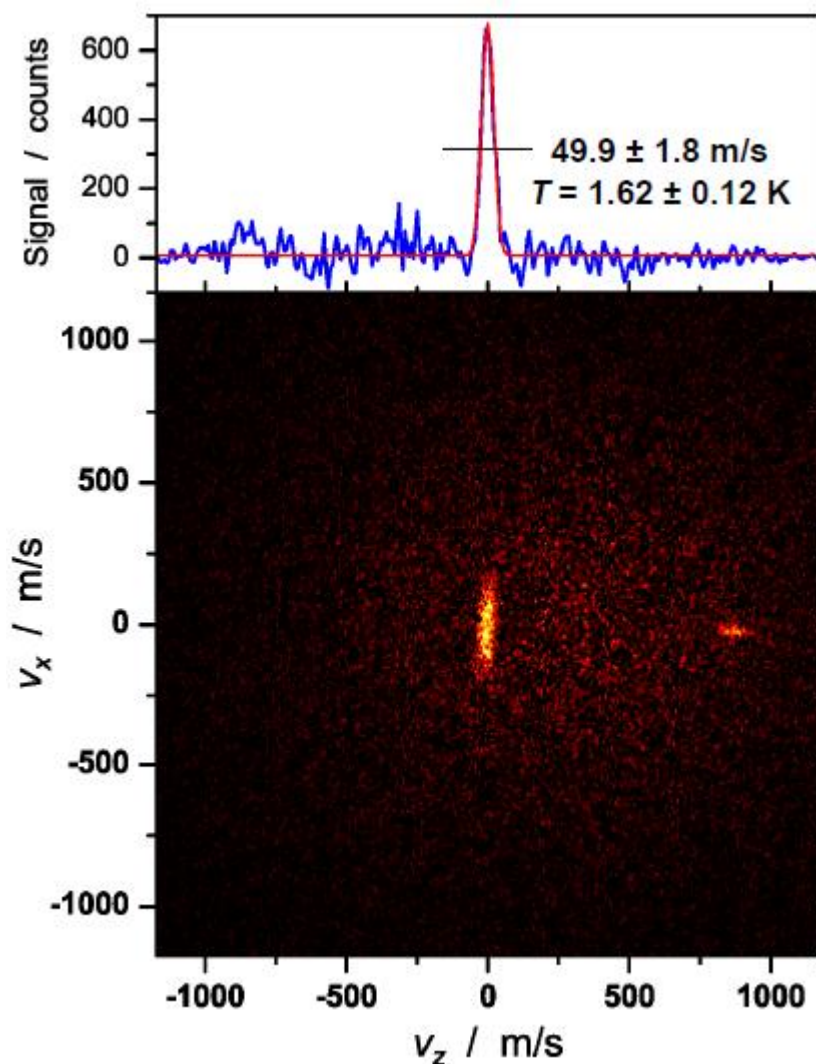
Figure 4.13: 10 μs delay ion image of photostopped NO, showing the temperature along the molecular beam axis.

4.6 An alternative photodissociation scheme for the photostop of NO?

At 249.2 nm, a second photodissociation channel opens for NO_2, involving excitation to the $(2)^2B_2$ level.[131] This second region was examined to see if it might be an improvement upon the existing NO_2 photodissociation scheme. Wavelengths around and above 240 nm were thought unlikely to be productive, because the absorption cross-section of NO_2 in this region is an order of magnitude lower than at 387 nm,[132] meaning that a rovibrational distribution spectacularly favourable to photostop (see section 7.3) would be required in order to improve upon the original photodissociation scheme. Experimental work conducted with a photodissociation wavelength in the region of 240 nm confirmed that little $NO(^2\Pi_{3/2}, v = 0, J = 1.5)$ was seen in this region.

The photodissociation of NO_2 at shorter wavelengths in this band – around 226 nm – was studied by Wilkinson *et al.*[131,133] Significant levels of rotational excitation of NO were found, but a definite proportional population of the $^2\Pi_{3/2}$, $v = 0$, $J = 1.5$ state was not explicitly stated, so the photodissociation in this region was investigated during some experimental down-time preceding the work presented in the next chapter.§ It was found that only a very small quantity of $NO(^2\Pi_{3/2}, v = 0, J = 1.5)$ was produced: so small that it could be detected only when the photodissociation laser wavelength coincided with a peak in the NO REMPI spectrum. It was presumed that at these wavelengths, the photodissociation laser excited the NO fragments to the intermediate A $^2\Sigma_+$ excited state used for REMPI, so that the REMPI laser performed only the ionisation step, an effect which would serve considerably to enhance the signal level.

---

§ In fact, the motivation for this investigation of an alternative photodissociation scheme was associated with problem of scattered light from the photodissociation laser discussed in the next chapter. If photodissociation could have been carried out near 226 nm, the filter present in the LIF set-up to block scattered light for the probe laser might have served to block scattered light from the photodissociation laser as well, and hence allowed some experimental work to be conducted whilst waiting for the completion of the modification work on the PMT.

5 Attempted magnetic trapping of NO

5.1 Introduction

Many applications of cold molecules require a trapped population, and the state of the art in cold molecule production involves trapping cold molecules, not simply creating them. Photostop may be a particularly suitable technique for combination with trapping, because it does not rely on magnetic or electric fields for slowing, and thus can be carried out within a trapping potential. This should allow for the repeated loading of a trap, a scheme proposed for several systems.[70]

For these reasons, it has been a long-standing aim of the photostop project to trap photostopped molecules. Most recently, this has been motivated by the "MMQA: Microkelvin Molecules in a Quantum Array" collaboration,[134] which works towards producing a regular array of ultracold polar molecules that can be used to simulate solid phase quantum effects. Photostop is one of the techniques for bringing molecules to rest being developed in this project. The aim of the work described in this chapter, then, was to demonstrate the trapping of cold NO.

5.2 The trap

As reviewed in chapter one, there are a number of options for trapping. Magnetic trapping with permanent magnets was chosen for use with photostop due to its economy and simplicity. An electric trap would require a certain amount of modification to the chamber to allow access for high voltage feeds, and would also require expensive control equipment; a magnetic trap generated by electromagnets suffers the same drawbacks.

A magnetic trap formed by permanent magnets, by contrast, requires no power supply, no control equipment, and no modification to the chamber beyond the drilling of mounting holes and the addition of two laser ports. It also brings the advantage of higher field gradients (and hence deeper traps) than can be generated by electromagnets of similar size. Further, permanent magnets are easy to cool, which could in future be a path to reduce black body radiation and hence decrease the occurrence of Majorana transitions.[135]

5.2.1 Magnetic trapping

Magnetic trapping relies upon the Zeeman effect, which is a manifestation of space quantisation, the phenomenon whereby the orientation of an atom or molecule is quantised in a magnetic field.

The orbital and spin angular momenta of the electrons in a molecule, and the rotational motion of the whole molecule, couple to give the total angular momentum of a molecule, J. When the molecule is within a magnetic field, J aligns with the field direction. The component of J along the field direction is given by $M_J\hbar$. M_J can take the values $J, J - 1..., -J$ – *i.e.*, the alignment of J with the applied field is quantised, as illustrated in Figure 5.1.

For a diatomic molecule following Hund's coupling case (a), the energy of the molecule varies with M_J according to the equation

$$\Delta E = \frac{(\Lambda + 2\Sigma)\Omega M_J \mu_B B}{J(J+1)} \qquad \text{(Eq. 4.1)}$$

where Λ is the projection of the total orbital angular momentum of the electrons onto the internuclear axis, Σ is the projection of the total spin angular momentum of the electrons onto the internuclear axis, μ_B is the Bohr magneton, and B is the applied field.[136] For $NO(^2\Pi_{3/2}, J)$, which we wish to trap, equation 4.1 simplifies to

$$\Delta E = \frac{3M_J \mu_B B}{J(J+1)}$$
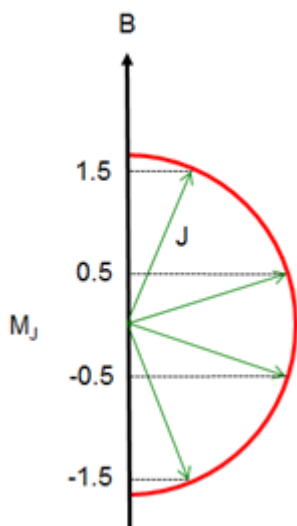
Figure 5.1: alignment of *J* with applied magnetic field for a molecule with *J* = 1.5.

The effect of increasing applied magnetic field on the internal energy of the molecule is shown in Figure 5.2. It can be seen that increasing magnetic field can cause an increase or a decrease in internal energy, depending on the orientation of *J* with the field. Molecules for which an increasing field induces a decrease in internal energy are called high field seekers. Molecules for which an increasing field induces an increase in internal energy are called low field seekers. Obviously, low field seekers are repelled by increasing magnetic field strength, and so can be confined within a region of space if the magnetic field strength around that region increases in all directions.
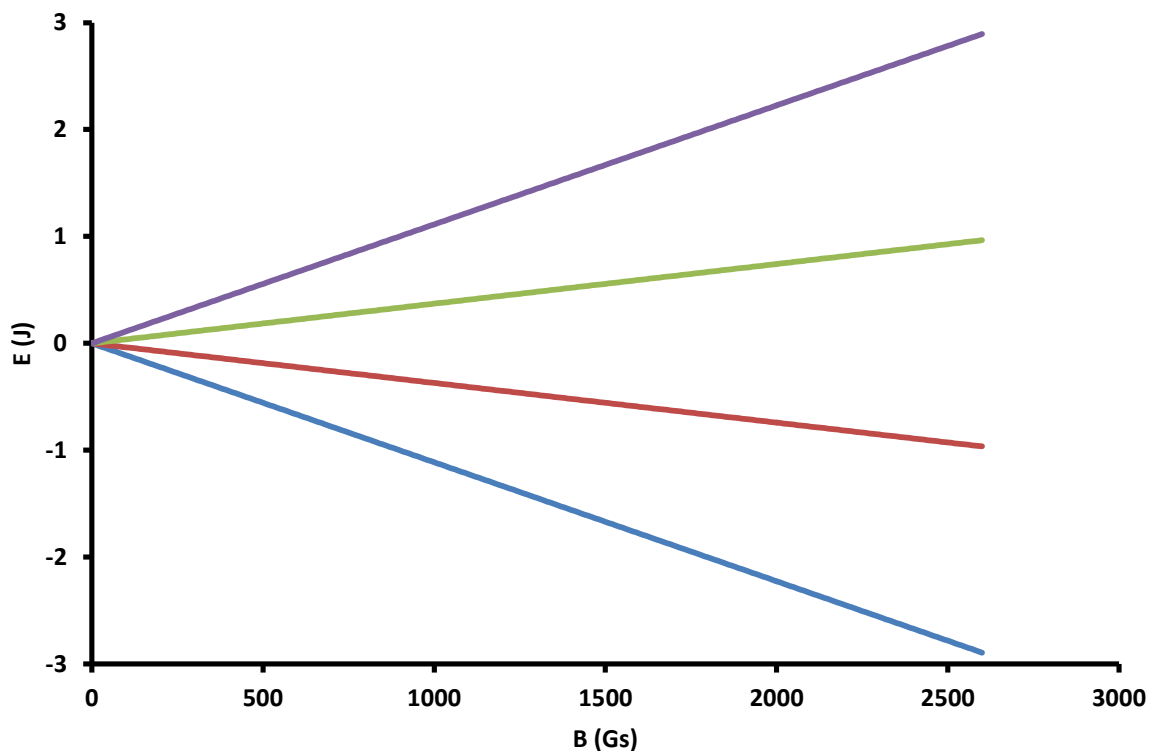
Figure 5.2: the Zeeman effect for a molecule with *J* = 1.5 and M$_J$ = 1.5 (purple), 0.5 (green), -0.5 (red), and -1.5 (blue).

5.2.2 Trap design

The trap was designed by Robert Rae[137] using Simion, which whilst not intended for the simulation of magnetic fields can be used to do so with reasonable accuracy. Rae found that a magnetic sextupole trap (3 pairs of opposing magnets in a cubic configuration) would provide several advantages over the more conventional quadrupole trap, with a deeper and more even potential barrier. It would also have a large field free region in the centre, which although potentially problematic in its encouragement of Majorana transitions, could also provide an interesting environment for field free experiments on cold molecules, an area of interest to theoreticians.

It was found that for the sextupole trap, conical magnets provided best balance between mass of magnetic material and closeness of approach. The magnet size and shape providing the best sextupole trap, within the spatial constraints of the experiment (*vide infra*), is shown in Figure 5.3.
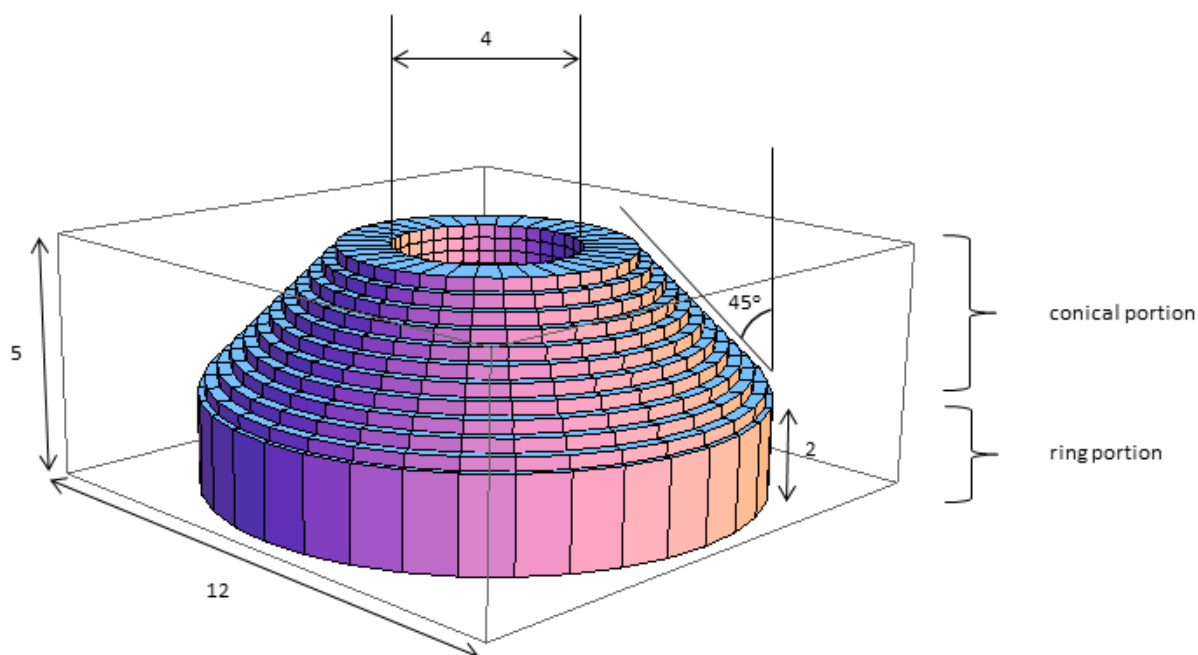
Figure 5.3: dimensioned diagram (in mm) of the magnets used in this work. Note that the magnets have a smooth chamfer - this image reflects the stepped approximation used in Mathematica simulations of the quadrupole trap (*vide infra*).

The trap holder was designed by Peter Lent, and a detailed description and explanation of its construction may be found in his thesis.[135] In summary, the trap holder is a cuboid formed of six parts, which are held together by screws, and within which the magnets are held in opposing pairs by their mutual repulsion. The design is such that two parts of the holder may be left out if not in use, allowing easier optical access to the trap volume.

5.2.3   Mathematica simulations

Whilst the magnets and holder had been designed to form the sextupole trap, the trap could easily be assembled as a quadrupole trap simply by placing only one pair of magnets in the holder, in opposing positions. All previous instances of magnetic trapping of molecules have used quadrupole traps, formed either from a pair of solenoids in an anti-Helmholtz configuration (trapping of CaH,[86] NH,[87] CrH and MnH,[88] and OH,[138]) or from a pair of permanent magnets (OH;[139,125] it was this trapping work that led to the choice of NdFeB magnets for the photostop experiment). Quadrupole traps have also been widely used for trapping atoms.[70] Conversely, little is known about sextupole traps,[137] and the effect of the large field free region in the centre of the

74

sextupole trap could not be anticipated, so it was decided that initial efforts to trap NO would use a quadrupole trap for simplicity.

Whilst the design of the trap holder had intentionally allowed alternative assembly as a quadrupole trap, no attention had been paid to the optimisation of the quadrupole trap: rather, the trap holder had been designed to give the closest possible approach between magnets in the sextupole trap. Before experimental work began, further simulation work was undertaken to optimise the trap holder for quadrupole trapping. This work was conducted using Radia, a Wolfram Mathematica plug-in developed by the Insertion Devices group at the European Synchrotron Radiation Facility (ESRF) that allows 3D magnetostatic modelling for a variety of objects, including permanent magnets, using a boundary element method. For a description of the simulation program, see appendix H.

The simulations probed two variables: the relative orientation of the magnets, and their separation.

Regarding the relative orientation: in the sextupole trap, the use of chamfered magnets allows close approach between the magnets. In a quadrupole trap, with no orthogonal magnet pairs intruding, there is no obvious advantage to using conical magnets. The expense and delay incurred in obtaining ring magnets for this trial stage of the experiment was not judged worthwhile, but the chamfered magnets could be made more "ring magnet like" by reversing them so that their ring portions faced each other (Figure 5.4).

Regarding the separation: in the sextupole trap, each pair of magnets intrudes between both other pairs; removing two pairs of magnets, therefore, allows the magnets of the remaining pair to approach each other more closely. The approach of the magnets in the quadrupole trap was constrained by the need to pass the photodissociation and probe lasers through the gap between the magnets. The minimum magnet spacing judged practical to allow easy laser alignment and avoid excessive scattering of light from the trap was 3 mm.

Radia simulations were run of quadrupole traps with magnets in both cone-facing and ring-facing orientations, and with intermagnet separation varied between 3 and 8 mm. It was found that a 4 mm separation, with the magnets orientated with rings facing (Figure 5.4) produced the deepest trap, with a trap depth of 2600 G (Figure 5.5). A 3 mm separation in this orientation does produce a higher maximum field strength, with

a saddle point on the axis between the magnets of about 4800 Gauss – but the contour lines run into the magnet at only 2200 G, giving a shallower trap.

The favoured quadrupole trap is depicted again in Figure 5.6, with the trap depth converted to Kelvin. It can be seen that the quadrupole trap should be able to trap $NO(^2\Pi_{3/2}, v = 0, J = 1.5)$ with a kinetic temperature of up to 0.21 K (a speed of up to 10.8 m s^{-1}). The phstop simulation program estimated that this trap depth should correspond to approximately 4 x 10^3 trapped $NO(^2\Pi_{3/2}, v = 0, J = 1.5)$ fragments. This would yield an initial density (in the production region) in the region of 3 x 10^5 cm^{-3}, which would diminish as the trapped molecules spread out through the trap. Detailed modelling of the trajectories of trapped molecules was not carried out, but some initial simulation work suggested qualitatively that most molecules would spend most of their time near the centre of the trap (*i.e.* in the region interrogated by the probe laser) and thus that 3 x 10^5 cm^{-3} was a reasonable starting estimate of density.

These numbers would be towards the lower end of achievement for magnetic trapping work carried out with molecules: an unspecified number of OH molecules were trapped with a density of 3 x 10^3 cm^{-3},[138] and approximately 10^3 were trapped with a density of 10^6 cm^{-3};[139] 10^8 CaH molecules were trapped with a density of 8 x 10^7 cm^{-3};[86] 10^8 NH molecules were trapped with a density greater than 10^8 cm^{-3};[87] and about 10^5 CrH and MnH were trapped (separately) with densities of about 10^6 cm^{-3}.[88] However, successful trapping of NO at the anticipated level would still be a significant achievement – and further, it was hoped that if the trap lifetime of $NO(^2\Pi_{3/2}, v = 0, J = 1.5)$ was long enough, repeat loading of the trap would be seen, increasing the trapped number and density.
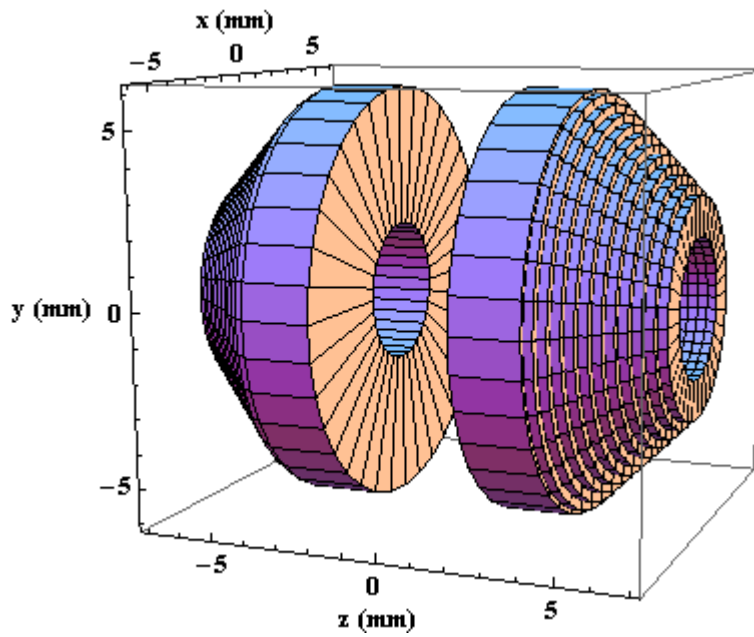
Figure 5.4: the quadrupole trap, with the ring sections of the magnets facing each other, and an intermagnet separation of 4 mm.
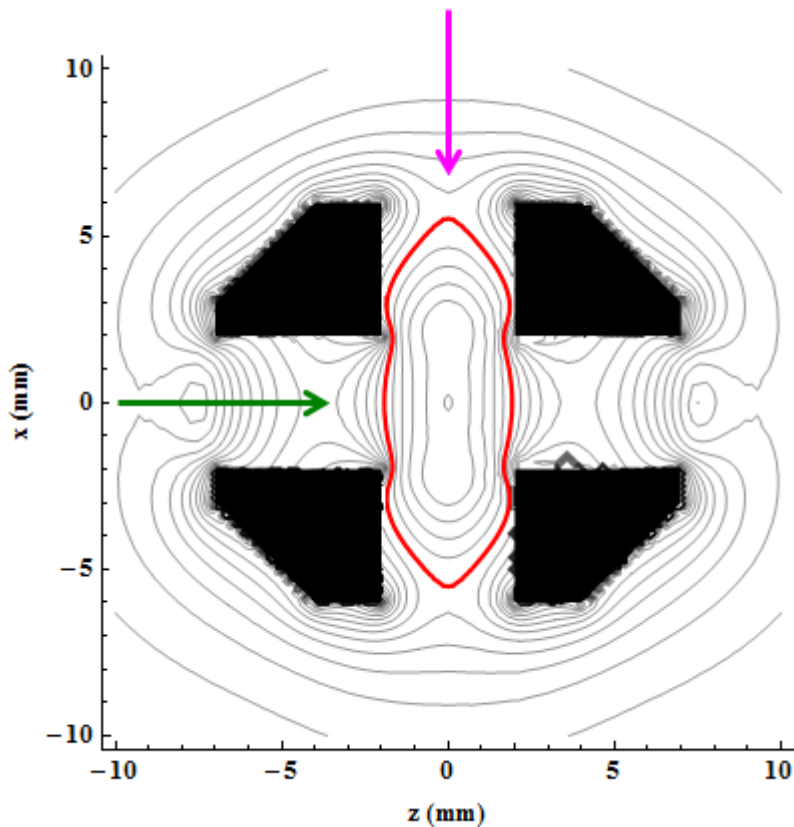
Figure 5.5: a section through the quadrupole trap depicted in the previous figure. The black shapes are the magnets. The green arrow demonstrates the route of the molecular beam through the bores of the magnets; the purple arrow shows the path of the laser beams through the gap between the magnets. The contour lines are in steps of 500 Gauss. The red separatrix denotes the 2600 Gauss trap.
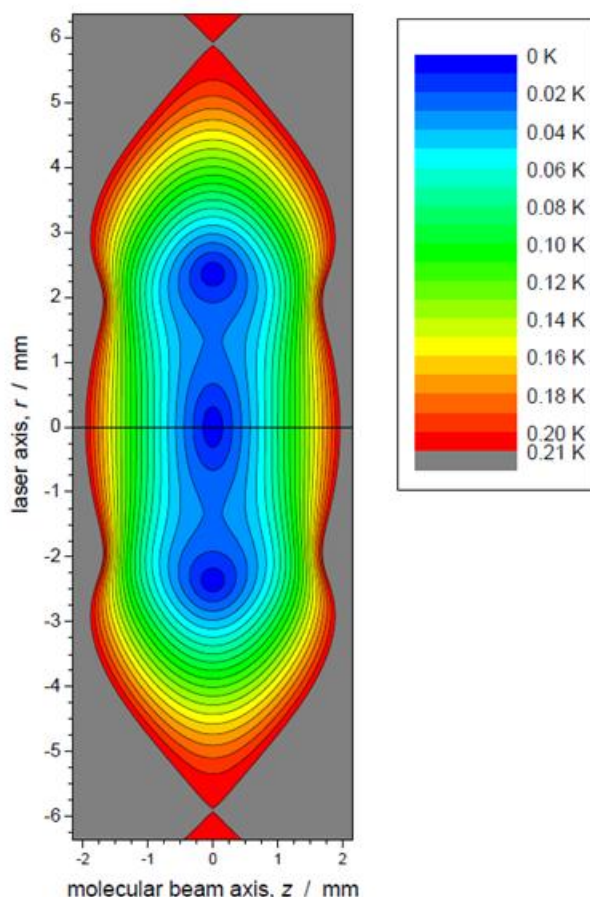
Figure 5.6: the region of Figure 5.5 enclosed by the separatrix, with contour lines in Kelvin. This figure has a higher resolution of contour lines than Figure 5.5, sufficient to reveal that the quadrupole trap in fact contains three potential minima.

5.2.4   Detection of trapped NO

Using REMPI for detection of NO fragments within the trap would have required substantial modification of the experiment to allow the mounting of the trap within the ion optics array. Instead, the simpler option of detecting the NO fragments with LIF was chosen. The trap was mounted on the back of the skimmer plate (the skimmer plate having been modified to facilitate the trap installation) in the space between the skimmer plate and the ion optics stack. The collection optics (designed by Lent using Radiant Zemax's "Zemax" optical design software) extended downwards from the ion optics flange above the trap. Figure 5.7 displays the trap and the LIF optics, and their position within the photostop machine (it may also be helpful to refer back to Figure 4.3 on page 56).
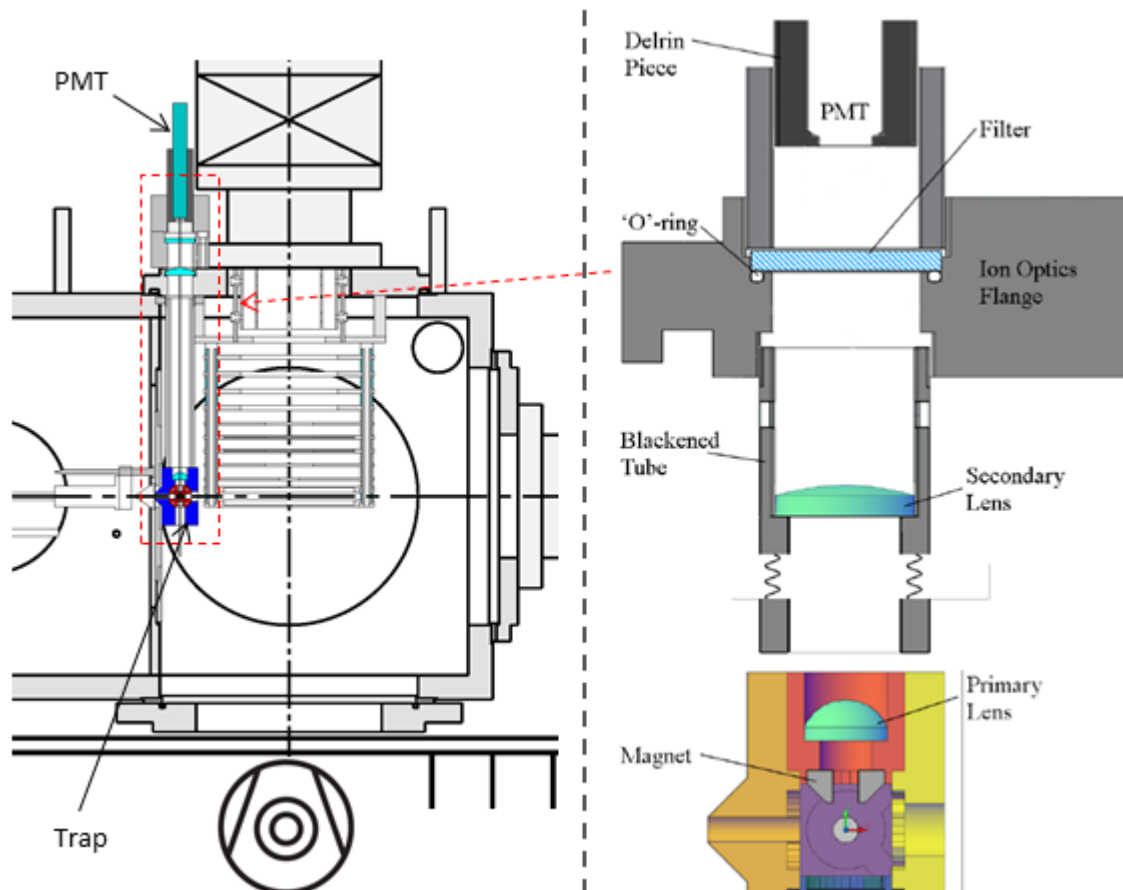
Figure 5.7: the situation of the magnetic trap and LIF collection optics within the photostop chamber, and a diagram of the LIF collection optics as designed by Lent. The collecting lens sits on top of the magnetic trap; the secondary lens is held in a tube descending from the ion optics flange of the vacuum chamber. A filter (for transmission details see below) to prevent the transmission of scattered light from the probe laser provides the seal to vacuum. The PMT is held within a Delrin tube that shields it from background light.

5.2.5 Estimate of detectable signal level

The detectable signal level was estimated in a fashion similar to the following.

With a low noise level and using long collection times for data acquisition, it should be possible to detect $NO(^2\Pi_{3/2}, v = 0, J = 1.5)$ at fragment densities lower than that required for the apparatus to detect one photon per laser shot. However, with the noise level unknown at this point, the one photon per laser shot level is chosen as an arbitrary measure of detection efficiency, and the density of $NO(^2\Pi_{3/2}, v = 0, J = 1.5)$ required for the apparatus to detect one photon per laser shot is calculated. For brevity, this density is henceforth referred to as the minimum detectable density.

The collection efficiency of the LIF optics was estimated at 5% by the Zeemax model. With the probe laser filter passing 64% of the LIF light,[140,141] a detector sensitivity in the region of 20%, and assuming a 10% loss at both lenses, 1 photon should be detected for about every 193 photons emitted.

The same excitation scheme would be used for the detection of NO with LIF as was used for the detection of NO with REMPI, but with a lower laser intensity so as to avoid the ionisation step.[142] NO(A $^2\Sigma^+$, v = 0) does not predissociate; and with a radiative lifetime of 206 ns,[143] collisional quenching is also insignificant considering the density of molecules in the molecular beam (about 2.2 x 10^{14} cm^{-3}). It is therefore assumed that the fluorescence quantum yield of NO is one, and hence that emission of 193 photons requires the excitation of 193 molecules.

Mayor et al[144]calculate the absorption cross section of NO($^2\Pi_{3/2}$, v = 0, J = 1.5) on the P12 band to be 2.19 x 10^{-18} cm^2 cm^{-1} at 295K. Correcting for the Boltzmann distribution of the rotational population of NO at this temperature (approximately 1.2% of NO($^2\Pi_{3/2}$, v = 0) in J = 1.5) yields a temperature-independent absorption cross section of 1.78 x 10^{-16} cm^2 cm^{-1}. With a 0.4 cm^{-1} probe laser bandwidth, the cross section becomes 4.45 x 10^{-16} cm^2. Meanwhile, a probe laser energy in the region of 50 µJ means about 6 x 10^{13} photons produced per laser pulse.

According to the Beer-Lambert law, the number of photons absorbed per unit distance travelled through the probe volume, $\frac{dN}{dx}$, is given by

$$\frac{dN}{dx} = N\,n\,\sigma \qquad \text{(Eq. 4.2)}$$

where N is the number of photons in the laser pulse, n is the density of absorbing molecules, and σ is the absorption cross section.

With a molecular beam width of 0.27 cm (predicted by the phstop program), and given the above derived figures: by rearrangement of equation 4.2, the generation of 193 photons per laser shot requires a fragment density of 3.3 x 10^4 cm^{-3}.

This estimate is complicated slightly by consideration of saturation effects. The entire probe volume, calculated from the molecular beam width (0.27 cm) and the intended laser beam 1/e^2 diameters (0.3 cm) is 0.024 cm^3; given the derived density, this corresponds to 800 molecules in the probe volume, of which 24% are expected to be excited. Undoubtedly, saturation of the absorption, particularly in the more intense central portion of the laser beam, will cause this number to be an overestimate. If it is

assumed for the sake of argument that saturation cost an order of magnitude in signal, that would put the minimum detectable density in the region of 3×10^5 cm^{-3} – a draconian assumption, perhaps, but given the uncertainty surrounding this whole estimate it does no harm to be conservative.

Figure 5.8 compares simulations of the expected NO($^2\Pi_{3/2}$, $v = 0$, $J = 1.5$) population decay curves expected following photodissociation (ignoring the effects of the magnetic trap) for both the presumed optimum experimental parameters for the experiment, and the parameters used in the following work; along with the estimated minimum detectable density, and the estimate of the trappable population (section 5.2.3). It can be seen that several hundred microseconds of the decay curve were expected to be observable, and it was thought there was a reasonable chance of observing a trapped population.
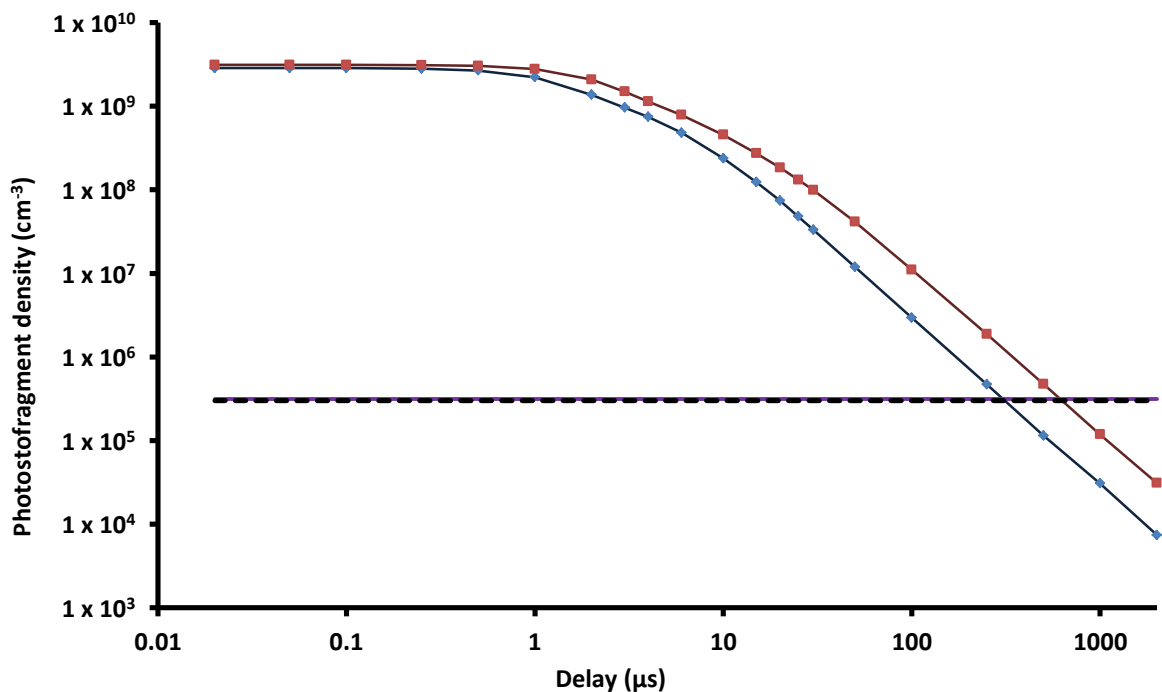
Figure 5.8: comparison of simulated NO($^2\Pi_{3/2}$, $v = 0$, $J = 1.5$) densities with the estimated detection limit. The red curve corresponds to the "ideal" experimental parameters, and the blue curve corresponds to the experimental parameters used in the following work (see appendix I). Laser beam diameters were measured as described in chapter 4. The purple line is the estimated trappable density as discussed in section 5.2.3, and the black dashed line is the estimated minimum detectable density. Notice that the estimated initial photofragment density is similar to that estimated for the previous work on NO, despite the use of a much larger photodissociation laser beam and a similar photodissociation laser energy; this is because photodissociation conducted inside the magnetic trap is occurring much closer to the skimmer, where the molecular beam is more intense.

Of course, the fragment densities were simulations, and the signal level was a ball-park estimate – but given that the difference between the predicted initial density of $NO(^2\Pi_{3/2}, v = 0, J = 1.5)$ and the predicted minimum detectable density was nearly four orders of magnitude, a large amount of $NO(^2\Pi_{3/2}, v = 0, J = 1.5)$ signal was expected to be visible even if the predictions were somewhat inaccurate,[**] providing a basis for development of the instrument and experiment (this being the group's first work with LIF).

5.3   Trapping experiment

The experimental set-up was largely as described in the previous chapter, with the exception of the above stated modifications involving the trap and LIF collection optics; additionally, the optical access flanges were modified with additional windows to allow the probe and photodissociation lasers to counterpropagate through the centre of the trap along the experimental *x* axis.

Signal from the PMT (Hamamatsu model R2496) was monitored using the LeCroy digital oscilloscope. The PMT could be used in two modes. Coupling to the oscilloscope with 1 MΩ resistance produced a response that was integrated by Trottier's labVIEW code in the same way as the signal from the MCP plates (see chapter 4); coupling to the oscilloscope with 50 Ω resistance, individual photon impacts produced single spikes of signal, which would have been counted individually had the experiment reached such a stage as to make this necessary.

5.3.1   Problems with scattered light

In the original LIF detection design by Lent described above, a filter was included to remove scattered light from the probe laser (see the caption of Figure 5.7). However, when the LIF detection apparatus was tested, the scattered light from the probe laser (when the laser was used at the intended energy) was sufficiently strong that it was detected despite the filter, causing a saturation spike at the instant of firing and

---

[**] And of course, it should be remembered that the simulated densities could have been underestimates rather than overestimates.

significant noise for 100-200 ns thereafter. This problem was circumvented in the short term by beginning signal acquisition 200 ns after the laser pulse (which considering the radiative lifetime of 206 ns[143] implies discarding 62% of the LIF signal) and limiting the probe laser energy to 10-15 µJ.

Much more problematic was the scattered light created by the photodissociation laser. No measures had been taken to prevent scattered light from the photodissociation laser reaching the PMT: it had been thought that with careful laser alignment and optical baffles along the laser entry and exit arms, the amount of scattered light reaching the PMT would be small, and certainly would be insignificant following all but the smallest of time delays between photodissociation and probe lasers.

In the event, the scattered light from the photodissociation laser was so strong that it saturated the PMT, making any measurement within a few microseconds of the photodissociation event impossible, reducing the sensitivity for several tens of microseconds thereafter, and creating noise for several hundred microseconds.

5.3.2 Minimising the exposure of the PMT to scattered light

It was decided that the PMT would be modified to allow it to be gated. This approach was chosen in preference to acquiring a filter that would cut out photodissociation laser light, partly because the gated PMT approach is more versatile, working for any photodissociation wavelength; and partly because filters opaque at 387 nm, but transmissive at in the 230-290 nm region, are both hard to source and expensive.

The gating modification was custom made; the PMT was configured to be "normally on". Figure 5.9 displays the change in sensitivity of the PMT as a function of delay after the gate was turned off. The rise time to full sensitivity was approximately 200 µs. Whilst longer than desirable – the specification had been for a rise time of 50 ns – it was not thought to be a problem. 50% sensitivity was achieved after approximately 2 µs, and thereafter it would be trivial to adjust data acquired with the PMT according to a sensitivity function derived from the data in Figure 5.9. There would be no need in the trapping experiment to characterise the early portion of the population decay curve, and certainly not prior to 2 µs.

Unfortunately, it was found that the gate was by no means sufficient to block all of the scattered light from the photodissociation laser when the laser was run at full energy (4 mJ per pulse). Extensive experimentation – checking of optical pathways, insertion

and removal of baffles in the laser ports, removal of the port windows to eliminate the possibility of fluorescence light reflecting back and forth between them, repeated attempts to realign the trap and LIF optics, irising, focussing, and telescoping of laser beams – did reduce the scattered light to some extent, with the most dramatic improvement brought about by reinserting the sides of the trap, which had been removed to improve optical access.

However, the improved level of scattered light was still far too large. It was not thought sensible to run the experiment in this condition and simply try to detect $NO(^2\Pi_{3/2}, v = 0, J = 1.5)$ at longer delays after the photodissociation laser had fired, when the noise from the photodissociation pulse had subsided: given that the gating function of the PMT was able to block light from the fluorescent light bulbs illuminating the laboratory with no difficulty whatsoever, the amount of scattered light incident upon the PMT when the photodissociation laser was run at 4 mJ per pulse was presumed to be very large indeed and thought likely to cause it damage.[145] Hence, no substantial photodissociation energy could be used; and no $NO(^2\Pi_{3/2}, v = 0, J = 1.5)$ could be detected when running the experiment with a reduced laser energy, presumably due to the concomitant decrease in fragment density. It was therefore decided that after all a filter would be used to block scattered light from the photodissociation laser.
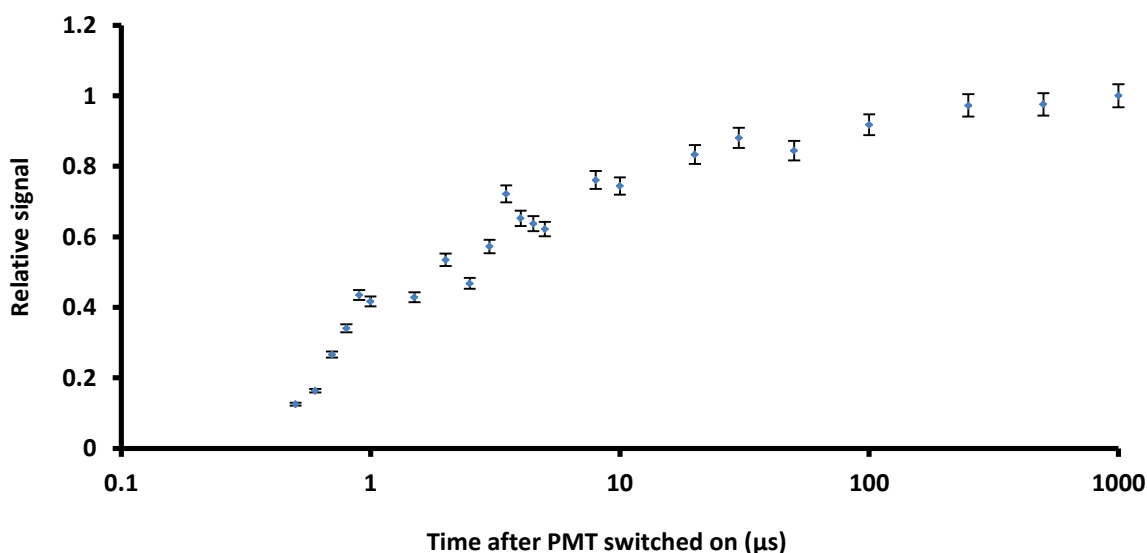
Figure 5.9: the sensitivity of the PMT as a function of the time elapsed after switching on the PMT.

5.3.3 Introduction of a filter for the photodissociation laser

A cavity ring down spectroscopy mirror (henceforth, "CRDS mirror") with a transmittance of approximately 0.02% at 387 nm was introduced to block scattered light from the photodissociation laser. The CRDS mirror was far from being an ideal filter for the experiment, blocking the majority of the fluorescence wavelengths produced by the A $^2\Sigma^+$, v = 0 - X $^2\Pi$ relaxation (causing a factor of 50 signal loss).[140,141] However, as stated above, filters suitable for the exclusion of 387 nm light, but transmissive in the 230-290 nm region, are both hard to source and expensive. Further, even with the use of such an unfavourable filter, it was thought that at least the first few tens of microseconds of the NO($^2\Pi_{3/2}$, v = 0, J = 1.5) decay curve should be visible. It was therefore decided that the CRDS mirror would be used as an interim measure, with the results of the work using it determining future investment in the experiment.

The revised minimum detectable density anticipated is shown in Figure 5.10. It was anticipated that enough signal should be present to collect a population decay curve over two orders of magnitude; and further that, with the scattered light reduced, optimisation should become easier. Further, the CRDS mirror would also act as a second filter for the probe laser beam, allowing the use of higher probe energies.
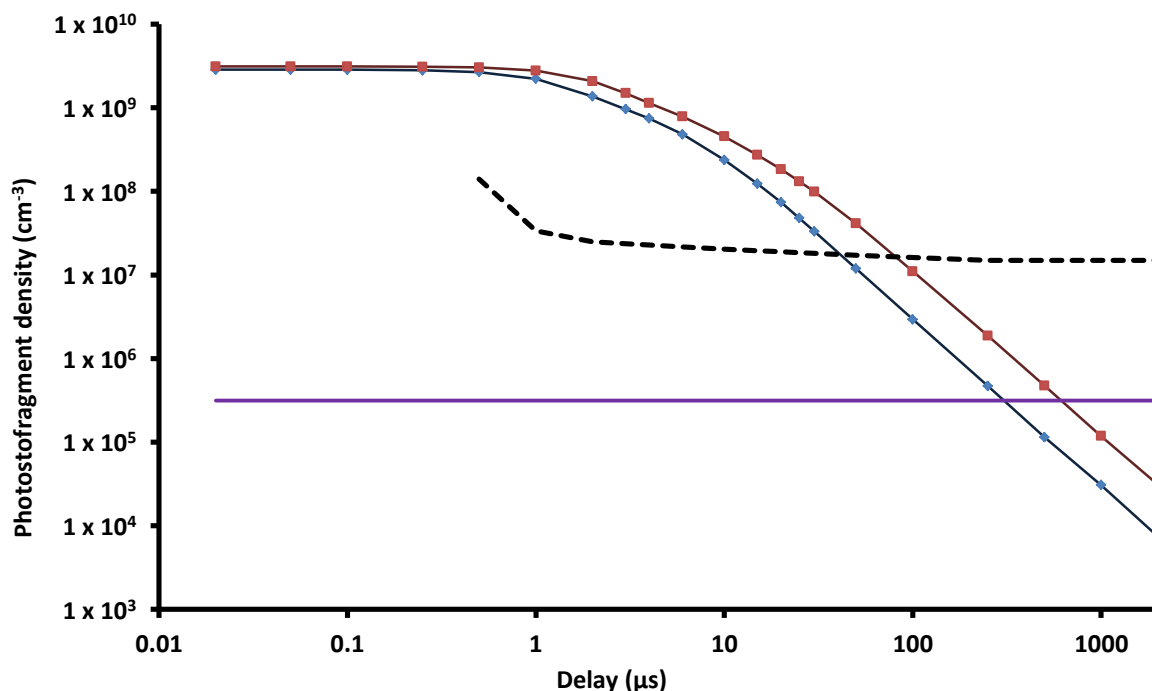
Figure 5.10: simulated NO($^2\Pi_{3/2}$, v = 0, J = 1.5) densities (red and blue; see Figure 5.8), the estimated trappable density (purple), and the revised minimum detectable density (black dotted line). The revised detection limit is calculated from the original detection limit estimate used in Figure 5.8, the factor of 50 signal loss caused by the CRDS mirror, and the PMT sensitivity/time curve.

The combination of the CRDS mirror and the gated PMT did allow the full photodissociation energy to be used (4.2 mJ), and also for the probe laser energy to be increased (to 35-40 µJ), to the extent that $NO(^2\Pi_{3/2}, v = 0, J = 1.5)$ could just about be detected. Figure 5.11 displays the best effort at producing a population decay curve with this experimental set-up. The data points were acquired with 1800 shots per data point, and in a similar fashion to the decay curve in chapter 4. They were adjusted to account for the changing sensitivity of the PMT during its rise period by a factor derived from a logarithmic fit to the relevant section of the PMT sensitivity curve (Figure 5.12).
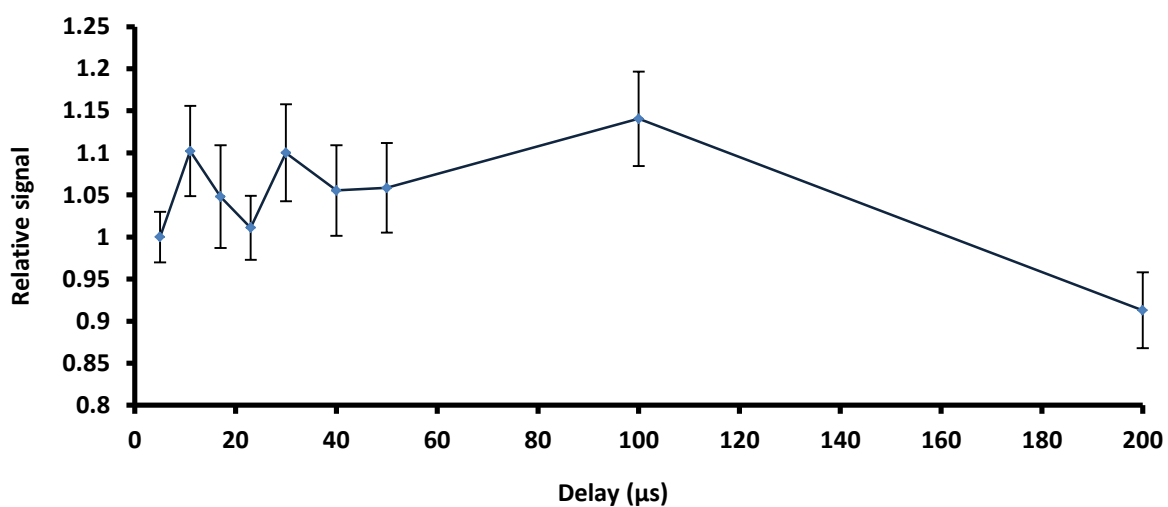
Figure 5.11: NO($^2\Pi_{3/2}$, v = 0, J = 1.5) population decay curve taken with the best signal level achieved. The error bars give the standard error to the 1σ level.
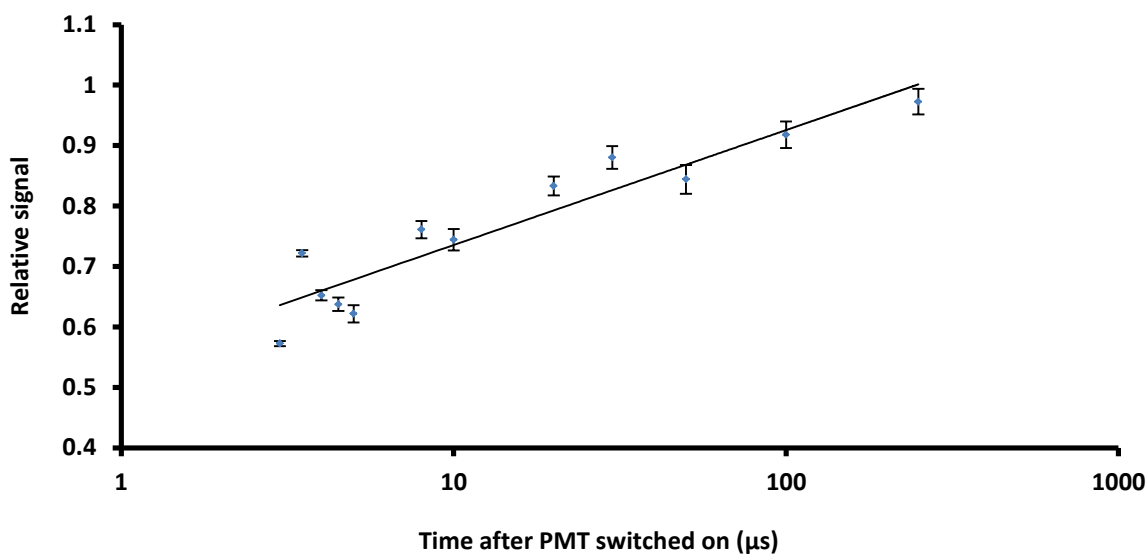
Figure 5.12: a linear fit to the relevant portion of the PMT sensitivity curve yields the relation: signal = 0.0826 ln(time) + 0.5453.

Figure 5.11 demonstrates that photostop signal was still essentially absent. The drop in signal between 1 and 200 μs is just about significant within error at the 1σ level, and probably does represent a drop in signal: but the shape and quality (or lack thereof) of the curve as a whole suggested that the signal level was orders of magnitude lower than expected, and that attempting to detect trapping would be entirely futile.

At this point, there were two obvious causes for the lower than anticipated signal level, the more obvious of which – barring the possibility that the NO_2 supply was inadequate – was experimental malfunction. REMPI/ion imaging had been used earlier in the LIF work to confirm that the experiment was in working order. After confirming that the NO_2 supply was in good order, a switch was therefore made to ion imaging as a detection technique, to confirm that the experiment was running correctly.

5.3.4   Diagnostic ion imaging

Ion images were taken of the photodissociation, and are shown in Figure 5.13. It is obvious that photostop was taking place as anticipated.

87
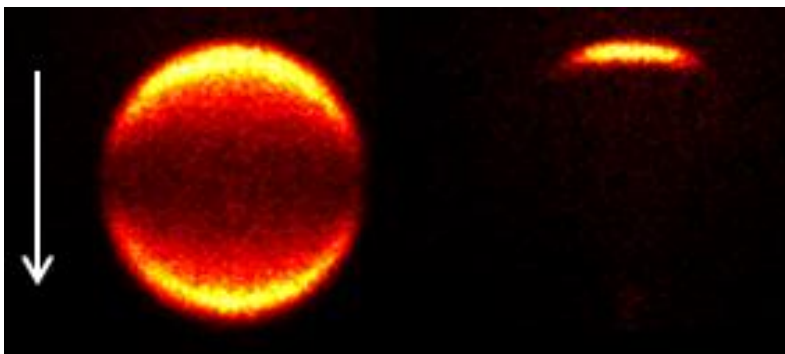
Figure 5.13: ion images of the photodissociation of NO_2 at 387.52 nm, probed on the P12, J = 1.5 line. The image on the left was taken with a photodissociation-probe delay of 10 ns, and was collected over ≈ 7100 laser shots. The image on the right was taken with a photodissociation-probe delay of 10 µs, and was collected over ≈ 3700 laser shots. The white arrow indicates the molecular beam direction. Laser beam diameters were similar to those used in chapter 4.

5.3.5   Estimation of the sensitivity of the LIF apparatus

Having confirmed that the experiment was running properly, the obvious inference to draw was that the sensitivity of the LIF apparatus had been over-estimated. It was decided that the sensitivity of the LIF apparatus (operating at peak efficiency with the CRDS mirror removed) would be determined using a molecular beam containing NO at a known concentration. A commercially supplied mixture of NO (1%) in helium was acquired and successively diluted to 0.0047% of its starting concentration; its LIF signal on the overlapping Q11P21 J = 1.5/2.5/3.5 line was measured for each dilution.

It should be stated at this point that these measurements were approximate in nature and intended only to give a rough idea of the signal level so that a decision could be made about continuing with the experiment; they were not intended or optimised for formal or rigorous analysis.

<u>Estimation of the fraction of the NO population in the probed states</u>

The portion of the NO population actually available to be probed (*i.e.* the population of the NO($^2\Pi_{1/2}$), J = 1.5/2.5/3.5 states as a fraction of the total NO present in the beam) was estimated by analysis of the molecular beam spectrum displayed in Figure 5.14. This spectrum is of NO at a concentration of 0.006 % in He.[††] It was assumed that with

---

[††] To put this concentration in context, it was towards the middle of the range of concentrations measured: it would produce a data point at an "NO density" of about 2.5 x 10^9 cm^{-3} on the graph in Figure 5.15.

NO constituting such a tiny fraction of the molecular beam, the degree of cooling did not vary significantly with changing dilution, and that this spectrum was representative of the whole concentration range studied.
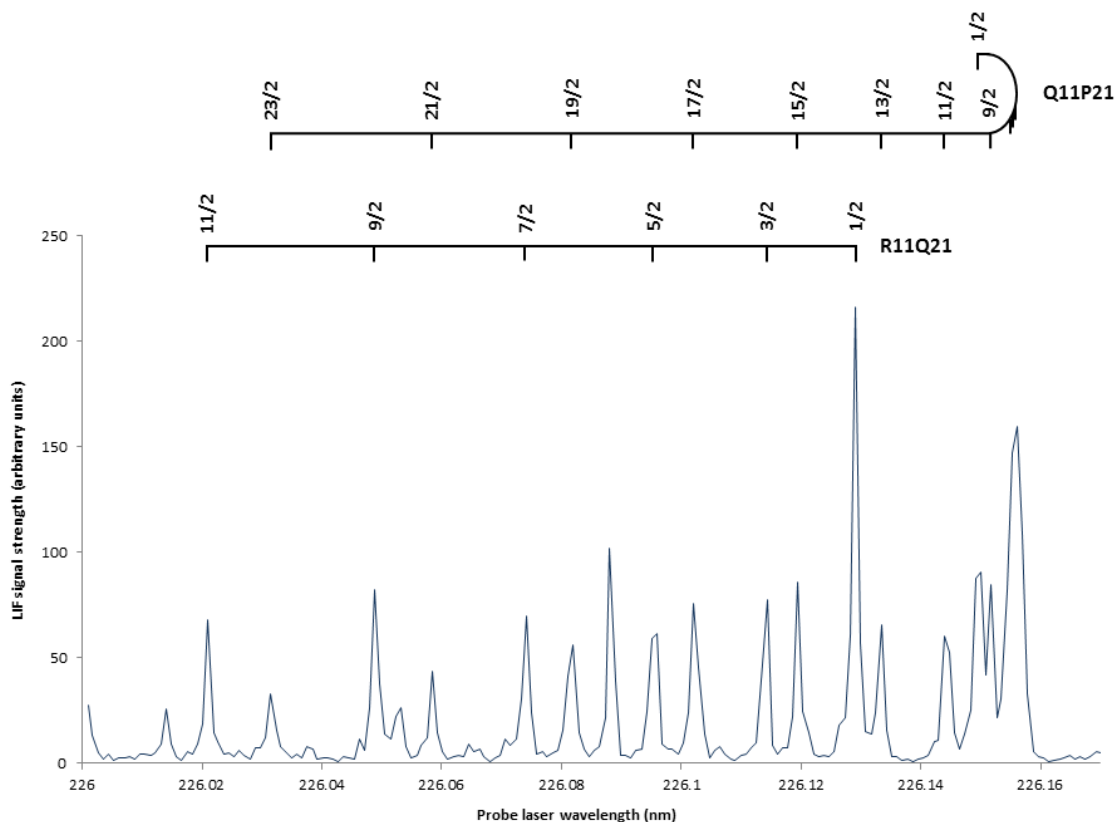
Figure 5.14: LIF spectrum of NO/He molecular beam, with assignments made for the spectral branches used in the analysis below.

The relative populations occupying states with J = 0.5-11.5 were determined by finding the area of each peak (*via* a Gaussian fit) and dividing this value by the absorption coefficient for that peak (in the form of the dimensionless oscillator strength).[110,108,146] The populations of states J = 12.5 upwards were ignored, as were the $^2\Pi_{1/2}$ states, which were expected to be largely unpopulated. It is worth noting that if these levels had been significantly populated, ignoring them would cause an over-estimation of the proportion of the molecular beam that was probed, and hence an under-estimation of the sensitivity.

The rotational state populations thus estimated are given in Table 5.1. It is doubtful that they are very accurate: the spectrum was collected with the probe laser

wavelength changing in 0.00087 nm increments, with 10 laser shots being averaged to acquire each point – a level of averaging that does not completely remove the effects of shot-to-shot fluctuation in the laser power. However, these populations are a useful starting point, and an upper bound on the detection limit is discussed below. From Table 5.1, it is estimated that about 19% of NO in the molecular beam was accessible *via* the probed Q11P21 *J* = 1.5/2.5/3.5 line.

The band width of the laser (1 pm) was compared with the widths of the Q11P21 *J* = 1.5/2.5/3.5 peaks by convolving Gaussian approximations of the laser width and each line width to yield a relative (probe and *J* = 1.5 state):(probe and *J* = 2.5 state):(probe and *J* = 3.5 state) overlap of 0.43:1:0.43. Weighting the contributions of each of the *J* = 1.5/2.5/3.5 states accordingly, it was estimated that approximately 16% of NO in the molecular beam was available to be probed.

Table 5.1: fractional populations of each *J* state for NO($^2\Pi_{1/2}$) in the molecular beam.

Branch	J	Area	Oscillator strength (x 10^4)	Fraction of population
R11Q21	0.5	562.7	4.38	0.13
	1.5	222.8	2.92	0.080
	2.5	262.5	2.79	0.098
	3.5	221.4	2.72	0.085
	4.5	259.3	2.66	0.10
	5.5	182.7	2.62	0.073
Q11P21	6.5	188.1	2.79	0.070
	7.5	239.3	2.82	0.088
	8.5	271.9	2.85	0.099
	9.5	235.4	2.88	0.085
	10.5	128.5	2.91	0.046
	11.5	112.9	2.93	0.040

<u>Estimation of the density of NO probed</u>

The total density of NO($^2\Pi_{1/2}$) in the probe region was estimated using the phstop program, which among its functions can provide an estimate of molecular beam density. These total densities were then modified according to the 16% estimate of the probed fraction derived above. The resulting "probed densities" are presented in Table 5.2.

Table 5.2: total NO densities (simulated) and probed NO densities (calculated from spectrum and simulation) for the known concentrations of NO used in these sensitivity measurements.

NO concentration in backing mixture (%)	Simulated total NO density at laser (x 10^{10} cm^{-3})	Density of NO probed on ($^2\Pi_{3/2}$, v = 0, J = 1.5/2.5/3.5) line (x 10^{10} cm^{-3})
0.078	18.8	3.16
0.012	2.94	0.494
0.0019	0.460	0.0772
0.00030	0.0718	0.0121
0.000047	0.0112	0.00189

For each concentration, data was accumulated with both the molecular beam and the probe laser running ("the signal") and with only the probe laser running ("the background"). The ratio of signal to background was then calculated for each concentration, with a signal/background ratio of 1 being taken as a good approximate indication of the point at which the limit of the experimental sensitivity was being reached. The probed NO densities are plotted against their respective signal/background ratios in Figure 5.15. A linear fit to Figure 5.15 suggests that the signal/background ratio should reach 1 at about 5.5 x 10^7 cm^{-3} for the states probed.
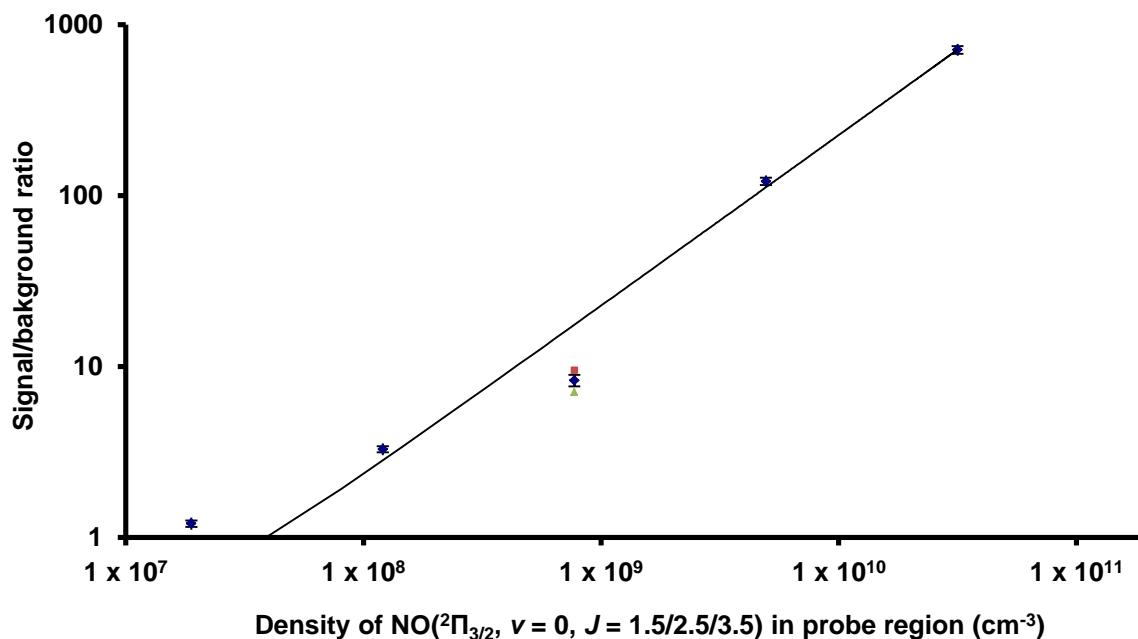
Figure 5.15: signal/background ratio for the NO concentrations/densities in Table 5.2 (blue). The two data points at highest density were acquired by integration of signal area using 1 MΩ coupling between the PMT and the oscilloscope (see section 5.3), and the two data points at lowest density were acquired using 50 Ω coupling between the PMT and the oscilloscope, and a pseudo photon-counting technique. The central point was collected twice, once with each method of measurement, and the mean value plotted. The data points generated by area integration (green) and pseudo photon-counting (red) are also shown. The mean and individual data points are identical within error (although error bars are not shown for the individual points because their overlap becomes confusing).

<u>Implication of this signal level for the viability of the experiment</u>

The strongest transition available for the interrogation of NO($^2\Pi_{3/2}$, $v = 0$, $J = 1.5$) is the P12, $J = 1.5$ peak, with an oscillator strength of 1.738×10^{-4}, which value is about 0.34 of the weighted sum of the Q11P21 $J = 1.5/2.5/3.5$ oscillator strengths. The limit at which the ratio of signal to background reaches 1 for NO($^2\Pi_{3/2}$, $v = 0$, $J = 1.5$) detected *via* the P12 band with our apparatus should therefore be, very approximately, 1×10^8 cm^{-3}.

The simulated decay curve from Figure 5.8 is again reproduced in Figure 5.16 below. The determined detection limit is shown (red dashed line), as is the expected signal level visible with the CRDS mirror *in situ* (black dashed line). It was apparent that a marginal signal level was the best that could be expected, and that detecting a trapped population would be impossible.
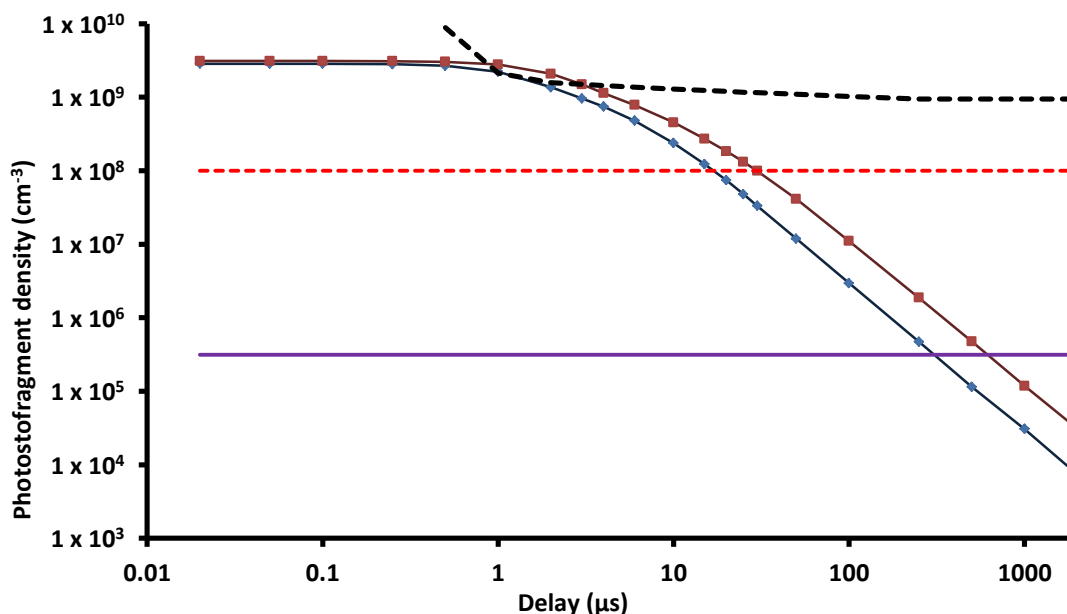
Figure 5.16: simulated NO($^2\Pi_{3/2}$, $v = 0$, $J = 1.5$) densities (red and blue; see Figure 5.8); the estimated trappable density (purple); the empirically estimated density at which the signal/noise ratio reaches 1:1 for the detection of NO($^2\Pi_{3/2}$, $v = 0$, $J = 1.5$) as described in the text above (red dashed line); and the density of NO($^2\Pi_{3/2}$, $v = 0$, $J = 1.5$) expected to be detectable with the countermeasures against scattered light in effect, calculated by modifying the red dashed line to reflect the signal losses due to the CRDS mirror and the PMT sensitivity/time curve to the red dashed line, and also the higher probe laser energy that could be used with the CRDS mirror in place (black dashed line).

Quality of the sensitivity estimate

Obviously the estimate derived relies on a number of assumptions and approximations, the worst of which is probably the estimation of the population of rotational states from the spectrum in Figure 5.14. However, its predictions are accurate insofar as they can be tested: it predicts a marginal signal level a few microseconds after photodissociation, which appears to be correct given both the decay curve shown in Figure 5.11, and the spectrum displayed later in Figure 5.17. Thus, the detection limit for NO($^2\Pi_{3/2}$, $v = 0$, $J = 1.5$) in the region of 1 x 10^8 cm^{-3} is asserted with moderate confidence.

The only significant doubt is raised by the consideration that the estimate of the detection limit relies on the initial density values provided by the phstop program, and is being compared to a simulated NO density also provided by the phstop program. It is therefore conceivable that an error arising from a systematic mis-calculation of precursor density in the molecular beam might render the detection limits and predicted photostop densities objectively wrong whilst appearing to be consistent –

but this is largely unimportant, because so long as they *are* consistent, the prediction of the timescale over which the decay should be detectable should still be valid.

Relation of sensitivity to original estimate of the minimum detectable density

The above derived limit was sufficient to inform a decision on the viability of the NO trapping experiment in this form, but it leaves open the question of why precisely the 1:1 signal/background limit was reached at this concentration: too much background, or not enough signal?

To allow this question to be addressed at least qualitatively, the lowest density data points in Figure 5.14 were recorded using what might be termed a pseudo photon counting technique (as specified in its accompanying caption). A single photon impact appeared on the oscilloscope trace as a peak composed of a number of points; the pseudo photon counting routine simply counted every point above a pre-set value. This would not be suitable as a photon counting technique had the experiment been successful, but was trivial to implement to allow a rough estimate of the single photon regime to be made *via* this measurement.

Analysis of oscilloscope traces suggested that the average single photon peak produces 3.8 ± 0.3 points. The background level on the three lowest concentrations is 2.8 ± 0.1 points – *i.e.* below the one photon per laser shot level. Hence, that the 1:1 signal/background ratio was reached implies that the one photon detected per laser shot signal regime had also been reached.

Implications for NO trapping experiment

Scattered light was creating severe problems. The worst stemmed from the scattered light generated by the photodissociation laser, which required countermeasures resulting in a factor of 50 signal loss, and probably still generated some noise with these in place. The noise level from the probe laser, whilst much smaller, was not acceptable either; when the CRDS mirror was not in place, significant scattered light reached the PMT in the first 100-200 ns after the probe laser beam passed through the chamber and meant that no measurement could be recorded during this time (causing the loss of around 60% of LIF signal), even with the probe energy limited to 10-15 µJ.

Even if the problems caused by scattered light were overcome, the LIF collection efficiency was not nearly good enough for the detection of magnetically trapped NO to be a realistic goal. The original estimate of LIF sensitivity (section 5.2.5) suggested an $NO(^2\Pi_{3/2}, v = 0, J = 1.5)$ density of somewhere near 3×10^5 cm^{-3} should be necessary to collect one photon per laser shot: but from the current section, it is seen that this one photon detected per laser shot limit was reached in the region of 10^8 cm^{-3}. Even allowing for the loss of 62% of LIF signal stated above (measured detection limit becomes 4×10^7 cm^{-3}), and recalculating the original estimate to account for the probe power used (predicted minimum detectable density becomes about 6×10^5 cm^{-3}), it appears that the efficiency of the LIF collection optics were overestimated by somewhere around two orders of magnitude.

5.3.6   Change of precursor molecule to H_2S

Overcoming the problems described above was possible. However, by this stage in the work the MMQA project mentioned in section 5.1 was underway, which provided a specific target for the number of trapped cold molecules: 10^7. As described in section 5.2.3, the photostop of NO was expected to produce only around 4×10^3 trapped NO molecules, making the target unattainable even with the prospect of repeated loading of the magnetic trap. Further, the quantum simulator that is the purpose of the MMQA project will function through the dipole-dipole interactions of its component molecules. NO has a dipole moment of only 0.15 D, whilst most of the preferred choices have a dipole moment in excess of 1 D.

By this time a review of alternative candidate molecules for the photostop experiment had been completed and a more promising precursor – in terms of both the likely density of photostopped fragments and its suitability for the quantum simulator – identified, in the form of H_2S. Accordingly, the decision was made to switch the experimental effort to the photostop of SH from H_2S. The review of alternative candidates is presented in chapter 7.

5.3.7   Post script: product state distribution

A photodissociation product spectrum is shown in Figure 5.17; a comparison with the spectrum of trace NO in the molecular beam is made in Figure 5.18, to demonstrate that the majority of NO observed in Figure 5.17 is due to photodissociation.

It should be stressed that this measurement was taken as an act of curiosity just before the experiment was ended – it was not optimised for rigorous analysis. However, there are still two points to be drawn from it. Firstly, the prior distribution (shown in Figure 5.19) used by the phstop program to estimate product density was incorrect in its prediction of the spin-orbit ratio of the photoproducts, a fact unsurprising in hindsight: Hunter *et al.*, in a study encompassing a number of points within the 358-400 nm photodissociation wavelength range, observed that the spin-orbit distribution is significantly colder than would be predicted statistically.[147]

The second point to draw is that, in spite of this error, the population estimate of 0.7% for the $NO(^2\Pi_{3/2}, v = 0, J = 1.5)$ state might still have been fairly reasonable. This (potential) serendipity arises because (as also described by Hunter) the prior distribution tends to underestimate the population of low J states. A rigorous quantitative analysis of the spectrum would be futile given that the peaks of the $NO(^2\Pi_{3/2})$ band are barely out of the noise, but by comparison of peak heights it appears that the spin-orbit distribution is very roughly 9:1 $NO(^2\Pi_{1/2}):NO(^2\Pi_{3/2})$.

Drawing on another observation in Hunter's study that the rotational distributions of the two spin-orbit components tend to be very similar, it might be possible to estimate the population of the $NO(^2\Pi_{3/2}, v = 0, J = 1.5)$ state by analysis of the $NO(^2\Pi_{1/2})$ spectrum. The (approximate) populations of the $NO(^2\Pi_{1/2})$ states are given in Table 5.3. The population of the $NO(^2\Pi_{1/2}, v = 0, J = 1.5)$ state is 10%, suggesting (by consideration of the spin-orbit splitting ratio given above) that the population of the $NO(^2\Pi_{3/2}, v = 0, J = 1.5)$ state is around 1%. Of course, this is a very rough estimate, given the significant error present in even the $NO(^2\Pi_{1/2})$ spectrum, and a way would need to be found to repeat the measurement with a better signal level if the NO study were to be pursued further. However, it does at least suggest that the assumed $NO(^2\Pi_{3/2}, v = 0, J = 1.5)$ density was probably valid to an order of magnitude. Likewise, a fit to the $NO(^2\Pi_{3/2}, v = 0, J = 1.5)$ peak produces an area of about the correct magnitude compared to the $NO(^2\Pi_{1/2}, v = 0, J = 1.5)$ peak; more than this cannot be said given the error in the $NO(^2\Pi_{3/2})$ spectrum.
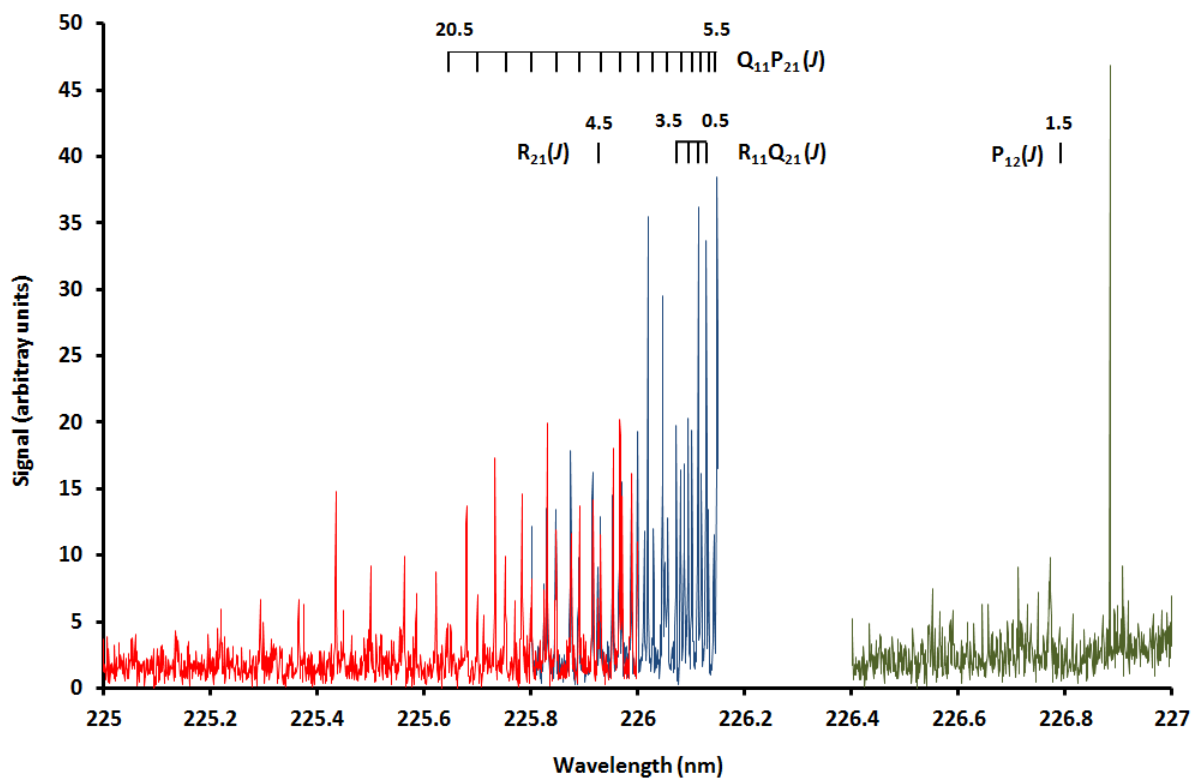
Figure 5.17: the NO($^2\Pi_{1/2}$) and NO($^2\Pi_{3/2}$) LIF spectra, with assignments for the peaks analysed in Table 5.3.
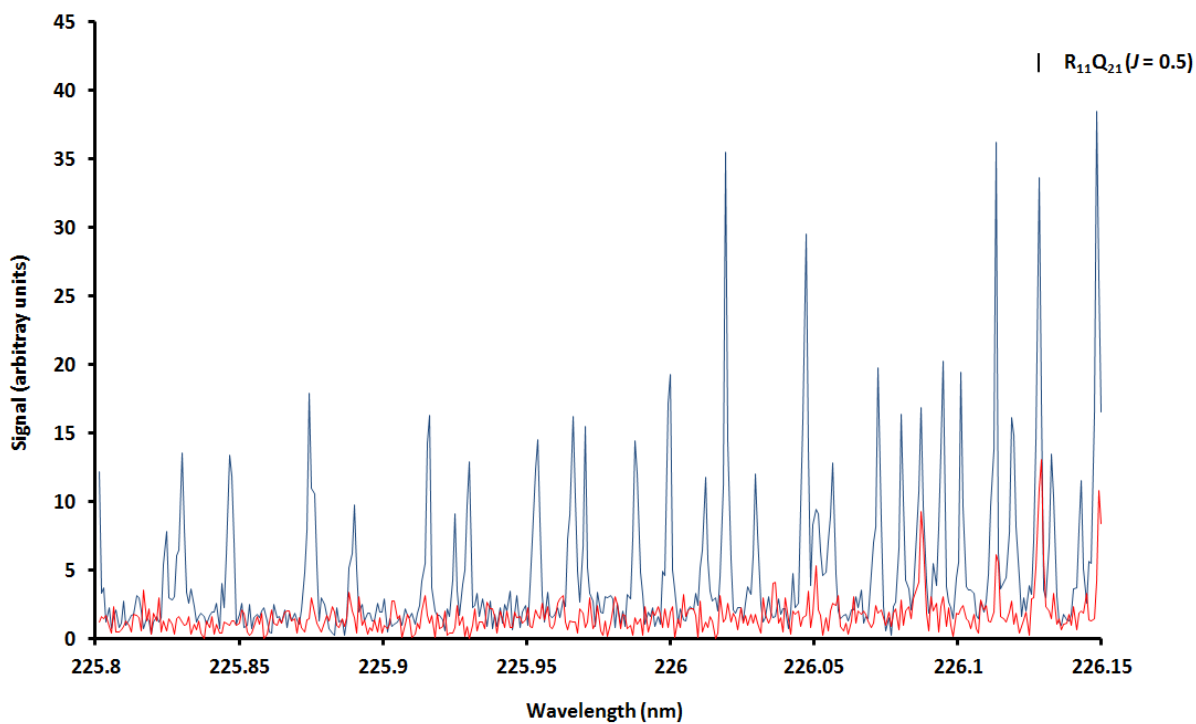
Figure 5.18: the NO($^2\Pi_{1/2}$) spectrum, from photodissociation (blue) and from native NO in the molecular beam (red), with the position of the R11Q21, J = 0.5 peak indicated.
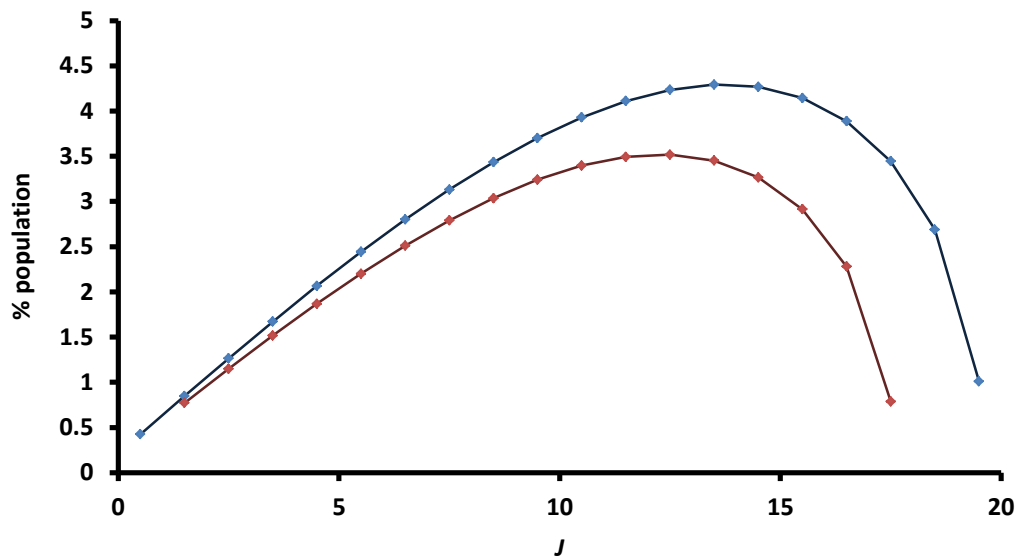
Figure 5.19: the prior distributions used by the phstop program to predict NO rotational state densities (NO($^2\Pi_{1/2}$) in blue, and NO($^2\Pi_{3/2}$) in red).

Table 5.3: fractional populations of each *J* state for NO($^2\Pi_{1/2}$) produced by photodissociation. The decay parameter accounts for the predicted loss in density for each state over the 3 µs delay between photodissociation and detection.

Branch	*J*	Area	Oscillator strength (x 10^4)	Decay parameter	% population
R11Q21	0.5	144	4.38	9.564	4.2
	1.5	227	2.92	9.568	9.8
	2.5	124	2.79	9.575	5.6
	3.5	141	2.72	9.584	6.5
R21	4.5	46.6	1.52	9.593	3.9
Q11P21	5.5	85.9	2.76	9.6	3.9
	6.5	113	2.79	9.604	5.1
	7.5	176	2.82	9.601	7.8
	8.5	123	2.85	9.588	5.4
	9.5	122	2.88	9.561	5.3
	10.5	92.3	2.91	9.514	4.0
	11.5	92.5	2.93	9.441	4.0
	12.5	169	2.95	9.333	7.4
	13.5	192	2.98	9.182	8.5
	14.5	97.4	3.00	8.975	4.4
	15.5	92.1	3.02	8.698	4.2
	16.5	124	3.04	8.334	5.9
	17.5	80.1	3.06	7.861	4.0
	18.5	76.5	3.07	7.258	4.1
	19.5	54.0	3.09	6.492	3.3
	20.5	40.6	3.10	6.329	2.5

6   Photostop of SH(X $^2\Pi$)

6.1   Introduction

This chapter describes the work leading to the first successful photostopping of SH(X $^2\Pi$) by the photodissociation of H_2S. The H_2S/SH pair was selected as a candidate for the photostop experiment following the literature review detailed in chapter 7. It is a significant improvement on NO_2/NO pair in terms of its suitability for use in the MMQA collaboration's quantum simulator: in contrast to NO's very small 0.15 D dipole moment, SH has a dipole moment of 0.76 D; and due to its larger rotational constant, SH is likely to be trapped in a purer rotational population than NO leading to a lower rate of trap loss through inelastic collisions (*i.e* the separation of the rotational states of NO is comparatively small – therefore, after the velocity spread of the molecular beam is taken into account, NO will be photostopped and trapped in a number of rotational states; the rotational levels of SH are more widely spaced, so fewer rotational states of SH will be photostopped and trapped). Perhaps more importantly, the likely density of photostopped molecules is higher, as described below.

The same general methodology, techniques *etc*. were used for the work in this chapter as for that in chapter 4. Likewise, largely the same experimental apparatus was used, except that the lasers used differed as follows.

The dissociation laser was a GAM excimer laser (EX5), running on ArF premix gas. The probe (REMPI) laser for detection of HS was a Lambda-Physik FL2002 dye laser (Coumarin 503, 0.4 g/L in methanol), fitted with a BBO doubling crystal and Pellin-Broca wavelength separator, and pumped by the third harmonic output of a Continuum Powerlite Nd:YAG laser (typical Powerlite output: 94-104 mJ pulse^{-1}). The probe (REMPI) laser for detection of H_2S was a Sirah Cobra dye laser (DCM, 0.3 g/L in methanol) fitted with a KDP doubling crystal] and Pellin-Broca wavelength separator, and pumped by the second harmonic output of a Continuum Surelite Nd:YAG laser (typical Surelite output: 90-100 mJ pulse^{-1}). The laser arrangement is shown schematically in Figure 6.1. All lasers ran at a frequency of 10 Hz.
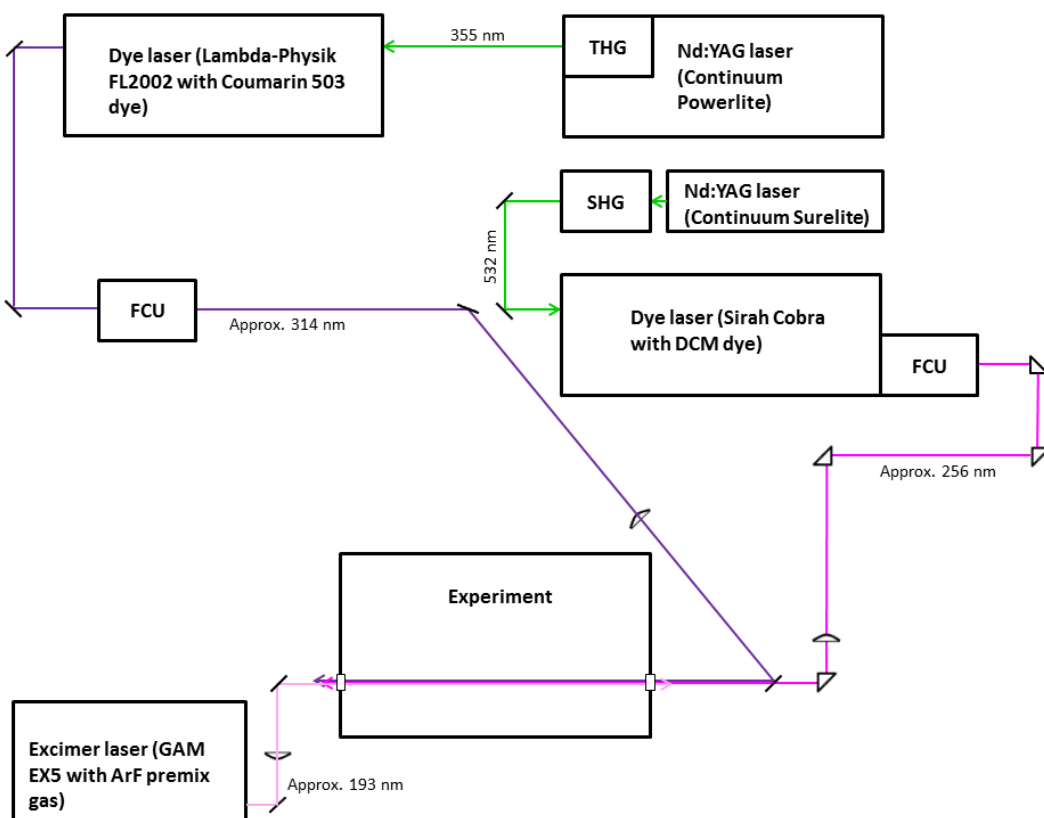
Figure 6.1: schematic diagram of the laser systems used for the work described in this chapter.

6.2   H$_2$S as a photostop precursor

H$_2$S first drew attention as a possible photostop precursor due to the very cold rovibrational distribution of SH(X $^2\Pi$) produced by photodissociation in its first electronic absorption band. The dissociation process is illustrated in Figure 6.2. It is thought to be a result of excitation to the $^1B_1$ excited state and subsequent predissociation *via* a repulsive $^1A_2$ state accessed by vibronic mixing: if either S-H bond elongates, the symmetry of the molecule is reduced from C$_{2V}$ to C$_S$, the two singlet states both acquire $^1A''$ symmetry, and the excited molecule can access the dissociative state. This process is extremely fast.[148,149,150]

As for the work with NO$_2$/NO, the target state for photostop with H$_2$S/SH would be the $^2\Pi_{3/2}$ state, again because it can be magnetically trapped. For SH(X $^2\Pi$), the spin-orbit splitting is inverted, with the $^2\Pi_{3/2}$ state lowered in energy by 376.835 cm^{-1} relative to the $^2\Pi_{1/2}$ state.[151]
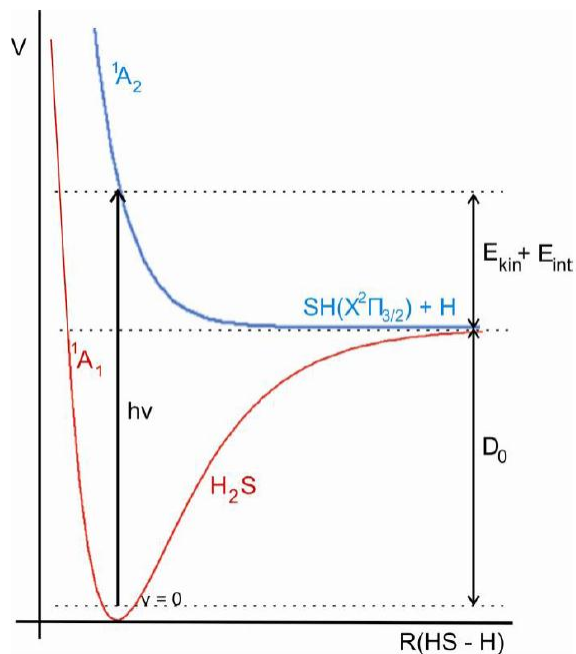
Figure 6.2: schematic diagram of the potential energy surfaces of H₂S involved in the photodissociation process following excitation in the first absorption band.

6.2.1 Choice of photodissociation wavelength

The first electronic absorption band of H_2S is shown in Figure 6.3. Two lasers were available for use at such wavelengths: a frequency doubled Sirah Cobra dye laser, capable of achieving wavelengths as low as ∼ 210 nm, or a GAM EX5 excimer laser with argon fluoride premix, producing radiation in the region of 193.3 nm. The excimer laser was chosen as the photodissociation laser because of the higher energy available thereby, and the much greater absorption cross section of H_2S at that wavelength.
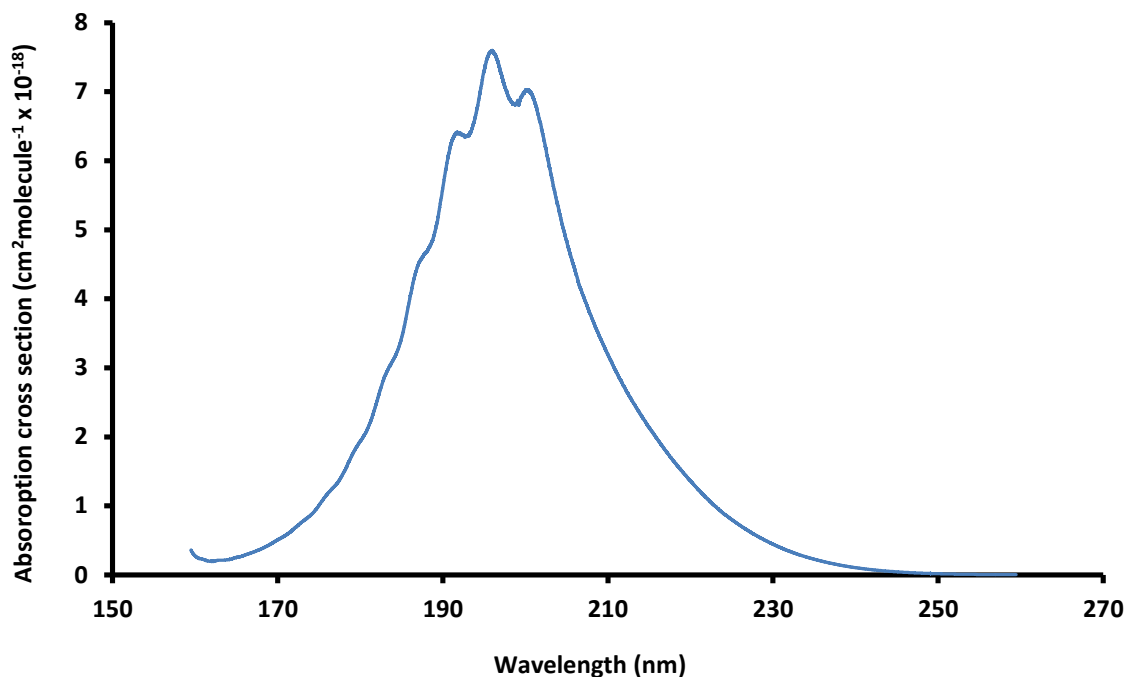
Figure 6.3: the first absorption band of H₂S. Data from Wu and Chen.[152]

6.2.2   Photostop of SH(X $^2\Pi_{3/2}$) by photodissociation of H₂S at 193 nm - a comparison to the photostop of NO

A number of studies have been made of the photodissociation of H₂S at 193 nm. The dynamics are very favourable for the photostop experiment: SH(X $^2\Pi$) is formed exclusively, and almost all the excess energy from the photodissociation is partitioned into translation, resulting in internally cold products. Approximately 63% of SH is formed in $v = 0$.[149] Within the $v = 0$ population, the majority of SH is in the 3/2 spin orbit state (3/2:1/2 = 1.57), and the rotational distribution strongly favours low quantum numbers, with the distribution peaking in the rotational ground state (approximately 23% population of $J = 1.5$).[148] Taken together, these figures suggest that approximately 9% of SH is formed in its absolute ground state, compared to the estimated <1% of NO formed similarly, as discussed in the last chapter: an order of magnitude gain (and it might also be said to be an advantage that the product yield can be anticipated more confidently).

H₂S has two further advantages over NO₂ as a photostop precursor. Firstly, the absorption cross section of H₂S at 193 nm is about an order of magnitude large than that of NO₂ at 387 nm. Secondly and crucially, H₂S is a gas at room temperature, which means a much richer molecular beam can be made – and not only made, but

successfully used, because H_2S does not necessarily need to be efficiently cooled in the molecular beam expansion. The absorption cross-section of H_2S is largely independent of temperature,[152] and the photofragment internal energy distribution is not much affected either.[148] This means that there is no need to use H_2S in a dilute molecular beam unless speed requirements demand it. It is this that potentially gives H_2S its greatest advantage over NO_2 as a photostop precursor, (although of course using a richer molecular beam does result in a certain deleterious effect from increased beam temperature).

The above notwithstanding, H_2S has two obvious disadvantages. One is that absorption at 193 nm provides energy far in excess of the dissociation threshold. Taking into account the relevant equations from chapter 3 and a dissociation threshold of 31440 cm^{-1},[150] a molecular beam speed in the region of 660 m s^{-1} is desirable for the photostop of $SH(^2\Pi_{3/2}, v = 0, J = 1.5)$ by the photodissociation of H_2S at 193 nm.[‡‡] By comparison with the sphere of recoiling NO produced by 387 nm photodissociation, the surface area of the sphere of recoiling SH is about 2.5 times larger, with a concomitant reduction in density at zero velocity.

The other disadvantage is that the dissociation anisotropy of H_2S at 193 nm (β = -1) in conjunction with an unpolarised photodissociation laser is much less favourable than that for NO_2 at 387 nm (β = 1.5)[13] with a horizontally polarised photodissociation laser, providing a factor of 2.6 reduction in photostopped density. Nonetheless, these disadvantages are outweighed by the effects of the very favourable product distribution, large absorption cross section, and the possibility of using a molecular beam rich in the precursor.

6.2.3   Density of H_2S in a molecular beam

Assuming substantial cooling in the expansion, molecular beam speeds for pure gases can be calculated by the relation[153]

$$V = \sqrt{\frac{2R}{W}\left(\frac{\gamma}{\gamma-1}\right)T_0} \qquad \text{(Eq. 6.1)}$$

where V is the molecular beam terminal velocity, R is the gas constant, W is the molecular weight, and γ is a thermodynamic quantity described in appendix G.

[‡‡] To avoid confusion, let it be explicitly stated that the threshold quoted here is for the production of the lowest energy state of the $SH(X\ ^2\Pi_{3/2})$ fragment.

Equation 6.1 produces a speed of 785 ms^{-1} for H$_2$S at a nozzle temperature of 40°C (a value almost identical to the H$_2$S beam speed measured in section 6.3 below, which not only demonstrates the reliability of this equation, but also suggests that the nozzle temperature presumed in the simulation appendices is a good estimate).

From equation 6.1, for a molecular beam of pure H$_2$S to have a speed of 660 ms^{-1}, the source must be cooled to 221 K. The nozzle can easily be cooled to this temperature, but H$_2$S has a vapour pressure in the region of only 1.5 bars at this temperature (Figure 6.4). On this basis it was thought likely that a diluted H$_2$S beam generated from an uncooled nozzle – which could (speed considerations aside) contain H$_2$S at a partial pressure of several bars – might produce better results. Speeds of mixed gas beams are harder to calculate, so were determined by measurement, as described in the next section.
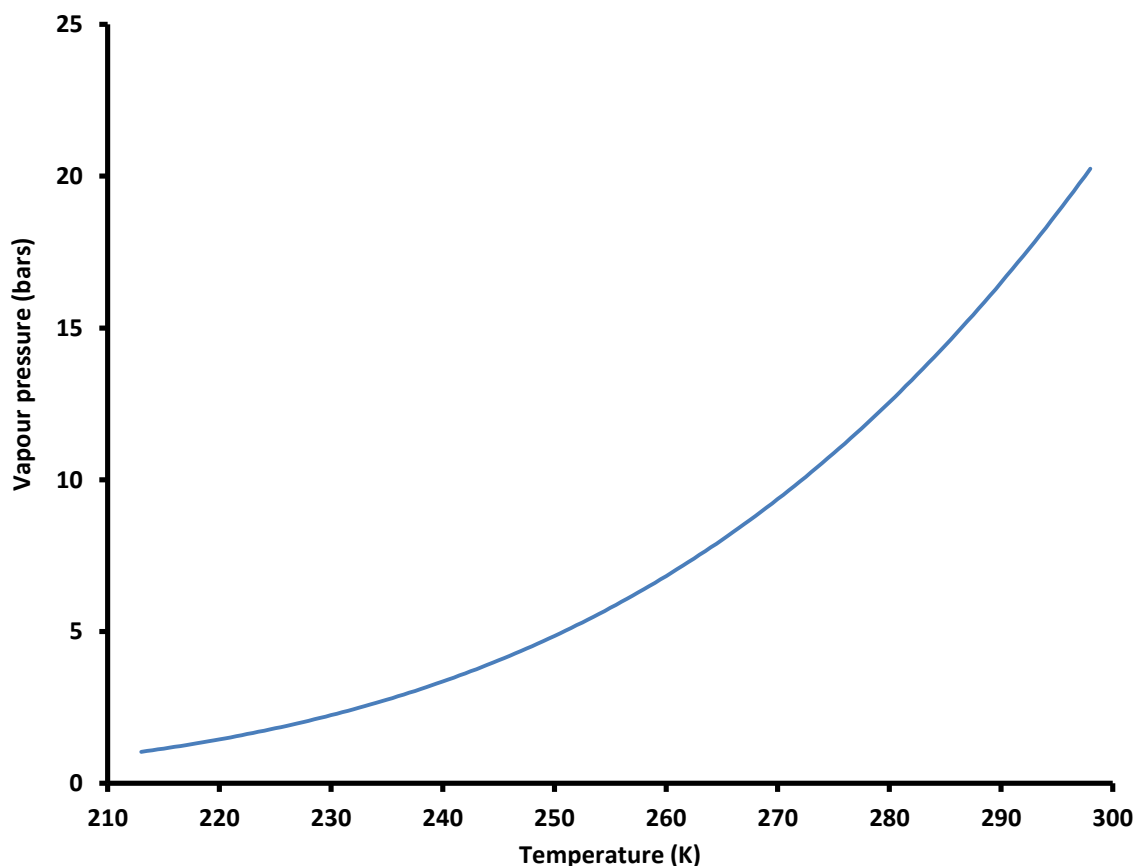
Figure 6.4: vapour pressure of H$_2$S as a function of temperature, calculated using the Antoine equation, with A = 4.52887, B = 958.587, and C = -0.539.[154]

6.3   Preliminary investigation I: producing a 660 ms^{-1} molecular beam of H$_2$S

H$_2$S was diluted with argon, with krypton, and with xenon, in each case to a total pressure of 5 bars. For each carrier gas, molecular beam speeds were measured across a range of dilutions, with H$_2$S being detected with 2+1 REMPI in the region of 314 nm according to the work of Steadman *et al.*[155] Mixtures in argon were examined first: it was found that the data scatter was small, so fewer points were used in the (more expensive) krypton and xenon studies. The effect of concentration on speed for each carrier gas is shown in Figure 6.5. It can be seen that the molecular beams produced by these mixtures are broad, and each carrier gas produces beams with a significant density at 660 ms^{-1} across a wide range of dilutions.   Favourable mixtures for photostop – *i.e.* those producing the molecular beam peak at 660 ms^{-1} – were found to be 25% H$_2$S in argon, 67% H$_2$S in krypton, and 84% H$_2$S in xenon.
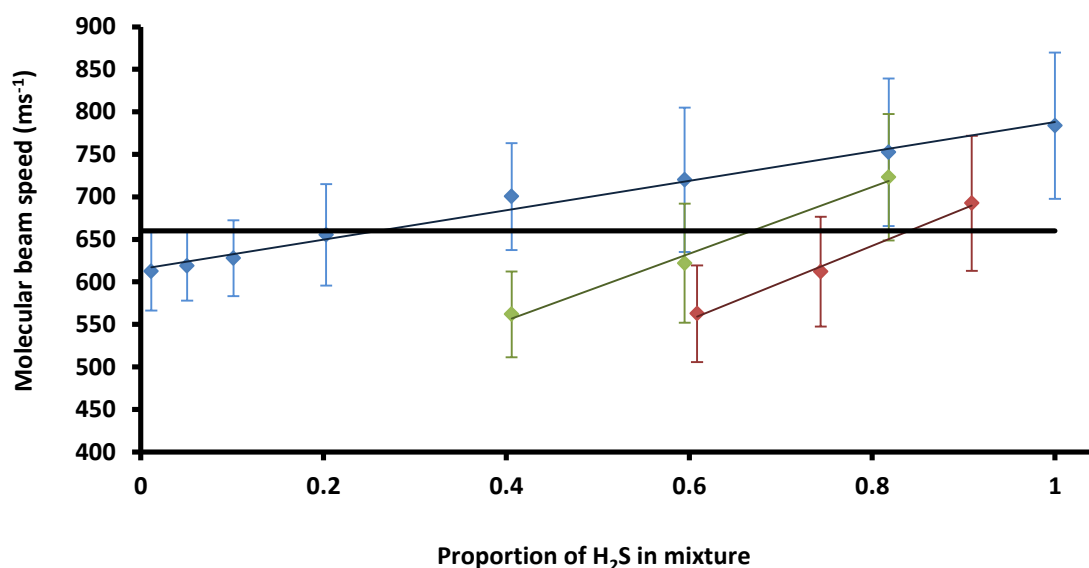
Figure 6.5: graphs showing molecular beam speed against H$_2$S concentration for mixtures of H$_2$S with argon (blue), krypton (green), and xenon (red). The error bars display the full width half maximum of the molecular beam velocity spread. The black line shows the target beam speed of 660 ms^{-1}.

6.4 Preliminary investigation II: the photodissociation of H_2S

6.4.1 Detection of SH

REMPI and velocity mapped ion imaging were used to detect SH. As stated previously, ion imaging is an excellent detection technique for photostop, being extremely sensitive, allowing direct and simple measurement of the recoil velocity and the velocity spread of photostopped molecules, and allowing the evaporation of hotter molecules from the photostop volume to be displayed over time as images, which provides a convincing demonstration of the photostop technique. Just as importantly, a detection technique that provides an image of the dissociation event is extremely useful when trouble shooting.

SH was detected with 2 + 1 REMPI *via* the $[a\ ^1\Delta]3d\pi\ ^2\Phi$ state, requiring absorption in the region of 256 nm.[151] Many branches of this REMPI spectrum are overlapped; the uncluttered S_1 branch was chosen for detection of SH ($^2\Pi_{3/2}$) in this work. This portion of the REMPI spectrum is displayed in Figure 6.6.
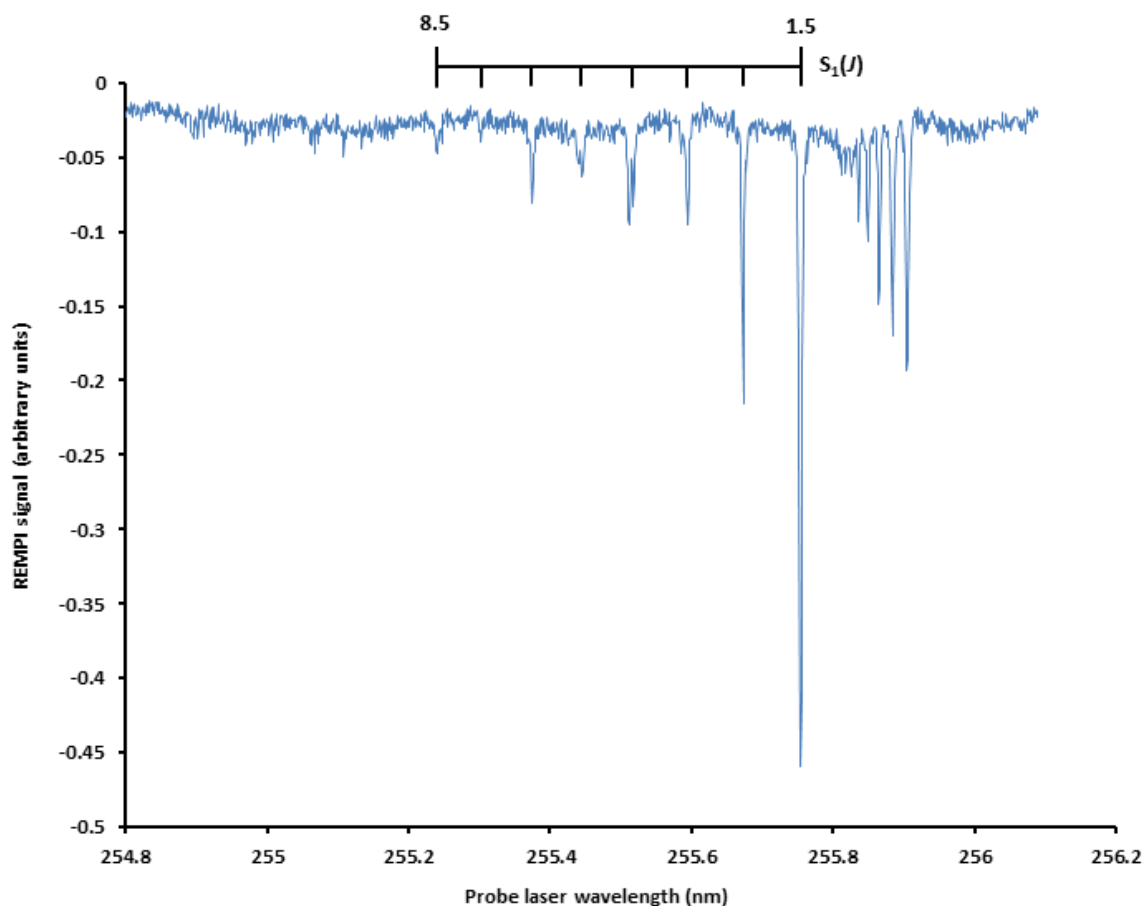
Figure 6.6: 2 + 1 REMPI spectrum of SH ($^2\Pi_{3/2}$). Assignments are made as per Milan *et al*.[151] The unassigned peaks to the right of the S_1 band belong to the R_1 band.

6.4.2 Detected products of photodissociation

Preliminary photodissociation studies were undertaken to optimise the experiment for photostop. The photodissociation of a molecular beam of pure H_2S with a backing pressure of 4 bars was examined. Both laser beams were focused inside the molecular beam. The excimer laser energy was ≈ 3.3 mJ per pulse. A high probe laser energy (≈ 1.6 mJ per pulse) was used to compensate for the need for two-photon absorption in the detection scheme.

Time of flight (TOF) spectra of the photodissociation products were recorded towards the leading edge of the molecular beam. Figure 6.7 shows the TOF spectrum produced by interrogation of the molecular beam with both the photodissociation and probe lasers; Figure 6.8, the TOF spectrum produced by the action of the probe laser alone. Mass/charge peaks corresponding to S^+, H_2S^+, and S_2^+ were seen in addition to the expected SH^+ peak. The additional peaks were probably seen due to the high laser intensities used. Peak assignments are given in

108

Table 6.1. Figure 6.9 displays an ion image that accompanies Figure 6.7. All of the mass peaks could be ascribed with confidence to features in the image, as described in the figure caption.

There are a number of points to be drawn from the TOF spectra and ion images, which for clarity are collected by ion rather than discussed on a figure-by-figure basis.

H_2S^+:

- H_2S was *ionised* largely by the photodissociation laser, as demonstrated by the comparative intensities of the two m/z = 34 peaks in Figure 6.7. (The ionisation energy of H_2S is 84331 cm^{-1}.[156] Hence, ionisation at 193.3 nm (photodissociation laser) is a two-photon process, and ionisation at 255.75 nm (probe) is a three-photon process.)

SH^+:

- $SH(X\ ^2\Pi_{3/2})$ was *produced* by the probe laser as well as by the photodissociation laser: SH^+ signal is seen in Figure 6.8 (when the probe laser was present but the photodissociation laser was not), and rings corresponding to both sources are seen in Figure 6.9.
- SH was *ionised* by the photodissociation laser as well as by the probe laser – although less efficiently, as can be seen from the comparative sizes of the m/z= 33 peaks in Figure 6.7.

S^+:

- S was *produced* almost entirely by the photodissociation laser: it can see from Figure 6.8 (probe only) that the contribution from the probe laser to the production of S was negligible. Production of S at 193 nm is a previously known phenomenon, and is discussed in section 6.5.3.
- S^+ was *ionised* by both the photodissociation and probe lasers (Figure 6.7)

S_2^+:

- The presence of S_2^+ implies some clustering/dimer formation in the molecular beam. This is discussed further in section 6.4.3.
- S_2 was only *ionised* by the photodissociation laser: there is no m/z = 64 peak due to the probe laser in either TOF spectrum.
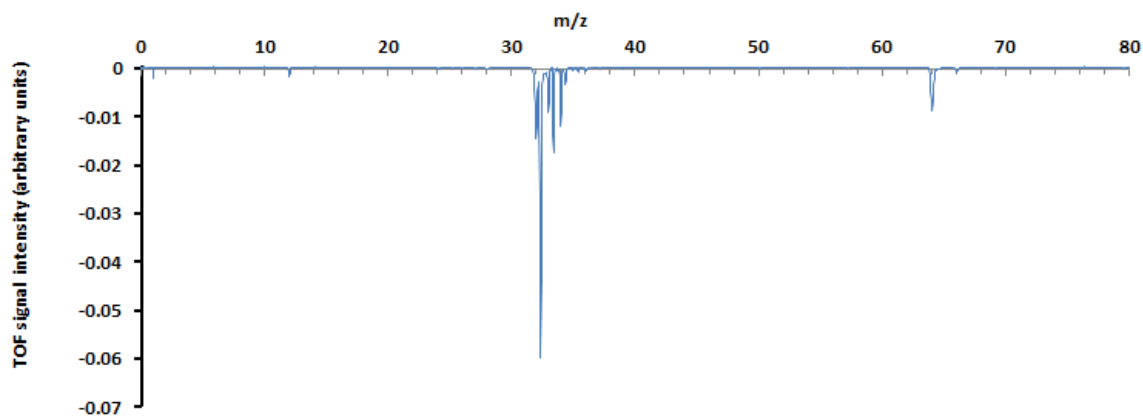
Figure 6.7: TOF spectrum produced by the action of the photodissociation and probe lasers in the earlier part of the molecular beam. Note that there are only three mass peaks in the m/z = 32–34 region – the illusion of six masses is created by the 50 ns time delay between the photodissociation and probe lasers.
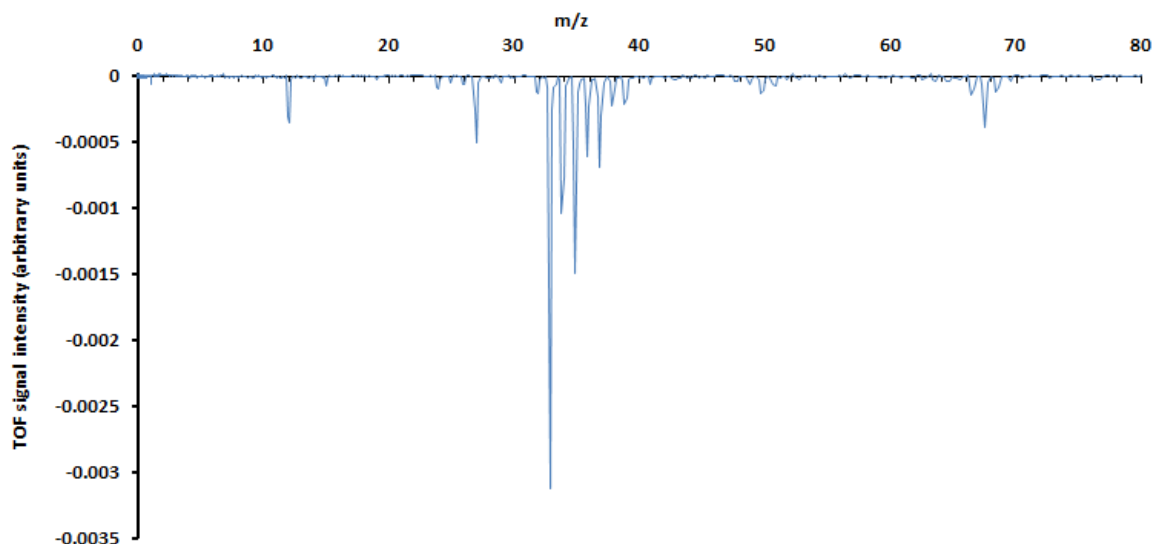
Figure 6.8: TOF spectrum produced by the action of the probe laser only.

Table 6.1: assignments of significant TOF peaks from Figure 6.7 and Figure 6.8. The peak at m/z = 12 is ascribed to carbon from pump oil.

m/z	Assignment
1.0	H
32	^{32}S
33	^{32}SH
34	$H_2{}^{32}S/^{34}S$
64	$^{32}S_2$
66	$^{32}S_2H_2/^{32}S\text{-}^{34}S$
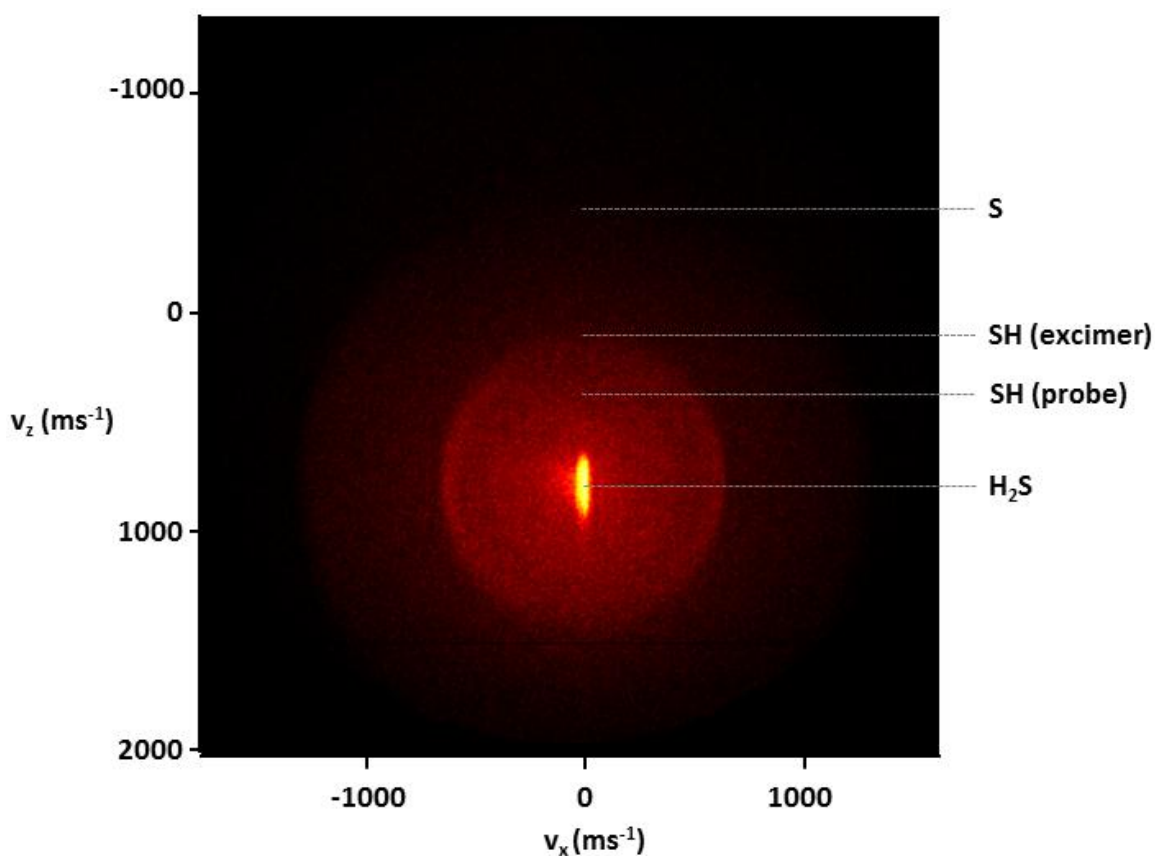
Figure 6.9: photodissociation of H$_2$S at 193 (and 256) nm, near the front of the molecular beam, with a delay of 50 ns between the photodissociation and probe lasers. The SH rings display some anisotropy, although this is largely obscured by the S signal. The ion image was analysed using a pixel calibration value 5.90 ms^{-1} pixel^{-1}.

6.4.3 Further investigation of dimer formation

The photodissociation became more complex in the more intense part of the molecular beam. Figure 6.10 compares Figure 6.9 with an ion image taken further into the molecular beam, in which at least one additional source of ions obscures the features described above. Figure 6.12 shows a TOF spectrum from approximately the same portion of the molecular beam as the second panel in Figure 6.10. Assignments are given in Table 6.2.

The appearance of the large, non-structured ion signal in Figure 6.10 was matched by a very large proportional increase in the m/z = 64 peak, and so was identified as being mostly due to S$_2^+$. This view is supported by the ion image displayed in Figure 6.11, which resembles the new signal in the second panel of Figure 6.10, and was recorded by gating the MCP for the m/z = 64 peak.

111
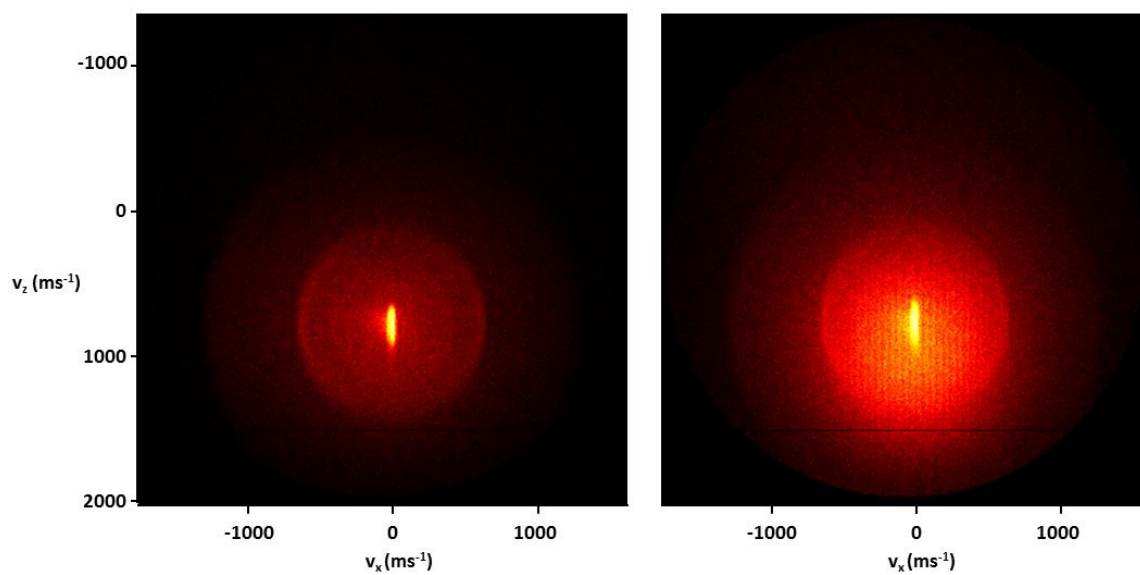
Figure 6.10: first panel: reproduction of Figure 6.9; second panel: ion image of photodissociation occurring in the more central portion of the molecular beam, 30 μs later in the molecular beam than the first panel.
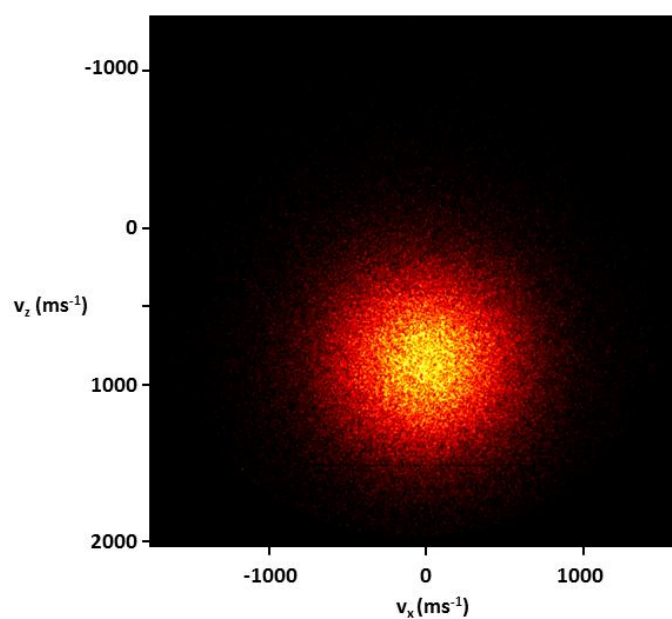
Figure 6.11: ion image produced under the same conditions as the second panel of Figure 6.10, but with mass gating to select the m/z = 64 signal.
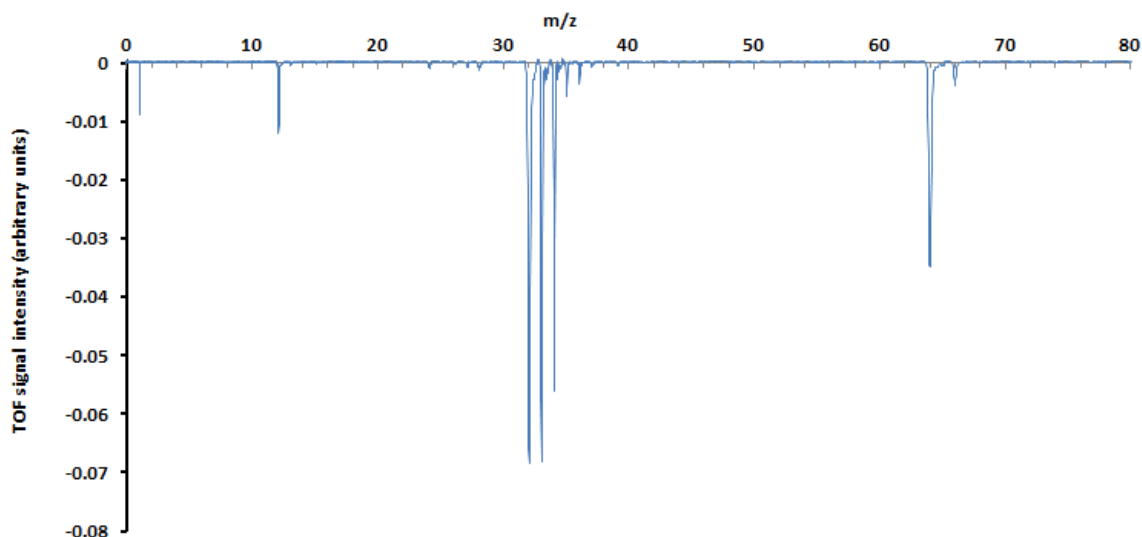
Figure 6.12: TOF spectrum accompanying the second panel of Figure 6.10.

Table 6.2: assignments of significant TOF peaks from figure 6.12 (*i.e.* peaks resulting from the presence of H₂S, and not due to pump oil *etc*).

m/z	Assignment
1.0	H
32	^{32}S
33	^{32}SH
34	$H_2^{32}S/^{34}S$
35	^{34}SH
36	$H_2^{34}S$
64	$^{32}S_2$
65	$^{32}S_2H$
66	$^{32}S_2H_2$

The presence of signal due to S_2 suggests that H_2S dimers are formed in the expansion, and then dissociated by the excimer laser. To test the clustering hypothesis, molecular beams were generated with lower backing pressures, and the products of their photodissociation compared with the above.

Figure 6.13 repeats the second panel of Figure 6.10, alongside a second ion image taken in the same part of the molecular beam but at a lower backing pressure of 2 bars; Figure 6.14 shows the TOF spectrum accompanying the second panel of Figure 6.13, from which the peaks due to S_2^+ and its isotope are essentially absent. This result – that signal due to S_2^+ is seen at a pressure of 4 bars, but not at 2 bars – supports the clustering hypothesis. That clustering is not seen at these lower pressures is in

agreement with the work of Weiner *et al.*, who observed no dimerization effects when using pure H_2S with a backing pressure of 2 atm.[148]
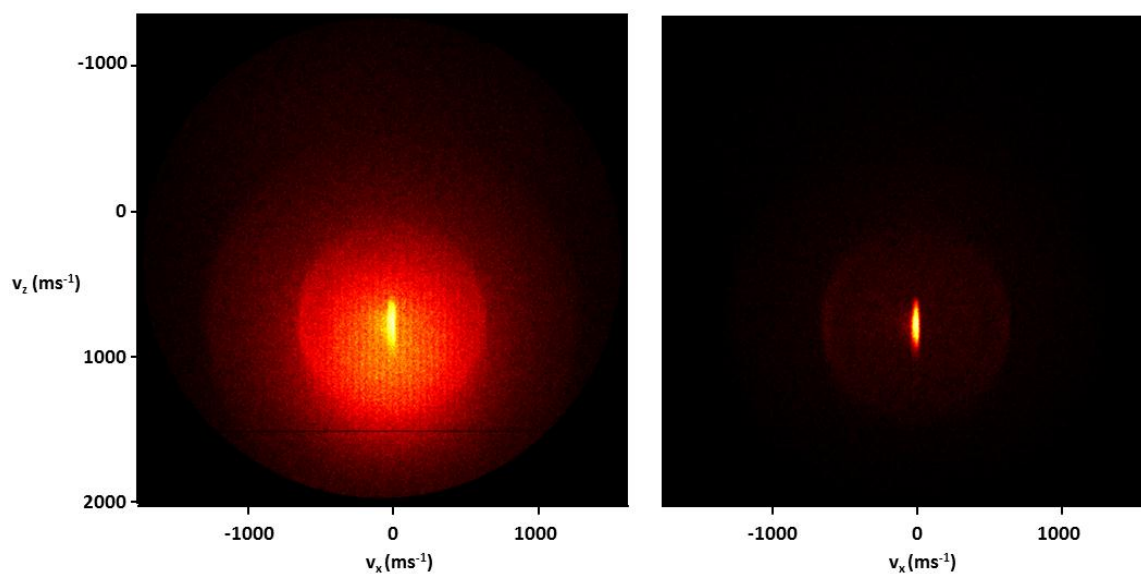
Figure 6.13: first panel: reproduction of second panel of Figure 6.10; second panel: ion image of photodissociation under the same conditions but with 1 bar backing pressure.
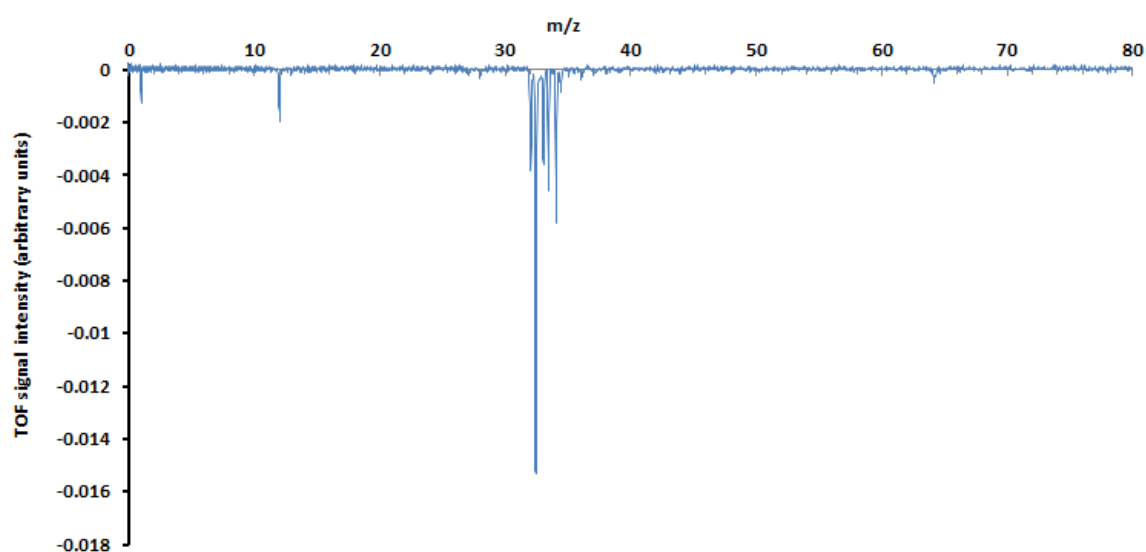
Figure 6.14: TOF spectrum to accompany the second panel of Figure 6.13 (taken under the same conditions as the earlier spectra, but using a backing pressure of 1 bar rather than 4 bars for the molecular beam). The peaks due to H_2S dimerization (at m/z = 64/65/66) are essentially absent. Again, there is a 50 ns delay between the photodissociation and probe lasers.

6.4.4   A second source of SH in higher pressure molecular beams

In the region of the 4 bar molecular beam that produced the large S_2^+ TOF peak, the nature of the SH dissociation changed. Figure 6.15 compares the product distribution of SH in the early part of the molecular beam, and in the centre. In the centre of the molecular beam, SH appears to be produced with a wide spread of velocities. Again, this phenomenon is not seen in the lower pressure molecular beams: presumably, it is the result of the photodissociation of clustered H_2S, perhaps after fragmentation of the dimer to $H_2S + H_2S^+$.[157,158]
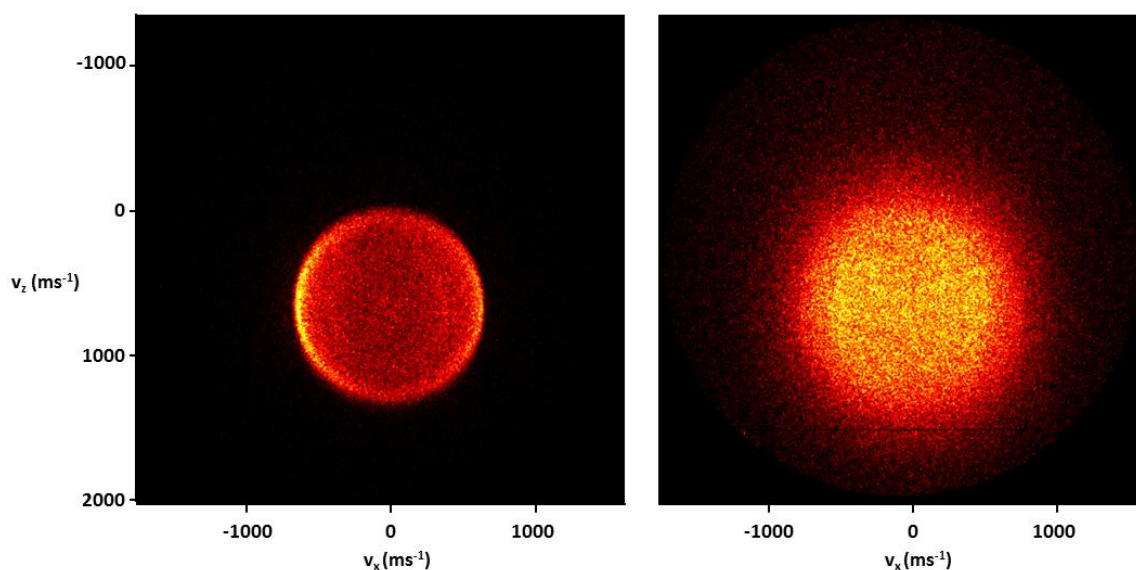
Figure 6.15: ion images produced by mass gating to select the m/z = 33 signal. The first image was recorded from the earlier part of the molecular beam, the second from the centre.

6.5   Photostop of SH

The work above established: the molecular beam compositions necessary to optimise the molecular beam velocity for photostop; that the use of higher pressure molecular beams could cause clustering; and that high laser intensities could produce secondary photodissociation of SH and a variety of undesired ions. The possible effect of these factors on the density of photostopped SH is discussed in section 6.5.3 below.

Informed by this work, photostop of SH was carried out using a molecular beam of 84% H_2S in xenon, to give the richest possible molecular beam. Photostop was not carried out at the peak of the molecular beam, but rather a little towards the leading edge, about 20 µs ahead of the peak of the pulse. At this point, the molecular beam intensity was about 85% of that at the beam maximum, and the beam had a velocity of 665 ms⁻¹,

with a longitudinal temperature of 11 K (corresponding to a FWHM velocity spread of 88 ms^{-1}) and a transverse temperature of 0.6 K. The experimental parameters (laser energies, laser beam sizes *etc*) are given in appendix J.

6.5.1 Population decay curve of photostopped SH(X $^2\Pi_{3/2}$, *v* = 0, *J* = 1.5)

An SH population decay curve was acquired by the method described in chapter 4. The data are shown in Figure 6.16, together with a simulated decay curve provided by the phstop program and used to estimate the density of photostopped SH. The experimental curve could follow only the first two orders of magnitude of signal decay, with the signal being lost in noise at delays greater than 10 µs. The ion images taken to accompany the curve (section 6.5.2) demonstrated that photostopped molecules could be detected at delays as great as 100 µs, so the failure of the decay curve to extend past 10 µs was attributed to the curve acquisition method. A second curve was recorded by the integration of ion images of the photostopped molecules, as in Trottier *et al.*[13] (Figure 6.17). The experimental conditions were similar, except that a (more economical) mixture of 25% H$_2$S in argon was used. This technique seems to be less susceptible to noise, and decay could be observed over three orders of magnitude, to a delay of 50 µs. Figure 6.16 is still displayed because it is the curve to which the ion images in section 6.5.2 correspond.
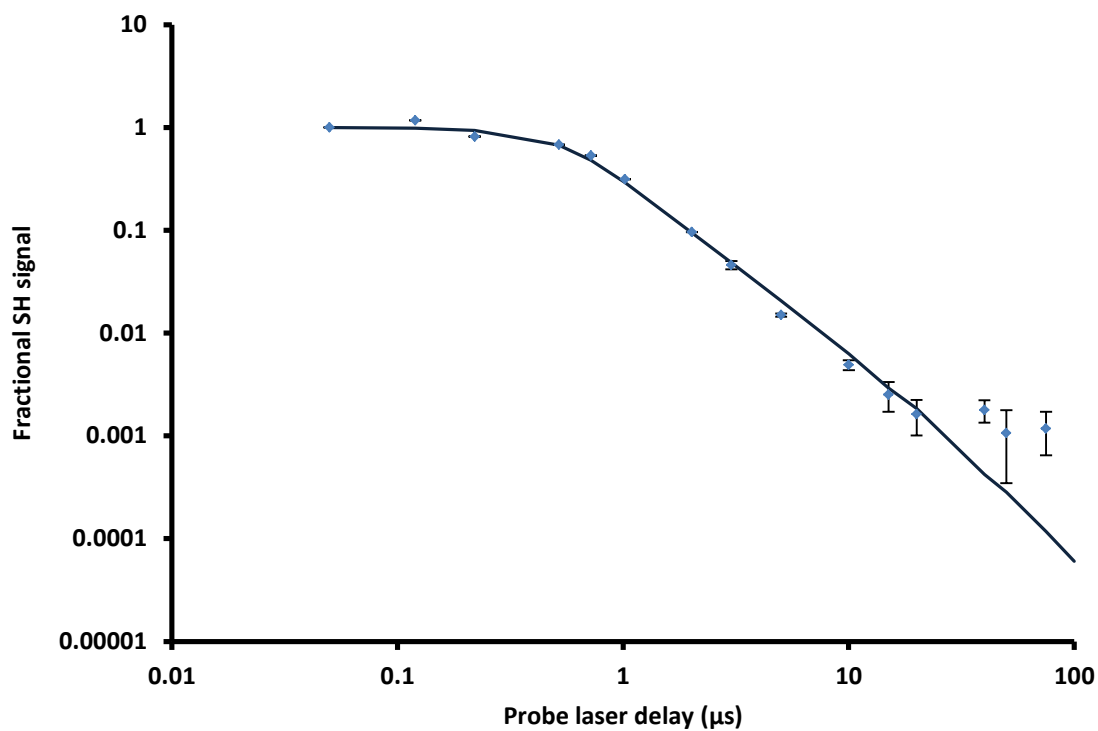
Figure 6.16: population decay curve of SH(X $^2\Pi_{3/2}$, v = 0, J = 1.5) acquired by REMPI (integration of TOF signal). Error bars represent one standard deviation. According to the photostop program, 3.6 x 10^8 SH(X $^2\Pi_{3/2}$) fragments were created in the probe volume, with a density of 1.2 x 10^{11} cm^{-3}. The detection limit was therefore in the region of 10^4 - 10^5 molecules, or a density of 10^7 - 10^8 cm^{-3}.
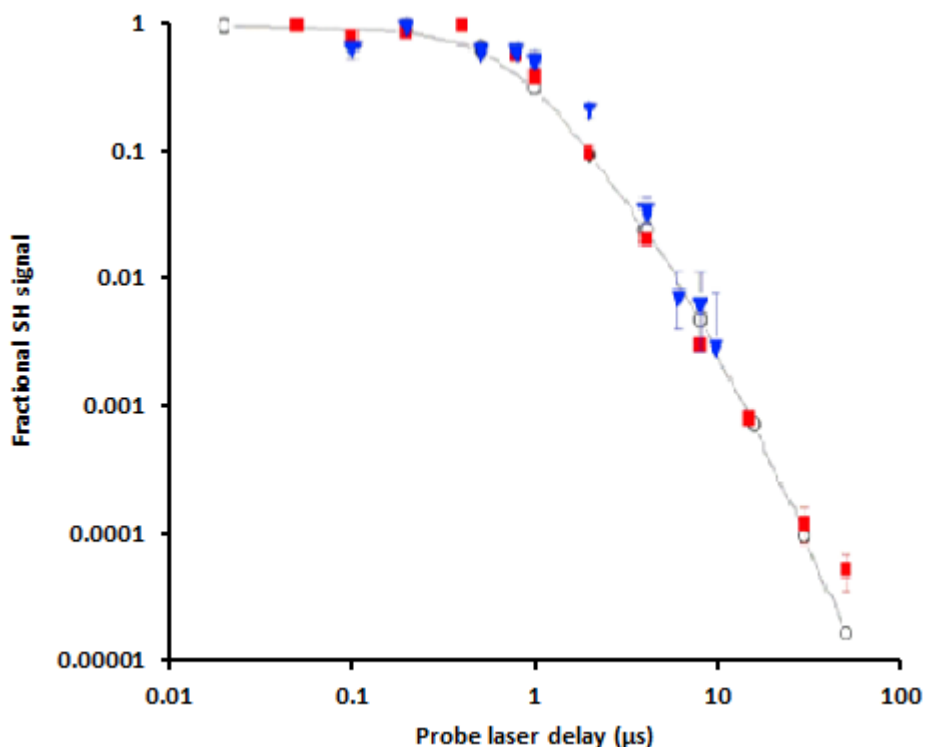
Figure 6.17: population decay curve of SH(X $^2\Pi_{3/2}$, v = 0, J = 1.5) acquired by REMPI (integration of ion images).

6.5.2 Ion images of photostopped SH(X $^2\Pi_{3/2}$, v = 0, J = 1.5)

Attempts directly to measure the velocity origin of the velocity mapped ion images, as was done for the work with NO and for the measurements of H_2S molecular beam speeds in section 6.3, were unsuccessful. However, simulation suggested that even if using a molecular beam with a velocity 30 ms^{-1} different to that required for optimum photostop, the photostopped molecules remaining after a 50 µs delay should be centred on zero velocity in z: so, the centre of the 50 µs image (Figure 6.18) was taken to be the velocity origin along the z axis. The centre of the SH ring produced at very short delays was taken to be the velocity origin along the x axis.

Ion images of photostopped SH are shown in Figure 6.18. As stated above, photostopped SH(X $^2\Pi_{3/2}$) was visible at delays of up to 100 µs, but only very weakly; the longest time delay for which a visible signal can be seen in print with reasonable ease is 75 µs. Indeed, the images obtained at the longest time delays were too weak to permit temperature analysis, but the images at up to 50 µs could be analysed. Maxwell-Boltzmann fits were made along the molecular beam axis for the data collected at delays of 20 µs and 50 µs (Figure 6.19 and Figure 6.20), yielding

temperatures of 3.1 ± 0.1 K and 1.7 ± 0.1 K respectively (corresponding to kinetic temperatures of 2.1 K and 1.2 K respectively).
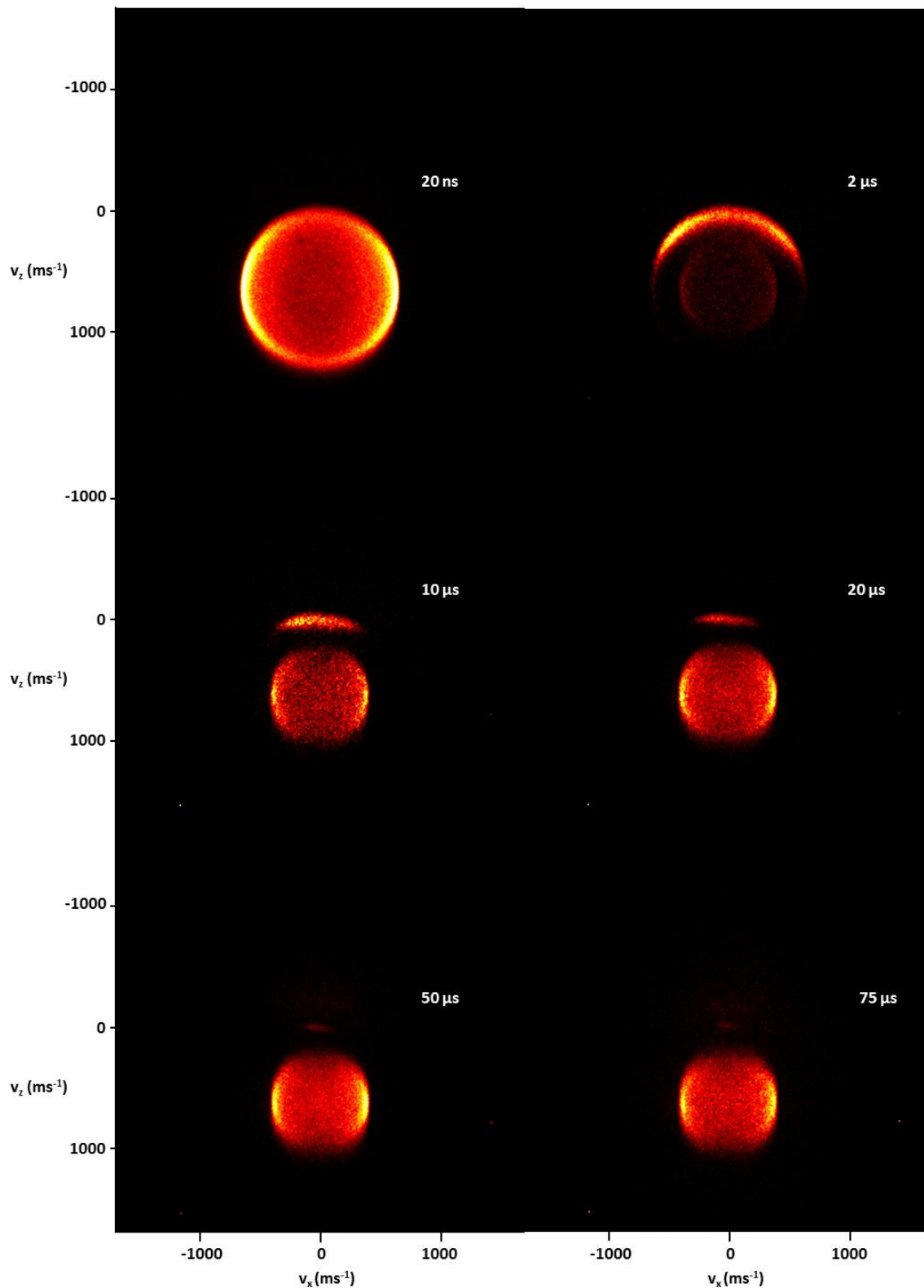
Figure 6.18: ion images of photostopped SH(X $^2\Pi_{3/2}$) at a series of photodissociation-probe intervals. The 100 μs image is not shown because the signal is very weak and cannot easily be seen. This figure is best viewed in the electronic copy of this thesis.

119
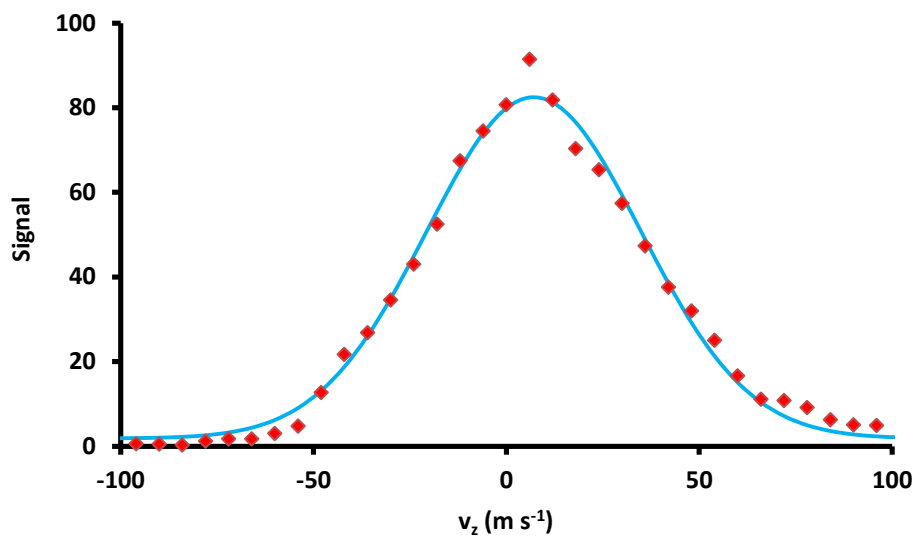
Figure 6.19: the velocity profile, along the *z* axis, of photostopped molecules after a delay of 20 μs. SH(X $^2\Pi_{3/2}$) remaining at this time was calculated to have a density of 4 x 10^7 – 4 x 10^8 cm^{-3}. A Maxwell-Boltzmann fit (blue line) yields a temperature of 3.1 ± 0.1 K. The kinetic temperature (calculated from the HWHM) is 2.1 K.
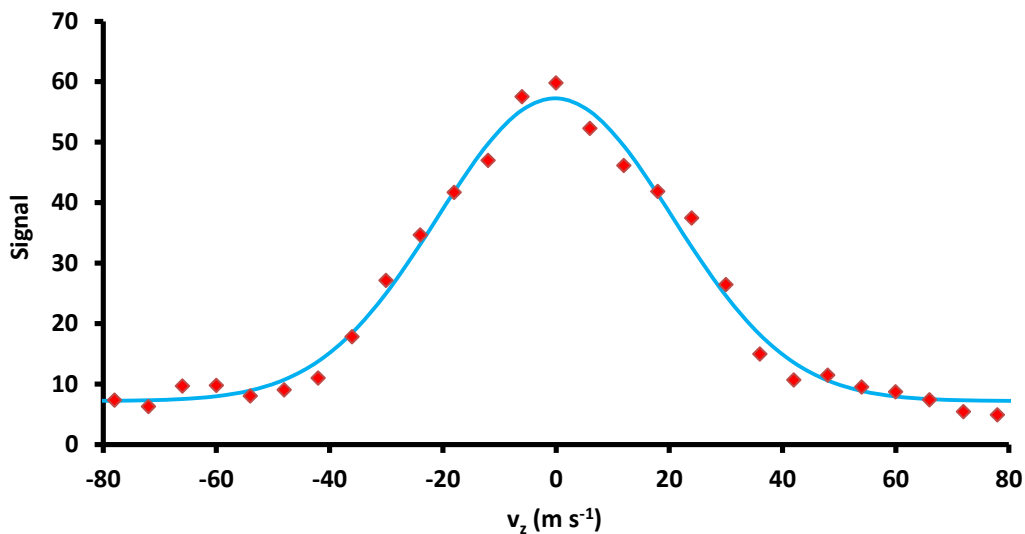
Figure 6.20: the velocity profile, along the *z* axis, of photostopped molecules after a delay of 50 μs. SH(X $^2\Pi_{3/2}$) remaining at this time was calculated to have a density of 1 x 10^7 – 1 x 10^8 cm^{-3}. A Maxwell-Boltzmann fit (blue line) yields a temperature of 1.7 ± 0.1 K. The kinetic temperature (calculated from the HWHM) is 1.2 K.

6.5.3 A note on the estimation of SH density

As for the work with NO, the density of SH could not be measured directly, and instead was estimated using the phstop program. Two complications arise here: the observed clustering introduces a degree of uncertainty to the density of H_2S (as opposed to $(H_2S)_2$) in the molecular beam; and both the secondary photodissociation and ionisation of SH by the photodissociation laser introduces a degree of uncertainty to the density of SH remaining at the end of the photodissociation laser pulse.

<u>Clustering</u>

Clustering makes the clustered H_2S useless as a photostop precursor, and hence causes the phstop program to overestimate the density of precursor molecules in the molecular beam. It would be nice in hindsight to have a measurement of the profiles of a high and a low pressure molecular beam, with these profiles obtained by the detection of SH^+ generated by action of the probe laser alone, so that only SH produced by the photodissociation of unclustered H_2S would be seen.[§§] Comparison of the amount of SH produced from the two beams would allow an inference of the proportion of H_2S effectively lost as a photostop precursor to clustering. Unfortunately, at the time of the experiment this was not properly considered.

A measurement taken at the time that allows some estimate to be made of the order of H_2S loss to clustering is the graph shown in Figure 6.21, which fulfils the description above except that it was obtained by the action of both photodissociation and probe lasers, and so the signal of the higher pressure curve is due to both clustered and unclustered H_2S. Ion images accompanying Figure 6.21 showed that signal due to clustered H_2S did not appear at nozzle delays of 460 us or greater, so in the region above 460 us the curves can be compared. It can be seen that the two beams are of a comparable magnitude in this region, when the higher pressure beam would normally be expected to be more intense, and so: i.) clustering probably causes a loss of density; but ii.) this loss is not large, and is certainly not an order-of-magnitude loss.

[§§] The action of the probe laser alone did not produce SH from clustered H_2S.
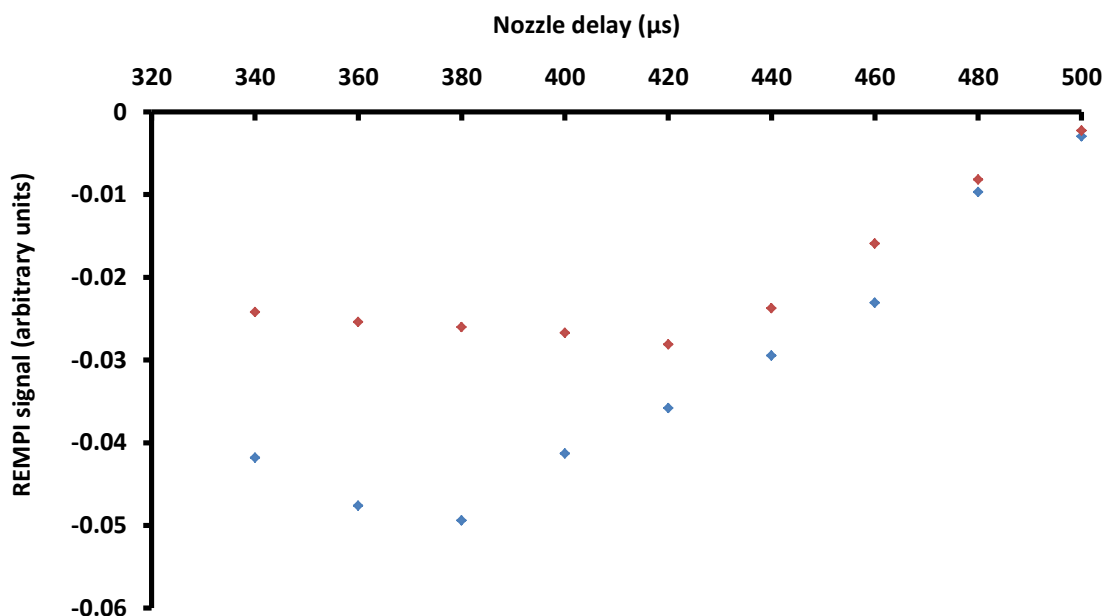
Figure 6.21: effect of pressure on SH($^2\Pi_{3/2}$, v = 0, J = 1.5) REMPI signal from the 193 nm photodissociation of molecular beams of 25% H$_2$S in argon, with backing pressures of 5 bars (blue points) and 2 bars (red points).

Ionisation and secondary photodissociation

Considering the effect of ionisation or secondary photodissociation of SH by the photodissociation laser, it is instructive to view Figure 6.22, which displays TOF spectra produced using a much lower intensity photodissociation laser beam. It is apparent that the secondary photodissociation process and the ionisation process are much less efficient that the primary photolysis (confirmed in the case of secondary photodissociation by Continetti *et al.*)[159] and so should become significant only in the limit when the photodissociation laser intensity is great enough largely to have bleached the molecular beam of H$_2$S molecules.

Figure 6.23 displays the measured relationship between SH REMPI signal and photodissociation laser energy in a range containing the laser energy used to obtain the decay curve, and compares this to the relationship calculated by the phstop program, which takes no account of the losses due to ionisation or secondary photodissociation of SH by the photodissociation laser. The difference in gradient between the two data sets is insignificant within error (0.33 ± 0.05 and 0.27 ± 0.01 respectively) and so it is concluded that the bleaching regime has not been reached at the photodissociation

laser intensities used, and consequently that loss of SH to ionisation or secondary photodissociation is minor.

Summary

Considering all these effects together: given the uncertainty in the H_2S density due to clustering, the small reduction in SH density resulting from the secondary action of the photodissociation laser, and the fact that the experiment was not conducted right on the peak of the molecular beam density, SH densities in the work above are given as order-of-magnitude range estimates, with the SH density calculated by the phstop program being the upper bound.
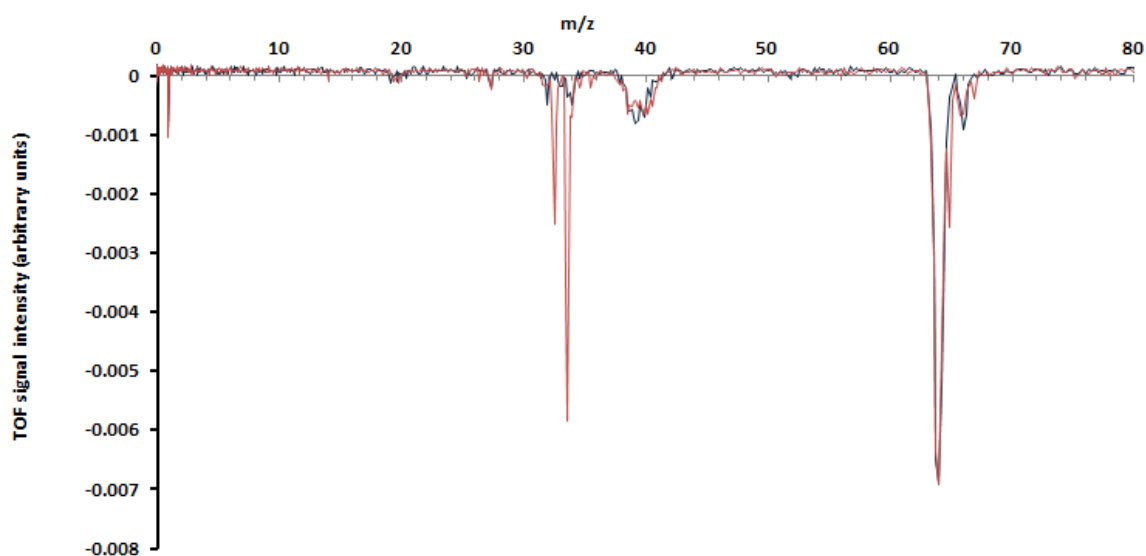
Figure 6.22: TOF spectra resulting from the action of the unfocussed photodissociation laser. The blue spectrum is the result of the action of the photodissociation laser only; the red is the result of the action of both the photodissociation and probe lasers.
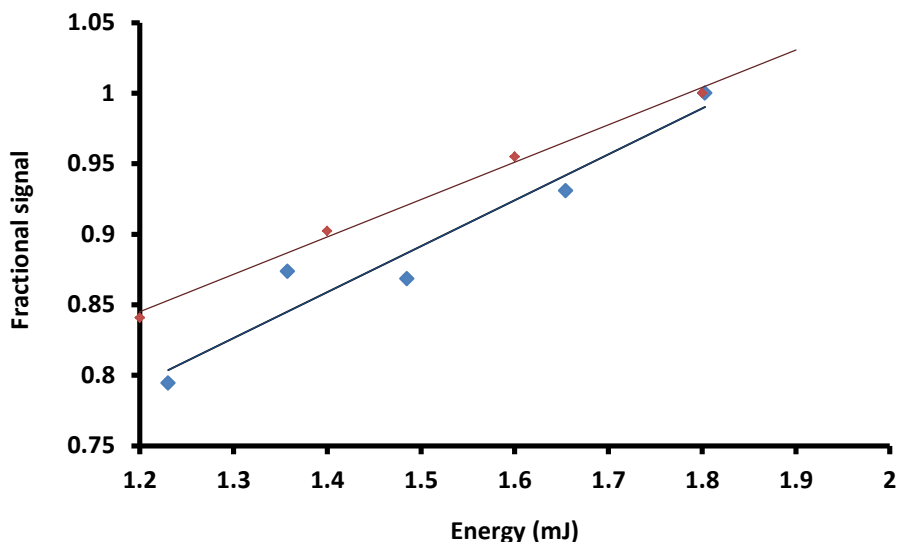
Figure 6.23: variation of measured (blue) and simulated (red) SH REMPI signal with photodissociation laser energy.

6.5.4 Significance of results and future development of the SH experiment

The densities achieved with SH are an improvement upon those achieved in the earlier work with NO/NO_2, and so are a worthwhile addition to the growing list of cold molecules that can be created in the laboratory. Moreover, with the successful photostop of SH, a significant step has been made towards the achievement *via* photostop of the aims of the MMQA project. There is scope for a small further increase in the density of photostopped SH with minimal experimental effort: the phstop program suggests that an improvement of about 40% in the density of SH should be made if photodissociation is carried out using the vertically polarised 5th harmonic output of a Nd:YAG laser. This approach would provide a more favourable combination of laser polarisation and dissociation anisotropy, as well as a smaller fragment recoil, at the cost of a small reduction in absorption cross section and a reduction in precursor concentration.

The next step is to return to the experiment described in the last chapter and attempt to trap it, to allow its use in the MMQA program. Simulation with the phstop program suggests that the photostop of SH should allow the initial trapping of approximately 10^5-10^6 SH molecules. If the true figure is towards the upper end of this range, then only modest further enhancement of the experiment, combined with repeat loading of the magnetic trap, should allow the attainment of the MMQA target of 10^7 trapped, cold, polar molecules.

Whilst SH is a good candidate for magnetic trapping (section 5.3.6) it is not a good candidate for magnetic trapping in the current set-up – *i.e.* for a trapping experiment in which the detection technique is LIF. SH(X $^2\Pi$) can be detected by LIF from the A $^2\Sigma^+$ state, but this state is severely predissociative. The predissociation lifetime of the $v = 0$ state of SH(A $^2\Sigma^+$) is 3 ± 2 ns, but the radiative lifetime is 820 ± 240 ns, and the predissociation becomes more severe in the higher vibrational levels.[160]

There are two obvious ways to solve this problem. One is to change the detection method (see next chapter); the other is to make a minor change to the experiment and work with D_2S/SD instead. The product state distribution of SD produced by the photodissociation of D_2S in its first absorption band is similarly favourable to photostop, and the predissociative lifetime of SD(A $^2\Sigma^+$, $v = 0$) is 260 ± 100 ns, compared with a radiative lifetime of 730 ± 180 ns.

7 Future directions

This final chapter deals with four aspects of the future development of the photostop experiment. The first aspect is the progress of the SH experiment (now the SD experiment) since the author left the lab, and the prospects for trapping cold SD. The second is some practical changes that might be made when constructing a new apparatus for photostop. The third is a review of alternative molecular candidates for the photostop experiment, and the fourth is a brief look at the prospect of increasing the densities achieved by photostop.

7.1 Progress of the SH/SD experiment: work towards magnetic trapping

Work on the photostop experiment has since focused on the detection of photostopped SD using LIF. A population decay curve of photostopped SD(X $^2\Pi_{3/2}$, $v = 0$, $J = 1.5$)is shown in Figure 7.1. According to the photostop program, around 5 x 10^9 SD (X $^2\Pi_{3/2}$, $v = 0$, $J = 1.5$) fragments were present in the probe volume at 1 μs delay, with a density of 1.2 x 10^{11} cm^{-3}, meaning that the detection limit was around 5 x 10^6 fragments, or a density of about 10^8 cm^{-3}. These numbers suggest that it might be possible to observe trapping with the current LIF arrangement, if the estimate given in the last chapter for the potential number of trapped molecules (10^5 - 10^6) was correct. The observation of trapping would not have been expected in the experiment that generated Figure 7.1, because the experimental conditions were distinctly sub-optimal in terms of laser beam diameter and energy, and precursor density, meaning that the number of trapped molecules produced would be substantially below the 10^5-10^6 estimate.
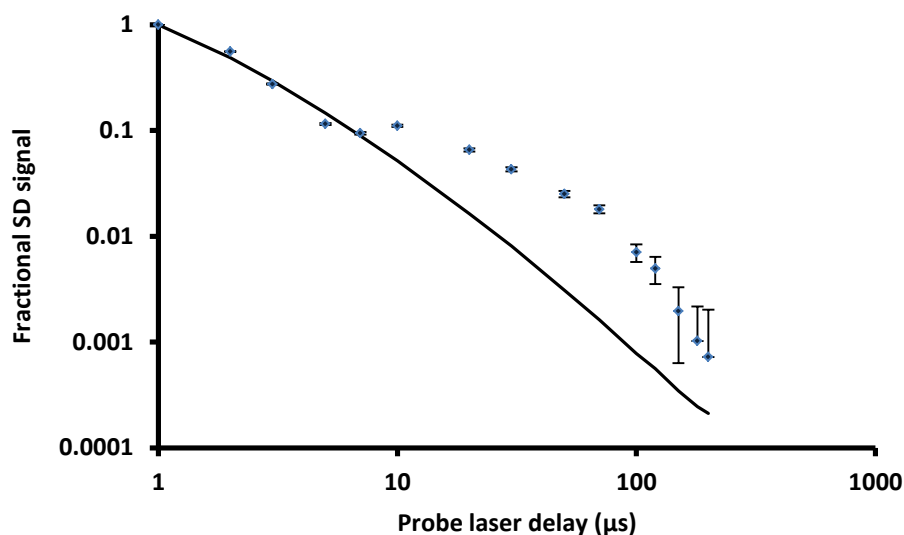
Figure 7.1: SD(X $^2\Pi_{3/2}$, v = 0, J = 1.5) population decay curve acquired using LIF detection (data points) and simulated decay curve (line). The rise in signal at about 10 μs is attributed to the return to the probe volume of faster fragments rebounding from the magnets and the trap body.

7.1.1 Detection of trapped molecules using REMPI

It is noted in passing that the only other group (to the author's knowledge) working on the trapping of photostopped fragments (the Softley group in Oxford, working with atomic bromine) monitor their trapped population by REMPI, and that this might be an approach to pursue if the attempt to observe trapping *via* LIF fails. It would also allow the pursuit of SH rather than SD for the MMQA project, which would be advantageous because SH has a much larger rotational constant than SD,[161] leading to the production of a purer trapped population.

7.2 Improvements in a new photostop machine

Work is due soon to begin on the construction of a purpose-built photostop apparatus. The project is already planned, and the new machine is described in the MMQA grant proposal.[134] The most notable features of the new machine (aside from a decrease in size) are the addition of a third differentially pumped chamber, an improved molecular beam nozzle that should be able to produce pulses shorter than 100 μs, and possibly also a chopper that should allow the pulses further to be abbreviated. In the current set-up, the vast majority of the molecular beam pulse is not lit by the photodissociation laser, and the gas in it serves only to sweep out photostopped molecules, and to

127

increase the background pressure to the same effect.*** Shorter pulses, produced in the first of the three chambers and chopped in the second, should mean that a much larger proportion of the gas reaching the third (photostop/trapping) chamber is photodissociated.

There are two further suggestions for the new machine that spring to mind from the work conducted previously. Firstly, a means to measure and control the molecular beam nozzle temperature would be useful, allowing more rigorous simulations, particularly for NO_2 and other gases that exist in equilibrium with other species. Perhaps more importantly, it would provide a way of controlling molecular beam speed that did not rely on changing the ratio of precursor to buffer gas: controlling molecular beam temperature, molecular beam speed, and product density by variation of a single variable is not ideal.

Secondly, it would also be nice to see a means for the measurement of product density. Whilst photostop is far from unique in the cold molecules field in estimating density rather than measuring it directly††† it would be more rigorous to be able to measure the product density. One way to do this would be the use of cavity ring down spectroscopy, considerable expertise on which exists within the group.

A cavity ring down experiment uses a cavity formed by two highly reflective mirrors, into which a laser pulse is introduced through the back of one of the mirrors. The pulse reflects back and forth between the mirrors many hundreds or thousands of times,

---

*** For comparison: assuming a trap volume of about 225 mm^3, 10^6 trapped molecules corresponds to a density (falsely assuming a constant density throughout the trap) of about 4 x 10^{12} m^{-3}; whilst with a background pressure in the order of 10^{-6} mbar, the density of thermal gas in the vacuum chamber is about 6 x 10^9 m^{-3}.

††† The author's favourite example of density estimation is found in the velocity selection work of Bertsche and Osterwalder:[162] "An estimate of the flux in this beam is possible by comparing the REMPI signal from the guided molecules to the signal from background molecules: During operation, the pressure in the detection chamber rises from below 5 × 10^{-9} mbar to around 2 × 10^{-8} mbar. The background gas produces a signal which, under operating conditions without discrimination, is comparable in intensity to the signal from the guided molecules. While the background pressure, which is read off of a pressure gauge some 30 cm away from the interaction region, can only be taken as an approximate value, it still allows for the estimation of a density in the beam. In the present case a density of 10^8 cm^{-3} is assumed. REMPI does not measure flux but rather density, which can be transformed into flux by assuming a laser diameter of 0.1mm at the focus…"

losing energy with each reflection by a factor of $1 - R$, where R is the mirror reflectivity. The characteristic "cavity ring-down time" of the cavity is the time taken for the intensity of the laser pulse to fall to $1/e$ of its starting value.

The presence in the cavity of gas particles that absorb the light decreases the cavity ring down time; from this decrease, the density of the gas (ρ) can be calculated from the relation

$$\rho = \frac{L}{d\sigma c}\left(\frac{1}{\tau'} - \frac{1}{\tau_0}\right)$$

where L is the cavity length, d is the sample pathlength, σ is the absorption cross section of the gas, τ_0 is the ring-down time of the empty cavity, and τ' is the ring-down time in the presence of the gas.

If the new photostop machine had additional optical access ports to create a cavity with the photostop region at its centre, the density of photostopped molecules could (following estimation of the pathlength by consideration of the molecular beam diameter) be measured. Whilst this measurement would still involve an estimation step, it would nonetheless be considerably less speculative than the current system.

7.3 Alternative candidates for the photostop experiment

Photostop is limited in its application by the absorption spectra and dissociation dynamics of possible precursor molecules. There are a number of characteristics required of a passable photostop precursor, which are as follows.

The current focus of the photostop experiment is on trapping cold molecules. Since the energy held within internal degrees of freedom is considerably in excess of any realistic trapping potential, it is desirable to produce fragments in the electronic, vibrational and rotational ground state so as to avoid inelastic collisions leading to trap loss. Ergo, the first requirement of any candidate is that photodissociation produces an appreciable fraction of products in the ground state.

To produce an appreciable density, it is also important that Newton sphere over which the products are distributed is not too large, as an increase in the diameter of the Newton sphere means a lower product density. That is to say, the translational energy

of the products should also not be too great (although it must of course be great enough to counteract the speed of the molecular beam).

These two requirements – low levels of fragment excitation coupled to modest fragment recoil – mean that it is necessary that the excess energy be small, which in turn implies that the precursor must absorb close to threshold. Finally, the absorption cross section at the photodissociation wavelength must be large enough to produce an appreciable fragment density with the laser energy available, and the photostop region must overlap with a wavelength that is practical to produce in the laboratory.

During the course of this PhD, a search was made for alternative triatomic candidates for the photostop experiment. Working from the considerations outlined above, the search looked for molecules:

- with cold rotational and vibrational product distributions;
- that absorbed sufficiently close to threshold to give a recoil from photodissociation of 350-1200 ms^{-1}, which is – roughly – the range of speeds with which a molecular beam can be generated in our apparatus. Faster beams can be generated using helium, but the surface area of a sphere scales with the square of its radius, so increasing the molecular beam velocity from 380 ms^{-1} (as used in the NO_2 work) to 1200 ms^{-1} already results in an order of magnitude loss of photostop density. The range of photodissociation wavelengths that would generate recoil over the desired speed range is referred to as the "photostop region" in the discussion below;
- with an absorption cross section in the photostop region of at least 10^{-19} cm^2. Simulation with the phstop program suggests that (when considering a dilute molecular beam, such as was used for the work with NO_2, and a dissociation laser intensity of 2.8 x 10^{17} cm^{-2}, as given for instance by a laser beam 1/e diameter of 3 mm, and a laser pulse energy of 10 mJ at 387 nm) for cross-sections of 10^{-18} cm^2 or less, an order of magnitude decrease in absorption cross section leads to approximately an order of magnitude decrease in photofragment density. Hence, an absorption cross section much lower than that of NO_2 is unlikely to be the mark of a better precursor.

Four points should be stressed. Firstly, this search does not claim to be exhaustive. Secondly, it relied on pre-existing photodissociation studies. There were many molecules for which little or no useful photodissociation literature could be found, and it is quite possible that among their number lurk one or more superb photostop

precursors. Thirdly, this search was conducted with the aim of replacing NO_2 with a better precursor, and thus that candidates were assessed on their ability to provide a higher photostop density than NO_2, and not on their ability to produce particularly interesting photofragments for any specific purpose. Fourthly, it assumed the use of a molecular beam source, rather than the combination of the photostop technique with *e.g.* a buffer gas beam source. In summary, this survey is reported here to prevent the duplication of effort in future planning of the photostop experiment, and to give an indication of the versatility of the technique, rather than as a comprehensive evaluation of all possible photostop precursors for all possible ends.

7.3.1 Molecules for which little or no relevant literature could be found

For the following molecules little useful literature could be found: KrF_2, HO_2, FCO, CF_2, INO, FO_2, F_2O, ClO_2, BrO_2, Br_2O, HCO, FNO, HOI, OIO, HCN and HOF.

7.3.2 Molecules that are inferior to NO_2 as photostop precursors

NOCl: photodissociated at 587 nm, it recoils with sufficient velocity to stop fragments seeded in a xenon beam, and produces NO with a cold rotational distribution and almost exclusively in the $^2\Pi_{3/2}$ state – but unfortunately, its absorption cross section in this region is only about 5×10^{-21} cm^2.

OCS: the dissociation threshold for the formation of CO(X $^1\Sigma^+$) and S ($^1P_2$) is 288.95 nm (this channel has a 95% yield; the CO(X $^1\Sigma^+$) + $^3D_2$ has a 5% yield),[163] and the absorption cross section of OCS does not rise above 10^{-19} cm^2 in the photostop region;[164] also, the rotational distribution of CO(X $^1\Sigma^+$) is hot.[163]

O_3: the threshold for photodissociation to O_2(X $^3\Sigma^-$) and O(^3P) is 1180 nm,[119] and its absorption cross section in the photostop region is in the order of 10^{-22} cm^2.[165]

ClCN: the threshold for photodissociation to produce CN(X $^2\Sigma^+$) and Cl(^2P) is 286 nm,[166] and there is no significant absorption in or near the photostop region.[167]

BrCN: the threshold for photodissociation to CN(X $^2\Sigma^+$) and Br($^2P_{3/2}$) is 344 nm,[168] and there is no absorption in the photostop region.[167]

N_2O: the threshold for the photodissociation to $N_2(X\ ^1\Sigma^+)$ + $O(^1D)$ is 340.6 nm,[169,170] and the absorption cross section in the photostop region is below 10^{-24} cm^2, and does not rise to an appreciable level until 190 nm.[171,172]

HOCl: the threshold for the production of $OH(X\ ^2\Pi)$ + $Cl(^2P)$ is 474 nm. The product state distribution at wavelengths below the photostop region is favourable,[173] but the absorption cross section in the photostop region is below 10^{-22} cm^2.[174]

HOBr: like HOCl, HOBr has a favourable product state distribution at wavelengths shorter than the photostop region,[175] but an absorption cross section below 10^{-21} cm^2 in the photostop region.[176,177]

H_2O: the threshold for dissociation to $OH(X\ ^2\Pi)$ + $H(^2S)$ is 242 nm, but there is no appreciable absorption cross section above 180 nm.[119]

NOBr: NO from the photodissociation of NOBr is formed with a high degree of rotational excitation.[178]

Cl_2O: the threshold for dissociation to $ClO(X\ ^2\Pi)$ + $Cl(^2P)$ is 840 nm,[179] and the absorption cross section of Cl_2O in the photostop region is of the order of 10^{-21} cm^2.

SO_2: the threshold for dissociation to $SO(^3\Sigma^-)$ and $O(^3P_2)$ is 218.7 nm.[180] Whilst it has a large absorption cross section in the photostop region (approaching 10^{17} cm^2)[181] preliminary investigation of the photodissociation of SO_2 in the photostop region found the rotational distribution to be substantially unfavourable. SO_2 was suggested as a possible photostop precursor in the MMQA grant application[134] due to its large dipole moment.

ICN: ICN was also suggested as possible photostop precursor in the MMQA grant application,[134] again due to its large dipole moment. ICN photodissociates to $CN(X\ ^2\Sigma^+)$ + $I(^2P_{3/2})$ below 392.4 nm; below 302.2 nm, the $CN(X\ ^2\Sigma^+)$ + $I(^2P_{1/2})$ channel opens. ICN initially appears a promising choice in that the $CN(X\ ^2\Sigma^+)$ + $I(^2P_{1/2})$ channel produces rotationally and vibrationally cold CN – but in its photostop region, this channel is the minority channel (30% at 280 nm),[119] and the absorption cross section of ICN is below 10^{-19} cm^2.[182] Absorption data for ICN could not be found for the photostop region for the $I(^2P_{3/2})$ channel, but the trend in the region at shorter wavelength suggests that the absorption cross section there is below 10^{-20} cm^2.

7.3.3 Molecules that might be suitable as photostop precursors

ClO_2 was suggested in reference 134 as a photostop precursor, with the specific motivation of producing ClO, which has a dipole moment of 1.3 D. Another route to the same photofragment is OClO, which dissociates below 484.6 nm to yield $ClO(X\ ^2\Pi)$ + $O(^3P)$ with greater than 96% yield in the photostop region.[183] The absorption cross section in the photostop region is between 10^{-19} and 10^{-17} cm^2.[184] The product state distribution tends towards vibrational excitation of ClO, but the proportion formed in v = 0 approaches 50% at the longer wavelength end of the photostop region (near 450 nm), and also at 395.2 nm (excitation of the (5,0,2) band).[183] Data on rotational state distributions at these wavelengths could not be found. It should be noted that OClO is explosive and dangerous to handle.

CS_2 irradiated below 277.7 nm yields $CS(X\ ^1\Sigma)$ and $S(^3P)$, and irradiated below 220.9 nm yields $CS(X\ ^1\Sigma)$ and $S(^1D_2)$.[119] CS_2 has an extremely large absorption cross section in the photostop region of the second of these channels (in the order of 10^{-16} cm^2)[185] but information on product state distributions could not be found.

7.3.4 Summary

OClO and CS_2 are well worth investigating as photostop precursors, particularly if motivated by specific uses for cold ClO or CS (the explosive nature of OClO notwithstanding). ICN and SO_2 may be worth investigating if the production of their photofragments is specifically desired, but do not appear likely to provide a substantial improvement over NO_2.

7.4 Enhancement to the photostop technique

Consider the work presented in the last chapter on the photostop of SH. Simulation with the phstop program suggests that for the experimental conditions used, 5.3 x 10^9 ground state SH molecules are created by the photodissociation, of which 3.6 x 10^8 are in the probe laser volume; but after 50 μs – the time shown by the experiment to be necessary to give a temperature near to 1 K – the number of ground state SH molecules remaining in the probe volume is only 2.0 x 10^5. This is approaching a factor of 2000 loss.

By far the largest contributing factor to this inefficiency is the lack of directionality in the photostop process: fragments fly in many directions following photodissociation,

with only a comparatively small proportion moving along the path antiparallel to the molecular beam that leads to their being photostopped. The fraction photostopped could be increased considerably if the precursors were aligned or oriented before photodissociation to encourage antiparallel recoil.

Molecules can be aligned with a high intensity laser beam. The dipole moment induced by the electric field of the laser interacts with the field, leading to alignment. The effect can be powerful. For example, when used on rotationally cooled I_2, it was able to confine 98% of molecules within a 45° cone, and 50% of molecules within a 12° cone. Similar results were achieved for ICl, CS_2, and C_6H_5I.[186] Unfortunately, such results require strong laser fields, on the order of 10^{12} W cm^{-2}.[187,117] Using a Nd:YAG laser as in reference 186, perhaps 1 J of IR radiation could be directed through the molecular beam. To achieve the required power density (with an 8 ns pulse length) a laser beam diameter of about 0.03 mm would be required. Compare this to the diameter of photodissociation laser beam required to dissociate a reasonable number of precursors (several mm) and it is obvious that alignment cannot be applied to the experiment in its current form.

There are two other techniques for orienting gas phase molecules: brute force orientation, and hexapole selection. Brute force alignment is achieved by the application of a strong electric field, with which the permanent dipole of a polar molecule will align if the rotational energy of the molecule is lower than the barrier to rotation created by the interaction of the dipole and the electric field. Brute force alignment is unlikely to be useful to the photostop experiment in its current form, being demonstrated to achieve, for example, the confinement of 50% of a molecular beam of pyridine molecules within a 45° cone by the application of a 60 kV field.[188] Pyridine has a dipole moment of 2.19 D, whereas the dipole moments of H_2S, NO_2, OClO, and CS_2 are 0.97 D, 0.32 D, 1.78 D, and 0 D respectively.[161] It can qualitatively be appreciated that the degree of alignment achievable with brute force orientation will not make an orders-of-magnitude difference to the density of photostopped fragments.

Hexapole focussing, meanwhile, causes a significant reduction in molecular beam intensity: only certain rotational states are selected, with others being discarded from the beam; perhaps more importantly, the hexapole itself occupies a significant length, which would preclude carrying out photodissociation close to the molecular beam nozzle.[189]

7.5   Conclusions

The work described in this thesis makes significant progress towards fulfilling the aim of the MMQA project: to provide 10^6-10^7 ultracold polar molecules for use in a quantum simulator. As reported in chapter 5, the upper limit on the number of trapped molecules that could be produced by the NO_2/NO experiment was only 4 x 10^3. The H_2S/SH experiment is believed to be far more favourable, and may be able to produce 10^5-10^6 trapped molecules. The further improvement necessary to reach the MMQA target is not likely to be achieved by enhancement of the photostop technique (section 7.4 above), and nor is there an immediately obvious superior precursor to H_2S (section 7.3.4). The obvious approach to increasing trapped density, then, is either to improve the magnetic trap itself – simulation work is currently underway to this end – or to use a more intense molecular beam source, as may be possible in the new photostop machine.

If the MMQA number requirement is not met, the future of the photostop project still appears hopeful: the work on SH demonstrates that photostop, when applied a suitable precursor, can produce cold molecules with a comparable density to Stark deceleration or kinematic cooling. The review of alternative candidate molecules reported above leads to the conclusion that photostop is not a very general technique, and thus that its future application will be led by finding useful things to do with the relatively small number of species for which it can generate cold molecules effectively. However, it is a relatively simple and economical way of making cold molecules, and hence a good choice for such precursors as are suitable.

Appendix A - the "phstop" simulation program

The photostop program written by Eckart Wrede is called phstop, and uses Monte Carlo methods to simulate the population decay of a specific product quantum state following photodissociation.

Conceptually, the operation of the program can be split into two parts. In the first part, the population of precursor molecules in the photodissociation volume is generated by consideration of the photodissociation volume, the molecule beam source volume (*i.e.* the nozzle orifice), their separation, and the skimmer between them. In the second, the photodissociation process is modelled.

The phstop program begins by picking a random point in the source volume, and a random point in the dissociation volume. The point in the source volume is a random point on the disc of the nozzle orifice; the point in the dissociation volume is chosen by to a flat random number generator across the width of the volume (experimental y and z axes), and a Gaussian random number generator along the length of the volume (experimental x axis). It is assumed that a molecule moves in a straight line between the starting point and the photodissociation volume. If the line passes through the skimmer, a molecule is created at the point in the dissociation volume; if it does not pass through the skimmer, the point is discarded.

The molecule thus created is assigned a velocity by a Gaussian random number generator weighted by the molecular beam speed and spread input by the user: so at this point, the molecule has a velocity vector and a position. The molecule is then weighted to reflect the density of the molecular beam at that point, determined using standard formulae which at such a distance approach $1/r^2$, where r is the radial distance from the central axis of the molecular beam.[153]

The above process is repeated many times to build a large population of molecules. The phstop program then calculates the probability that photodissociation will occur for each molecule by using kinetics based on a three level system (with the simplifying assumption that the rate of dissociation of excited molecules is much greater than the rate of stimulated absorption/emission), taking account of the photodissociation laser intensity at that molecule (photon flux across the photodissociation volume is given by a Gaussian random number generator) and of the absorption cross-section (modified to account for the molecular orientation with respect to the electric polarisation vector of the photodissociation light). Note that the three level system is appropriate for the

photodissociation dynamics of NO_2, for which the phstop program was initially developed, but potentially inappropriate for other precursors).

The fragments thus created are assigned velocity vectors. This done, phstop provides information on photofragment densities *etc.* for any desired dissociation-probe delay simply by propagating all the fragments for the appropriate length of time and examining the density of fragments that would be probed, given the user input probe laser diameter and assuming a Gaussian probe laser shape.

The phstop program can also provide a rudimentary indication of the trapped fragment population expected if photostop occurs within a magnetic trap, by assessing for each fragment at the instant of its creation whether its velocity vector and position within the trap will lead to its being initially confined. No attempt is made to model loss mechanism, or trajectories inside the trap.

Appendix B - origin of the spectral branches of the NO A-X transition
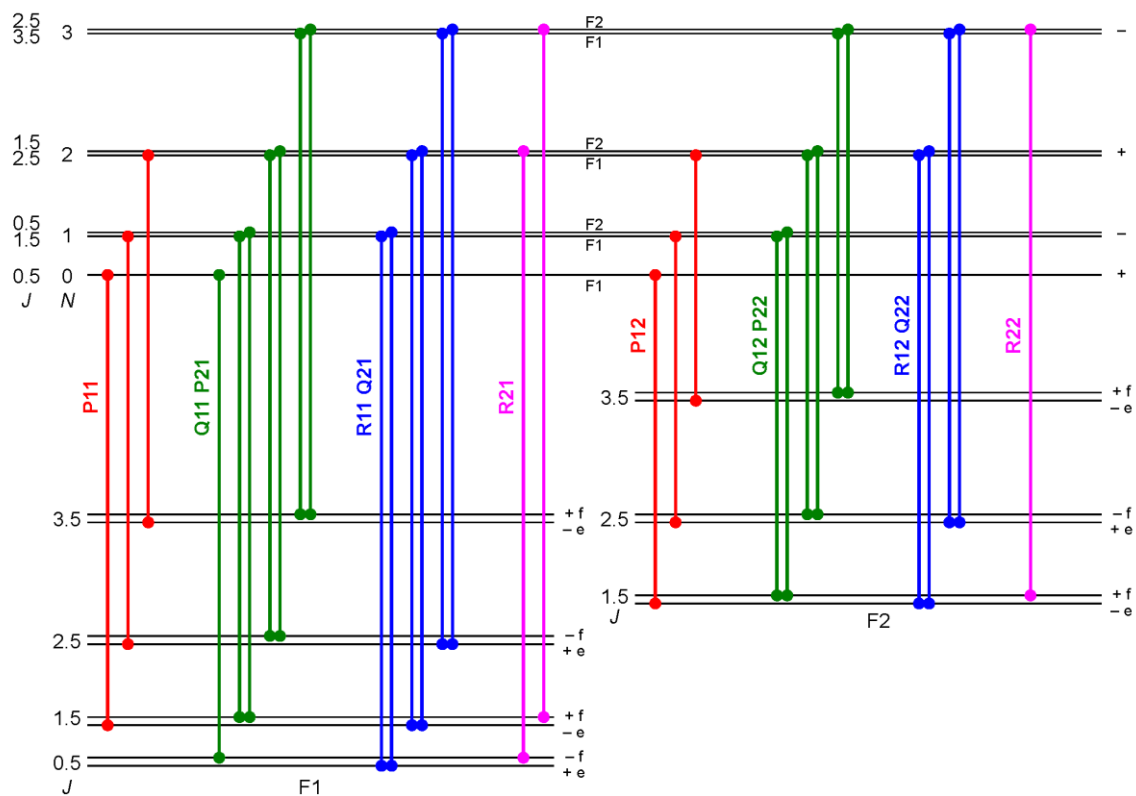
Figure B.1: energy level diagram of the NO A-X system. Reproduced from Chen *et al*.[190]

Appendix C - wavelengths in nm of the NO X $^2\Pi$ -> A $^2\Sigma^+$ transitions

J		P11	Q11P21	R11Q21	R21	P12	Q12P22	R12Q22	R22
0.5	1/2		226.250	**226.229**	**226.189**				
1.5	3/2	**226.275**	226.255	**226.214**	226.153	**226.891**	226.870	**226.829**	226.768
2.5	5/2	**226.298**	226.257	**226.196**	**226.115**	**226.915**	226.874	**226.812**	226.731
3.5	7/2	**226.317**	226.256	**226.175**	**226.073**	**226.936**	226.874	**226.792**	226.690
4.5	9/2	**226.333**	226.252	226.150	**226.028**	**226.954**	226.872	226.770	226.647
5.5	11/2	**226.346**	**226.244**	**226.122**	225.980	**226.970**	226.867	**226.745**	226.602
6.5	13/2	**226.355**	**226.234**	**226.091**	**225.929**	226.982	**226.860**	**226.717**	226.553
7.5	15/2	226.362	**226.220**	**226.057**	225.875	226.992	**226.849**	226.686	226.502
8.5	17/2	226.365	**226.203**	**226.019**	225.817	227.000	**226.836**	226.652	226.449
9.5	19/2	226.365	**226.182**	225.979	225.757	227.004	**226.820**	**226.616**	226.392
10.5	21/2	226.362	**226.159**	**225.935**	225.693	227.006	**226.802**	**226.577**	226.333
11.5	23/2	226.355	**226.132**	225.888	225.626	227.005	**226.780**	**226.535**	226.271
12.5	25/2	226.345	**226.102**	225.838	225.556	227.001	226.756	**226.491**	226.206
13.5	27/2	226.333	**226.069**	225.785	225.483	226.995	226.729	226.444	226.139
14.5	29/2	226.317	**226.033**	225.729	225.407	226.985	226.699	226.394	226.069
15.5	31/2	226.298	225.994	225.670	225.327	226.973	226.667	226.341	225.996
16.5	33/2	226.275	225.952	225.607	225.245	226.958	226.631	226.286	225.921
17.5	35/2	226.250	225.906	225.542	225.160	226.940	226.593	226.227	225.843
18.5	37/2	226.221	225.858	225.473	225.071	226.919	226.552	226.166	225.762
19.5	39/2	226.189	225.806	225.401	224.980	226.896	226.509	226.102	225.678
20.5	41/2	226.155	225.751	225.327	224.886	226.869	226.462	226.036	225.592

Wavelengths in bold typeface are non-overlapping transitions.

Wavelengths taken from LIFBASE.[146]

Appendix D - energies in cm^{-1} of the NO X $^2\Pi$ -> A $^2\Sigma^+$ transitions

J		P11	Q11P21	R11Q21	R21	P12	Q12P22	R12Q22	R22
0.5	1/2		44198.9	**44203**	**44210.8**				
1.5	3/2	**44194**	44197.9	**44205.9**	44217.9	**44074.1**	44078.1	**44086**	44097.9
2.5	5/2	**44189.5**	44197.5	**44209.4**	**44225.3**	**44069.5**	44077.4	**44089.3**	44105.2
3.5	7/2	**44185.8**	44197.7	**44213.6**	**44233.5**	**44065.4**	44077.3	**44093.2**	44113
4.5	9/2	**44182.7**	44198.5	44218.4	**44242.3**	**44061.8**	44077.7	44097.6	44121.4
5.5	11/2	**44180.1**	**44200.1**	**44223.9**	44251.7	**44058.8**	44078.7	**44102.5**	44130.3
6.5	13/2	**44178.4**	**44202**	**44230**	**44261.7**	44056.3	**44080.1**	**44107.9**	44139.7
7.5	15/2	44177	**44204.8**	**44236.6**	44272.3	44054.3	**44082.1**	44113.9	44149.6
8.5	17/2	44176.4	**44208.1**	**44244.1**	44283.6	44052.9	**44084.7**	44120.4	44160.1
9.5	19/2	44176.4	**44212.2**	44251.9	44295.4	44052	**44087.8**	**44127.5**	44171.2
10.5	21/2	44177	**44216.7**	**44260.5**	44308	44051.7	**44091.4**	**44135.1**	44182.7
11.5	23/2	44178.4	**44222**	44269.7	44321.1	44051.9	**44095.6**	**44143.2**	44194.8
12.5	25/2	44180.3	**44227.8**	44279.5	44334.9	44052.6	44100.3	**44151.9**	44207.4
13.5	27/2	44182.7	**44234.3**	44289.9	44349.2	44053.9	44105.5	44161.1	44220.6
14.5	29/2	**44185.8**	**44241.3**	44300.9	44364.2	44055.7	44111.3	44170.8	44234.3
15.5	31/2	44189.5	**44249**	44312.5	44379.9	44058.1	44117.6	44181.1	44248.5
16.5	33/2	44194	44257.2	44324.9	44396.1	44061	44124.5	44192	44263.3
17.5	35/2	44198.9	44266.2	44337.6	44412.9	44064.5	44131.9	44203.3	44278.6
18.5	37/2	44204.6	44275.6	44351.2	44430.4	44068.5	44139.9	44215.3	44294.5
19.5	39/2	44210.8	44285.8	44365.4	44448.4	44073.1	44148.4	44227.7	44310.9
20.5	41/2	44217.5	44296.6	44379.9	44467	44078.2	44157.5	44240.8	44327.9

Energies in bold typeface are non-overlapping transitions.

Energies taken from LIFBASE.[146]

Appendix E - the measurement of laser beam diameters

The diameter of a laser beam can (in theory) be described by geometric optics at a distance greater than the so-called Rayleigh range from the focus. Within the Rayleigh range of the focus, the beam curves towards a beam waist of finite diameter, ω_0, as illustrated in Figure E.1.
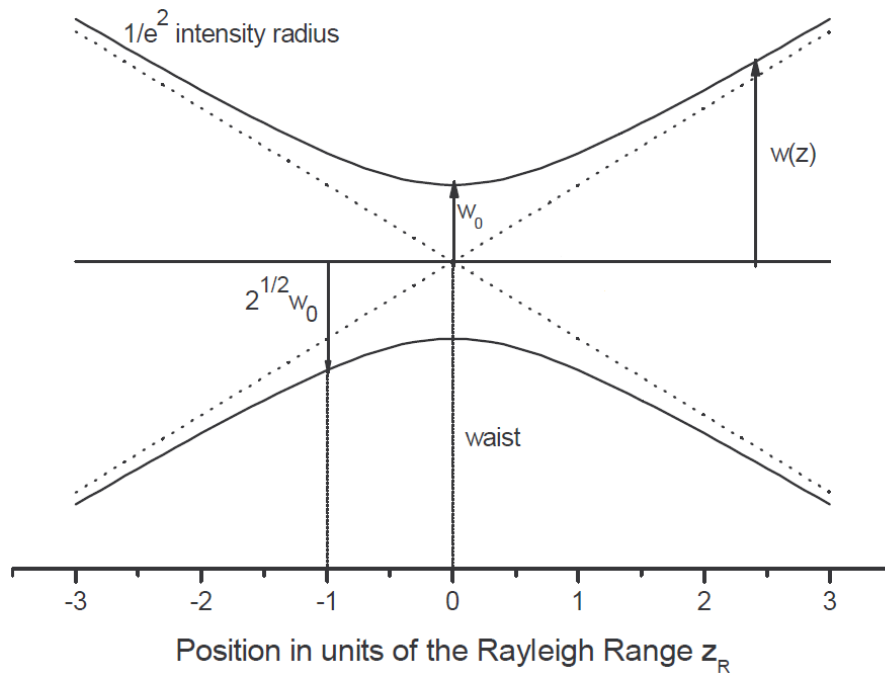
Figure E.1: a Gaussian beam in the region of its waist. The parameters are defined in the text.

The Rayleigh range, z_R, is given by

$$z_{R(ideal)} = \frac{\pi \omega_{0(ideal)}^2}{\lambda} \qquad \text{(Eq. E.1)}$$

Within the Rayleigh range, the beam diameter is given by

$$\omega_{(ideal)}(z) = \omega_{0(ideal)} \left[1 + \left(\frac{z\lambda}{\pi \omega_{0(ideal)}^2} \right)^2 \right]^{1/2} \qquad \text{(Eq. E.2)}$$

It is apparent from equation E.2 that the beam diameter within the Rayleigh range can only be accurately calculated if ω_0 is known; and whilst beam diameters at greater

141

distances from the focus may be accurately calculated by geometric optics, it is apparent from equation E.1 that without knowledge of ω_0 it is not possible to say precisely at what distance the transition from Gaussian to geometric optics occurs.

Further, equation E.2 is for an ideal beam. A real laser beam is described by

$$\omega(z) = \omega_0 \left[1 + \left(\frac{z\lambda M^2}{\pi\omega_0^2} \right)^2 \right]^{1/2}$$

where $M^2 > 1$, and is known as the beam quality factor. Its presence implies that a real laser beam converges and diverges faster than the ideal.[191,192]

Note, for a real beam, the Raleigh range is

$$z_R = \frac{\pi\omega_0^2}{\lambda M^2}$$

It is obvious from the above that without knowledge of ω_0 and M^2, beam diameter cannot be calculated and must be measured directly.

For the work described herein, laser beam diameters were measured using a razor blade and an energy meter. The razor blade was fixed to a lens mount (the vertical and horizontal translation of which could be controlled with micrometre screws) and placed in the path of the laser beam at the desired distance after the focussing lens, so that the razor blade could be gradually moved across the beam, from a position of not blocking the beam at all to a position in which the beam was totally blocked. A pyroelectric energy sensor was placed after the razor blade so that the power of the laser beam could be monitored and recorded throughout this process. The process is depicted in Figure E.2.[‡‡‡] A neutral density filter was used to attenuate the beam to avoid etching the razor blade. The FL2002 beam required additional attenuation: this was achieved by replacing the last dichroic mirror before the lens with a UV fused silica window, so that only a small portion of the beam was reflected.

[‡‡‡] Before settling on the razor blade method, an attempt was made to measure beam diameter by photographing the beam with a digital camera through several thicknesses of paper, and analysing the images pixel by pixel, but this approach proved unsuccessful due to the bleaching of the paper, and the fact that fluorescence tends to spread sideways through paper.
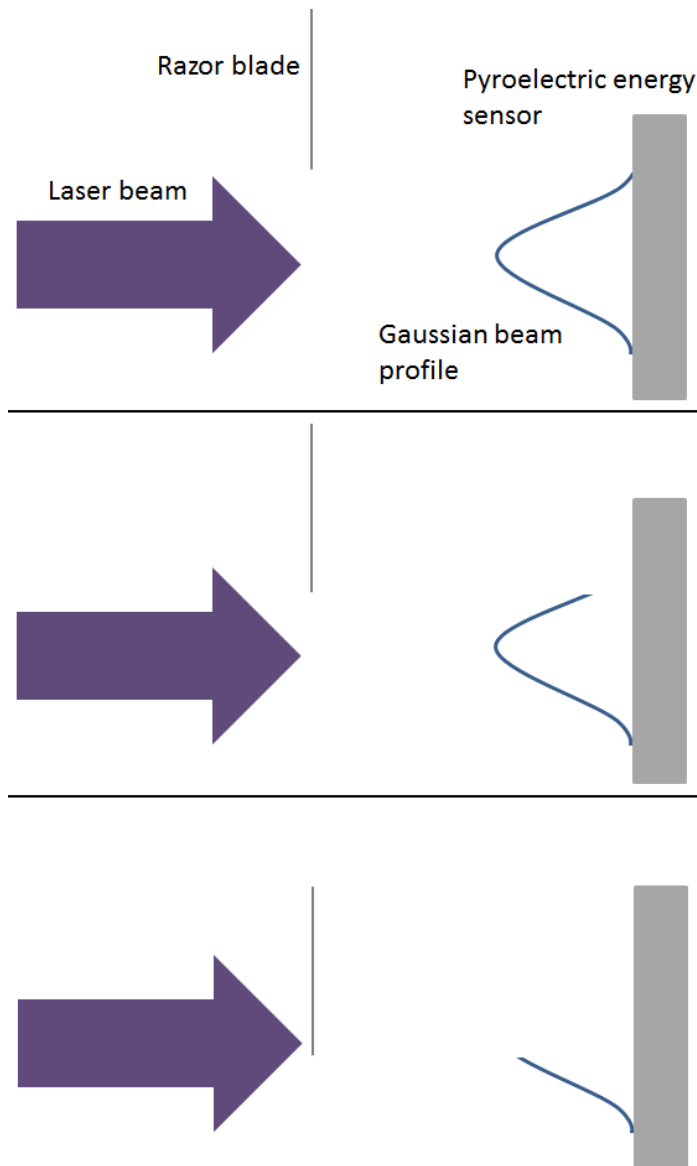
Figure E.2: the measurement of laser beam diameter using a razor. With each panel, the razor is moved further into the path of the beam, progressively blinding the pyroelectric energy sensor.

Following the subtraction of the residual pyroelectric sensor signal, the position/power data thus obtained were analysed using a short Mathematica script (appendix F) which fitted the data to a Gaussian profile and reported the beam width as its $1/e^2$ diameter. The vertical profile of the probe laser used for the acquisition of the $J = 1.5$ decay curve in chapter 4 is shown as an example in Figure E.3.
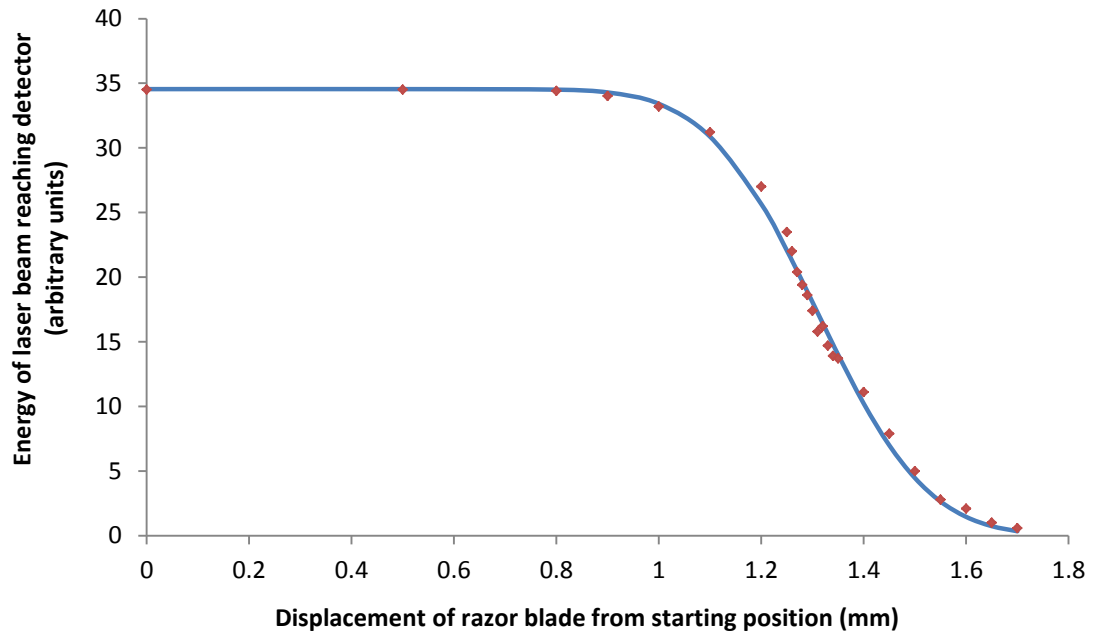
Figure E.3: profiling data for the vertical diameter of the probe laser used in chapter 4. The red diamonds are measured data points, and the blue line the Gaussian fit. The $1/e^2$ diameter of this beam is 0.68 mm.

Appendix F - Mathematica script for fitting laser beam diameter

```
knifedata = Import[(*insert file path*)]

profile = ptot / 2 * (1 - Erf[Sqrt[2] * (x - p) / w])
(*ptot is total power, w is beam RADIUS (not diameter), and p is an
  offset to account for the initial position of the razor blade, which
  will never be perfectly at the beam's edge.*)

fit = FindFit[knifedata, profile, {{ptot, (*insert starting value for fit*)},
    {w, (*insert starting value for fit*)},
    {p, (*insert starting value for fit*)}}, x]

dataplot = ListPlot[knifedata]

fitplot = Plot[profile /. fit, {x, 0,
    (*insert maximum displacement of razor blade here*)}]

Show[dataplot, fitplot, PlotRange → All]
```

Appendix G - parameters for the NO decay simulation in section 4.4.4

Molecular mass NO_2: 46

Molecular mass NO: 30

Source pressure: 6 bars (as measured)

Nozzle temperature: 318K (estimated)

Precursor concentration: 2%*

γ: 1.66**

Molecular beam speed: 380 ms^{-1} – as measured

Molecular beam FWHM: 51 ms^{-1} – as measured

Distance from nozzle to photodissociation region: 121 mm

Distance from skimmer to photodissociation region: 98.9 mm - known parameter of machine

Nozzle diameter: 0.2 mm

Nozzle orifice: 0.5 mm

Skimmer orifice: 1 mm

Precursor dissociation energy = 25128.6 cm^{-1}

β parameter of precursor dissociation = 1.5

Dissociation cross section = 6.8 x 10^{-19} cm^2

Dissociation quantum yield = 0.96

Dissociation laser intensity (pulse energy) = 4.1 mJ pulse^{-1}

Dissociation laser 1/e^2 horizontal diameter = 0.41 mm

Dissociation laser 1/e^2 vertical diameter = 0.68 mm

Dissociation laser polarisation = 90° with respect to experimental y axis

Dissociation laser wavelength = 387.518 nm

Internal energy of probed fragment = 119.8 cm^{-1}

Quantum yield of dissociation into probed fragment state = 0.007***

Probe laser $1/e^2$ horizontal diameter = 0.41 mm

Probe laser $1/e^2$ vertical diameter = 1.04 mm

* NO_2 exists in equilibrium with N_2O_4. The mean of the equilibrium constants for the dimerization at 318K given by Roscoe and Hind is 0.610, and the partial pressure of NO_2 is given by

$$P_{NO_2} = \frac{2P_{total}}{\left(1 + \left(4P_{total}/K_pP^0\right)^{1/2}\right) + 1}$$

where P_{total} is the sum of the partial pressures of NO_2 and N_2O_4 and P^0 is the pressure of the mixture.[193] The gas mixture used was 0.25 bars NO_2/ N_2O_4 in xenon, with a total pressure of 6 bars. The partial pressure of NO_2 in our mixture was calculated to be 0.12 bars, and the partial pressure of N_2O_4 was 0.13 bars. Hence, NO_2 formed 2% of the mixture.

** γ is a thermodynamic quantity used in modelling the expansion, being the ratio between the heat capacity at constant pressure and the heat capacity at constant volume. For an ideal gas,

$$\gamma = \frac{f + 2}{f}$$

where f is the number of degrees of freedom of the gas.

As a monoatomic gas, xenon has three translation degrees of freedom, so

$$\gamma_{Xe} = \frac{3 + 2}{3} = 1.67$$

NO_2 has three vibrational modes: bending (750 cm^{-1}), symmetric stretching (1318 cm^{-1}), and antisymmetric stretching (1618 cm^{-1}).[ref NIST web-book] If the nozzle temperature is 318 K, k_BT = 218 cm^{-1}, and $e^{-\frac{750}{218}} = 0.032$ – $i.e.$ only a very small proportion of the NO_2 population will have sufficient thermal energy to access the bending mode, and by extension almost none will be able to access either stretching mode. NO_2 effectively has 6 degrees of freedom: 3 translational, 3 rotational, and no vibrational, and

$$\gamma_{NO_2} = \frac{6 + 2}{6} = 1.33$$

Following a similar analysis, N_2O_4 has seven degrees of freedom, and

$$\gamma_{N_2O_4} = \frac{7 + 2}{7} = 1.29$$

γ for the overall mixture was approximated by the weighted sum of the values for each gas:

$$\gamma_{mixture} = 1.67 \times 0.958 + 1.33 \times 0.02 + 1.29 \times 0.022 = 1.65$$

*** This value was estimated, assuming a statistical product state distribution.[13]

Appendix H - magnetic trap simulation using Radia

Radia is a Wolfram Mathematica plug-in developed by the Insertion Devices group at the European Synchrotron Radiation Facility (ESRF) that allows 3D magnetostatic modelling for a variety of objects, including permanent magnets, using a boundary element method. It functions by drawing objects and applying material properties to these objects. The objects are then subdivided into smaller objects, with the magnetisation being treated as uniform within each object. The objects are allowed to interact, and their magnetisation determined by iteration.

Briefly, the code written for our simulations functioned as follows. It began by making a single magnet. It constructs the ring and cone sections of the magnet separately. Radia can form curved sections for wires, but not for permanent magnets, so the curved shape was approximated by making each part out of many small segments. The approximation is valid: varying the number of segments over an order of magnitude (*e.g.* radial division into 10 segments versus radial division into 100 segments) made ≈ 1% difference to the calculated field strength. Constructing the magnet from many small pieces also removes the need to apply subdivision at the end of the process.

Having constructed the magnet, the program groups it together into a "container" so that it can be treated as a single object (*i.e.* referred to as a single object by the code, not treated as a single object for the purposes of computation) and applies the magnetic material NdFeB to the magnet. The trap geometries are assembled by duplication of the first magnet, and rotation and translation of the duplicates.

The simulation code is given below. Radia's simple and user-friendly nature should be apparent.

Trap simulation code

```
(*Execute 1*)
<< Radia`
Radia Version: 4.29 is loaded
Radia is copyright ESRF, France.
Portions copyright Synchrotron SOLEIL, France.
Portions copyright Wolfram Research, Inc.


(*Execute 2*)
(*Manually enter here the number of azimuthal segments from
 which the ring and cone should be comprised.*)
nazs = 36;
(*Manually enter here the number of axial (vertical) segments
 from which the ring should be comprised.*)
naxrs = 1;
(*Manually enter here the number of radial segments from
 which the ring should be comprised.*)
nrrs = 1;
(*Manually enter here the number of axial segments from
 which the cone should be comprised.*)
naxcs = 11;
(*Manually enter here the number of radial segments from
 which the cone should be comprised.*)
nrcs = 1;


(*Execute 3*)
(*Clears all variables.*)
Clear[stepsize, s, maxi, raxoffset, rroffset, caxoffset,
  coffset, anrcs, croffset, maxq, ringfours, ringsegment,
  slopingfours, slopingsegment, objref, mag1, matrix, relaxation1,
  mag2, twotrap, pair2, pair3, strap];

(*"radUtiDelAll[]" is a Radia function that deletes all
 previously generated Radia reference numbers
 (the numbers used to refer to each segment).*)
radUtiDelAll[];
```

(*Note that the use of the word "offset" in the variables
 below is a relic of the way in which this code was first
 written. It's not now appropriate for any variable except
 "coffset",
but changing it throughout to something more accurate would
  be entirely too much effort. Note also that some of these
  variables are not strictly necessary - however,
I thought defining them explicitly rather than calculating
  their results within functions would make this code clearer.*)

(*Variable "stepsize" is the angle subtended by each polygon
 at the centre of the ring. Taken by "fours" and "slopingfours"
 as "n".*)

(*Variable "coffset" (cone offset) is the reduction in
 radius between the layers of the cone. It is identical
 to caxoffset because the slope of the cone is 45 degrees. I
 have renamed it in the hope doing so will make this code
 easier to understand.*)
coffset = caxoffset;

(*Variable "anrcs" is the number of radial segments in any
 given axial section of the cone. The number of radial
 segments must vary between axial levels so that the size
 (well, radial length) of radial segments remains roughly
 constant at all levels of the cone. If the number of
 radial segments were the same in each axial level,
the top layer would have very many very tiny segments.*)
anrcs[d_] := Ceiling[nrcs ((naxcs + 1 - d) / naxcs)];

(*Variable (or, I suppose more accurately, function)
 "croffset" is the radial length of the cone section. It
 varies from layer to layer,
since the radius decreases layer on layer going up the cone,
as does, but not in a perfectly concurrent fashion,
the number of radial segments. "a" is the axial iteration
 number.*)
croffset[a_] := (4 - (a - 0.5) coffset) / (anrcs[a]);

```
(*Variable "coffset" (cone offset) is the reduction in
 radius between the layers of the cone.  It is identical
 to caxoffset because the slope of the cone is 45 degrees.  I
 have renamed it in the hope doing so will make this code
 easier to understand.*)
coffset = caxoffset;

(*Variable "anrcs" is the number of radial segments in any
 given axial section of the cone.  The number of radial
 segments must vary between axial levels so that the size
 (well, radial length) of radial segments remains roughly
 constant at all levels of the cone.  If the number of
 radial segments were the same in each axial level,
the top layer would have very many very tiny segments.*)
anrcs[d_] := Ceiling[nrcs ((naxcs + 1 - d) / naxcs)];

(*Variable (or, I suppose more accurately, function)
 "croffset" is the radial length of the cone section.  It
 varies from layer to layer,
since the radius decreases layer on layer going up the cone,
as does, but not in a perfectly concurrent fashion,
the number of radial segments.  "a" is the axial iteration
 number.*)
croffset[a_] := (4 - (a - 0.5) coffset) / (anrcs[a]);

(*Variable (or, rather, list) "maxq" gives the number of
 radial segments in each axial level of the cone.  The
 radial iterator in the cone generating Do loop below takes
 maxq[[axial iterator]] as its maximum value.  It seems
 that this can't be done (at least, not by me) in the
 iterator bounds of the Do loop itself,
so this table is generated to provide the values.*)
maxq = Table[anrcs[c], {c, 1, naxcs, 1}];
```

```
(*Function "ringfours" generates the four coordinate pairs
 defining each polyhedron from initial angle theta
  (received from ringsegment as a product of the step size
    and the azimuthal iteration number), step size n,
and some multiple of the ring radial offset,
where the multiple is (based upon) the Do loop radial
 iteration number, passed to ringfours as "r".*)
ringfours[θ_, n_, r_] :=
   {{(6 - (r - 1) rroffset) Cos[θ Degree],
      (6 - (r - 1) rroffset) Sin[θ Degree]},
    {(6 - (r - 1) rroffset) Cos[(θ + n) Degree],
      (6 - (r - 1) rroffset) Sin[(θ + n) Degree]},
    {(6 - r rroffset) Cos[(θ + n) Degree],
      (6 - r rroffset) Sin[(θ + n) Degree]},
    {(6 - r rroffset) Cos[θ Degree], (6 - r rroffset) Sin[θ Degree]}};

(*Function "slopingsegment" generates a segment of the cone
 using the Radia function for generating polygons and the
 coordinates from "slopingfours".*)
slopingsegment[k_, x_, y_] :=
   radObjThckPgn[(2 + (x - 0.5) caxoffset - 9), caxoffset,
     slopingfours[(s k), s, y, x], {1, 0, 0}];




(*Uses "ringsegment" to create the ring at the base of the
 magnet.  i is azimuthal iteration.  q is radial iteration.  j
 is axial iteration.*)
Do[ringsegment[i, q, j], {i, 0, maxi, 1}, {q, 1, nrrs, 1},
 {j, 1, naxrs, 1}]
(*Uses "slopingsegment" to create the cone shaped upper
 part of the magnet.  i, q and j retain their significance,
but the order of q and j is reversed so that the upper
 bound of q can depend upon j
  (so that the number of radial segments can decrease going
    up the cone).*)
Do[slopingsegment[i, j, q], {i, 0, maxi, 1}, {j, 1, naxcs, 1},
 {q, 1, maxq[[j]], 1}](*},Print["Enter new value"]]
(*Displays the magnet!  Output now suppressed,
but left in in case it's ever useful.*)*)
Show[Graphics3D[Table[radObjDrw[label],
    {label, 1, ((maxi + 1) nrrs naxrs + (maxi + 1) Total[maxq])}],
   Axes → True, AxesLabel → {x, y, z}]];
```

153

```
(*Groups all the elements created above into one container,
applies the magnetic material NdFeB to the container,
and displays the magnet.*)
objref = Table[i, {i, 1, ((maxi + 1) nrrs naxrs + (maxi + 1) Total[maxq]),
     1}];
mag1 = radObjCnt[objref];
NdFeB = RadMatNdFeB[1.2];
radMatApl[mag1, NdFeB];
Show[Graphics3D[radObjDrw[mag1], Axes → False], Axes → False]
```


```
(*Necessary.*)
(*Creates and relaxes the matrix for mag1.  Displays the
 time taken for the relaxation process,
and the number of iterations involved.*)
matrix = radRlxPre[mag1];
relaxation1 =
 Flatten[
   Timing[radRlxAuto[matrix, 0.00000000000000000000001, 500]]]
Time1 = "seconds" relaxation1[[1]]
numberofiterations1 = relaxation1[[5]] "iterations"

(*Examines the variation of B along various lines through
 and about the magnet.*)
sectionxb = Table[radFld[mag1, "B", {x, 0, 0}], {x, -20, 20, 0.01}];
sectionxbm = Table[Norm[sectionxb[[i]]], {i, 1, Length[sectionxb]}];
ListPlot[sectionxbm, Axes → True, AxesLabel → {x, B (Tesla)},
   PlotRange → All];

Max[sectionxbm]
0.01 Position[sectionxbm, Max[sectionxbm]]

sectionxb2 = Table[radFld[mag1, "B", {x, 0, 0}], {x, -20, -3, 0.01}];
sectionxbm2 = Table[Norm[sectionxb2[[i]]],
   {i, 1, Length[sectionxb2]}];
```

154

```
Max[sectionxbm2]
0.01 Position[sectionxbm2, Max[sectionxbm2]]
Min[sectionxbm2]
0.01 Position[sectionxbm2, Min[sectionxbm2]]

sectionxb3 = Table[radFld[mag1, "B", {x, 0, 0}], {x, 2.5, 20, 0.01}];
sectionxbm3 = Table[Norm[sectionxb3[[i]]],
    {i, 1, Length[sectionxb3]}];
Max[sectionxbm3]
0.01 Position[sectionxbm3, Max[sectionxbm3]]
Min[sectionxbm3]
0.01 Position[sectionxbm3, Min[sectionxbm3]]

FindMinimum[{Norm[radFld[mag1, "B", {x, y, z}]], y == 0, z == 0},
  {{x, 0}, {y, 0}, {z, 0}}];

comp1 = Show[{g, h}, AxesLabel → {x, B (Tesla)}, PlotRange → All];

g2 = Plot[Norm[radFld[mag1, "B", {x, 0, 0}]], {x, -20, 20},
   AxesLabel → {"x (mm)", "B (Tesla)"}, AxesOrigin → {-20, 0},
   PlotRange → All]

h2 = Plot[Norm[radFld[mag1, "B", {x, 0, 0}]], {x, -20, 20},
   AxesLabel → {"x (mm)", "B (Tesla)"}, AxesOrigin → {-20, 0},
   PlotRange → All, PlotStyle → Red]

comp2 = Show[{g2, h2}, AxesLabel → {"x (mm)", "B (Tesla)"},
   AxesOrigin → {-20, 0}, PlotRange → All]


ContourPlot[Norm[Flatten[radFld[mag1, "b", {x, y, 0}], 1]],
 {x, -11, -2}, {y, -7, 7}, Frame → {True, True, False, False},
 FrameLabel → {"x (mm)", "y (mm)"},
 Contours → Table[i, {i, 0.05, 0.9, 0.05}], ContourShading → None]

ContourPlot[Norm[Flatten[radFld[mag1, "b", {x, y, 0}], 1]],
 {x, -11, -2}, {y, -7, 7}, Frame → {True, True, False, False},
 FrameLabel → {"x (mm)", "y (mm)"},
 Contours → Table[i, {i, 0.05, 0.9, 0.05}], ContourShading → None]

ContourPlot[Norm[Flatten[radFld[mag1, "b", {x, y, 0}], 1]],
 {x, -11, -2}, {y, -7, 7}, Frame → {True, True, False, False},
 FrameLabel → {"x (mm)", "y (mm)"},
 Contours → Table[i, {i, 0.05, 0.9, 0.05}], ContourShading → None]
```

(*Necessary. Edit the x coordinate to change the separation
 distance.*)
(*Constructs and displays a quadrupole trap.*)

```mathematica
mag2 = radObjDpl[mag1, FreeSym → False];
reflect = radTrfPlSym[{-11, 0, 0}, {1, 0, 0}];
radTrfOrnt[mag2, reflect];
Show[Graphics3D[{radObjDrw[mag1], radObjDrw[mag2]}]];
twotrap = radObjCnt[{mag1, mag2}];
Show[Graphics3D[radObjDrw[twotrap]], Axes → True,
  AxesLabel → {x, y, z}];
```

(*Probably necessary. Edit the coordinates to get the
 correct position.*)
(*Moves twotrap
 (so that can centre it on (0,0,0) after changing separation.*)

```mathematica
move = radTrfTrsl[{11, 0, 0}];
radTrfOrnt[twotrap, move];

Show[Graphics3D[radObjDrw[twotrap]], Axes → True,
 AxesLabel → {"z (mm)", "x (mm)", "y (mm)"},
 LabelStyle → Directive[Bold, Medium]]
```

(*Necessary.*)
(*Creates and relaxes the matrix for twotrap. Displays
 the time taken for the relaxation process,
(*Creates and relaxes the matrix for twotrap. Displays
 the time taken for the relaxation process,
and the number of iterations involved.*)

```mathematica
matrix = radRlxPre[twotrap];
relaxation1 =
 Flatten[
  Timing[radRlxAuto[matrix, 0.00000000000000000000001, 300]]]
Time1 = "seconds" relaxation1[[1]]
numberofiterations1 = relaxation1[[5]] "iterations"
```

```
(*This section plots B in Tesla for lines through the bores,
and along the y and z axes in the centre of the trap.*)
x8 = Plot[Norm[radFld[twotrap, "B", {x, 0, 0}]], {x, -20, 20},
   AxesLabel → {"x (mm)", "B (Tesla)"}, PlotRange → All,
   AxesOrigin → {-20, 0}]
y8 = Plot[Norm[radFld[twotrap, "B", {0, y, 0}]], {y, -20, 20},
   AxesLabel → {"y (mm)", "B (Tesla)"}, PlotRange → All,
   AxesOrigin → {-20, 0}]

x6 = Plot[Norm[radFld[twotrap, "B", {x, 0, 0}]], {x, -20, 20},
   AxesLabel → {"x (mm)", "B (Tesla)"}, PlotRange → All,
   PlotStyle → Red, AxesOrigin → {-20, 0}]
y6 = Plot[Norm[radFld[twotrap, "B", {0, y, 0}]], {y, -20, 20},
   AxesLabel → {"y (mm)", "B (Tesla)"}, PlotRange → All,
   PlotStyle → Red, AxesOrigin → {-20, 0}]

x4 = Plot[Norm[radFld[twotrap, "B", {x, 0, 0}]], {x, -0.01, 0.01},
   AxesLabel → {"x (mm)", "B (Tesla)"}, PlotRange → All,
   (*PlotStyle→Purple,*)AxesOrigin → {-0.01, 0}]
y4 = Plot[Norm[radFld[twotrap, "B", {0, y, 0}]], {y, -0.5, 0.5},
   AxesLabel → {"y (mm)", "B (Tesla)"}, PlotRange → All,
   (*PlotStyle→Purple,*)AxesOrigin → {-0.5, 0}]

Show[{x6, x8}, AxesLabel → {"x (mm)", "B (Tesla)"},
 AxesOrigin → {-20, 0}, PlotRange → All]

Show[{y6, y8}, AxesLabel → {"y (mm)", "B (Tesla)"},
 AxesOrigin → {-20, 0}, PlotRange → All]

(*This is left as a useful example of some styling options
 that it took me a while to work out.*)
(*Plot[Norm[radFld[twotrap,"B",{0,y,0}]],{y,-10,10},
 Axes→{False,True},AxesOrigin→{-10,0},
 AxesLabel→{"y (mm)","B (Tesla)"},PlotRange→All,
 AxesStyle→Directive[Thick],LabelStyle→Directive[Bold,Medium],
 PlotStyle→Directive[Thick]]*)

ContourPlot[Norm[Flatten[radFld[twotrap, "b", {x, y, 0}], 1]],
 {x, 1, 2}, {y, 1, 5}, Frame → {True, True, False, False},
 FrameLabel → {"x (mm)", "y (mm)"},
 Contours → Table[i, {i, 0.01, 1.2, 0.01}], ContourShading → None,
 AxesStyle → Directive[Thick], LabelStyle → Directive[Bold, Medium]]
```

```
DC2 = ContourPlot[Norm[Flatten[radFld[twotrap, "b", {x, y, 0}], 1]],
   {x, -2, 2}, {y, -5.6, 5.6}, Frame → {True, True, False, False},
   FrameLabel → {"z (mm)", "x (mm)"}, Contours → {0.26},
   ContourShading → None, ContourStyle → {Red, Thick},
   AxesStyle → Directive[Thick], LabelStyle → Directive[Bold, Medium]]

DC1 = ContourPlot[Norm[Flatten[radFld[twotrap, "b", {x, y, 0}], 1]],
   {x, -10, 10}, {y, -10, 10}, Frame → {True, True, False, False},
   FrameLabel → {"z (mm)", "x (mm)"},
   Contours → Table[i, {i, 0.01, 1.2, 0.05}], ContourShading → None,
   AxesStyle → Directive[Thick], LabelStyle → Directive[Bold, Medium]]

DC3 = Graphics[Polygon[{{-2, 2}, {-7, 2}, {-7, 3}, {-4, 6}, {-2, 6}}]];

DC4 =
   Graphics[Polygon[{{-2, -2}, {-7, -2}, {-7, -3}, {-4, -6},
      {-2, -6}}]];

DC5 = Graphics[Polygon[{{2, -2}, {7, -2}, {7, -3}, {4, -6}, {2, -6}}]];

DC6 = Graphics[Polygon[{{2, 2}, {7, 2}, {7, 3}, {4, 6}, {2, 6}}]];

Show[DC1, DC2, DC3, DC4, DC5, DC6]

EW = Table[radFld[mag1, "B", {x, 0, 0}], {x, -20, 20, 0.01}];
EW = Table[Norm[sectionxb[[i]]], {i, 1, Length[sectionxb]}];

EW1 = Table[radFld[twotrap, "b", {x, y, 0}], {x, -0, 10, 0.05},
   {y, 0, 10, 0.05}];

Norm[EW1[[1, 1]]]

Dimensions[EW1]

EW2 = Table[Norm[EW1[[i, j]]], {i, 1, (10 / 0.05)}, {j, 1, (10 / 0.05)}];

Export["quadrupolematrix3.xls", EW2]

EW = Norm[Flatten[radFld[twotrap, "b", {x, y, 0}], 1]], {x, -4, 4},
{y, -4, 4},

EW = Norm[Flatten[radFld[twotrap, "b", {x, y, 0}], 1]], {x, -4, 4},
{y, -4, 4},

separatrix3d =
   ListContourPlot3D[Table[Norm[radFld[twotrap, "b", {x, y, z}]],
      {x, -2, 2}, {y, -5.6, 5.6}, {z, -5.6, 5.6}], Contours → 0.25]
```

Appendix I - parameters for the NO decay simulation in section 5.2.5

Molecular mass NO_2: 46

Molecular mass NO: 30

Source pressure: 6 bars (as measured)

Nozzle temperature: 318K (estimated)

Precursor concentration: 2%

γ: 1.66

Molecular beam speed: 380 ms^{-1}

Molecular beam FWHM: 51 ms^{-1}

Distance from nozzle to photodissociation region: 60 mm

Distance from skimmer to photodissociation region: 37.9 mm

Nozzle diameter: 0.2 mm

Nozzle orifice: 0.5 mm

Skimmer orifice: 1 mm

Precursor dissociation energy = 25128.6 cm^{-1}

β parameter of precursor dissociation = 1.5

Dissociation cross section = 6.8 x 10^{-19} cm^2

Dissociation quantum yield = 0.96

Dissociation laser intensity (pulse energy) = 5 mJ pulse^{-1}

Dissociation laser 1/e^2 horizontal diameter = 3 mm

Dissociation laser 1/e^2 vertical diameter = 3 mm

Dissociation laser polarisation = 90° with respect to experimental *y* axis

Dissociation laser wavelength = 387.518 nm

Internal energy of probed fragment = 119.8 cm^{-1}

Quantum yield of dissociation into probed fragment state = 0.007

Probe laser 1/e^2 horizontal and vertical diameter = 3 mm

Appendix J - parameters for the SH decay simulation in section 6.5.1

Molecular mass H_2S: 34

Molecular mass SH: 32

Source pressure: 5 bars

Nozzle temperature: 313K

Precursor concentration: 83%

Precursor degrees of freedom: 6

Carrier degrees of freedom: 3

Molecular beam speed: 665 ms^{-1}

Molecular beam FWHM: 88 ms^{-1}

Distance from nozzle to photodissociation region: 121 mm

Distance from skimmer to photodissociation region: 98.9 mm

Nozzle diameter: 0.2 mm

Nozzle orifice: 0.5 mm

Skimmer orifice: 1 mm

Precursor dissociation energy = 31440.0 cm^{-1}

β parameter of precursor dissociation = -1

Dissociation cross section = 6.0 x 10^{-18} cm^2

Dissociation quantum yield = 1

Dissociation laser intensity (pulse energy) = 1.7 mJ pulse^{-1}

Dissociation laser 1/e^2 horizontal diameter = 1.387 mm

Dissociation laser 1/e^2 vertical diameter = 0.8742 mm

Dissociation laser polarisation = unpolarised

Dissociation laser wavelength = 193.3 nm

Internal energy of probed fragment = 36 cm^{-1}

Quantum yield of dissociation into probed fragment state = 0.105

Probe laser 1/e^2 horizontal diameter = 0.763 mm

Probe laser $1/e^2$ vertical diameter = 0.9313 mm

References

1.   Krems, R. V., Molecules near absolute zero and external field control of atomic and molecular dynamics. *International Reviews in Physical Chemistry* 2005, *24* (1), 99-118.

2.   Dulieu, O.; Raoult, M.; Tiemann, E., Cold Molecules: a chemistry kitchen for physicists? *Journal of Physics B-Atomic Molecular and Optical Physics* 2006, *39* (19), 11.

3.   Carr, L. D.; DeMille, D.; Krems, R. V.; Ye, J., Cold and ultracold molecules: science, technology and applications. *New Journal of Physics* 2009, *11*, 055049.

4.   Bell, M. T.; Softley, T. P., Ultracold molecules and ultracold chemistry. *Molecular Physics* 2009, *107* (2), 99-132.

5.   Dulieu, O.; Gabbanini, C., The formation and interactions of cold and ultracold molecules: new challenges for interdisciplinary physics. *Reports on Progress in Physics* 2009, *72* (8), 35.

6.   Quemener, G.; Julienne, P. S., Ultracold Molecules under Control! *Chemical Reviews* 2012, *112* (9), 4949-5011.

7.   Nesbitt, D. J., Toward State-to-State Dynamics in Ultracold Collisions: Lessons from High-Resolution Spectroscopy of Weakly Bound Molecular Complexes. *Chemical Reviews* 2012, *112* (9), 5062-5072.

8.   Chandler, D. W.; Strecker, K. E., The Quest for Cold and Ultracold Molecules. *Chemphyschem* 2009, *10* (5), 751-754.

9.   Metcalf, H. J.; Straten, P. v. d., *Laser Cooling and Trapping*. Springer: New York, 1999.

10.   Atkins, P.; de Paula, J., *Atkins' Physical Chemistry*. 7th ed.; Oxford University Press: Oxford, 2002.

11.   Weidemuller, M.; Zimmermann, C., *Cold Atoms and Molecules*. Wiley: 2009.

12.   Elioff, M. S.; Valentini, J. J.; Chandler, D. W., Subkelvin cooling NO molecules via "billiard-like" collisions with argon. *Science* 2003, *302* (5652), 1940-1943.

13.   Trottier, A.; Carty, D.; Wrede, E., Photostop: production of zero-velocity molecules by photodissociation in a molecular beam. *Molecular Physics* 2011, *109* (5), 725-733.

14.   Rangwala, S. A.; Junglen, T.; Rieger, T.; Pinkse, P. W. H.; Rempe, G., Continuous source of translationally cold dipolar molecules. *Physical Review A* 2003, *67* (4), 043406.

15.   Kay, J. J.; van de Meerakker, S. Y. T.; Strecker, K. E.; Chandler, D. W., Production of cold ND3 by kinematic cooling. *Faraday Discussions* 2009, *142*, 143-153.

16.   Hutzler, N. R.; Lu, H. I.; Doyle, J. M., The Buffer Gas Beam: An Intense, Cold, and Slow Source for Atoms and Molecules. *Chemical Reviews* 2012, *112* (9), 4803-4827.

17.   Atkins, P.; Friedman, R., *Molecular Quantum Mechanics*. 4th ed.; Oxford University Press: Oxford.

18.   Krems, R. V., Cold controlled chemistry. *Physical Chemistry Chemical Physics* 2008, *10* (28), 4079-4092.

19.   Narevicius, E.; Raizen, M. G., Toward Cold Chemistry with Magnetically Decelerated Supersonic Beams. *Chemical Reviews* 2012, *112* (9), 4879-4889.

20.   Sims, I. R.; Smith, I. W. M., Gas-Phase Reactions and Energy-Transfer at Very-Low Temperatures. *Annual Review of Physical Chemistry* 1995, *46*, 109-137.

21.   Ospelkaus, S.; Ni, K. K.; Wang, D.; de Miranda, M. H. G.; Neyenhuis, B.; Quemener, G.; Julienne, P. S.; Bohn, J. L.; Jin, D. S.; Ye, J., Quantum-State Controlled Chemical Reactions of Ultracold Potassium-Rubidium Molecules. *Science* 2010, *327* (5967), 853-857.

22.   Fernandez-Alonso, F.; Zare, R. N., Scattering resonances in the simplest chemical reaction. *Annual Review of Physical Chemistry* 2002, *53*, 67-99.

23.   Chefdeville, S.; Stoecklin, T.; Bergeat, A.; Hickson, K. M.; Naulin, C.; Costes, M., Appearance of Low Energy Resonances in CO-Para-H-2 Inelastic Collisions. *Physical Review Letters* 2012, *109* (2), 5.

24.   Henson, A. B.; Gersten, S.; Shagam, Y.; Narevicius, J.; Narevicius, E., Observation of Resonances in Penning Ionization Reactions at Sub-Kelvin Temperatures in Merged Beams. *Science* 2012, *338* (6104), 234-238.

25.   Willitsch, S.; Bell, M. T.; Gingell, A. D.; Procter, S. R.; Softley, T. P., Cold reactive collisions between laser-cooled ions and velocity-selected neutral molecules. *Physical Review Letters* 2008, *100* (4), 4.

26.   Levy, D. H., Laser Spectroscopy of Cold Gas-Phase Molecules. *Annual Review of Physical Chemistry* 1980, *31*, 197-225.

27.   Van De Meerakker, S. Y. T.; Bethlem, H. L.; Meijer, G., Taming molecular beams. *Nature Physics* 2008, *4* (8), 595-602.

28.   van Veldhoven, J.; Kupper, J.; Bethlem, H. L.; Sartakov, B.; van Roij, A. J. A.; Meijer, G., Decelerated molecular beams for high-resolution spectroscopy - The hyperfine structure of (ND3)-N-15. *European Physical Journal D* 2004, *31* (2), 337-349.

29.   Hudson, J. J.; Kara, D. M.; Smallman, I. J.; Sauer, B. E.; Tarbutt, M. R.; Hinds, E. A., Improved measurement of the shape of the electron. *Nature* 2011, *473* (7348), 493-U232.

30.   Kara, D. M.; Smallman, I. J.; Hudson, J. J.; Sauer, B. E.; Tarbutt, M. R.; Hinds, E. A., Measurement of the electron's electric dipole moment using YbF molecules: methods and data analysis. *New Journal of Physics* 2012, *14*, 32.

31.   Ketterle, W., When atoms behave as waves: Bose-Einstein condensation and the atom laser (Nobel lecture). *Chemphyschem* 2002, *3* (9), 736-+.

32.   Harris, J. G. E.; Michniak, R. A.; Nguyen, S. V.; Campbell, W. C.; Egorov, D.; Maxwell, S. E.; van Buuren, L. D.; Doyle, J. M., Deep superconducting magnetic traps for neutral atoms and molecules. *Review of Scientific Instruments* 2004, *75* (1), 17-23.

33.   Junglen, T.; Rieger, T.; Rangwala, S. A.; Pinkse, P. W. H.; Rempe, G., Slow ammonia molecules in an electrostatic quadrupole guide. *European Physical Journal D* 2004, *31* (2), 365-373.

34.   http://nobelprize.org/nobel_prizes/physics/laureates/1997/ (accessed 13th May).

35.   Weck, P. F.; Balakrishnan, N., Importance of long-range interactions in chemical reactions at cold and ultracold temperatures. *International Reviews in Physical Chemistry* 2006, *25* (3), 283-311.

36.   Ashkin, A., Acceleration and Trapping of Particles by Radiation Pressure. *Physical Review Letters* 1970, *24* (4), 156-&.

37.   Stenholm, S., The Semiclassical Theory of Laser Cooling. *Reviews of Modern Physics* 1986, *58* (3), 699-739.

38.   Chu, S., The manipulation of neutral particles. *Reviews of Modern Physics* 1998, *70* (3), 685-706.

39.   Cohen-Tannoudji, C. N., Manipulating atoms with photons. *Reviews of Modern Physics* 1998, *70* (3), 707-719.

40.   Phillips, W. D., Laser cooling and trapping of neutral atoms. *Reviews of Modern Physics* 1998, *70* (3), 721-741.

41.   deCarvalho, R.; Doyle, J. M.; Friedrich, B.; Guillet, T.; Kim, J.; Patterson, D.; Weinstein, J. D., Buffer-gas loaded magnetic traps for atoms and molecules: A primer. *European Physical Journal D* 1999, *7* (3), 289-309.

42.   Di Rosa, M. D., Laser-cooling molecules - Concept, candidates, and supporting hyperfine-resolved measurements of rotational lines in the A-X(0,0) band of CaH. *European Physical Journal D* 2004, *31* (2), 395-402; Stuhl, B. K.; Sawyer, B. C.; Wang, D.; Ye, J., Magneto-optical Trap for Polar Molecules. *Physical Review Letters* 2008, *101* (24), 243002.

43.   Marian, A.; Friedrich, B., Light Gives Molecules the Chills. *Chemphyschem* 2011, *12* (2), 259-261.

44.   Shuman, E. S.; Barry, J. F.; DeMille, D., Laser cooling of a diatomic molecule. *Nature* 2010, *467* (7317), 820-823.

45.   Barry, J. F.; Shuman, E. S.; Norrgard, E. B.; DeMille, D., Laser Radiation Pressure Slowing of a Molecular Beam. *Physical Review Letters* 2012, *108* (10), 5.

46.   Nguyen, J. H. V.; Odom, B., Prospects for Doppler cooling of three-electronic-level molecules. *Physical Review A* 2011, *83* (5), 7.

47.   Chieda, M. A.; Eyler, E. E., Prospects for rapid deceleration of small molecules by optical bichromatic forces. *Physical Review A* 2011, *84* (6), 10.

48.   Sanna, G.; Tomasesetti, G., *Introduction to Molecular Beams Gas Dynamics*. Imperial College Press: 2005.

49.   Friedrich, B.; Doylei, J. M., Why are Cold Molecules so Hot? *Chemphyschem* 2009, *10* (4), 604-623.

50. Takase, K.; Rahn, L. A.; Chandler, D. W.; Strecker, K. E., The kinematic cooling of molecules with laser-cooled atoms. *New Journal of Physics* 2009, *11*, 10.

51. Elioff, M. S.; Valentini, J. J.; Chandler, D. W., Formation of NO(j '=7.5) molecules with sub-kelvin translational energy via molecular beam collisions with argon using the technique of molecular cooling by inelastic collisional energy-transfer. *European Physical Journal D* 2004, *31* (2), 385-393.

52. Strecker, K. E.; Chandler, D. W., Kinematic production of isolated millikelvin molecules. *Physical Review A* 2008, *78* (6), 063406.

53. Liu, N. N.; Loesch, H., Kinematic Slowing and Electrostatic Guiding of KBr Molecules Formed by the Reactive Collision Process: K + HBr -> KBr + H. *Journal of Physical Chemistry A* 2010, *114* (9), 3247-3255.

54. Narevicius, E.; Libson, A.; Riedel, M. F.; Parthey, C. G.; Chavez, I.; Even, U.; Raizen, M. G., Coherent slowing of a supersonic beam with an atomic paddle. *Physical Review Letters* 2007, *98* (10), 103201.

55. Gupta, M.; Herschbach, D., A mechanical means to produce intense beams of slow molecules. *Journal of Physical Chemistry A* 1999, *103* (50), 10670-10673.

56. Sheffield, L.; Hickey, M. S.; Krasovitskiy, V.; Rathnayaka, K. D. D.; Lyuksyutov, I. F.; Herschbach, D. R., Pulsed rotating supersonic source for merged molecular beams. *Review of Scientific Instruments* 2012, *83* (6), 9.

57. Gupta, M.; Herschbach, D., Slowing and speeding molecular beams by means of a rapidly rotating source. *Journal of Physical Chemistry A* 2001, *105* (9), 1626-1637.

58. Strebel, M.; Stienkemeier, F.; Mudrich, M., Improved setup for producing slow beams of cold molecules using a rotating nozzle. *Physical Review A* 2010, *81* (3), 12.

59. Vanhaecke, N.; Meier, U.; Andrist, M.; Meier, B. H.; Merkt, F., Multistage Zeeman deceleration of hydrogen atoms. *Physical Review A* 2007, *75* (3), 031402.

60. Narevicius, E.; Libson, A.; Parthey, C. G.; Chavez, I.; Narevicius, J.; Even, U.; Raizen, M. G., Stopping supersonic oxygen with a series of pulsed electromagnetic coils: A molecular coilgun. *Physical Review A* 2008, *77* (5), 051401.

61. Hogan, S. D.; Sprecher, D.; Andrist, M.; Vanhaecke, N.; Merkt, F., Zeeman deceleration of H and D. *Physical Review A* 2007, *76* (2), 11.

62. Hogan, S. D.; Wiederkehr, A. W.; Andrist, M.; Schmutz, H.; Merkt, F., Slow beams of atomic hydrogen by multistage Zeeman deceleration. *Journal of Physics B-Atomic Molecular and Optical Physics* 2008, *41* (8), 081005.

63. Trimeche, A.; Bera, M. N.; Cromieres, J. P.; Robert, J.; Vanhaecke, N., Trapping of a supersonic beam in a traveling magnetic wave. *European Physical Journal D* 2011, *65* (1-2), 263-271.

64. Narevicius, E.; Parthey, C. G.; Libson, A.; Narevicius, J.; Chavez, I.; Even, U.; Raizen, M. G., An atomic coilgun: using pulsed magnetic fields to slow a supersonic beam. *New Journal of Physics* 2007, *9*, 358.

65.   Lavert-Ofir, E.; Gersten, S.; Henson, A. B.; Shani, I.; David, L.; Narevicius, J.; Narevicius, E., A moving magnetic trap decelerator: a new source of cold atoms and molecules. *New Journal of Physics* 2011, *13*, 8.

66.   Narevicius, E.; Libson, A.; Parthey, C. G.; Chavez, I.; Narevicius, J.; Even, U.; Raizen, M. G., Stopping supersonic beams with a series of pulsed electromagnetic coils: An atomic coilgun. *Physical Review Letters* 2008, *100* (9), 093003.

67.   Hogan, S. D.; Wiederkehr, A. W.; Schmutz, H.; Merkt, F., Magnetic trapping of hydrogen after multistage Zeeman deceleration. *Physical Review Letters* 2008, *101* (14), 143001.

68.   Bethlem, H. L.; Berden, G.; van Roij, A. J. A.; Crompvoets, F. M. H.; Meijer, G., Trapping neutral molecules in a traveling potential well. *Physical Review Letters* 2000, *84* (25), 5744-5747; Bethlem, H. L.; Berden, G.; Meijer, G., Decelerating neutral dipolar molecules. *Physical Review Letters* 1999, *83* (8), 1558-1561.

69.   Bethlem, H. Katholieke Universiteit Nijmegen, 2002.

70.   van de Meerakker, S. Y. T.; Bethlem, H. L.; Vanhaecke, N.; Meijer, G., Manipulation and Control of Molecular Beams. *Chemical Reviews* 2012, *112* (9), 4828-4878.

71.   Yamakita, Y.; Procter, S. R.; Goodgame, A. L.; Softley, T. P.; Merkt, F., Deflection and deceleration of hydrogen Rydberg molecules in inhomogeneous electric fields. *Journal of Chemical Physics* 2004, *121* (3), 1419-1431.

72.   Hogan, S. D.; Seiler, C.; Merkt, F., Rydberg-State-Enabled Deceleration and Trapping of Cold Molecules. *Physical Review Letters* 2009, *103* (12), 4.

73.   Seiler, C.; Hogan, S. D.; Merkt, F., Trapping cold molecular hydrogen. *Physical Chemistry Chemical Physics* 2011, *13* (42), 19000-19012.

74.   Vliegen, E.; Merkt, F., Stark deceleration of hydrogen atoms. *Journal of Physics B-Atomic Molecular and Optical Physics* 2006, *39* (11), L241-L247.

75.   Vliegen, E.; Worner, H. J.; Softley, T. P.; Merkt, F., Nonhydrogenic effects in the deceleration of Rydberg atoms in inhomogeneous electric fields. *Physical Review Letters* 2004, *92* (3), 033005.

76.   Fulton, R.; Bishop, A. I.; Barker, P. F., Optical Stark decelerator for molecules. *Physical Review Letters* 2004, *93* (24), 243004.

77.   Fulton, R.; Bishop, A. I.; Shneider, M. N.; Barker, P. F., Controlling the motion of coldmolecules with deep periodic optical potentials. *Nature Physics* 2006, *2* (7), 465-468.

78.   Fulton, R.; Bishop, A. I.; Shneider, M. N.; Barker, P. F., Optical Stark deceleration of nitric oxide and benzene molecules using optical lattices. *Journal of Physics B-Atomic Molecular and Optical Physics* 2006, *39* (19), S1097-S1109.

79.   Ramirez-Serrano, J.; Strecker, K. E.; Chandler, D. W., Modification of the velocity distribution of H-2 molecules in a supersonic beam by intense pulsed optical gradients. *Physical Chemistry Chemical Physics* 2006, *8* (25), 2985-2989.

80.   Doyle, J. M.; Friedrich, B.; Kim, J.; Patterson, D., Buffer-Gas Loading of Atoms and Molecules into a Magnetic Trap. *Physical Review A* 1995, *52* (4), R2515-R2518.

81.	Bakker, J. M.; Stoll, M.; Weise, D. R.; Vogelsang, O.; Meijer, G.; Peters, A., Magnetic trapping of buffer-gas-cooled chromium atoms and prospects for the extension to paramagnetic molecules. *Journal of Physics B-Atomic Molecular and Optical Physics* 2006, *39* (19), S1111-S1123.

82.	Kim, J. H.; Friedrich, B.; Katz, D. P.; Patterson, D.; Weinstein, J. D.; DeCarvalho, R.; Doyle, J. M., Buffer-gas loading and magnetic trapping of atomic europium. *Physical Review Letters* 1997, *78* (19), 3665-3668.

83.	Weinstein, J. D.; deCarvalho, R.; Kim, J.; Patterson, D.; Friedrich, B.; Doyle, J. M., Magnetic trapping of atomic chromium. *Physical Review A* 1998, *57* (5), R3173-R3175.

84.	Hancox, C. I.; Hummon, M. T.; Nguyen, S. V.; Doyle, J. M., Evaporative cooling of magnetically trapped atomic molybdenum. *Physical Review A* 2005, *71* (3), 031402.

85.	Hancox, C. I.; Doret, S. C.; Hummon, M. T.; Luo, L. J.; Doyle, J. M., Magnetic trapping of rare-earth atoms at millikelvin temperatures. *Nature* 2004, *431* (7006), 281-284.

86.	Weinstein, J. D.; deCarvalho, R.; Guillet, T.; Friedrich, B.; Doyle, J. M., Magnetic trapping of calcium monohydride molecules at millikelvin temperatures. *Nature* 1998, *395* (6698), 148-150.

87.	Campbell, W. C.; Tsikata, E.; Lu, H.-I.; van Buuren, L. D.; Doyle, J. M., Magnetic trapping and Zeeman relaxation of NH (X3Sigma-). *Phys Rev Lett* 2007, *98* (21), 213001.

88.	Stoll, M.; Bakker, J. M.; Steimle, T. C.; Meijer, G.; Peters, A., Cryogenic buffer-gas loading and magnetic trapping of CrH and MnH molecules. *Physical Review A* 2008, *78* (3), 032707.

89.	Weinstein, J. D.; deCarvalho, R.; Amar, K.; Boca, A.; Odom, B. C.; Friedrich, B.; Doyle, J. M., Spectroscopy of buffer-gas cooled vanadium monoxide in a magnetic trapping field. *Journal of Chemical Physics* 1998, *109* (7), 2656-2661.

90.	Egorov, D.; Weinstein, J. D.; Patterson, D.; Friedrich, B.; Doyle, J. M., Spectroscopy of laser-ablated buffer-gas-cooled PbO at 4 K and the prospects for measuring the electric dipole moment of the electron. *Physical Review A* 2001, *63* (3), 030501.

91.	Maussang, K.; Egorov, D.; Helton, J. S.; Nguyen, S. V.; Doyle, J. M., Zeeman relaxation of CaF in low-temperature collisions with helium. *Phys Rev Lett* 2005, *94* (12), 123002.

92.	Rieger, T.; Junglen, T.; Rangwala, S. A.; Rempe, G.; Pinkse, P. W. H.; Bulthuis, J., Water vapor at a translational temperature of 1 K. *Physical Review A* 2006, *73* (6), 4.

93.	Bell, M. T.; Gingell, A. D.; Oldham, J. M.; Softley, T. P.; Willitsch, S., Ion-molecule chemistry at very low temperatures: cold chemical reactions between Coulomb-crystallized ions and velocity-selected neutral molecules. *Faraday Discussions* 2009, *142*, 73-91.

94.	Tsuji, H.; Sekiguchi, T.; Mori, T.; Momose, T.; Kanamori, H., Stark velocity filter for nonlinear polar molecules. *Journal of Physics B-Atomic Molecular and Optical Physics* 2010, *43* (9), 8.

95.   Jones, K. M.; Tiesinga, E.; Lett, P. D.; Julienne, P. S., Ultracold photoassociation spectroscopy: Long-range molecules and atomic scattering. *Reviews of Modern Physics* 2006, *78* (2), 483-535.

96.   Ni, K. K.; Ospelkaus, S.; de Miranda, M. H. G.; Pe'er, A.; Neyenhuis, B.; Zirbel, J. J.; Kotochigova, S.; Julienne, P. S.; Jin, D. S.; Ye, J., A high phase-space-density gas of polar molecules. *Science* 2008, *322* (5899), 231-235.

97.   Viteau, M.; Chotia, A.; Allegrini, M.; Bouloufa, N.; Dulieu, O.; Comparat, D.; Pillet, P., Optical pumping and vibrational cooling of molecules. *Science* 2008, *321* (5886), 232-234.

98.   Ulmanis, J.; Deiglmayr, J.; Repp, M.; Wester, R.; Weidemuller, M., Ultracold Molecules Formed by Photoassociation: Heteronuclear Dimers, Inelastic Collisions, and Interactions with Ultrashort Laser Pulses. *Chemical Reviews* 2012, *112* (9), 4890-4927.

99.   Kleppner, D., Professor Feshbach and his resonance. *Physics Today* 2004, *57* (8), 12-13.

100.   Danzl, J. G.; Haller, E.; Gustavsson, M.; Mark, M. J.; Hart, R.; Bouloufa, N.; Dulieu, O.; Ritsch, H.; Nagerl, H. C., Quantum gas of deeply bound ground state molecules. *Science* 2008, *321* (5892), 1062-1066.

101.   Zeppenfeld, M.; Englert, B. G. U.; Glockner, R.; Prehn, A.; Mielenz, M.; Sommer, C.; van Buuren, L. D.; Motsch, M.; Rempe, G., Sisyphus cooling of electrically trapped polyatomic molecules. *Nature* 2012, *491* (7425), 570-573.

102.   Barry, J. F.; DeMille, D., LOW-TEMPERATURE PHYSICS A chilling effect for molecules. *Nature* 2012, *491* (7425), 539-540.

103.   Chan, H. W.; Black, A. T.; Vuletic, V., Observation of collective-emission-induced cooling of atoms in an optical cavity. *Physical Review Letters* 2003, *90* (6), 4.

104.   Vuletic, V.; Chu, S., Laser cooling of atoms, ions, or molecules by coherent scattering. *Physical Review Letters* 2000, *84* (17), 3787-3790.

105.   Wieman, C. E.; Pritchard, D. E.; Wineland, D. J., Atom cooling, trapping, and quantum manipulation. *Reviews of Modern Physics* 1999, *71* (2), S253-S262.

106.   Julienne, P. S., LOW-TEMPERATURE PHYSICS Cool molecules. *Nature* 2012, *492* (7429), 364-365.

107.   Stuhl, B. K.; Hummon, M. T.; Yeo, M.; Quemener, G.; Bohn, J. L.; Ye, J., Evaporative cooling of the dipolar hydroxyl radical. *Nature* 2012, *492* (7429), 396-+.

108.   Bernath, P. F., *Spectra of Atoms and Molecules*. Oxford University Press: 2005.

109.   http://www.atmosphere.mpg.de/enid/2295.

110.   Hollas, J. M., *Modern Spectroscopy*. 4th ed.; John Wiley and Sons Ltd: Chichester, 2004.

111.   http://arxiv.org/abs/physics/0202029v1.

112.   Ashfold, M. N. R.; Howe, J. D., Multiphoton Spectroscopy of Molecular-Species. *Annual Review of Physical Chemistry* 1994, *45*, 57-82.

113.   Schmidt, P.; Schafer, R., *Methods in Physical Chemistry*. Wiley-VCH: Weinheim, 2012; Vol. 1.

114.   Parker, D. H.; Eppink, A. T. J. B., Velocity map imaging. In *Imaging in Molecular Dynamics*, Whitaker, B. J., Ed. Cambridge University Press: Cambridge, 2003.

115.   Houston, P. L., Charged particle imaging: an historical perspective. In *Imaging in Molecular Dynamics*, Whitaker, B. J., Ed. Cambridge University Press: Cambridge, 2003.

116.   Demtroder, W., *Laser Spectroscopy*. 2nd ed.; Springer: 1998.

117.   Telle, H. H.; Urena, A. G.; Donovan, R. J., *Laser Chemistry: Spectroscopy, Dynamics and Applications*. Wiley: 2007.

118.   Schinke, R., *Photodissociation Dynamics*. Cambridge University Press: Cambridge, 1993.

119.   Sato, H., Photodissociation of simple molecules in the gas phase. *Chemical Reviews* 2001, *101* (9), 2687-2725.

120.   Lewars, E. G., *Computational Chemistry: Introduction to the theory and applications of molecular quantum mechanics*. Springer: 2011.

121.   Zare, R. N., *Molecular Photochemistry* 1972, *4*, 1.

122.   Matthews, S. J.; Willitsch, S.; Softley, T. P., Fully state-selected VMI study of the near-threshold photodissociation of NO2: variation of the angular anisotropy parameter. *Physical Chemistry Chemical Physics* 2007, *9* (42), 5656-5663.

123.   Zhao, B. S.; Shin, S. E.; Park, S. T.; Sun, X.; Chung, D. S., Slow Molecules Produced by Photodissociation. *Journal of the Physical Society of Japan* 2009, *78* (9), 5.

124.   Doherty, W. G.; Bell, M. T.; Softley, T. P.; Rowland, A.; Wrede, E.; Carty, D., Production of cold bromine atoms at zero mean velocity by photodissociation. *Physical Chemistry Chemical Physics* 2011, *13* (18), 8441-8447.

125.   Sawyer, B. C.; Stuhl, B. K.; Yeo, M.; Tscherbul, T. V.; Hummon, M. T.; Xia, Y.; Kios, J.; Patterson, D.; Doyle, J. M.; Ye, J., Cold heteromolecular dipolar collisions. *Physical Chemistry Chemical Physics* 2011, *13* (42), 19059-19066.

126.   Flynn, E. L. Reactive Scattering of Rydberg Atoms. Durham, 2008.

127.   Townsend, D.; Minitti, M. P.; Suits, A. G., Direct current slice imaging. *Review of Scientific Instruments* 2003, *74* (4), 2530-2539.

128.   Wrede, E.; Laubach, S.; Schulenburg, S.; Brown, A.; Wouters, E. R.; Orr-Ewing, A. J.; Ashfold, M. N. R., Continuum state spectroscopy: A high resolution ion imaging study of IBr photolysis in the wavelength range 440-685 nm. *Journal of Chemical Physics* 2001, *114* (6), 2629-2646.

129.   Willis, O. R. Enhancement and Optimisation of the Photostop Experiment to Produce Ultra-Cold Molecules. University of Durham, 2009.

130.   Jost, R.; Nygard, J.; Pasinski, A.; Delon, A., The photodissociation threshold of NO2: Precise determination of its energy and density of states. *Journal of Chemical Physics* 1996, *105* (3), 1287-1290.

131.   Wilkinson, I.; Whitaker, B. J., Photodissociation of NO(2) in the (2)(2)B(2) state: A slice imaging study and reinterpretation of previous results. *Journal of Chemical Physics* 2008, *129* (15), 15.

132.   Vandaele, A. C.; Hermans, C.; Simon, P. C.; Carleer, M.; Colin, R.; Fally, S.; Merienne, M. F.; Jenouvrier, A.; Coquart, B., Measurements of the NO2 absorption cross-section from 42 000 cm(-1) to 10 000 cm(-1) (238-1000 nm) at 220 K and 294 K. *Journal of Quantitative Spectroscopy & Radiative Transfer* 1998, *59* (3-5), 171-184.

133.   Wilkinson, I.; de Miranda, M. P.; Whitaker, B. J., Photodissociation of NO(2) in the (2) (2)B(2) state: The O((1)D(2)) dissociation channel. *Journal of Chemical Physics* 2009, *131* (5), 19.

134.   http://gow.epsrc.ac.uk/NGBOViewGrant.aspx?GrantRef=EP/I012044/1.

135.   Lent, P. D. Durham, 2010.

136.   Herzberg, G., *Molecular Spectra and Molecular Structure*. 2nd ed.; D. Van Nostrand Company Inc: Princeton, Vol. I.

137.   Rae, R. The Production and Trapping of Ultracold Molecules Produced via the Photostop Method. University of Durham, 2009.

138.   Sawyer, B. C.; Lev, B. L.; Hudson, E. R.; Stuhl, B. K.; Lara, M.; Bohn, J. L.; Ye, J., Magnetoelectrostatic trapping of ground state OH molecules. *Physical Review Letters* 2007, *98* (25), 4.

139.   Sawyer, B. C.; Stuhl, B. K.; Wang, D.; Yeo, M.; Ye, J., Molecular Beam Collisions with a Magnetically Trapped Target. *Physical Review Letters* 2008, *101* (20), 4.

140.   Ory, H. A.; Gittleman, A. P.; Maddox, J. P., Franck-Condon Factors for NO Beta + Gamma Band Systems. *Astrophysical Journal* 1964, *139* (1), 346-&.

141.   Luque, J.; Crosley, D. R., Transition probabilities and electronic transition moments of the A (2)Sigma(+)-X (2)Pi and D (2)Sigma(+)-X (2)Pi systems of nitric oxide. *Journal of Chemical Physics* 1999, *111* (16), 7405-7415.

142.   Ionov, S. I.; Brucker, G. A.; Jaques, C.; Chen, Y.; Wittig, C., Probing the NO2- NO+O Transition-State via Time-Resolved Unimolecular Decomposition. *Journal of Chemical Physics* 1993, *99* (5), 3420-3435.

143.   Luque, J.; Crosley, D. R., Radiative and predissociative rates for NO A(2)Sigma(+)v '=0-5 and D-2 Sigma(+)v '=0-3. *Journal of Chemical Physics* 2000, *112* (21), 9411-9416.

144.   Mayor, E.; Velasco, A. M.; Martin, I., Theoretical study of the rotational structure of the gamma(0,0) band of NO. Molecular quantum defect orbital (MQDO) calculations of Einstein absorption coefficients and line-integrated rotational cross sections. *Chemical Physics Letters* 2007, *436* (1-3), 268-275.

145.   http://sales.hamamatsu.com/assets/applications/ETD/pmt_handbook_complete.pdf. (accessed 20.10.12).

146.   Luque, J.; Crosley, D. R. *LIFBASE: Database and Spectral Simulation Program*, 1.5.

147.	Hunter, M.; Reid, S. A.; Robie, D. C.; Reisler, H., The Monoenergetic Unimolecular Reaction of Expansion-Cooled NO2 - NO Product State Distributions at Excess Energies 0-3000 cm-1. *Journal of Chemical Physics* 1993, *99* (2), 1093-1108.

148.	Weiner, B. R.; Levene, H. B.; Valentini, J. J.; Baronavski, A. P., Ultraviolet Photodissociation Dynamics of H2S and D2S. *Journal of Chemical Physics* 1989, *90* (3), 1403-1414.

149.	Xie, X. X.; Schnieder, L.; Wallmeier, H.; Boettner, R.; Welge, K. H.; Ashfold, M. N. R., Photodissociation Dynamics of H2S(D2S) Following Excitation Within Its 1st Absorption Continuum. *Journal of Chemical Physics* 1990, *92* (3), 1608-1616.

150.	Wilson, S. H. S.; Howe, J. D.; Ashfold, M. N. R., On the near ultraviolet photodissociation of hydrogen sulphide. *Molecular Physics* 1996, *88* (3), 841-858.

151.	Milan, J. B.; Buma, W. J.; deLange, C. A., Two-photon resonance enhanced multiphoton ionization photoelectron spectroscopy of the SH (SD) radical below and above the lowest ionization threshold. *Journal of Chemical Physics* 1996, *105* (16), 6688-6712.

152.	Wu, C. Y. R.; Chen, F. Z., Temperature-dependent photoabsorption cross sections of H2S in the 1600-2600 A region. *Journal of Quantitative Spectroscopy & Radiative Transfer* 1998, *60* (1), 17-23.

153.	Miller, D. R., Free Jet Sources. In *Atomic and Molecular Beam Methods*, Scoles, G., Ed. Oxford University Press: Oxford, 1988; Vol. I.

154.	http://webbook.nist.gov/cgi/cbook.cgi?ID=C7783064&Units=SI&Mask=4#Thermo-Phase. (accessed 9.11).

155.	Steadman, J.; Cole, S. K.; Baer, T., Visible and Ultraviolet Resonance Enhance Multiphoton Ionization Photoelectron-Spectroscopy of H2S in the One-Photon Wavelength Region 143-158 nm. *Journal of Chemical Physics* 1988, *89* (9), 5498-5506.

156.	http://webbook.nist.gov/cgi/cbook.cgi?ID=C7783064&Units=SI&Mask=20#Ion-Energetics. (accessed 25.11.12).

157.	Walters, E. A.; Blais, N. C., Molecular-Beam Photoionization and Fragmentation of D2S, (H2S)2, (D2S)2, and H2S.H2O. *Journal of Chemical Physics* 1984, *80* (7), 3501-3502.

158.	Sodupe, M.; Oliva, A.; Bertran, J., Theoretical-Study of the Ionization of the H2S-H2S, PH3-H2S, and CLH-H2S Hydrogen-Bonded Molecules. *Journal of the American Chemical Society* 1995, *117* (32), 8416-8421.

159.	Continetti, R. E.; Balko, B. A.; Lee, Y. T., Photodissociation of H2S and the HS Radical at 193.3 nm. *Chemical Physics Letters* 1991, *182* (5), 400-405.

160.	Friedl, R. R.; Brune, W. H.; Anderson, J. G., Radiative and Predissociative Lifetimes of the v'=0 Level of the A2-Sigma+ State of SH and SD from Chemical and Spectroscopic Studies. *Journal of Chemical Physics* 1983, *79* (9), 4227-4236.

161.	http://cccbdb.nist.gov/. (accessed 4th December).

162.   Bertsche, B.; Osterwalder, A., State-selective detection of velocity-filtered ND3 molecules. *Physical Review A* 2010, *82* (3), 8.

163.   Lipciuc, M. L.; Janssen, M. H. M., Slice imaging of quantum state-to-state photodissociation dynamics of OCS. *Physical Chemistry Chemical Physics* 2006, *8* (25), 3007-3016.

164.   Wu, C. Y. R.; Chen, F. Z.; Judge, D. L., Temperature-dependent photoabsorption cross sections of OCS in the 2000-2600 angstrom region. *Journal of Quantitative Spectroscopy & Radiative Transfer* 1999, *61* (2), 265-271.

165.   El Helou, Z.; Churassy, S.; Wannous, G.; Bacis, R.; Boursey, E., Absolute cross sections of ozone at atmospheric temperatures for the Wulf and the Chappuis bands. *Journal of Chemical Physics* 2005, *122* (24), 9.

166.   Bai, Y. Y.; Segal, G. A.; Reisler, H., Ab Initio Calculations of Dissociative Electronic States of ClCN - Implications to the Photodissociation Dynamics of the Cyanogen Halides. *Journal of Chemical Physics* 1991, *94* (1), 331-340.

167.   Felps, W. S.; Rupnik, K.; McGlynn, S. P., Electronic Spectroscopy of the Cyanogen Halides. *Journal of Physical Chemistry* 1991, *95* (2), 639-656.

168.   Russell, J. A.; McLaren, I. A.; Jackson, W. M.; Halpern, J. B., Photolysis of BrCN between 193-nm and 266-nm. *Journal of Physical Chemistry* 1987, *91* (12), 3248-3253.

169.   Daud, M. N.; Balint-Kurti, G. G.; Brown, A., Ab initio potential energy surfaces, total absorption cross sections, and product quantum state distributions for the low-lying electronic states of N2O. *Journal of Chemical Physics* 2005, *122* (5), 9.

170.   Shafer, N.; Tonokura, K.; Matsumi, Y.; Tasaki, S.; Kawasaki, M., The Doppler Spectra of O(1D) from the Photodissociation of O2, NO2, AND N2O. *Journal of Chemical Physics* 1991, *95* (9), 6218-6223.

171.   Johnston, H. S.; Selwyn, G. S., New Cross-Sections for Absorption of Near Ultraviolet-Radiation by Nitrous-Oxide (N2O). *Geophysical Research Letters* 1975, *2* (12), 549-551.

172.   Selwyn, G.; Podolske, J.; Johnston, H. S., Nitrous-Oxide Ultraviolet-Absorption Spectrum at Stratospheric Temperatures. *Geophysical Research Letters* 1977, *4* (10), 427-430.

173.   Hickman, C. G.; Shaw, N.; Crawford, M. J.; Bell, A. J.; Frey, J. G., 266 nm Photolysis of HOCl and DOCl - Laser-Excitation Fluorescence Detection of OH and OD. *Journal of the Chemical Society-Faraday Transactions* 1993, *89* (11), 1623-1630.

174.   Barnes, R. J.; Sinha, A.; Michelsen, H. A., Assessing the contribution of the lowest triplet state to the near-UV absorption spectrum of HOCl. *Journal of Physical Chemistry A* 1998, *102* (45), 8855-8859.

175.   Shaw, N.; Bell, A. J.; Crawford, M. J.; Frey, J. G., Photolysis of HOBr and DOBr at 266-nm - OH and OD Product-State Distributions. *Journal of the Chemical Society-Faraday Transactions* 1994, *90* (6), 817-823.

176.   Barnes, R. J.; Lock, M.; Coleman, J.; Sinha, A., Observation of a new absorption band of HOBr and its atmospheric implications. *Journal of Physical Chemistry* 1996, *100* (2), 453-457.

177.   Ingham, T.; Bauer, D.; Landgraf, J.; Crowley, J. N., Ultraviolet-visible absorption cross sections of gaseous HOBr. *Journal of Physical Chemistry A* 1998, *102* (19), 3293-3298.

178.   Loock, H. P.; Qian, C. X. W., Photodissociation studies on nitrosyl bromide: I. Photofragment spectroscopy and electronic structure. *Journal of Chemical Physics* 1998, *108* (8), 3178-3186.

179.   Tanaka, Y.; Kawasaki, M.; Matsumi, Y.; Fujiwara, H.; Ishiwata, T.; Rogers, L. J.; Dixon, R. N.; Ashfold, M. N. R., The ultraviolet photodissociation of Cl2O at 235 nm and of HOCl at 235 and 266 nm. *Journal of Chemical Physics* 1998, *109* (4), 1315-1323.

180.   Becker, S.; Braatz, C.; Lindner, J.; Tiemann, E., Investigation of the Predissociation of SO2 - State-Selective Detection of the SO-Fragment and O-Fragment. *Chemical Physics* 1995, *196* (1-2), 275-291.

181.   Prahlad, V.; Kumar, V., Temperature dependence of photoabsorption cross-sections of sulfur dioxide at 188-220 nm. *Journal of Quantitative Spectroscopy & Radiative Transfer* 1997, *57* (5), 719-723.

182.   Hess, W. P.; Leone, S. R., Absolute I-Star Quantum Yields for the ICN A-State by Diode-Laser Gain-vs-Absorption Spectroscopy. *Journal of Chemical Physics* 1987, *86* (7), 3773-3780.

183.   Davis, H. F.; Lee, Y. T., Photodissociation dynamics of OClO. *Journal of Chemical Physics* 1996, *105* (18), 8142-8163.

184.   Wahner, A.; Tyndall, G. S.; Ravishankara, A. R., Absorption Cross-Sections for OClO as a Function of Temperature in the Wavelength Range 240-480 nm. *Journal of Physical Chemistry* 1987, *91* (11), 2734-2738.

185.   Xu, H.; Joens, J. A., CS2 Absorption Cross-Section Measurements from 187 nm to 230 nm. *Geophysical Research Letters* 1993, *20* (11), 1035-1037.

186.   Larsen, J. J.; Sakai, H.; Safvan, C. P.; Wendt-Larsen, I.; Stapelfeldt, H., Aligning molecules with intense nonresonant laser fields. *Journal of Chemical Physics* 1999, *111* (17), 7774-7781.

187.   Stapelfeldt, H.; Seideman, T., Colloquium: Aligning molecules with strong laser pulses. *Reviews of Modern Physics* 2003, *75* (2), 543-557.

188.   Li, H. Z.; Franks, K. J.; Hanson, R. J.; Kong, W., Brute force orientation and alignment of pyridazine probed by resonantly enhanced multiphoton ionization. *Journal of Physical Chemistry A* 1998, *102* (42), 8084-8090.

189.   Bulthuis, J.; Vanleuken, J. J.; Stolte, S., Hexapole State Selection and Focusing vs Brute Force Orientation of Beam Molecules. *Journal of the Chemical Society-Faraday Transactions* 1995, *91* (2), 205-214.

190.   Chen, J.; Matsiev, D.; White, J. D.; Murphy, M.; Wodtke, A. M., Hexapole transport and focusing of vibrationally excited NO molecules prepared by optical pumping. *Chemical Physics* 2004, *301* (2-3), 161-172.

191.   Siegman, A. E. In *NEW DEVELOPMENTS IN LASER RESONATORS*, Conf on Optical Resonators, Los Angeles, Ca, Jan 16-18; Spie - Int Soc Optical Engineering: Los Angeles, Ca, 1990; pp 2-14.

192.   Sun, H. Y., Thin lens equation for a real laser beam with weak lens aperture truncation. *Optical Engineering* 1998, *37* (11), 2906-2913.

193.   Roscoe, H. K.; Hind, A. K., The Equilibrium-Constant of NO2 with N2O4 and the Temperature-Dependence of the Visible Spectrum of NO2 - a Critical-Review and the Implications for Measurements of NO2 in the Polar Stratosphere. *Journal of Atmospheric Chemistry* 1993, *16* (3), 257-276.